Local approach to fatigue of concrete

Local approach to fatigue of concrete

Proefschrift

ter verkrijging van de graad van doctor aan de Technische Universiteit Delft, op gezag van de Rector Magnificus, prof. drs. P.A. Schenck, in het openbaar te verdedigen ten overstaan van een commissie aangewezen door het College van Dekanen op 29 oktober 1991 te 16.00 uur door

Dirk Arend Hordijk

geboren te Westmaas
civiel ingenieur

Dit proefschrift is goedgekeurd door de promotor:
Prof. dr. -Ing. H.W. Reinhardt

Acknowledgements

Contents page

1 Introduction

1.1 Scope

In the last fifteen years or so, the fatigue behaviour of concrete has received considerable attention from investigators in the field of concrete structures. There are several reasons for the interest in this type of loading for concrete. Firstly, the use of new types of structures subjected to dynamic loadings, like wind and/or wave loading. Examples include offshore platforms, which came on the scene especially after the oil crisis in the nineteen seventies. Secondly, the use of higher strength concrete and lightweight concrete, as well as reductions in safety margins, have resulted in more slender structures in which the dead load forms a smaller part of the total load. Thirdly, it is recognized that the material properties may be significantly affected by repeated loading. Despite all this, the importance of fatigue of the concrete in reinforced concrete structures is sometimes doubted. This is mainly because no clear concrete fatigue failures are known from the literature. For this reason, CEB General Task Group 15[88] "Fatigue of Concrete Structures" collected and evaluated case histories of problems in which fatigue may have contributed to the structural damage. Although no fatigue collapses of concrete structures were found, it could be concluded that fatigue was a contributory factor in the progressive deterioration observed in most of the cases studied.

In the Netherlands an extensive research programme concerning fatigue of concrete was performed under the auspices of CUR research committee C 33 "Alternating load" (CUR [83,84,88,89]); see also Cornelissen[84] and Siemes[88]. Several thousand experiments were performed in order to study concrete fatigue behaviour under tensile, compressive and tensile-compressive loading, while constant amplitude, variable amplitude and random loadings were applied. This investigation yielded an enormous amount of data, like the so-called S-N curves. Such information is very valuable, since it serves as input for fatigue analyses based on Miner sums. However, the investigations did not explain the cause and mechanism of concrete fatigue behaviour. In order to gain more insight in the mechanism, it is necessary to study the fatigue phenomenon on a theoretical basis. In steel structures, it is known that fatigue cracks initiate at points of stress concentrations in the material. These stress concentrations may be due to flaws present in the material or may be caused by discontinuities in the geometry of the structure. After the crack is initiated, its propagation is studied with the aid of fracture mechanics. In this report, a similar *local approach to fatigue* will also be applied to concrete. In the author's opinion, this has so far only been done by Gylltoft[83]. In the approach for concrete, it is assumed that a crack already exists. Such a crack may result from some kind of mechanical loading, but an imposed deformation due to shrinkage or temperature may also cause cracking.

In the case of short-term static loading these cracks mostly have no consequences, since their existence has been taken into account. Following cyclic or fatigue loading, however, this crack will propagate, resulting in redistributions of stress and increased deformations. It may then be possible that the serviceability limit state of the structure is reached due to excessive deformations and/or cracking. Obviously, the crack growth can be of great importance, especially for concrete structures in harsh environments.

Examples of concrete structures in which crack growth may occur due to fatigue or some kind of cyclic loading are: bridges, towers, offshore rigs, crane runways, tall buildings, windmills and roads (see figure 1.1). As far as loading is concerned, this may be caused by environmental factors such as wind, waves, temperature differences and freezing, or it may be due to mechanical effects such as the passage of vehicles, machine tool loading and impacts.
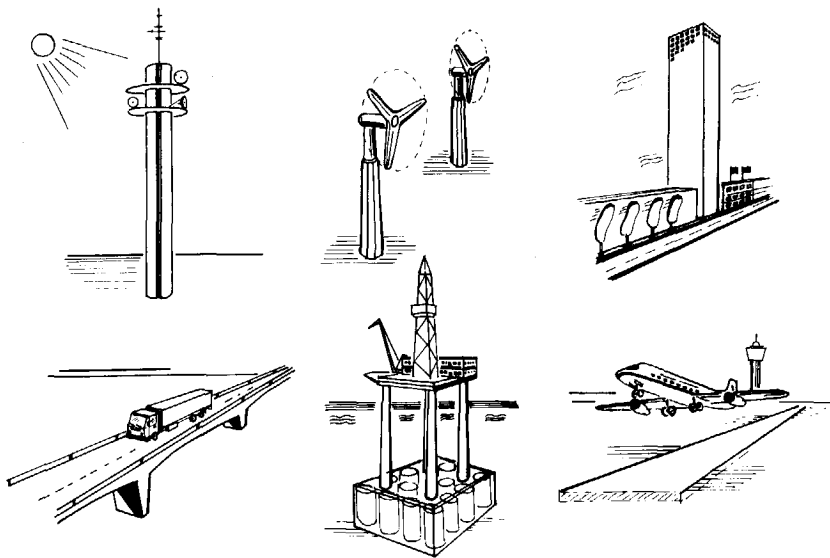
Figure 1.1   Examples of structures subjected to dynamic or cyclic loading.

As part of this study, the tensile behaviour of concrete is investigated. Interest in this material property of concrete has increased enormously in recent years. The most important reason for this is the introduction of fracture mechanics in the field of concrete structures and, because of the advent of much more powerful computers, the increasing importance of numerical techniques. Today, phenomena like bending, (punching) shear and bond between steel and concrete can be studied more thoroughly, while it can also be clearly shown that the tensile property of concrete is a relevant parameter in these phenomena.

1.2 Aim

The main objective of this study is to improve the knowledge about the causes and mechanism of concrete fatigue. For that reason the aim is to develop a model based on fracture mechanics. Since the description of the concrete tensile properties forms an essential part of this modelling, but also because only few experimental data are available on these properties and their dependency on several variables, a substantial part of this research project is related to concrete tensile behaviour. In this respect, the intention is to improve the deformation-controlled uniaxial tensile testing procedure and to supply information about the dependency of fracture mechanics parameters on several variables.

1.3 Outline of contents

A number of chapters can easily be read without studying the remainder of the report. Therefore, the contents of the various chapters will be described in brief.

In *Chapter 2* some basic facts will be discussed about the tensile behaviour of concrete, as known from the literature. Furthermore, a review of the fatigue behaviour of concrete and available models will be given. *Chapter 3* describes the approach that is adopted in this study, while *Chapter 4* contains information about the applied equipment and test procedure.

In this study it was found that the deformation-controlled uniaxial tensile test is always accompanied by a so-called structural behaviour. That affects the results in the sense that the deduced stress-deformation relation or stress-crack opening relation do not represent the actual material property. The results of a thorough investigation of this phenomenon, which is apparently effective not only in tensile tests, are presented in *Chapter 5*.

Based on experimental results, a new constitutive model for the tensile behaviour (including post-peak cyclic loading), is proposed in *Chapter 6*. The model is compared with other available models and its validity is checked by comparisons with experimental results known from the literature.

The way in which a number of variables affect the tensile behaviour of concrete, or the fracture mechanics parameters included in it, is the subject of discussion in *Chapter 7*. The effect of a certain variable may be an undesired structural behaviour like the influence of initial stresses due to differential shrinkage (variable: curing condition) as well as a material property, like the influence of the maximum aggregate particle size.

But the influence of a certain loading history is also studied. The parameters discussed are: type of concrete, maximum aggregate size, concrete quality (or water-cement ratio), curing condition (including water content) and compressive preloading.

In order to verify the proposed material model, a number of experiments were performed in which mode I fracture is the leading mechanism. Results of these experiments and simulations using different numerical techniques are presented in *Chapter 8*. For simulation of the experiments, analyses were made using the DIANA FE code, the multi-layer model and a hybrid method.

In *Chapter 9* numerical predictions of the fatigue behaviour of plain concrete are presented. The results are compared qualitatively with fatigue results known from the literature. *Chapter 9* also presents some experimental results of fatigue experiments. The aim of these experiments was to measure deformations during fatigue loading more accurately.

Finally, concluding remarks can be found in *Chapter 10*.

2 Characteristics of concrete tensile and concrete fatigue behaviour

2.1 General

In this chapter the main characteristics of the behaviour of concrete under tensile and fatigue loading will be discussed. It is not the intention to give a complete survey of the literature on these subjects, but rather to discuss the basic phenomena that have been observed in different types of experiments. First, some remarks on the level of observation for the concrete in this report.

Level of observation
Concrete is an inhomogeneous material consisting of larger aggregates embedded in a matrix material. In its turn, the matrix material consists of smaller aggregates and cement paste. When describing the material behaviour of concrete, one should as in the case of any other material define the level of observation for which certain models are valid. If the concrete is looked upon as a two-phase material as described above, then one should take irregular stress distributions into consideration. These stress irregularities are due to the difference in Young's modulus between the aggregates and the matrix material and due to existing pores and micro-cracks. Concrete, however, can also be considered at a level where the irregular stresses can be regarded to be averaged. In this report this latter level, referred to as the "macro-level", is considered when modelling the concrete behaviour. This means that concrete will be treated as a homogeneous, isotropic continuum. In this continuum it is assumed that, after reaching the tensile strength, a crack will arise perpendicular to the direction of the maximum tensile stress. For the sake of clarity, the term 'crack' is used here for a crack in which stresses cannot be transferred as well as for a softening zone (see Section 2.2).

The experimental results that are obtained from different types of tests also belong to the macro-level. To explain these results, however, the concrete will in most cases have to be considered at a level one level lower than the macro-level; i.e. a two-phase material including micro-cracks.

2.2 Tensile behaviour of concrete

Compared to the compressive behaviour of concrete, its tensile behaviour has received only very little attention in the past. Various reasons for the increased interest in the tensile behaviour of concrete have already been mentioned in Section 1.1. This report focuses on the behaviour of a concrete bar loaded uniaxially in tension. In other words:

the different types of fracture mechanics models, like those originating from elastic fracture mechanics, and the more recently proposed models for concrete, will not be discussed here. As regards the behaviour of concrete in deformation-controlled uniaxial tensile tests, the reader is also referred to Hordijk[89c]. Here, the knowledge about the tensile behaviour of concrete will be discussed by sketching a little bit of the history.

History

Compared to compression tests on concrete, tensile tests are much more difficult to perform because of difficulties in applying the load properly. Over the years, for instance, special grips and specimen shapes, like the dog-bone type specimens, have been designed in order to prevent stress concentrations. The best way seemed to be the method of glueing the specimen to the loading platens.

In the early investigations the tensile load was increased (load-controlled) until the specimen fractured (figure 2.1a). As long ago as 1928 Gonnerman and Shuman[28] performed a comprehensive investigation in which the load was applied by special grips. It was not until about 1960 that, in analogy to what was observed in compression, it was investigated whether a post-peak behaviour also exists for tensile loading (figure 2.1b). The first extensive investigation into this was by Rüsch and Hilsdorf[63]. They were the first to identify several difficulties which occur in such a test and which only became clear many years later (see also Hordijk[89c]). They were already making use of a servo-control system, a very advanced method in those days. Other investigators loaded steel bars in parallel with the tensile specimen (for instance, Evans and Marathe[68]) in order to obtain a descending branch.
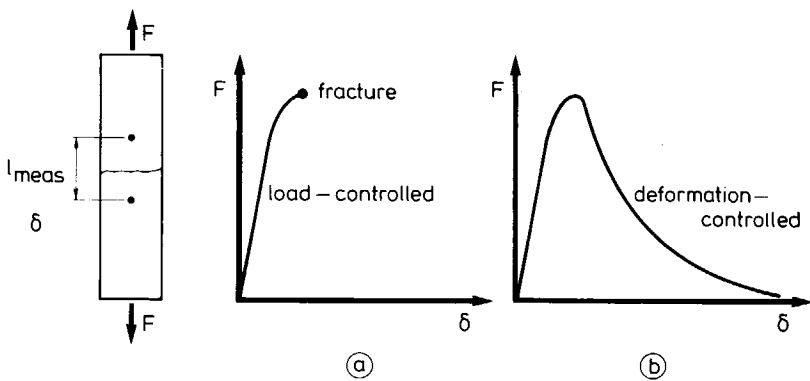
Figure 2.1   Schematic representation of the behaviour of concrete in a
load-controlled (a) and a deformation-controlled (b) tensile test.

6

In the early investigations the results were presented in stress-strain relationships. In the experiments, however, it is not a strain which is measured, but a deformation over a certain measuring length. By assuming a uniform stress distribution over this measuring length, this deformation results in a strain. In the pre-peak region, this is more or less acceptable. In the post-peak region, however, the total deformation is the sum of elastic deformation and crack opening, so that a representation by strain has no meaning. This was demonstrated in a thorough investigation by Heilmann et al.[69]. Previously, however, Evans and Marathe[68] had also recognized this phenomenon. In fact, both publications refer to Blakey and Beresford[55], who had apparently already observed this behaviour in the tension zone of bending tests in 1955. This behaviour implies that fracture of concrete in tension is a local phenomenon.

In 1976 Hillerborg et al.[76] proposed the "fictitious crack model" for the fracture behaviour of concrete. This model, which is still a major model in FE simulations and other fracture mechanics analyses of concrete, assumes the existence of a "fictitious" crack ahead of a visible crack (see figure 2.2a). In this respect a visible crack is understood to mean a crack that cannot transfer tensile stress, while in the "fictitious" crack (also called the process zone), so-called crack-closing stresses are active. This model resembles the Dugdale-Barenblatt model (Dugdale[60], Barenblatt[62]) for yielding materials, where a plastic zone with crack-closing stresses is assumed ahead of a crack tip (see figure 2.2b). In the Dugdale-Barenblatt model, however, the crack closing stresses are equal to the yield stress of the material, while in a softening material like concrete, the stress depends
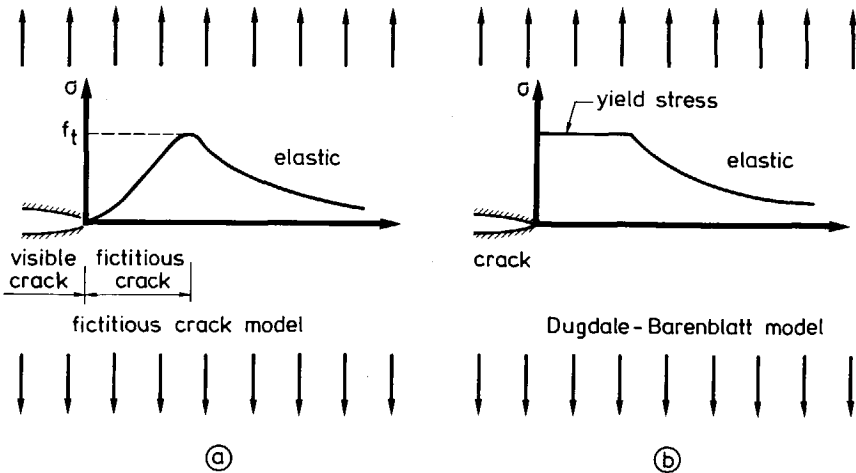
Figure 2.2   Assumed stress distribution ahead of a visible crack according to a
model for a softening material like concrete (a) and a
model for a yielding material (b).

on the crack opening in the fictitious crack. The relation between crack opening and stress can be obtained from a deformation-controlled uniaxial tensile test.

Concrete behaviour in a deformation-controlled uniaxial tensile test
When a concrete bar is strained in uniaxial tension (figure 2.3), it first reacts elastically. A linear load-deformation relation almost up to the peak load will be obtained. At a macro-level the stresses and strains are uniformly distributed over the specimen and the load-deformation relation for the specimen (concrete tensile bar) can therefore be directly replaced by a stress-strain relation for the material (concrete). At peak load the strains start to localize within a narrow zone of micro-cracks (process zone or softening zone), after which a continuous macro-crack will develop. The process zone will occur at the weakest section of the tensile bar. If the process zone develops within the measuring length whose deformation is used as control parameter, then a load-deformation relation, as indicated by line I in figure 2.3, will be obtained. The load that can be transferred decreases with an increasing deformation of the process zone. As a result of this load reduction, the concrete outside this zone unloads (line II in figure 2.3). As mentioned before, due to the fact that the deformation in the descending branch is built up by strains and crack opening, it is no longer correct to use strain (deformation divided by measuring length) for the horizontal axis instead of deformation.
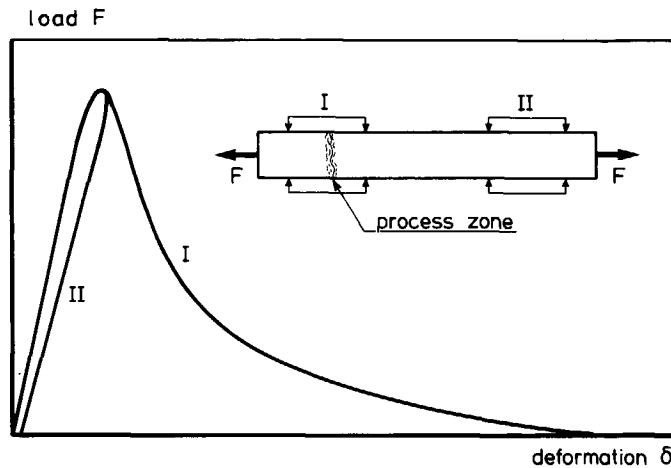
Figure 2.3   Load-deformation relations for a concrete bar under uniaxial tensile loading.

According to the fictitious crack model by Hillerborg and co-workers, the behaviour of concrete under tensile loading can be split into a stress-strain relation for the concrete outside a crack (process zone), and a stress-crack opening relation for the crack itself (see

figure 2.4). More or less similar to this model is the crack band model by Bazant and Oh[83]. In that model, however, the width of the process zone is taken into account, which results in a stress-strain relation for this crack band width instead of a stress-crack opening relation for an infinitely small width.
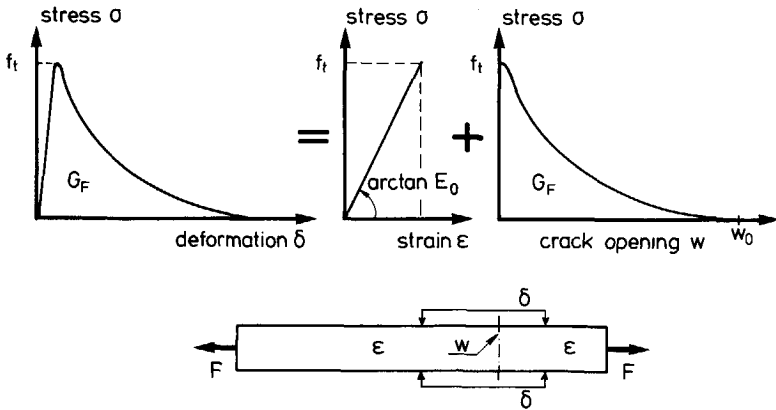
Figure 2.4   Separation of the complete tensile stress-deformation relation for concrete into a stress-strain and a stress crack opening relation according to the fictitious crack model.

Stress-deformation relation as influenced by measuring length
As explained above, the deformation measurement over the process zone in a uniaxial tensile test on concrete always consists of two contributions. The first contribution is the crack opening, which is the result of opening micro-cracks in the process zone, and the second contribution is the elastic deformation over the total measuring length. When varying the measuring length, the first contribution remains constant, while the latter one changes. Figure 2.5 shows the influence of the measuring length on the load-deformation relation for material parameters corresponding to a normal-weight concrete with $f_{cc} \approx 50$ MPa. It can be seen that the descending branch becomes steeper for an increasing measuring length. In this example, a measuring length of 500 mm yields a σ-δ relation with a so-called "snap-back". If this measuring length is used as control parameter for the deformation, then a sudden jump will occur, as indicated by the dashed line. In most experimental set-ups, the equipment will not be fast enough to overcome such a jump and the result will be unstable fracture. Nevertheless, if the equipment can survive such a jump, then the obtained stress-deformation relation no longer represents the actual material behaviour. In the past, insufficient stiffness of the test rig has mostly been regarded as the main cause of unstable post-peak tensile behaviour. Although the stiffness of the equipment is still important for performing a stable deformation-control-led tensile test, the measuring length of the feed-back signal also appears to play an

important role. Finally, it can be remarked that the same phenomenon is also of great importance in numerical analyses.
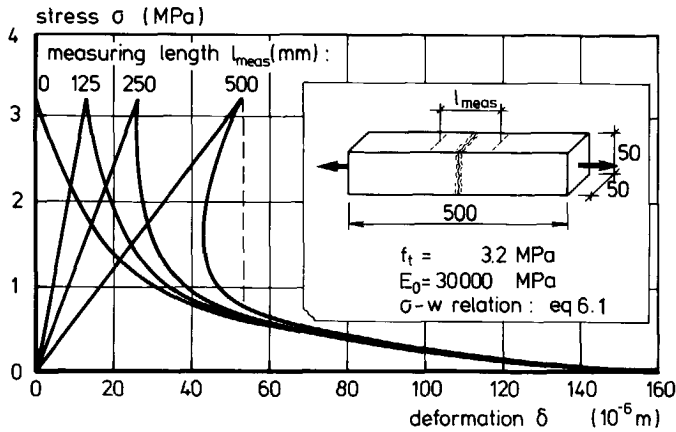
Figure 2.5   Stress-deformation relation as influenced by measuring length.

Tensile test results blurred by several effects

So far, the behaviour of concrete in a deformation-controlled uniaxial tensile test has been discussed for an ideal test performance. There are, however, several effects that may blur the results of a deformation-controlled tensile test. Or to put it even more plainly, the ideal situation will never occur in an experiment. In this section, no attention will be paid to these effects, like structural behaviour and the influence of initial stresses, because they are subject of study in several parts of this report.

In the description given of the tensile behaviour, a distinction is also made between the process zone, where fracture occurs, and the rest of the specimen which remains linear-elastic. In fact, tensile fracture of concrete is a localized phenomenon. Although the author believes that such an assumption is valid for most tensile tests, there are some situations in which one should also consider damaging effects in the rest of the specimen (bulk behaviour). In this respect, fatigue and compressive preloaded concrete can be mentioned (see also Section 7.6).

2.3 Concrete fatigue behaviour

For a comprehensive review of the fatigue behaviour of concrete, the reader is referred to the state of the art report produced by RILEM committee 36- RDL "Long term random

10

dynamic loading of concrete structures" (RILEM[84]) and to Cornelissen[86d]. Here, the main findings for concrete fatigue behaviour will be presented, with emphasis being placed on the observed tendencies rather than on quantitative descriptions.

Like in the case of static loading, a distinction can be made between the different loading types, as there are compression, tension, bending and bond between concrete and steel. It appeared, however, that qualitatively more or less the same results were found for these different loading types. See in this respect, for instance, the results by Balázs[86], for bond behaviour under repeated loading. It should also be mentioned, however, that the fracture type of a member, especially a prestressed member, may be different under fatigue loading from that under short-term static loading (RILEM[84]).

As far as cyclic loading or fatigue is concerned, a distinction is generally made between low cycle high amplitude fatigue and high cycle low amplitude fatigue. The former involves few load cycles of high stress at a lower rate of loading (earthquakes, storms, etc.), while the latter is characterized by a great number of cycles of low stress at a higher rate of loading (traffic loading, wind and wave loading, etc.). Although there is no clear distinction between these two loading types, usually 10^3 to 10^4 cycles is chosen as the limit between loading types.

S-N curve or Wöhler curve
The main characteristic of fatigue behaviour of concrete, but also of other materials, is that the number of load cycles, N, that can be performed before failure occurs, increases for a decreasing upper load level. When the relative upper load (or stress) level is plotted against the logarithm of the number of cycles to failure, then a linear relation will be found (see figure 2.6a). These types of curves are known as Wöhler curves or S-N curves. The fatigue strength, which is defined as the fraction of the static strength that can be supported repeatedly for a given number of load cycles, can be taken from the S-N curve.

Generally, a significant scatter in fatigue results can be observed. It has been demonstrated that the scatter in the number of cycles to failure is largely due to variations in the static strength (Cornelissen[84]). In contrast to steel, no fatigue limit of concrete has been found until now. Compressive fatigue strengths ranging from 57 to 67 per cent of the static strength have been reported for 2 million cycles and a zero lower stress level (Holmen[79]). The fatigue strength as can be obtained from figure 2.6a is not a constant value because it depends on the lower stress level applied in the cycles. For instance, for 1 million cycles and a zero lower stress level a fatigue strength equal to 60% of the static tensile strength has been reported, while for a small compressive lower stress level this value can reduce to about 40% of the static tensile strength, as will be shown below.

11
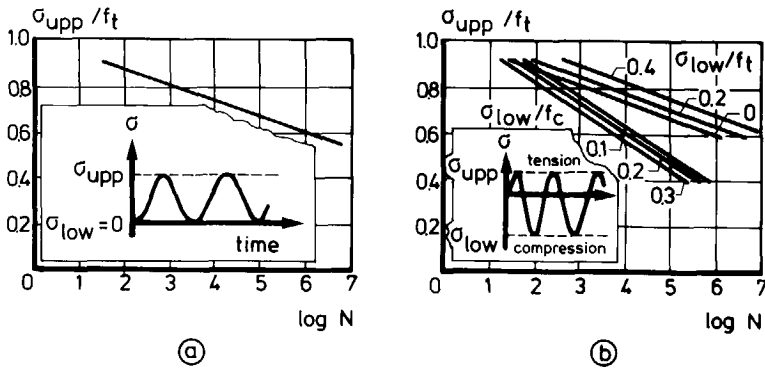
Figure 2.6   Relation between relative upper stress level and number of cycles to
failure (Wöhler curve or S-N curve) (a) and the influence of the
lower stress level (b) (Cornelissen[84]).

Influence of lower stress level

To show the influence of the lower stress level on the number of cycles to failure, a result
obtained from tensile fatigue tests is plotted in figure 2.6b. As can be seen from this figure,
a decreasing lower stress level results in a decreasing number of cycles to failure.
Furthermore, stress reversals appeared to have a more detrimental effect on tensile
fatigue than repeated tensile stresses. To show the combined influence of the lower and
upper stress levels on the number of cycles to failure, a Goodman diagram or a Smith
diagram is usually drawn. An example of a Goodman diagram is presented in figure 2.7.
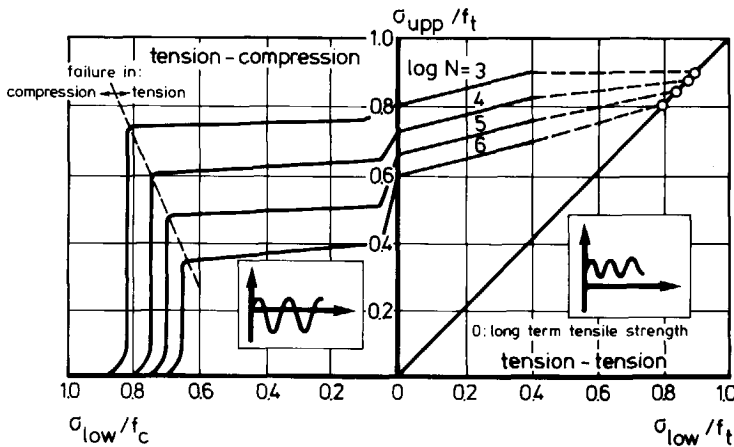
Figure 2.7   Goodman diagram for concrete (Cornelissen and Siemes[85]).

12

Cyclic creep curve

If the deformations are recorded during a fatigue test on concrete and plotted against the number of cycles performed, then a curve will generally be obtained that is known as a cyclic creep curve (figure 2.8). This curve is characterized by three specific parts. First, the increase of deformation per cycle decreases with increasing number of cycles n. This first branch of the curve is followed by a secondary branch where this increase is constant. Then, just before failure occurs, the increase of deformation per cycle increases rapidly. The same type of curve can also be found by plotting the deflection in a bending test or the slip in a bond test (see Balázs[86]) against the number of cycles. For compressive tests Holmen [79] reported the three different stages to be about 10, 70 and 20 per cent of the fatigue life (N) respectively.

strain ε or deformation δ

arctan $(\dot{\varepsilon}_{sec}/\omega)$

secondary branch

number of cycles n
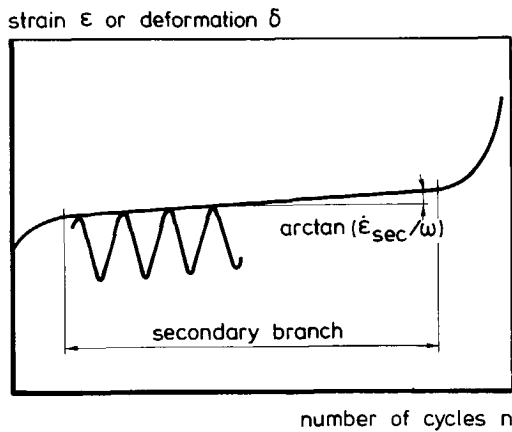
Figure 2.8   Schematic representation of a cyclic creep curve.

Holmen [79] studied the development of the modulus of elasticity in a compressive test during fatigue loading. A typical result showing the reduction of the secant modulus with the number of cycles is plotted in figure 2.9.

Relation between secondary creep rate and number of cycles to failure

There appeared to be a strong relation between the increase of strain per cycle in the secondary branch of the cyclic creep curve and the number of cycles to failure (see figure 2.10). Hence, the remaining life of a cyclically preloaded specimen can be assessed by measuring the total strain variation. This further indicates that the ultimate strain can be used as a fatigue failure criterion for concrete. A formal strain at fracture can be

13

calculated as:

$$\varepsilon = \frac{d\varepsilon}{dn} N = \frac{d\varepsilon}{dt} \frac{dt}{dn} N = \dot{\varepsilon} \frac{N}{\omega} \tag{2.1}$$

with ω =frequency. For the logarithm of the strain at fracture this results in:

$$\log \varepsilon = \log \dot{\varepsilon} + \log N - \log \omega \tag{2.2}$$

In figure 2.10 it can be seen that $\log \dot{\varepsilon} + \log N$ is practically constant for ω is constant. For $\omega = 6\,Hz$ we find that $\log \varepsilon = -4.2 - \log 6 = -5.0$ (corresponding to $\varepsilon = 10^{-5}$).
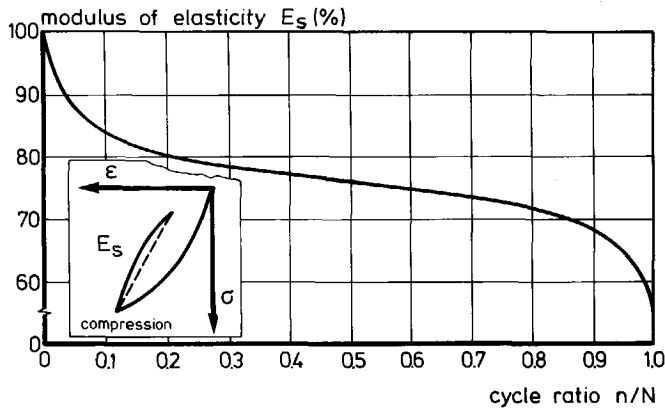
Figure 2.9   Development of the secant modulus of elasticity in a compressive fatigue test (Holmen [79]).

Influence of loading frequency

The number of cycles to failure depends not only on the applied stress levels, but also on the testing frequency. The fatigue life in terms of number of cycles to failure appeared to be lower for the lower applied frequency (0.06 Hz) than for the higher one (6 Hz) (Cornelissen [84]). This indicates that the damage is not only due to the cyclic loading, but that there is also a time effect. In figure 2.10 it can be seen that for equal secondary creep (per unit time) the number of cycles to failure at 0.06 Hz is approximately 100 times less than at 6 Hz. As a result the strain at fracture for $\omega = 6$ Hz and $\omega = 0.06$ Hz is the same.

Sequence effect

So far, the discussed results of fatigue tests were mainly related to constant amplitude tests. This means that loading cycles were performed with constant values for the lower and upper load levels. When two different stages of constant amplitude loading are applied subsequently, a "sequence effect" can be observed. This means that the fatigue life depends on the order of application of the two stages. Consequently, Holmen[79]

14

observed a shorter fatigue life in compressive fatigue tests with first a number of load cycles at a given upper stress level, followed by load cycles at a lower upper stress level, compared with the reverse order of load application.
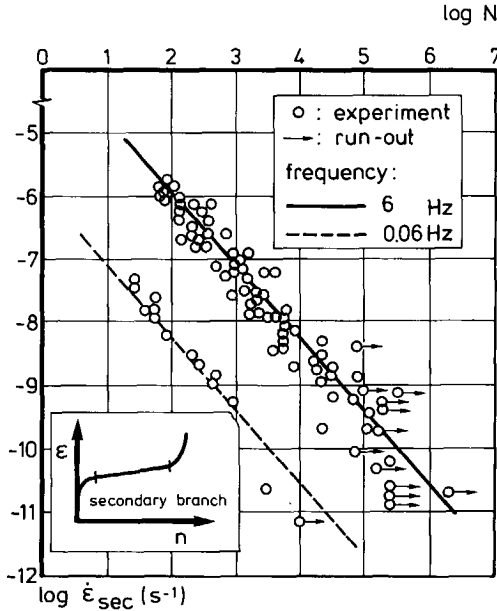
Figure 2.10   Relation between secondary cyclic creep rate in tensile fatigue and number of cycles to failure (CUR [88]).

Strength increase after fatigue preloading
When fatigue tests are performed at a rather low upper stress level, it may sometimes occur that no failure is found after a great number of load cycles. Then the experiment is stopped and in the presentation of the fatigue results, this test is denoted with the term "run-out" (see also figure 2.10). In his experiments, Holmen[79] also encountered a number of run-out specimens (stopped after twelve million cycles at a maximum stress level of 60%). He subsequently loaded these specimens statically to failure. When comparing the results of these specimens with similar specimens which had not undergone repeated loading, he observed an increase in strength of about 7 per cent. Besides the increase in strength, the stress-strain curve also differed significantly (figure 2.11). The specimen that was preloaded with repeated loading displayed a stress-strain curve that was much straighter than that of the "virgin" specimens. According to Holmen, similar results, with a strength increase up to 15 per cent, have also been reported by other investigators. In results by Cornelissen and Reinhardt[86c], a small increase for the reloading tensile

strength can be observed in the case of tensile-tensile preloading and a decrease in the case of tensile-compressive preloading.
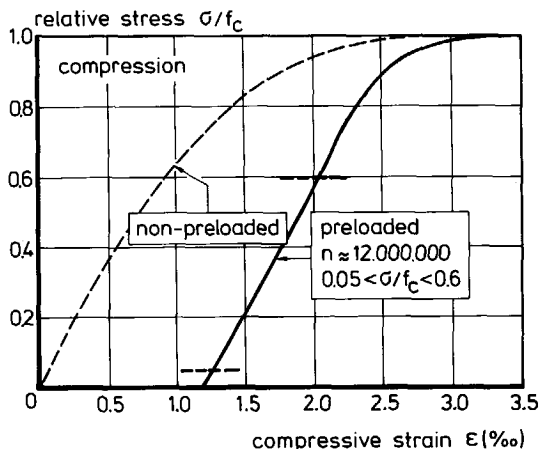
Figure 2.11   Shape of the compressive stress-strain curve of non-preloaded specimens and a preloaded specimen (Holmen [79]).

General remarks
For the different phenomena as observed in fatigue tests and qualitatively described above, empirical relations have been given by several investigators. For more information on the different expressions for the relation between, for instance, stress levels and number of cycles to failure, the reader is referred to, among others, Holmen[79] and Cornelissen [84].

Fatigue strength did not appear to be affected by variables such as mix proportions, age and curing conditions, i.e. the static and the fatigue strength are affected in about the same proportion. In case of variables like wet concrete, high strength concrete and low frequency, reduced relative fatigue strengths were found (Cornelissen[88]).

2.4 Fatigue modelling

Two basic approaches are used for the fatigue life assessment of structural elements. One approach is based on fracture mechanics and considers the propagation of a crack. This method is in very common use in fatigue analyses in metals, where linear elastic fracture mechanics (LEFM) can be applied. Generally, the same method cannot be applied for concrete elements, since LEFM is not applicable to normal-sized concrete structures.

16

Nevertheless, if the behaviour of the softening zone in front of a visible crack is modelled properly and if a finite element method (FEM) is used, a fracture mechanics approach is still possible for concrete. In the author's opinion this fatigue approach based on nonlinear fracture mechanics has so far only been used by Gylltoft[83] and Reinhardt et al.[86] and is the basic approach of this study.

The other method is based on the empirically derived S-N curves. This method, which is very simple and is known as the Palmgren-Miner hypothesis, is much more important for engineering practice than the method based on fracture mechanics. Codes for concrete structures comprise more and more design rules for fatigue calculations. These rules are based on the Palmgren-Miner hypothesis (for a review of some of them, see Siemes[88]).

Finally, as already mentioned in Section 2.2, it may be possible to define a fatigue failure criterion based on strains or deformations. Below, the basics of the different approaches will be further explained.

Palmgren-Miner hypothesis
From experiments, the number of cycles to failure for loading variations between two fixed stress levels are known. In actual structures, however, the stress cycles vary greatly in magnitude, number and sequence. In the Palmgren-Miner hypothesis (Palmgren[24], Miner[45]) the supposition is that damage accumulates linearly with the number of cycles applied at a particular stress level. The failure criterion is written as:

$$\sum_{i=1}^{k} \frac{n_i}{N_i} = 1 \tag{2.3}$$

where n_i is the number of cycles at stress level i, N_i is the number of cycles to failure at stress level i and k is the number of stress levels.

The hypothesis does not accurately reflect the concrete's properties. One reason for this, for instance, is that sequence effects are not taken into account. Nevertheless, it is applied in design practice, first of all because it is simple, secondly, because no better method is available and, thirdly, because the description of concrete behaviour under random loading is adequate enough for most cases.

Approach based on fracture mechanics
The discipline of fracture mechanics is mainly concerned with the local treatment of the conditions around the crack tip in a body. Since for metals fatigue failure is very clearly associated with the development of a crack, fracture mechanics is a suitable tool for

studying fatigue of those materials. The development of a crack can be subdivided into three stages (figure 2.12a); crack initiation, crack propagation and unstable crack growth. The similarity to the behaviour observed in fatigue tests on concrete (compare figure 2.8) is evident. The difference between the fatigue behaviour in steel and concrete relates to the visibility and measurability of the crack. For concrete, the approach is more indirect, because it is only possible to measure the elongation of the total specimen or to measure the deformation for a certain measuring length.
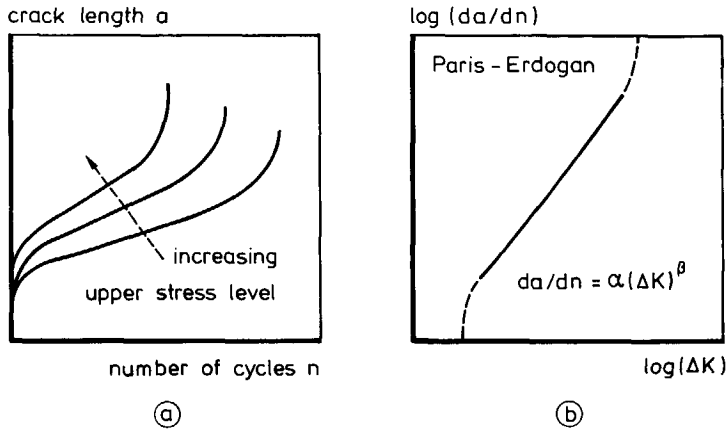
Figure 2.12   Typical fatigue results for metals; a) crack length versus number of cycles and b) crack propagation law.

The initiation of a crack is often associated with points of stress concentrations in the material, which may be due to flaws, surface discontinuities or changes in shape. However, most of the research into the fatigue phenomenon in metals deals with the crack propagation stage. The best known crack propagation law was suggested in 1963 by Paris and Erdogan[63]. The law reads (figure 2.12b):

$$\frac{da}{dn} = \alpha\,(\Delta K)^{\beta} \tag{2.4}$$

in which a is the crack length, ΔK is the stress-intensity factor and α and β are constants. ΔK depends on the geometry and the upper and lower stress level in accordance with:

$$\Delta K = \gamma(\sigma_{max}-\sigma_{min})\sqrt{(\pi a)} \tag{2.5}$$

in which γ is a geometrical factor.

This crack propagation law and most of the others that have been proposed are empirical. The parameters of the laws must be obtained from experimental findings. For a better understanding of the fundamentals of fatigue, the phenomenon of crack propagation has to be studied more theoretically. A possible way of doing that is to describe the behaviour in front of the crack tip more closely, especially for cyclic loading, and to perform FE analyses.

For concrete, a theoretical model based on the fictitious crack model and a constitutive relation for cyclic behaviour in the softening zone was proposed by Gylltoft[83]. By means of FE analyses incorporating this model, it was possible to study low cycle high amplitude fatigue of a plain concrete beam under four-point loading. Stress redistribution and crack propagation (increase in deflection) as a function of the number of cycles were studied. Furthermore, it was possible to obtain numerically a S-N curve for the notched beam (figure 2.13). The same approach was used by Reinhardt et al.[86] and will be applied in this study. The only differences are in the description of the cyclic behaviour in the softening zone.
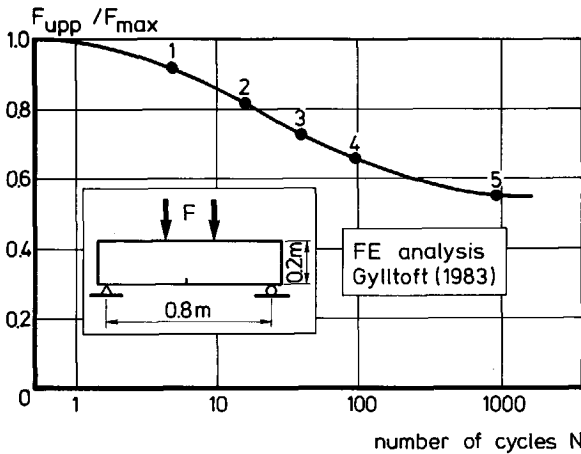
Figure 2.13   Numerical result for the relation between upper load level F_{upp} as proportion of maximum load in a static analysis and the number of cycles to failure.

Failure criterion based on deformations
In several investigations, the strong relation between the development of strain and the number of cycles to failure was observed. Subsequently, the possibility of a fatigue failure criterion based on ultimate strain was surmised several times. In the author's opinion, such a failure criterion will require an investigation in which the development of defor-

mations in a fatigue test and deformations in a deformation-controlled static test are compared (see also Chapter 3). One investigation was found in which a model was proposed along these lines. Balázs[86] assumed for bond behaviour a relation between the cyclic creep curve in a fatigue test and the stress-slip relation in a static test, as shown in figure 2.14. The slip at peak load in a static test is assumed to coincide with the end of the secondary branch in the cyclic creep curve.
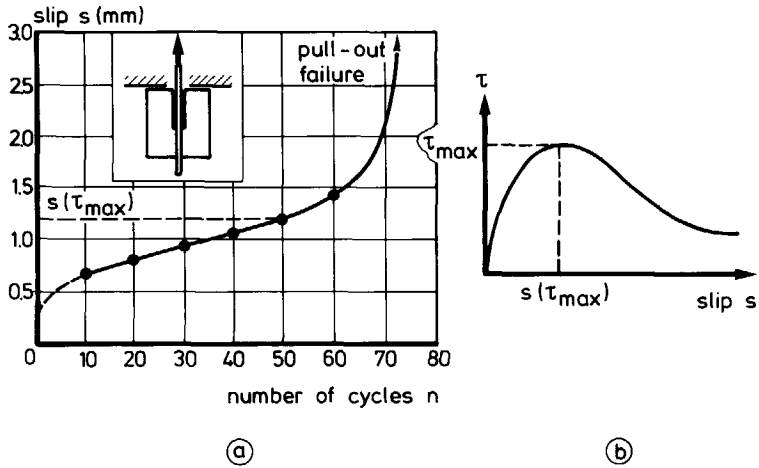
Figure 2.14   Relation between slip at peak load in a static pull-out test and the end of the secondary branch of the cyclic creep curve in a fatigue pull-out test (Balázs [86]).

3 Approach for the tensile and fatigue study

3.1 General

In this report, the approach for studying the cause and mechanism of concrete fatigue behaviour is based on nonlinear fracture mechanics. Via this approach fatigue crack growth will be investigated. Attention will also be paid to the possible existence of a fatigue failure criterion based on ultimate deformations. Therefore, the results of numerical analyses will be used. Besides the results of a close inspection of some tensile fatigue tests also provide information in this respect. In the approach, deformation-controlled uniaxial tensile tests play a very important role. Since the results of such tests may be affected by experimental conditions, like specimen dimensions and stiffness of the test rig and by such conditions as the curing procedure of the specimens, the influence of these variables on the test results is first investigated. Furthermore, the influence of some other variables on the tensile behaviour of concrete will also be investigated.

3.2 Approach based on nonlinear fracture mechanics

The approach is based on the fictitious crack model in combination with a description for the cyclic behaviour of concrete in the softening zone. It is similar to what has been done by Gylltoft[83]. The only difference is in the constitutive relation for the crack cyclic behaviour. Gylltoft based this relation on an energy criterion, as will be discussed in Section 6.4, while the present study proposes a new constitutive model based on a close inspection of experimental results. Now the approach will be further explained.

From deformation-controlled uniaxial tensile tests on concrete, it is known that a loading cycle in the post-peak region of the σ-δ relation displays a behaviour as sketched in figure 3.1. It appears that after an unloading-reloading cycle, the curve will not return to the same point of the envelope curve where it started from, but to a point which belongs to a lower stress. This phenomenon is due to the damage which is caused in such an unloading-reloading loop. Obviously, some mismatch of the crack surfaces will occur at unloading, resulting in a propagation of existing micro-cracks. From experiments, it is known that the envelope curve is not significantly affected by the cyclic loading.

In figure 3.2 the stress-state in front of a visible crack after n loading cycles ($n \geq 0$) is plotted (solid line). Suppose that this is part of a total structure which is loaded up to a certain load F. If this structure is subjected to another unloading-reloading cycle, then we know from the post-peak tensile behaviour (figure 3.1) that the various areas in the
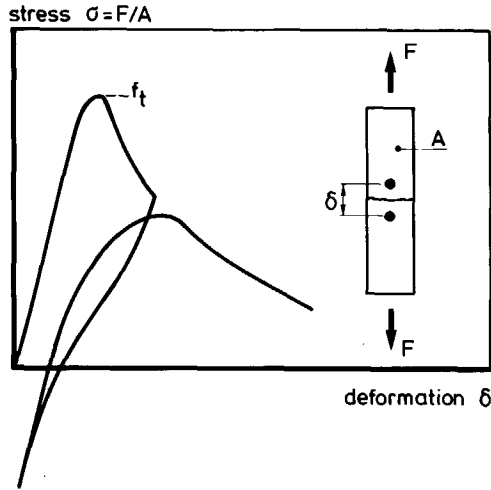
Figure 3.1   Post-peak cyclic tensile behaviour of concrete.

softening zone cannot attain the same stress as they had at the beginning of this load cycle. This means that for the same maximum external load F, an internal stress-redistribution has to take place. The dashed line in figure 3.2 plots a possible stress-distribution after the load cycle. The actual new stress distribution depends on the total structure in combination with its load application. Nevertheless, the basic idea is that the softening zone propagates under cyclic or fatigue loading. Furthermore, it can be assumed that deformations increase with the number of load cycles and that this will continue until
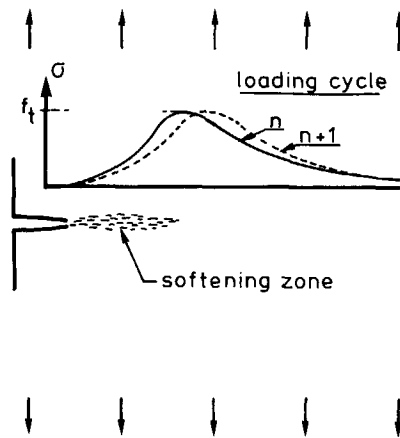
Figure 3.2   Assumed stress distribution near a crack; before and after a loading cycle.

22

equilibrium can no longer be found. For the load-deformation relation of the structure, it means that in that case the descending branch is reached. To illustrate this, figure 3.3 shows an assumed load-deformation relation for a certain structure under a continuously increasing deformation. The maximum load bearing capacity is equal to F_{max}. If the same structure is loaded cyclically, loops as sketched in figure 3.3 will probably be found. The loops shift a little to the right each time a loading cycle is performed. This will proceed until, in a certain cycle, the reloading curve meets the descending branch which forms the boundary for combinations of load and deformation that fulfill the requirement of equilibrium. Then failure of the structure occurs.
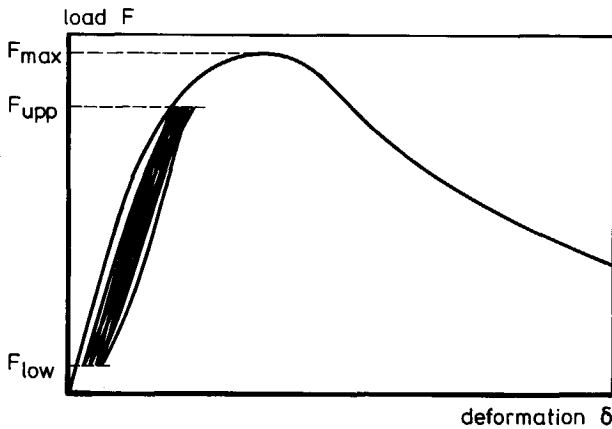
Figure 3.3 Schematic representation for the load-deformation relation of a structure loaded under continuous increasing deformation or cyclically loaded between F_{low} and F_{upp}.

To enable the proposed model to be used for studying the fatigue behaviour of concrete, the following steps have to be taken (see figure 3.4). First, the post-peak tensile behaviour has to be determined experimentally in deformation-controlled uniaxial tensile tests. Then, on basis of the observed behaviour, a constitutive model for the stress-crack opening relation will be proposed and implemented as a mathematical subroutine in a FE code. The validity of the material model will be verified by numerical simulation of some specimens loaded cyclically. Four-point bending tests on notched beams and tensile tests on single notched plates will be used for that purpose. Finally, the FE code will be used to perform fatigue analyses for the four-point bending beam. It will be interesting to see if the results from these analyses coincide with the phenomena that are found in fatigue tests (see Section 2.3).
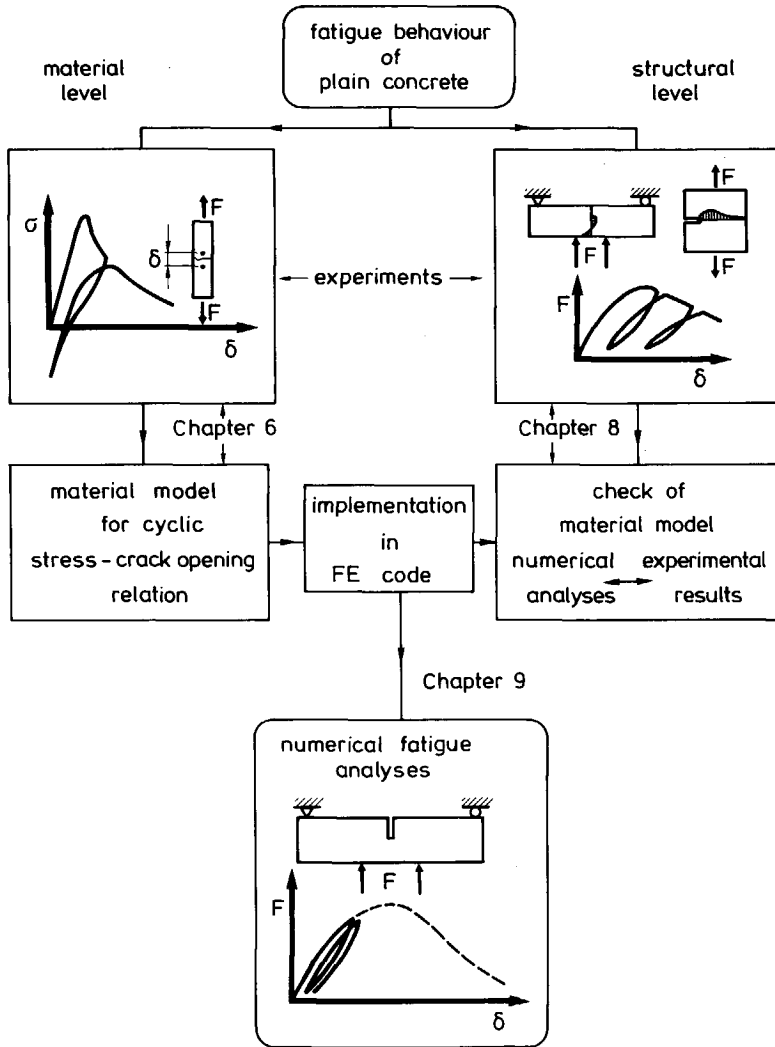
Figure 3.4   Different steps in the study of the fatigue behaviour of plain concrete.

Numerical fatigue analyses are rather time-consuming. Therefore, a special purpose programme will be made to study several fatigue phenomena. In that programme only a small zone encompassing the softening zone (smeared crack approach) will be modelled, while the rest of the specimen is modelled simply by means of springs (bending theory). Despite the rather crude way of modelling, the programme is very suitable for studying various phenomena. It will be used for studying the structural behaviour in a static tensile test on concrete (Section 5.5), as well as for studying fatigue crack growth in the bending tests (Section 9.3).

24

3.3 Fatigue failure criterion based on deformations

So far, fatigue test results for compression as well as for tension have always been presented by means of applied stress levels and the development of strain. As far as tensile fatigue behaviour is concerned, it is questionable whether the presentation by strains is a correct one. For static tensile tests, for instance, it is now clear that fracture is confined to only a small zone, while the rest of the specimen reacts more or less in a linear-elastic manner.

On the basis of experimental results from some tensile fatigue tests, it is intended to study the development of deformations in a fatigue test in relation to those in a static test. By doing this, more information can perhaps be obtained concerning the following questions:

− What is the relation between deformations in a static test and deformations in a fatigue test (see figure 3.5)?
− To what extent are the deformations measured in a tensile fatigue test due to crack extension in the final failure zone (localized behaviour) or due to increased deformations in the rest of the specimen (bulk behaviour)?
− Is there a failure criterion based on deformations?

These and other questions will be dealt with in the following chapters.
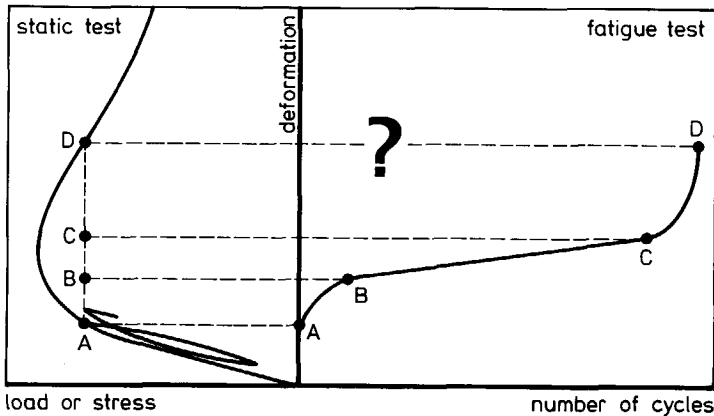
Figure 3.5   Schematic representation of a possible relation between deformations in a static test and in a fatigue test.

4 Experimental technique

4.1 Introduction

Experimental results from deformation-controlled tensile tests (static and post-peak cyclic), tensile fatigue tests and bending tests are presented in this report. All these results have been obtained on one and the same tensile-compressive loading rig (figure 4.1). In this chapter, the testing rig and the generally applied procedure for specimen preparation and test performance will be described. More specific information regarding the performed test series can be found in Appendix A, which sets out experimental data such as mix composition and 28-day mechanical properties.
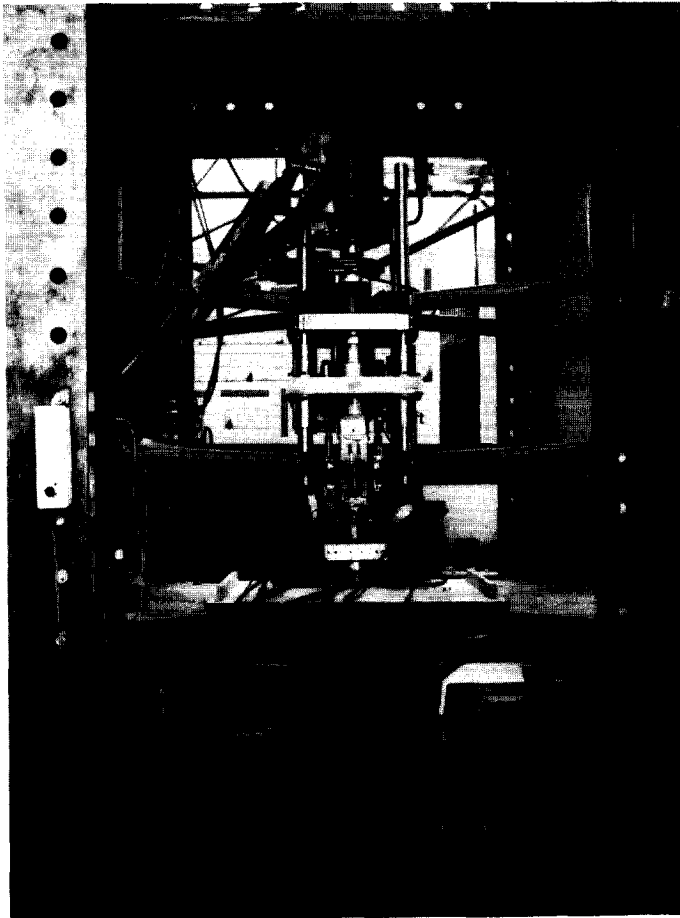
Figure 4.1   Photo of the testing rig used.

History of the testing rig

The tensile equipment was first built at the end of the nineteen seventies and has been adapted over the years. A schematic representation of the testing rig initially applied can be seen in figure 4.2a. Cylindrical specimens ø120*300 mm^3 were used. This equipment was used in conducting a comprehensive investigation into the tensile and tensile-compressive fatigue behaviour of plain concrete (see Cornelissen[84]). For the deformation-controlled uniaxial tensile tests, the intention was to create a crack or softening zone, while the deformation distribution over this zone would be uniform during the entire test. It appeared, however, that the crack opening was extremely non-uniform. Consequently, it was decided to design a guiding system in order to prevent rotation of the loading platens (see figure 4.2b). Meanwhile, the specimen dimensions were reduced to
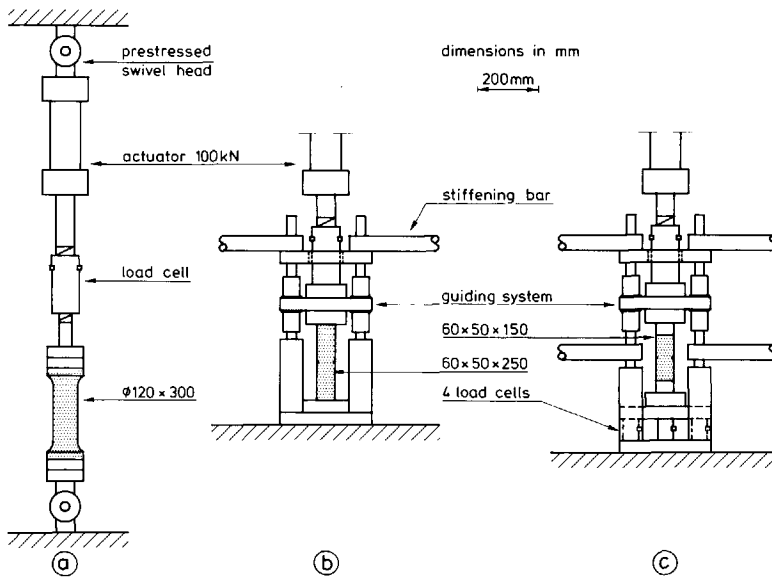
Figure 4.2   Adaptations to the tensile equipment; from a to c in chronological order.

60*50*250 mm^3 with two saw cuts, resulting in a middle cross-sectional area of 50*50 mm^2. The results presented by, for instance, Reinhardt[84a] were obtained on this same equipment. One of the test series which will be presented in this report (denoted as "preliminary") was also performed using this device. Close inspection of the results showed that even with this equipment it was not possible to prevent the crack opening from being non-uniform. Then it was realized that not only the rotational stiffness of the loading platens was responsible for this result, but also the rotational stiffness of the specimen itself. This phenomenon, to which Chapter 5 of this report is devoted, was then

27

extensively investigated. The next step was to reduce the specimen length from 250 mm to 150 mm.

For the guiding system, ball bushings were used in order to minimize friction in the system. This is important since the load cell was positioned outside this guiding system. Nevertheless, it appeared that a small frictional force (≈ 250 N) was still active in the system. For a cross-sectional area of $50*50$ mm^2, this means an average stress of about 0.1 MPa. This error in stress corresponds to only about 3% of the tensile strength of the concrete. In the tail of the descending branch, however, it becomes very important. Furthermore, it changes sign when reversals in the deformation direction are performed. Therefore, an inner loading platen was designed with four 50 kN load cells underneath it (see figure 4.2c). Four instead of three load cells had to be applied due to a lack of space and because of rotational stiffness requirements. In addition, for the rotational stiffness of the loading platens (upper and lower platen together) a value of 10^6 Nm/rad was calculated. For the translational stiffness of the test rig a value of 148 kN/mm was measured.

Test series
A number of different test series were performed. Results can be found at several places in this report. The tests series can roughly be divided into three groups. The first and largest group consists of deformation-controlled uniaxial tensile tests on narrow specimens. This includes static (continuously increasing deformation) and post-peak cyclic tests. Results can be found in Sections 5.3, 6.3, 6.4, Chapter 7 and Sections 8.1 and 9.4. The second group concerns verification tests. This includes deformation-controlled tests on notched beams under four-point bending as well as single edge notched plates under uniaxial tension. Results of these tests are presented in Chapter 8. Finally, a limited number of uniaxial tensile fatigue tests were performed. The results of these can be found in Section 9.4. In the remainder of this chapter, the essentials for the different types of test will be described.

4.2 Manufacturing of the specimens and applied measuring devices

Specimens
Except for a few experiments, all specimens were sawn out of plates with a thickness of 50 mm. Two types of mould were used. For the bending specimens, three slabs $500*300*50$ mm^3 were cast vertically in a battery mould, while similarly, five slabs $300*300*50$ mm^3 were cast for all other types of specimen. The density of the mixes was determined by means of an air entrain meter. Two days after casting, the slabs were demoulded and subsequently cured under water for two weeks. Then specimens with the

desired dimensions were cut out of the slabs. For the generally applied procedure of curing condition, the specimens were stored in the laboratory (20°C, 60% relative humidity) until testing.

Together with each mould, six cubes with a 150 mm edge were cast to determine of the 28-day splitting strength and compressive strength. These cubes were demoulded together with the slabs and cured under water until testing at the age of 28 days.

Load and deformation measurement
For the load measurement, the four 50 kN load cells placed under the lower loading platen were used. For the tensile tests ($F_{max} \approx 7.5$ kN), these load cells are active in only a very small range of their capacity. Calibration with a load cell between the loading platens showed that the resolution (see for instance figure 7.3a) and accuracy were sufficient for these tensile tests.

For the deformation measurements, two different types of electro-mechanical measuring devices were applied. LVDTs (linear variable differential transducers) and a type of clip gauge were used. These clip gauges were supplied with two strain gauges which, after calibration, could be used to determine the deformation. In the remainder of this report, these gauges will be referred to as "extensometers". For both types of measuring devices small supports were designed which could be used to glue them to the specimen. The cross-sectional area of the glue surface was $5*10$ mm^2. For the measuring length, the arbitrary distance between the centre of two supports was taken. An example of extensometers and LVDTs can be seen in the photos of figure 4.3a and figure 4.9a respectively. The signals of the LVDTs and extensometers were amplified, sent to a personal computer, converted from analog to digital and stored on a floppy disk.

As far as the data-acquisition system is concerned, it can be mentioned that special requirements had to be fulfilled regarding resolution of the measuring devices, amplification of the signal and AD conversion. For the tensile tests, with a peak load at a deformation of about 5 μm (for l_{meas} = 35 mm), a resolution of well below 1 μm was required. For the fatigue tests with a difference in deformation of about 1 μm between the ascending and descending branch, the requirements regarding resolution were even more stringent (see Section 4.5).

4.3 Deformation-controlled uniaxial tensile tests

By far the majoriy of the experiments were deformation-controlled uniaxial tensile tests on narrow specimens. Several different specimen dimensions were used, but generally a

150*60*50 mm^3 specimen with two saw cuts reducing the middle cross-sectional area to 50*50 mm^2 was applied. In order to apply the tensile load to the specimen, the procedure of glueing the end-faces to the loading platens was applied. Figure 4.3 shows a specimen glued in the testing rig and a schematic representation of it.
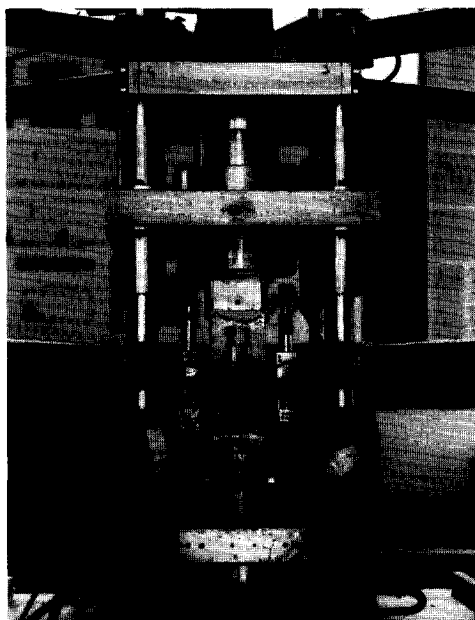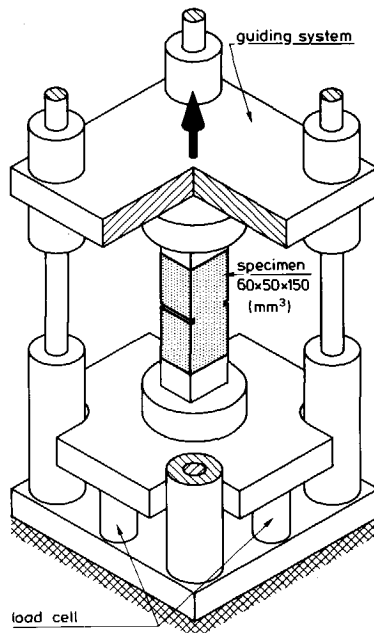
Figure 4.3   Photo (a) and schematic representation (b) of a tensile specimen glued in the testing equipment.

Specimen preparation
Before testing, the exact dimensions of the specimen were carefully determined. Then the end-faces of the specimen were prepared for glueing. The applied procedure was that the end-faces with a sawn surface were coated with a polyester resin (Setarol 3606 MV manufactured by Kunsthars Synthese B.V., the Netherlands). When this coating was sufficiently hardened (mostly, one or more days elapsed between coating and further preparation), the surface was sandpapered until it looked dull. Then the steel supports for mounting the measuring devices to the specimen were glued to the specimen.

Glueing procedure
Two different types of two-component glue proved suitable for this test and have been used through the years. These are, respectively, F88 manufactured by Tridox Products

30

(Philadelphia, USA) and Plexilit 7742F (powder) with Pleximon 801 (fluid) manufactured by Röhm Chemische Fabrik (Darmstadt, Germany). The end-faces of the specimen were coated with glue, after which the specimen was placed between the loading platens. Then the specimen was loaded with a small compressive force (about 500 N). In order to prevent the glue from being pressed away completely, small pieces of cardboard were glued to the end-faces in advance. These pieces (ø 7 mm) also ensured a certain thickness of the glue layer, which was about 1.5 mm.

For clarity's sake it should be mentioned that the described procedure proved successful for most of the experiments, but that fracture near the glue surface also sometimes occurred. It seems impossible to describe a procedure which ensures that this undesired type of fracture is prevented. It should be obvious, however, that the ratio between cross-sectional area in the fracture zone and that of the glue layer is a parameter that can be varied in order to minimize such a type of fracture. Apart from fracture due to insufficient adhesion between the glue and the steel loading platen or between the glue and the concrete surface, several causes can be mentioned for a so-called glue fracture. In such cases, however, this is an incorrect name since fracture actually takes place in the concrete near the glue surface. One possible cause, for instance, is a three-dimensional tensile stress state, resulting from prevented lateral deformations due to the stiff loading platens (see also Hordijk[89c]). A difference between lateral deformations of the concrete end-face and the glue (or steel) may occur due to a too small glue layer (Hughes and Chapman[65]) or drying shrinkage of the specimen (Rüsch and Hilsdorf[63]). Obviously, these effects become more important with an increasing size of the glue surface and an increasing time between glueing the specimen in the equipment and testing. In the experiments, glue fracture occurred not only in the pre-peak region, but also in the descending branch, where one would expect the situation to become less critical due to a decreasing overall stress. However, this can be explained by the phenomenon of non-uniform crack opening, which will be discussed in Chapter 5 and which causes non-uniform stress distributions.

Deformation measurements and applied control parameter
Two different bases (35 mm and 110 mm) were applied for the deformation measurements. The arrangement of these measuring devices was not the same for all test series. Initially, the intention was to check the uniformity of the crack opening. Therefore, four (or in the preliminary test series even five) measurements (l_{meas} = 35 mm) were taken at the front and rear sides of the specimen (see figure 4.4a). After the results showed that the deformations for the four extensometers on one side were more or less in line with each other, these measurements were confined to only two on one side (see figure 4.4b). Appendix A gives an overview of the different arrangements applied for the measuring

devices. For the determination of Young's modulus, sometimes the measurement with the 110 mm extensometers and sometimes the difference between those of the 110 mm and the 35 mm extensometers were used.
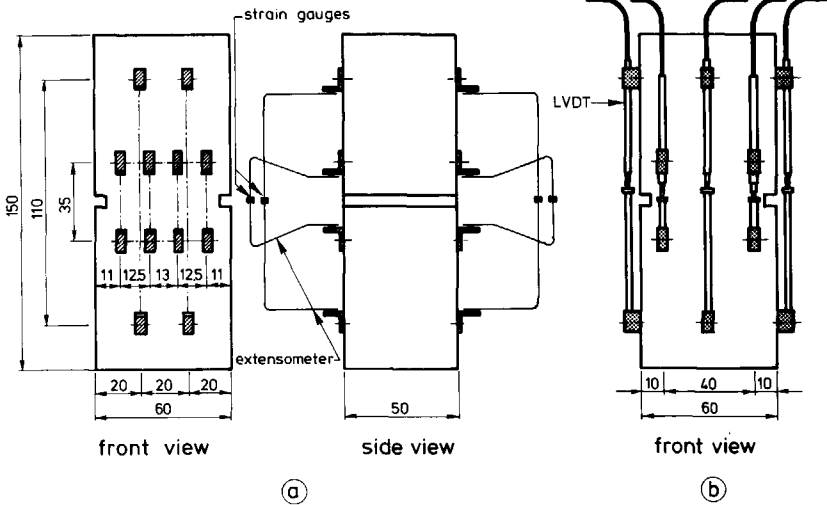
Figure 4.4   Two arrangements of measuring devices applied.

Besides these deformation measurements, two LVDTs (one on each specimen side) were used as control parameter. In the early experiments, a base of 50 mm was used for these LVDTs, while for the verification tests (Section 8.1) the base was 15 mm (supports for the LVDTs placed directly next to the saw cuts). In a number of test series, no special measurements were made for the deformation control parameter, but the average signal of four LVDTs with a base of 35 mm was used for that purpose. It should be noted that generally the applied control parameter will probably have no influence on the results obtained. Though, of course, in the case of steep slopes in the descending branch, or even load drops due to, for instance, a "snap-back", the 15 mm base is preferable to the 50 mm base and, due to three-dimensional non-uniform crack opening (see Chapter 5), using the average signal of the deformations on the four corners of the specimen is preferable to taking the mean signal of only two measurements. For the prepeak part of the σ-δ curve the loading rate depends on the applied deformation rate in combination with the measuring length for this deformation. For the experiments, a loading rate of 0.08 μm/s corresponding to a measuring length of 50 mm was applied. It can be remarked that l_{meas} is not important for the descending branch since deformations in that part are mainly due to crack opening. Furthermore, a change in deformation rate of one order did not seem to influence the results significantly.

Test performance

Before the specimen was placed in the loading equipment, a fist scan was performed, of which the load was used as reference (zero load) during test performance. After the specimen was glued in the loading equipment and the glue pressure was removed, a second scan was performed which was used as reference for the deformation measurements. Then the test was started and scans were taken at regular intervals. During test performance, the results appeared directly on the screen of a PC and scan time could be changed manually.

For the deformation control, the measured deformations were compared with a specially designed ramp generator. In the post-peak cyclic tests, the direction of deformation was reversed either along the envelope curve, when the loading dropped by a certain amount (≈ 120 N), or at a preset lower force level which could be tensile or compressive. There was also an option for reversing the deformation direction manually at any point in the loading history.

After the deformation reached a certain value (mostly in the range from 100 to 140 μm), the test was stopped, after which the specimen was fully separated manually into two parts. Then some final measurements were taken of which the average value for the load was taken as the actual zero load for the experiments. In the subsequent analysis of the test results, this zero load in combination with the first linear part of the σ-δ curve was used to determine the origin for the σ-δ relation (reference deformation for a zero load).

4.4 Verification tests

A test series was performed in which different types of fracture tests were applied to specimens made from the same type of concrete originating from one and the same batch. Besides the normally applied tensile tests on narrow specimens, the experiments in this test series, denoted as "verification tests", are: bending tests on notched beams and uniaxial tensile tests on single edge notched plates. Figure 4.5 shows the different specimens. Three different depths, 10, 30 and 50 mm, were applied for the notches in the bending specimens (total height: 100 mm).

Bending tests

In order to perform the bending tests on the same equipment, a specially designed loading arrangement was used which could be directly mounted in the tensile equipment (see figure 4.6). It was chosen to use a four-point bending test instead of a three-point bending test in order not to have a support in the fracture zone, since this would introduce compressive stresses parallel to the fracture zone. Furthermore, the load and its reactions
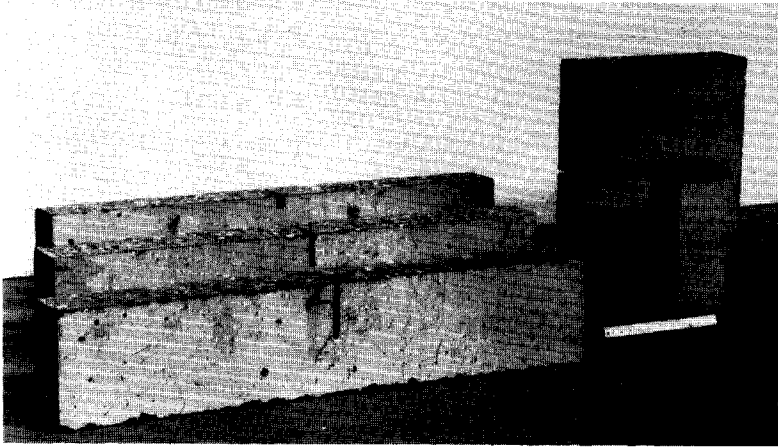
Figure 4.5   Specimens applied for the test series "verification tests".

in the supports are introduced by tensile bars which could easily undergo horizontal movements. Frictional forces in the supports which may be reasonably active in the three-point bending test usually applied and which affect the G_F measurement (see Planas and Elices[89]) are avoided by using this type of support.
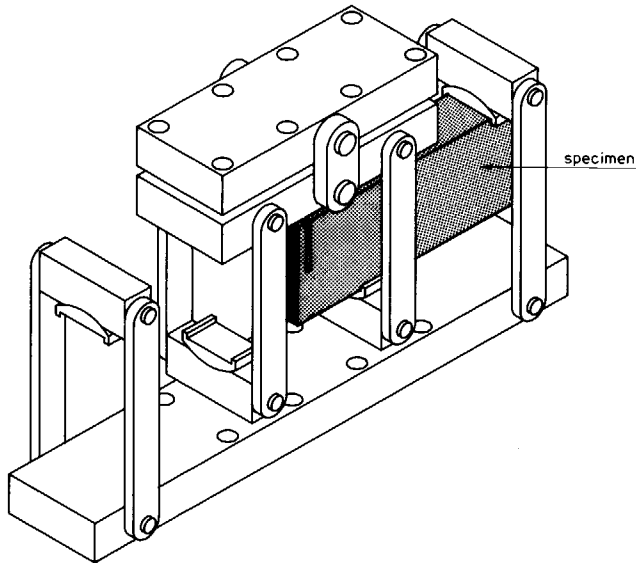
Figure 4.6   Schematic representation of the loading arrangement for the four-point bending tests (specimen plotted partly).

Since the total bending equipment (loading arrangement and specimen) had to be placed in the tensile equipment, for which only a certain maximum amount of free space was available, the specimen height was limited to 100 mm. Then a beam with the dimensions $500*100*50$ mm^3 was chosen (see figure 4.7). The distance between the centres of the outer supports (width: 30 mm) was 450 mm, while the distance between the inner supports was 150 mm. The arrangement of the LVDTs (l_{meas}: 35 mm), which was equal at the front and rear sides of the specimen and which was kept the same for the three notch depths, can be seen in figure 4.7. Two LVDTs, one at the front and one at the rear of the specimen (placed on opposite sides of the notch) were used for measuring the deflection. A steel platen, placed on small steel supports located in the centre of the beam below the outer supports, was used as reference for this measurement. Finally, in figure 4.8 a photo of the total loading arrangement is presented.
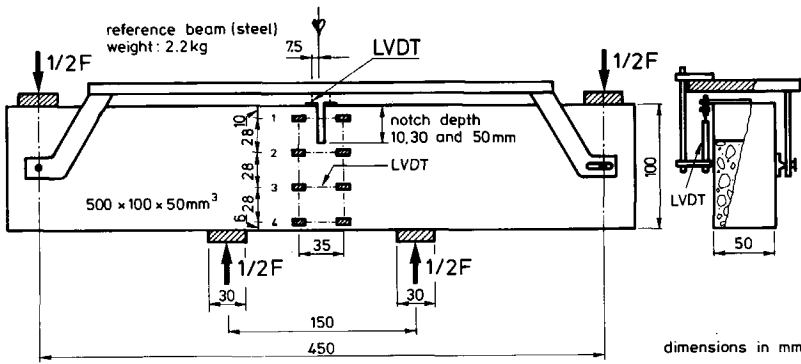
Figure 4.7   Schematic view of a bending test.

A limited number of tests were performed with this equipment. In the analysis (Chapter 8) only one static (continuously increasing deformation) and one post-peak cyclic test are taken into account. In these experiments, the average signal of the two upper LVDTs was used as control parameter. The applied deformation rate was 0.16 μm/s. Similarly as for the previous described uniaxial tensile tests, the load in the load cells was determined before the specimen was placed in the loading equipment and after the specimen had been broken in two halves. With these measurements, taking into account the self-weight of the specimen, the zero load was determined, while again with the first linear part of σ-δ curves the corresponding reference deformation (zero) was calculated.
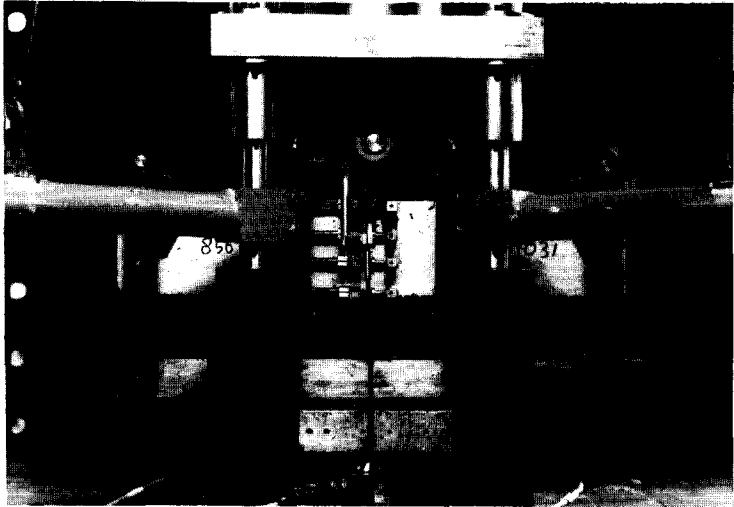
Figure 4.8   Photo of a four-point bending specimen in the testing equipment.

Tensile tests on single notched plates

A picture of a single notched specimen glued in the testing rig can be seen in figure 4.9a. In these experiments, deformations were recorded at five positions over the fracture
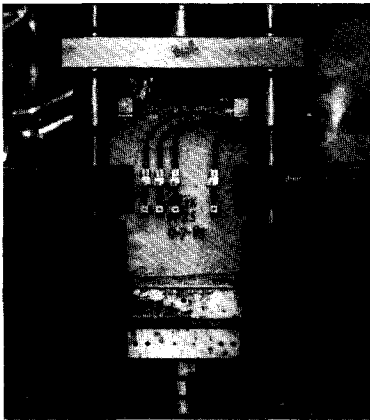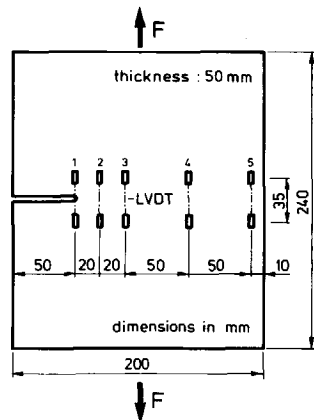
(a)   (b)

Figure 4.9   Photo of a tensile test on a single notched specimen (a) and
arrangement of the measuring devices (b).

zone. The arrangement of these measurements can be obtained from figure 4.9b. The average of two measurements was taken as control parameter. Otherwise, the test procedure is the same as applied for the tensile tests on narrow specimens.

4.5 Uniaxial tensile fatigue tests

In order to investigate several phenomena of the behaviour of a specimen in a tensile fatigue experiment (see Section 3.3), a limited number of tensile-tensile and tensile-compressive fatigue tests were also performed. The results of these experiments will be discussed in Section 9.4. Initially, it was intended to use unnotched specimens. However, due to the fact that fracture mostly occurred near a glue platen, this proved to be impossible. Nevertheless, two experiments on unnotched specimens, one loaded statically and one loaded dynamically, were successful. For the rest of the experiments, notched specimens were applied. The arrangement of the LVDTs as used for these tests was the same as sketched in figure 4.4b (see also appendix A). Furthermore, the procedure of specimen preparation does not differ from that applied for the deformation-controlled uniaxial tensile tests. The test ran load-controlled with cycles between an upper and lower load level. These levels could be chosen freely. For generating the load signal, the equipment applied previously in the Stevin Laboratory (see Cornelissen[84]), was used. The loading frequency was 6 Hz, while the dynamic load was applied gradually so that the upper and lower load levels were attained after about six cycles.

   The difference compared to fatigue tests previously performed is that load-deformation cycles were measured more precisely, while furthermore deformations were recorded at more locations on the specimen. For measuring the deformations at different loading points in a loop, it is necessary to have a measuring system which is able to measure very accurately. This is understandable if it is realized that for a measuring length of 35 mm, the deformations of the unloading and reloading curves in a loop differ less than 1 μm. On the other hand, the measuring system must be very fast. In order to get some idea about the shape of a loop, the number of measuring points in such a loop must not be too small. It is very hard to meet these two requirements at the same time: a measuring system that is accurate as well as fast. A new data-acquisition equipment was specially built for these experiments[*]. The principles of the system will be shown below.

---

[*]   The data-acquisition system was designed by ir. H. Voorsluis, whose help is greatly acknowledged.

For the analog-digital conversion a fast A/D-converter was chosen. The resolution and accuracy that could be attained with that converter was not enough. Therefore, for each measurement, eight samples were averaged. The frequency of the fatigue loading was 6 Hz. This means that every second, 6 loops are performed (see figure 4.10). The principle of the data-acquisition system is such that the first half of each second is used to sample and the second half of the second is used to process the data. In the three loops that are recorded, 75 measuring points are available. For each measuring point, the deformation of eight LVDTs (see figure 4.4b) and the load in the four load cells are recorded. Consequently, 900 (=75*12) measurements are taken in 0.5 seconds (sampling frequency: 14400 Hz). The accuracy of the measurements is already rather good. Nevertheless, in order to improve this, the three loops are averaged. It can be expected that the shapes of the loops in three successive cycles will not differ significantly from each other, except for the cycles in the beginning and at the end of the experiment. For averaging the three loops, the measuring points i, i+25 and i+50 ($1 \le i \le 25$) were averaged. As an example, an experimental result is shown in figure 4.11. The measurement as described above was taken at regular intervals. The first loop that was measured was loop 144. Thereafter, cycles were recorded after intervals equal to $3*2^a$ cycles, in which a has the value 6,7,8 and so on, up to a selected maximum. So far, the procedure for measurements at regular intervals is described.
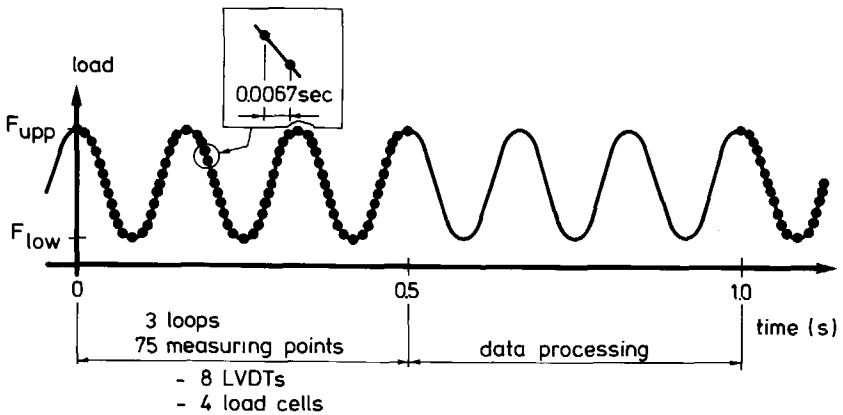
Figure 4.10   Principle of the data acquisition for the fatigue tests.

The most interesting part of the experiment is certainly the last part. In that part, the deformations increase strongly. Since it is intended to compare deformations at the envelope curve in a static test and at failure in a fatigue test (see Section 3.3), it is necessary to record data near failure. For that reason a buffer is used, in which the data of the last 20 seconds are stored. This buffer is updated in each second half of a second in which
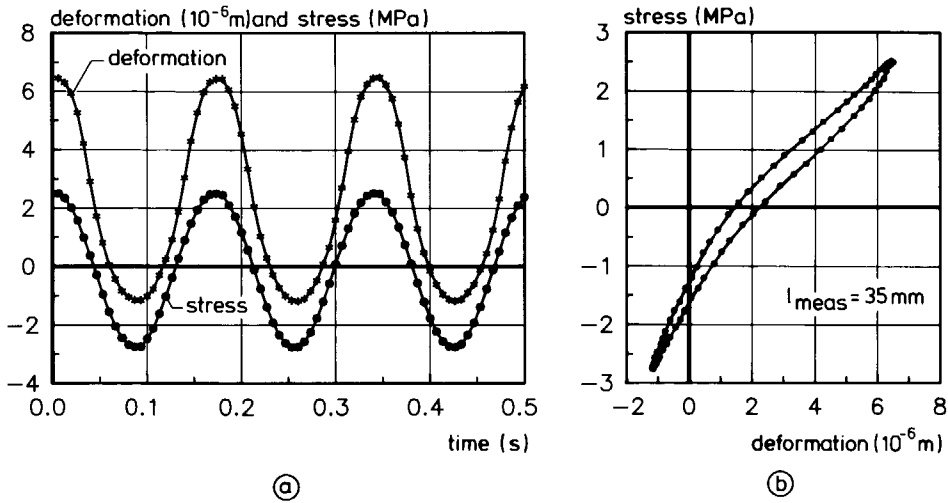
Figure 4.11   Experimental result of 3 loops (not averaged) in a fatigue test;
stress and deformation versus time (a) and corresponding
stress-deformation relation (b).

data processing takes place and therefore contains 20 times the data of three loops (not averaged). As soon as the test is stopped, the data in the buffer can be read and stored in a data-file. In order to detect the ending of the experiment, the recorded load at the upper load level is checked. After failure of the specimen, the upper load level will no longer be reached. When this had occurred a preset number of times, the test and measurements were stopped. It was also possible to stop the experiment after a preset number of cycles.

As far as the above described measurements are concerned, the following remarks can be made. It is not claimed that the data-acquisition system is able to measure reproducible deformations of less than 0.1 μm. It was only intended to improve the measurements in such a way that the unloading and reloading curves in a loop do not cross each other. It is realized that some hysteresis may be present in the measurements. Nevertheless, the development of loops can very well be studied. Furthermore, a difference in temperature between day and night, as well as a difference in temperature due to an open door, may influence these measurements significantly. Therefore, an environmental chamber was built around the specimen, in which the temperature could be kept more or less constant during the experiment.

5 Structural behaviour in a uniaxial tensile test

5.1 Phenomena

The uniaxial tensile test is probably the most fundamental fracture test there is. The former supposition was that this test, when performed under deformation control, directly yields a stress-deformation relation that includes all relevant fracture mechanics parameters. Recently, however, it has been found that this type of test is more complicated than it looks at first sight (Van Mier[86], Hordijk et al.[87]). It appears that it is often accompanied by a phenomenon that can be regarded as structural behaviour. Since basic material models are derived from this test, it may be obvious that it is very important to know exactly the influence of such a structural behaviour on the obtained test results. This structural behaviour will be elucidated in this chapter by means of tensile experiments with specimens of different length (Section 5.3), a finite element analysis (Section 5.4) and a simple numerical model (Section 5.5). Details of these experiments and analyses have been published before (see respectively, Hordijk et al.[87], Rots et al.[87] and Hordijk and Reinhardt[89a]).

A precondition for regarding the obtained σ-δ relation as a material property is a uniform deformation distribution over the fracture zone during the entire test. In most of the reported deformation-controlled tensile tests, however, it appeared that this precondition could not be fulfilled (for a review see Hordijk[89c]). For the purpose of discussing the results from the literature, the deformation-controlled tensile tests will be subdivided into two groups according to the boundary conditions that have been applied. Firstly, there are the testing rigs in which the loading platens can freely rotate (hinges). Most of the early investigations used this type of boundary condition in order to ensure centric load application. The results that have been obtained with such an equipment (Rüsch and Hilsdorf[63], Notter[82], Scheidler[87]) can be schematically represented by the plot in figure 5.1. The centric loading led to equal deformations on both sides of the specimen in the pre-peak region. At peak load, a crack was initiated on one side of the specimen and with further increasing average deformation, this crack opened while the deformations on the opposite side decreased until, finally, compressive stresses acted in that part. In fact, the crack grew gradually through the specimen. After the average deformation had proceeded well in the descending branch, either the test was stopped or instability occurred (Rüsch and Hilsdorf[63]). Since most investigations only give information about an average deformation, it is not known whether this behaviour occurred in every tensile test in which rotation of the loading platens was not prevented. At least one contradictory result is known. Gopalaratnam and Shah[85] reported more or less symmetric deformations for comparable boundary conditions.
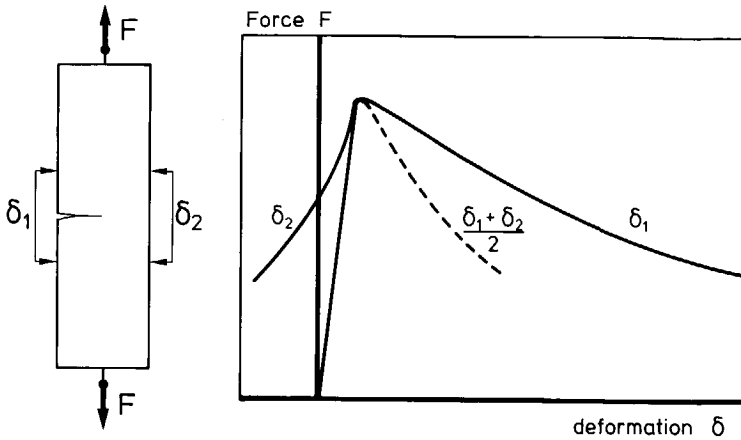
Figure 5.1   Typical result for a tensile test with rotational loading platens.

The other group of tensile testing equipments is characterized by the fact that rotation of the loading platens is counteracted by a certain rotational stiffness (denoted as "non-rotatable" loading platens). For reasons as discussed above, the testing rig of the Stevin Laboratory was equipped with a guiding system which kept the loading platens parallel to each other (see Section 4.1). In the tests on rectangular specimens, the deformation distributions between the saw cuts showed an almost uniform crack opening in every stage except a small part just beyond peak load (Reinhardt[84a]). A subsequent thorough investigation on tests on a normal-weight concrete (NC) and a lightweight concrete (LC) yielded the following observations:

- the non-uniform crack opening was a three-dimensional phenomenon,
- dependent on the type of concrete applied, the same maximum non-uniform crack opening was reached in every test and was greater in case of LC than in case of NC,
- the descending branch sometimes displayed irregularities of a type as sketched in figure 5.2, which was most pronounced for LC.

Stress-deformation relations with similar irregularities in the descending branch have been reported by, among others, Van Mier[86], Budnik[85], Willam et al.[85] and Van Mier and Nooru-Mohamed[90]. In all these investigations non-rotatable loading platens were used.

It was inferred that a relation exists between the phenomenon of non-uniform crack opening, the typical shape of the descending branch and the boundary condition of the specimen. Van Mier[86], in studying the same phenomena, also pointed to this interrelation. The tensile test results with a crack gradually growing through the specimen (figure 5.1) caused him at that time to doubt the softening behaviour as a material

41

property and consequently to doubt the correctness of process zone models. In his opinion the shape of the softening branch can be explained by a decreasing effective load carrying area during macro-crack propagation (structural property). Results obtained on tests with non-rotatable loading platens were explained by Van Mier and Nooru-Mo-hamed [90] with a two stage fracture mechanism. In their approach, perimeter cracks develop along the circumference of the specimen, followed by bending of intact ligaments between perimeter cracks. For possible physical explanations of the softening behaviour of concrete, see Section 6.2.
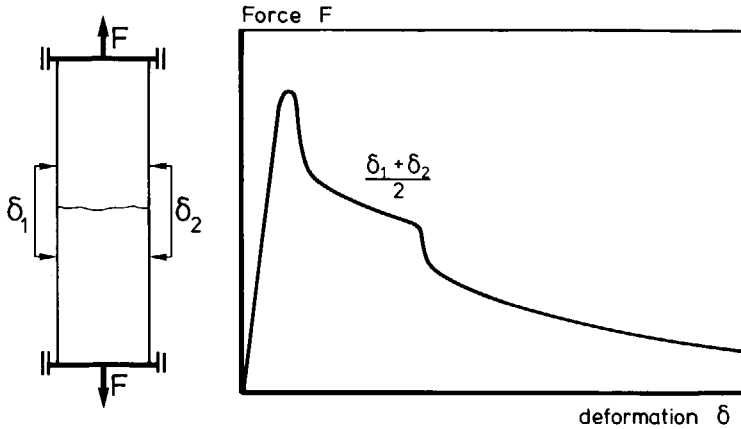
Figure 5.2   F-δ relation as can be obtained in a tensile test with non-rotatable loading platens.

Possibly, the structural behaviour in a uniaxial tensile test tends to obscure the softening behaviour as a material property. In this chapter, however, it will be demonstrated that there is no reason to question this material property. In fact, process zone models can very well be used to explain the observed phenomena.

5.2 Notion for structural behaviour

The observations in the tensile tests as discussed in previous section formed the grounds for thinking that a structural behaviour plays an important role in these tests. Especially the fact that the same maximum non-uniform crack opening was found for different experiments with the same specimen size and boundary condition, led to the belief that it cannot solely be the result of some accidental eccentricity (non-symmetric material property due to heterogeneity or eccentric loading). Much more it was believed that there is a second equilibrium path for a uniaxial tensile test on an elastic-softening material.

The question arose as to whether a state of equilibrium may exist for a non-uniform crack opening. In order to show that there might indeed be a second solution for the same average deformation (the first solution is a uniform crack opening), the tensile specimen for the case of non-rotatable loading platens is subdivided into two linear elastic parts A and a small zone B, that encompasses the fracture zone (figure 5.3a,b). If for a certain average deformation of zone B the interfaces, which are assumed to remain plane, are rotated (figure 5.3d), then the tensile force in the remainder of the specimen will be eccentric. Due to the tensile-softening behaviour of zone B (figure 5.3c), there may be a stress distribution in this zone that results in the same eccentricity, as schematically shown in figure 5.3d. So far, qualitatively, it has been made plausible that there might be an equilibrium path with non-uniform crack openings. A quantitative extension of the same model will be presented in Section 5.5. There it will also be discussed why in a tensile experiment the path with non-uniform crack openings will always be followed. Here, finally, the influence of a non-uniform crack opening on the total force at, or just beyond peak load is illustrated in figure 5.4. It can be seen that, for the same average deformation, the tensile force is the lowest in case of a non-uniform crack opening (dashed lines).
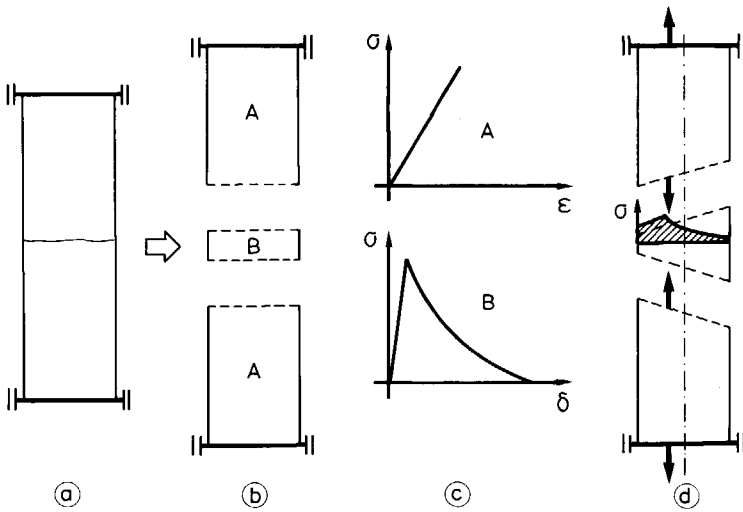
Figure 5.3   Subdivision of a tensile experiment (a) into two linear elastic parts
and a linear softening zone (b,c) and a possible equilibrium state for
non-uniform crack opening.

Based on the mechanical model for the tensile test on a softening material presented above and on the previously obtained experimental results for different boundary conditions (see Section 5.1), it was suspected that a direct relation exists between the degree

of non-uniform crack opening and the rotational stiffness of the boundary of the softening zone. In this respect, this boundary condition is determined by the boundary of the specimen (loading equipment), but also by the specimen itself. In order to check this supposition, a test series was performed in which the specimen length was varied and, with it, the rotational stiffness of the boundary of the softening zone (non-rotatable loading platens!). Principal results of this investigation are presented in the next section.
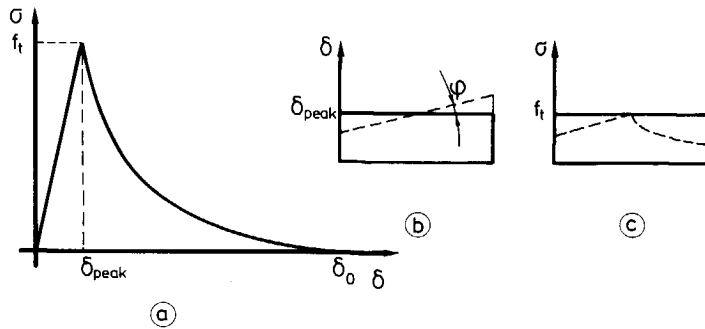
Figure 5.4   Assumed σ-δ relation (a), deformation distributions (b) and stress distributions (c).

5.3 Experimental verification

In order to verify the surmised relation between the boundary rotational stiffness of the softening zone and the degree of non-uniform crack opening, a test series was performed using the specimen length as a variable. Since previous tests on a lightweight concrete (low Young's modulus of about 18000 MPa) had proved that the features which will be investigated are more pronounced for this material than for normal-weight concrete, the former type of concrete was used in the experiments. Four different specimen sizes were investigated, denoted as types A,B,C and D. Compared to the dimensions of type A (250*60*50 mm^3), the length of the type B and C specimens was reduced to 125 and 50 mm respectively, while for type D a cross-sectional area of 50*40 mm^2 was applied for a length of 250 mm. Further experimental details can be found in (Hordijk et al.[87]) and Appendix A.

The rotational stiffness of the loading platens was in the order of 10^6 Nm/rad, which was much higher (from about 3 times for specimen C to about 50 times for specimen D) than the rotational stiffness of the specimens (EI/ l). This means that the influence of the boundary conditions of the softening zone can very well be studied using the specimen length as a variable.

44

For each type of specimen, typical deformation distributions for different loading stages are plotted in figure 5.5. From these diagrams, it can be seen that for shorter specimens, i.e. higher rotational stiffness, the non-uniform crack opening is less pronounced. For type C the crack surfaces remain parallel to each other in almost every loading stage. Furthermore, this figure clearly demonstrates that the deformations must be considered three-dimensionally.
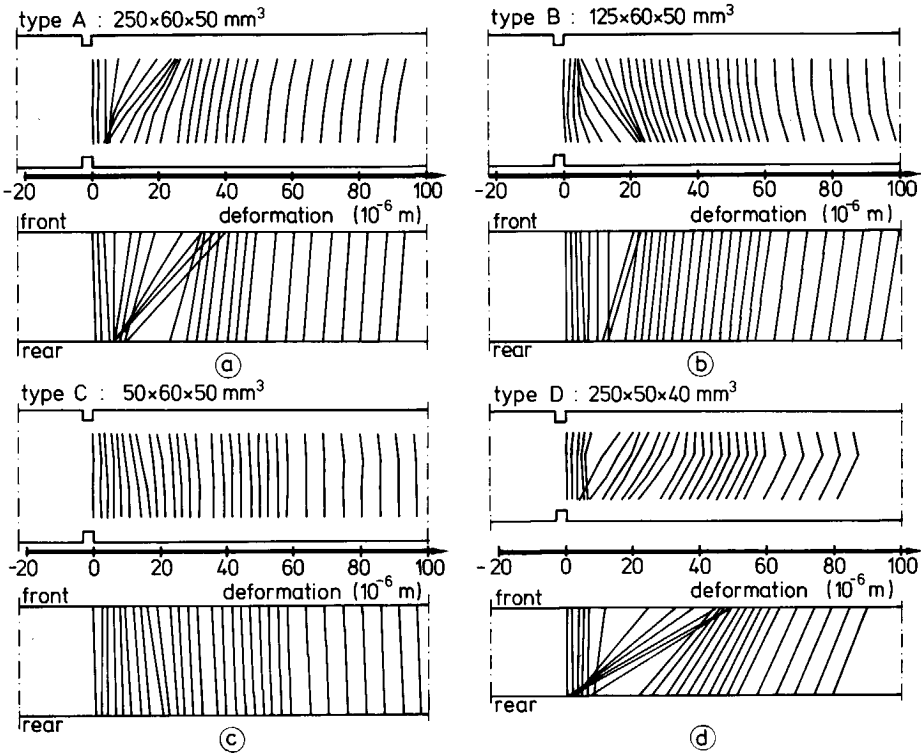
Figure 5.5   *Typical deformation distributions obtained on specimen types A, B, C and D.*

Average stress-deformation curves corresponding to the deformation plots of figure 5.5 are plotted in figure 5.6. Most notable in these diagrams is the smooth descending branch for specimen type C. In the other tests, irregularities of varying degrees of importance can be observed.

The results shown in figures 5.5 and 5.6 pertain to individual tests. The same tendencies were observed in all other tests. In order to compare maximum non-uniform crack

45

openings in the different experiments, two rotations belonging to the principle axes of the critical cross-section are defined (see inset of figure 5.7). For the in-plane rotation φ_{ip}, the extensometers (l_{meas}: 35 mm) at the corner positions were used and for the out-of-plane rotation φ_{op}, the average deformations at the front and rear side of the specimen. It appeared that maximum non-uniform crack openings for specimen types A,B and C were very well positioned on a straight line (figure 5.7), which confirms the relation between rotational stiffness and maximum non-uniform crack opening. The results of the slender type D specimens were somewhat divergent.
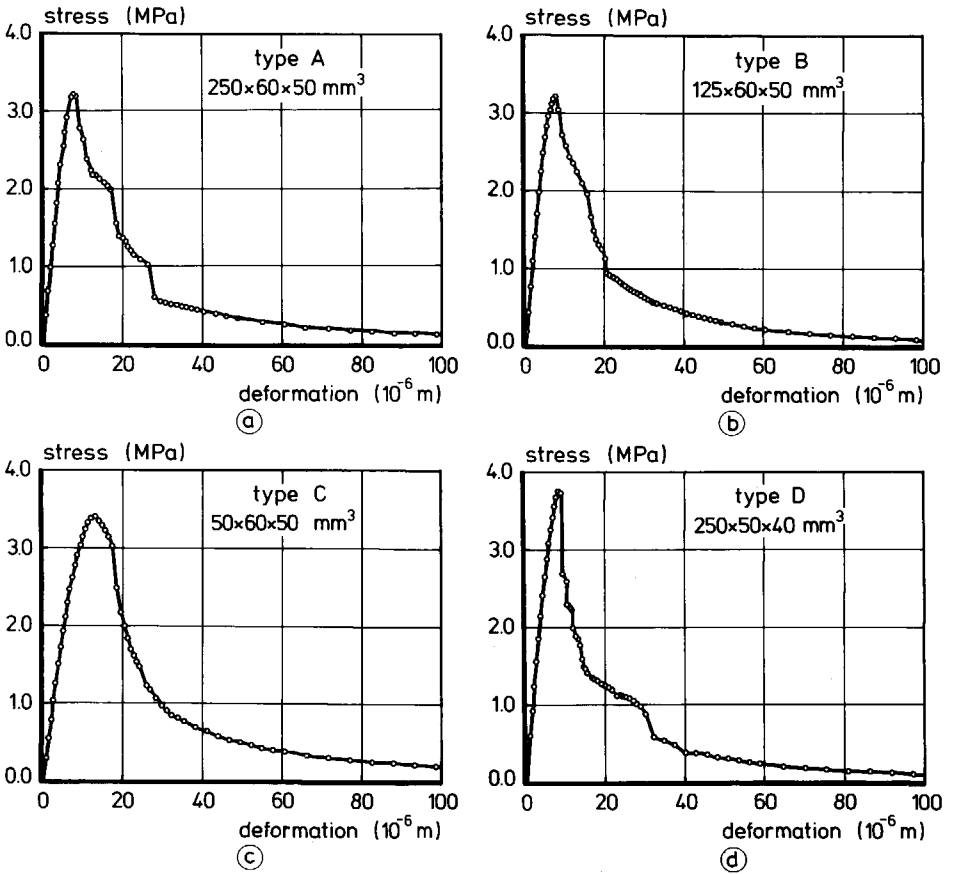
Figure 5.6   Average stress-deformation relations corresponding to the results presented in figure 5.5 (l_{meas} = 35 mm).

From the results shown, the question that immediately arises is whether the shortest specimen (type C) is most suitable for determining the tensile properties. The mean
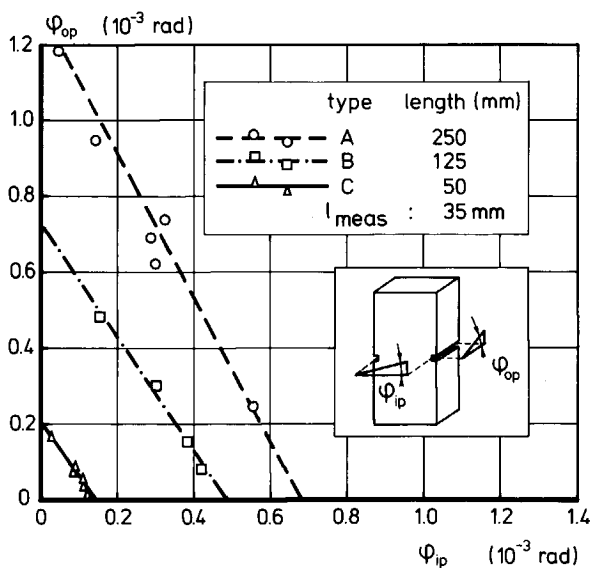
*Figure 5.7   Maximum non-uniform crack opening for different tests,
represented by a combination of in-plane rotation φ_{ip}
and out-of-plane rotation φ_{op}.*

results for the different specimen types (figure 5.8) demonstrate that a quick positive
answer to this question cannot be given. The fact that the average results for specimen
type C deviate significantly from those for the other specimen types may be explained by
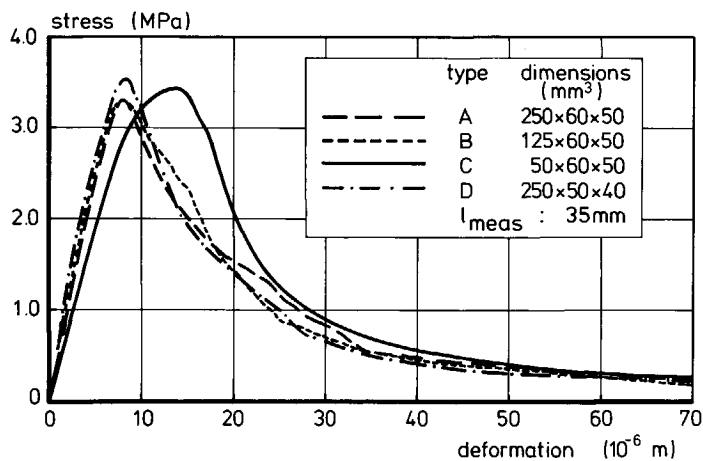
Figure 5.8   Mean stress-deformation relations for specimen types A, B, C and D.

47

an influence of the stiff loading platens (preventing lateral deformations), which can be expected to be important for such a small specimen length.

Finally, one experiment will be discussed in more detail, because some features can be extracted from it which were also revealed by the numerical analyses presented in the following sections. It concerns a post-peak cyclic experiment. It appeared that only out-of-plane non-uniform crack opening occurred in this test, as can be seen in figure 5.9a, where the deformation distributions for loading points at the envelope curve are plotted. In figure 5.9b, the σ-δ envelope curve for the average deformation over the total cross-section is plotted, while figure 5.9c shows the curves for the front and the
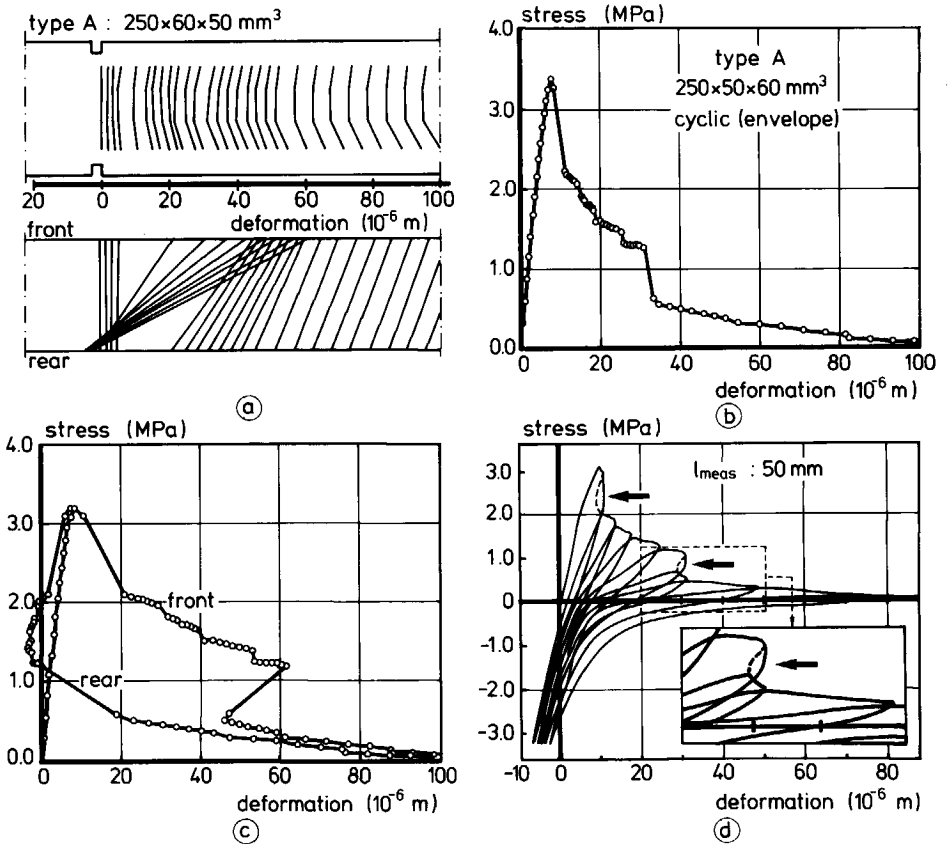
Figure 5.9   Typical result for specimen type A and loading type IV;
a)deformation distributions, b) average σ-δ relation (l_{meas} = 35 mm),
c) average σ-δ relation for front and rear sides of the specimen
and d) X-Y recorder plot.

rear sides of the specimen separately. It appears that in two parts of these curves no measurements were taken despite the regular time intervals for these measurements. This fact points to a snap-back for these parts of the σ-δ relations, because snap-backs in deformation-controlled tests are passed by sudden stress drops. Figure 5.9d is the X-Y recorder plot for this test. The surmised snap-backs are indicated by dashed lines. By change, the second snap-back was confirmed by the experiment; at least partly. Probably the loading direction was reversed just at the beginning of the snap-back. In the sub-sequent loading cycle, the envelope curve was reached at an average deformation which was lower than that at the instant of leaving the envelope curve. The parts of the σ-δ curves beside the dashed lines (indicated by arrows) are created instantaneously and are, according to the above explanation, not genuine.

5.4 FE simulation

Analysis with a finite element code seems to be the obvious means to study the observed structural behaviour in a uniaxial tensile test. Therefore such an analysis was performed with the DIANA[*] code, utilizing the smeared crack approach. Here, only the applied FE idealization with the material model and the numerical results will be discussed in close relation to the experimental results. Details of this analysis can be found in (Rots et al.[87]). For the sake of clarity, the aim was to study the phenomena rather than to fit an experimental result as accurately as possible.

The finite element mesh with the applied boundary conditions is presented in figure 5.10a. The lower boundary was assumed to be fixed, whereas the upper boundary was provided with a translational spring (k_t = 148000 N/mm) and a rotational spring (k_r = 10^6 Nm/rad). Dependence relations were used to prevent distortion of the upper boundary which is in agreement with a rigid loading platen in an experiment. For the deformation-control mechanism in the analysis, the average crack opening displacement was used, which is comparable with the control parameter in the experiments (the deformation of a 50 mm long section). This procedure of "indirect displacement control" was proposed by De Borst[86] and was required in order to obtain a stable analysis.

---

[*]   DIANA is the finite element code being developed at TNO Building and Construction Research in combination with other institutes and universities in the Netherlands. The discussions with Dr. J.G. Rots, who performed the analysis, are gratefully acknowledged.
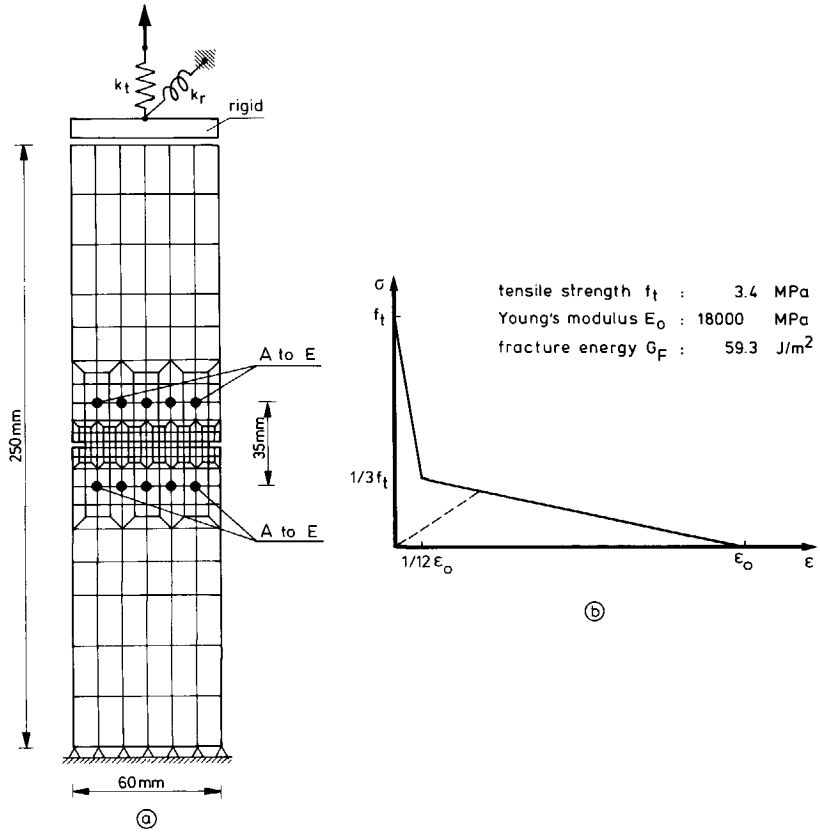
Figure 5.10   Finite element mesh (a) and material input (b) for the FE analysis of a uniaxial tensile test.

The applied bilinear softening relation and assumed material parameters can be seen in figure 5.10b. The crack band width (2.5 mm) was taken as being equal to the width of the centre elements between the notches, while fracture was assumed to localize within this centre band of elements. One element in front of the right-hand notch was given a material imperfection by means of a 1 per cent reduction of G_F. The importance of this will become clear later on in this section.

The computational results will be presented by means of incremental deformations and σ–δ relations. In conformity with the experiments, stress is given as the applied force divided by the central cross-sectional area, whereas deformation is the mean of five values measured between the points A to E (figure 5.10a). In figure 5.11, the incremental deformations are shown which refer to key events in the fracture localization process. The resemblance to the experimental results is obvious. Pre-peak deformations appeared

50

to be symmetric (here the term symmetric instead of uniform will be used, because notches also cause some non-uniformity in the deformations). The deformations in the post-peak region are non-symmetric in the first part, i.e. the right-hand side and left-hand side open successively, which is followed by symmetric deformations for larger average crack openings. In a second analysis the material imperfection was omitted and the deformation distributions were kept symmetric. The σ-δ relations for both analyses are
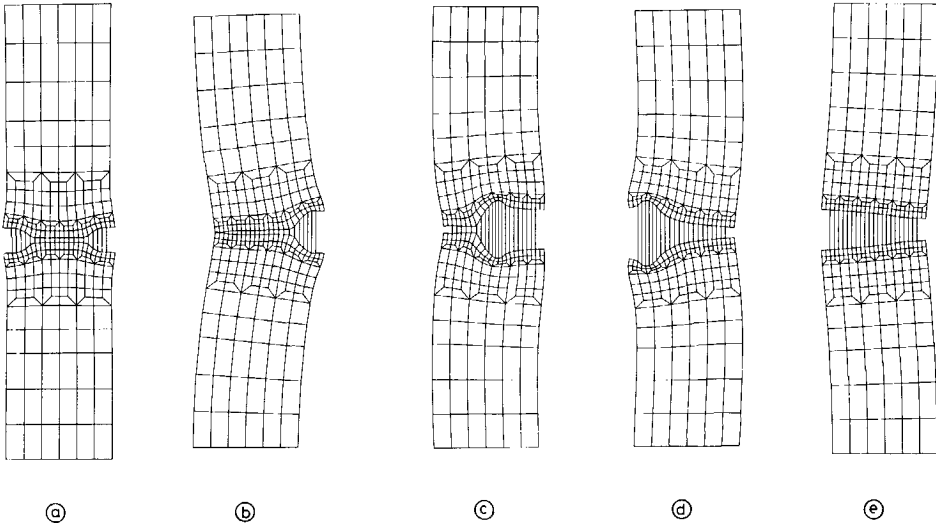
Figure 5.11   Incremental deformations for different loading points;
a) pre-peak, σ = 2.837 MPa, b) at peak, σ = 2.856 MPa, c), d) and
e) post-peak σ is 1.865 MPa, 1.101 MPa and 1.026 MPa respectively.

plotted in figure 5.12. The curve for the symmetric deformations resembles the bilinear input for the softening. The difference between the peak stress and the tensile strength as well as the rounded curve at peak load can be explained by the stress-concentrations near the notches, which cause the different areas in the centre cross-section to pass their peak stress (f_t) one after another. The other σ-δ relation for the non-symmetric deformations shows the typical shape for the descending branch (compare figure 5.2), especially if it is realized that in experiments the dashed line will be found instead of the snap-back. The fact that this snap-back could be traced in the numerical analysis is due to the fact that the average crack opening was controlled, while δ in figure 5.12 is the average deformation for a specimen section with the depth of 35 mm. For practical reasons, the feed-back parameter in the experiments is always the average deformation over a certain specimen length. Therefore, sudden drops (dashed line) will occur. Or, in cases where the stress drop is too pronounced, it may also occur that it cannot be followed by the equipment, which results in unstable fracture. Nevertheless, the snap-back as was in-

ferred by the experimental result (see figure 5.9d) has been made plausible by the numerical results.
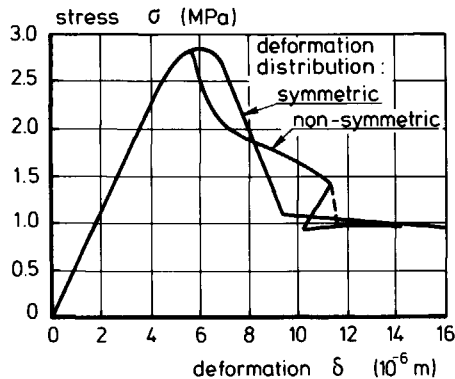
Figure 5.12   Average stress-deformation relations (l_{meas} = 35 mm).

Due to the material imperfection, one equilibrium path (non-symmetric deformations) was found. If this material imperfection is omitted and the deformations are not forced to be symmetric, as applies in cases where only half of the specimen is modelled, then the equilibrium path reaches a point (known as the bifurcation point), where it splits into two different possible paths (see Rots[88]). For more information about the bifurcation point in a uniaxial tensile test and the implication of such points for numerical analyses, the reader is referred to Rots[88] and De Borst[86].

5.5 Simple numerical model

In previous sections, the inferred structural behaviour was already clearly confirmed by experimental and numerical results. The FE code can now further be used to study the influence of parameters like boundary conditions, specimen dimensions and material input. However, if one is only interested in the way these parameters are influenced by the different phenomena, then it may be more convenient to reduce the problem to a simple mechanical model. Firstly, the advantage is that a parameter study can be performed easily and quickly and, secondly, such a simple model may bring more transparency in the problem. In this section, the modelling according to figure 5.3, which is based on the theory of bending in combination with a process zone model, will be worked out (see also Hordijk and Reinhardt[89a]).

The mechanical model can be represented by figure 5.13a. It basically consists of a small fracture zone (zone B in figure 5.3) that deforms only in one direction according to a defined tensile softening relation, while the edges of this zone remain plane. The specimen and its boundary are represented by rotational and translational springs. Besides Young's modulus, the tensile strength and the stress-crack opening relation (material input), the tensile softening relation for the fracture zone is mainly determined by the depth of this fracture zone (similar to the smeared crack approach). For the sake of clarity, there is no direct relation between the depth of the fracture zone, which will be arbitrarily chosen, and the width of the process zone in an actual experiment. In fact, the depth of the fracture zone links the deformation distribution in that part of the cross-section where a process zone is active with the strain distribution in that part where the material still shows linear elastic behaviour.
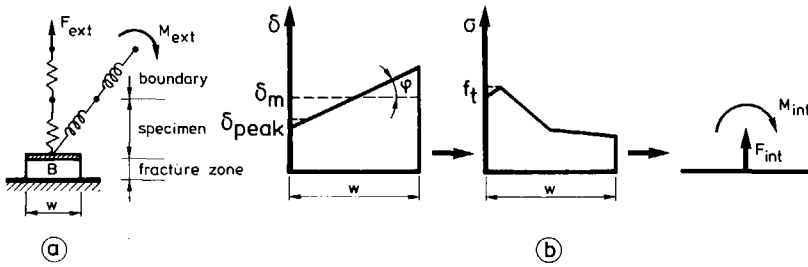
Figure 5.13   Model for the tensile test (a) and relation between deformation distribution, stress distribution and internal force and moment (b).

The solution procedure for this model is as follows. For an arbitrarily chosen combination of mean deformation δ_m and rotation φ of the fracture zone, the deformation distribution of this zone is defined (figure 5.13b). Using the σ-δ relation, the corresponding stress distribution can be calculated, which can be replaced by an internal force F_{int} and an internal moment M_{int}. This combination of δ_m and φ will only be a solution for the model where equilibrium and compatibility exist at the boundary of the fracture zone. For the boundary in this tensile experiment, this means that the internal moment M_{int} must be equal to the external moment M_{ext} which is the result of the same imposed rotation φ. Obviously, for every δ_m, there exists at least one solution, which belongs to a rotation equal to zero. These solutions belong to the uniform crack openings and yield the applied σ-δ relation (input) as result. The interesting point, however, is to find solutions for non-zero rotations. The procedure to find these solutions will be demonstrated by the example in figure 5.14.

53
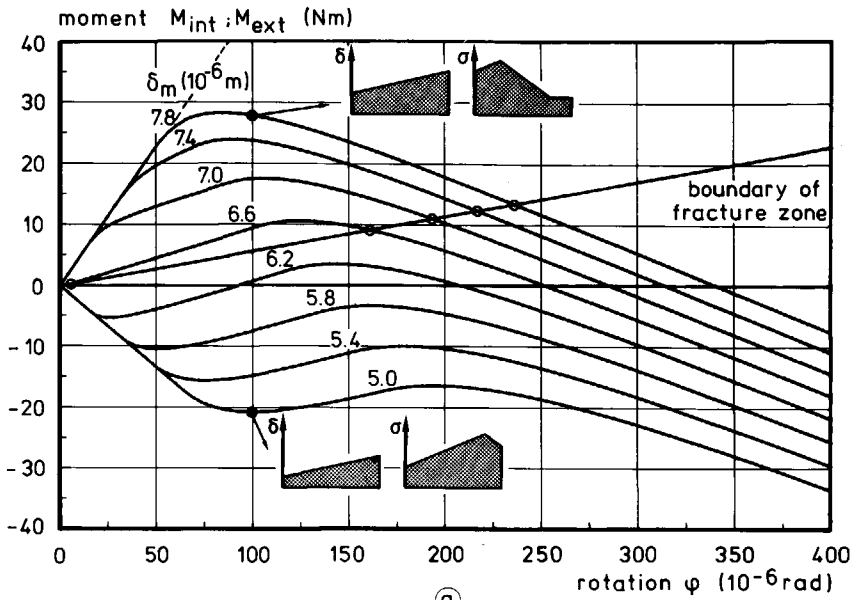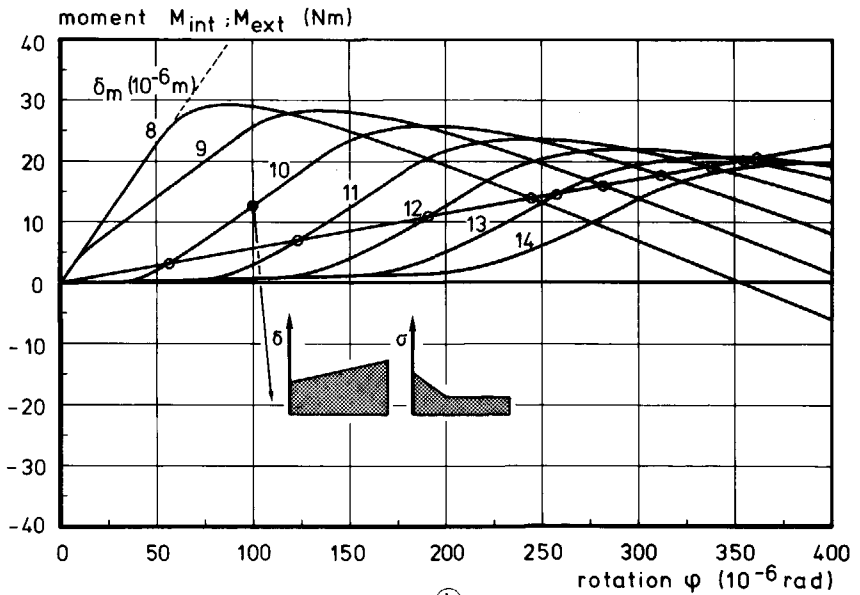
Figure 5.14   M-φ relations for the fracture zone and average deformations from 5 to 7.8 μm (a) and from 8 to 14 μm (b).

Comparison with FE analysis

For comparison purposes, the FE analysis as described in the previous section is simulated. Initially, 35 mm is taken for the depth of the fracture zone, which is equal to the measuring length in the experiments. Furthermore, this 35 mm base will be used as reference length for the σ-δ relations throughout this section.

For values of the mean deformation δ_m ranging from 5 μm to 15 μm with steps of 0.1 μm and rotation angles varying between 0 and 400 10^{-6} rad with steps of 4 10^{-6} rad, the corresponding internal moment and internal force were calculated. The relation between M_{int} and φ for a number of δ_m values is given in figure 5.14. The deformation at peak load, δ_{peak} is equal to 6.61 μm. It appears that firstly negative moments are found for rotations starting from zero in case $\delta_m < \delta_{peak}$ and positive moments in case $\delta_m > \delta_{peak}$. In figure 5.14, the linear relation between the external moment at the boundary of the fracture zone, M_{ext} and an imposed rotation φ, is included so that solutions can be directly taken from the figure, as being the points of intersection of the straight line and the curved lines. As can be seen, solutions exist for non-zero rotations. For a number of average deformations, there are even two points of intersection besides the origin, which again points to the occurrence of a snap-back.

The average stress for the points of equilibrium is determined by the corresponding internal force divided by the critical cross-sectional area. In figure 5.15a the σ-δ relation, which was applied as input, is represented by the straight lines. This relation belongs to the solutions with uniform deformations (origin in figure 5.14). After connecting the solution points found for non-uniform deformations, a second equilibrium path appears to start at peak load and to end in the kink of the descending branch. Thus the point at
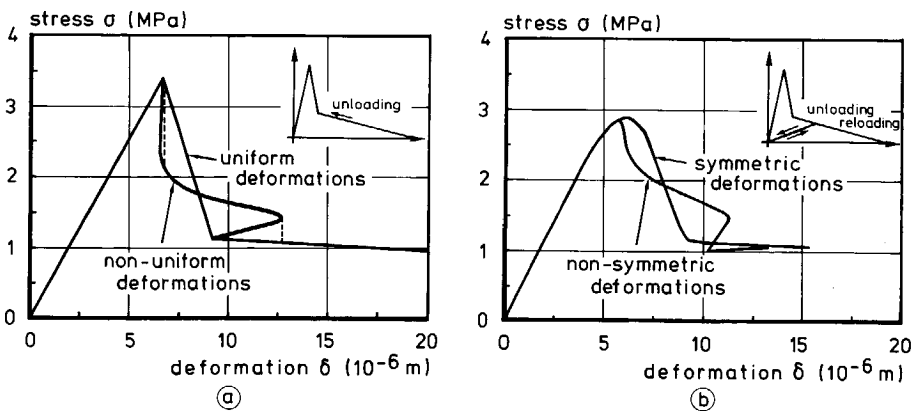
Figure 5.15 σ-δ relations predicted by the simple numerical model (a) and the FE analysis (b).

55

the peak is a bifurcation point. As far as the existence of snap-backs is concerned, this analysis also revealed such a snap-back just beyond peak load, as sometimes also seems to occur in experiments (see figure 5.9d).

If the σ-δ relations are being compared with the FE results (figure 5.15b), then it appears that both analyses display the same features. Nevertheless, two differences of minor importance can be observed. The first one concerns the shape of the curves near peak load. The rounded peak for the FE results is due to the stress concentrations at the notches which do not play a role in the model discussed above. The second difference can be observed in that part of the σ-δ curve where the path with non-uniform deforma-tions again reaches the path with the uniform deformations. A different modelling for unloading is responsible for this difference. In the FE analysis a secant unloading was applied (see inset in figure 5.15b). In the model as described in this section, possible solutions for an arbitrarily chosen deformation are calculated directly. This solution procedure demands an unambiguous relation between deformation and stress, which means that the loading and unloading path are the same.

The deformation distributions for a number of δ_m-values, whereby the equilibrium path with the non-uniform deformations is followed and δ continuously increases like in a deformation controlled experiment, are plotted in figure 5.16. The resemblance with results obtained in an actual experiment is good (compare figure 5.5).
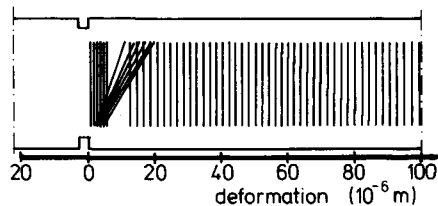
Figure 5.16   Deformation distributions predicted by the model.

Influence of fracture zone depth and boundary conditions
The analysis presented above clearly demonstrates that the model can be used to study the structural behaviour. However, the model loses its power if the results depend strongly on the chosen depth of the fracture zone. In order to investigate the influence of this parameter, the same calculation has been repeated using 2.5 mm and 50 mm respectively for this parameter. A comparison of σ-δ relations with that for the 35 mm base is presented in figure 5.17a. It can be concluded that, although there is an influence, the special features of the tensile test are not significantly affected by varying this parameter between 2.5 mm and 50 mm.

56
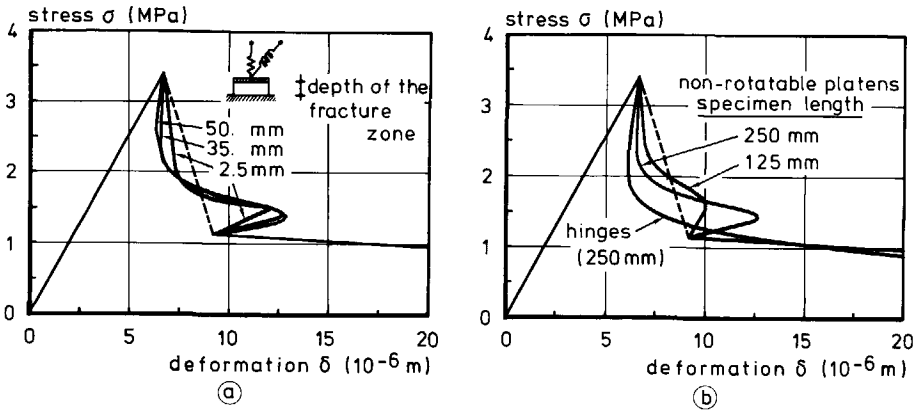
Figure 5.17   Predicted σ-δ relations as influenced by the depth of the fracture zone (a) and by specimen size and boundary conditions (b).

The fact that internal and external M-φ relations are determined separately means that a parameter study for the length, stiffness (Young's modulus) and boundary rotational stiffness of the specimen is fairly easy to perform. For a given material input, the M_{int}-φ relations only have to be determined once. For different values of the said parameters, the relation M_{ext}-φ can simply be determined and compared with the M_{int}-φ relations. As far as the specimen length is concerned, a shorter length means that the rotational stiffness is higher. In figure 5.14 it can be seen that for a steeper slope of the M_{ext}-φ relation, the maximum attainable rotation decreases. This result, as well as the influence on the σ-δ relation (figure 5.17b) is in agreement with the experimental results (Section 5.3). For rotatable loading platens the boundary condition is given by $M_{ext}= 0$, for which the model predicts a continuously increasing rotation and a smooth descending branch (see figures 5.14 and 5.17b). This result also seems to be in accordance with experimental results. It must be realized, however, that in this simple model geometrical effects have not been taken into account. For this boundary condition, the effect of bending out may have a significant influence for greater rotations. For a rotation φ in the fracture zone, the eccentricity e is equal to $1/4.l$ φ (l = specimen length). Solutions can now be found by using e-φ relations ($e_{int}= M_{int}/F_{int}$) instead of M - φ relations, but otherwise the procedure is the same. This has not been worked out here. Maybe geometrical effects also played a role in the experiments on the slender type D specimens (see Section 5.3).

Imperfection in relation to bifurcation point
Besides the examples that have been given, more phenomena can be studied with the aid of the model. For instance, it is possible to study the influence of imperfections in test

57

performance, like eccentric loading in case of hinges, or the existence of an initial rotation in case of non-rotatable loading-platens. In the latter case, the line for the M_{ext}-φ relation in figure 5.14 is shifted to the right. Then, only one equilibrium path (non-uniform deformations) will be found, because the origin ($\varphi = 0$) no longer leads to a solution. This result is in accordance with the theory that bifurcation points occur only in perfect structures (see De Borst[86]). Since concrete is an inhomogeneous material, the equilibrium path with the non-uniform deformations will always be found in experiments.

Role of initial slope of σ-w relation and stability criterion

So far, the discussed parameters all concerned experimental conditions. It is also evident that the input for the material properties, i.e. E_0, f_t and the shape of the softening curve (including G_F and δ_0), can be subjected to a parameter study (as performed by Rots[88], Zhou [88] and Rots and De Borst[89b]). In this respect, the initial slope of the descending branch seems to be an interesting parameter. This initial slope (here assumed to be the steepest part of the descending branch), in combination with softening zone boundary conditions, determines whether non-uniform crack opening can occur in a uniaxial tensile test. Hassanzadeh et al.[87] presented the following stability criterion for the uniaxial tensile test (see also Hillerborg[89]):

$$\frac{1}{\dfrac{1}{k_r} + \dfrac{6l}{Edb^3}} > - \frac{db_c^3}{6} \frac{d\sigma}{dw} \tag{5.1}$$

b*d*l : width*depth*length
b_c : width in critical cross-section
k_r : specimen boundary rotational stiffness

The derivation of this stability criterion is based on the condition that a stabilizing moment due to an imposed rotation in the fracture zone must be greater than the moment due to load eccentricity in this zone. This approach is similar to the model presented in this section and therefore the criterion can very well be visualized by figure 5.14. The left part of eq. 5.1 represents the rotational stiffness of the boundary of the fracture zone, which is the slope of the straight line in figure 5.14. The two contributions, rotational stiffness of the specimen's boundary (k_r) and the specimen itself (EI/l), can clearly be seen in eq. 5.1. It should be noted, however, that eq. 5.1 was derived for half the specimen with axis of symmetry in the fracture zone, while the curves in figure 5.14 relate to the total specimen. In principle, the right part of eq. 5.1 corresponds to the initial slope of the M-φ curves in the positive moment region (dashed line in figure 5.14). This is not exactly true, because the M-φ curves of figure 5.14 were derived for a depth of the fracture zone equal to 35 mm, which should be zero to ensure equality with eq. 5.1. Nevertheless,

the stability criterion presented by Hassanzadeh et al.[87] is similar to the precondition that the slope of the straight line for the boundary of the fracture zone in figure 5.14 must be steeper than the slope of the dashed line for the initial internal M-φ relation. The latter slope increases for a more steep slope of the descending branch. This explains why Van Mier[86], when making FE analyses of a tensile specimen between non-rotatable loading platens, observed non-symmetric crack opening only in the case of a steep descending branch. As far as the real initial slope of the descending branch is concerned, the analyses in this chapter show that in case of non-uniform crack opening, the measured slope is steeper than the real slope (see figure 5.15).

If the steepest slope of the descending branch is known, then it is possible to use eq. 5.1 to define the combination of specimen dimensions and boundary rotational stiffness that yields a stable deformation-controlled uniaxial tensile test. This slope, however, is not known in advance. If, for example, the material input for the FE calculation ($d\sigma/dw$ = -325 MPa/mm) is considered, then for the same boundary condition and cross-sectional dimensions as used in the analyses in this section, the maximum specimen length that ensures a stable tensile test is 31 mm. Roughly, this confirms the fact that for the investigated lightweight concrete (Section 5.3) only uniform crack openings were found for a very short (50 mm) specimen length. Furthermore, from the stability criterion it can clearly be seen that for rotatable loading platens (k_r = 0), this requirement for a stable tensile test cannot be fulfilled, which is in agreement with previously discussed experimental results. Therefore, the results of FE analyses by Rots and De Borst[89b], who observed hardly any difference between loading platens that were fixed and those that could rotate freely (figure 5.18), seems to contradict these results. A possible explanation for their results, however, might be found in the way the boundary conditions (especially those perpendicular to the loading direction) were modelled (see inset of figure 5.18). In order to illustrate this, figure 5.19 shows schematically three deformed specimens for non-uniform crack opening and different boundary conditions. The situation in figure 5.19a resembles a test in which the upper as well as the lower loading platen can rotate freely. In this case, the specimen can bend out freely and horizontal reactions at the point of load application are zero. Although hinges are applied, a counteracting moment equal to Fe is present due to the deformation of the specimen. It is this effect that is meant by "geometrical effects" as mentioned previously in this section. Normally, this effect is assumed to be of minor importance. In figure 5.19b, the lower platen is fixed, while the upper platen can rotate and also move in a horizontal direction. Compared to the boundary conditions in figure 5.19a, the counteracting moment for the same non-uniform crack opening is probably larger. Another difference is that for this case the upper loading platen has to undergo a horizontal displacement. In the analyses by Rots and De Borst[89b], this horizontal displacement could not occur

due to a horizontal support. As a result, a horizontal force H must have acted at that point, resulting in a moment M in the centre cross-section equal to $Hl/2$ (see figure 5.19c). As can be seen, for the boundary conditions in figure 5.19c, the non-uniform crack opening can only occur in case of distortion of the specimen, while for the other cases such a distortion is not necessary. Figure 5.19, is merely intended to show that not only the rotational stiffness of the loading platens itself, but for some cases also the total set of boundary conditions, including the boundary conditions perpendicular to the loading direction, determine the total rotational stiffness of the boundary of the specimen. In the analyses by Rots and De Borst[89b], the contribution of the horizontal support to a counteracting moment was probably greater than the contribution of the rotational stiffness of the loading platen. Further research should clarify whether these suppositions are true. Nevertheless, in the author's opinion, the results presented by Rots and De Borst[89b] do not clearly demonstrate that the effect of the boundary conditions in a tensile experiment are negligible. On the contrary, the author believes that the boundary conditions have a significant influence.
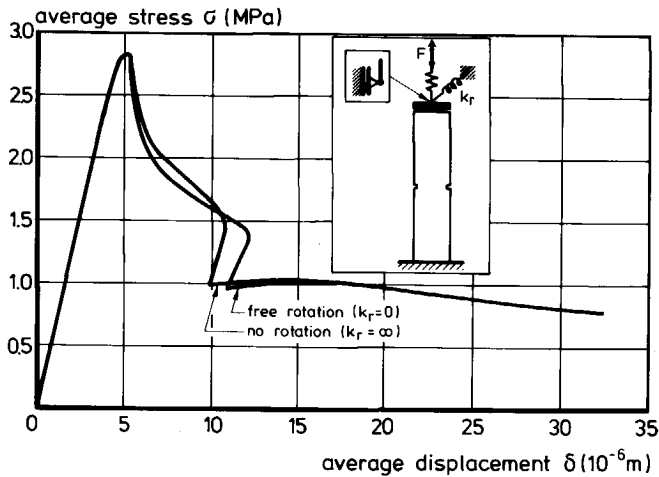
Figure 5.18   Results of FE analyses (same model and material input as in Section 5.4) for two extreme values of the rotational stiffness of the upper loading platen (Rots and De Borst [89b]).

In this section, the applicability of a simple numerical model for studying special features of uniaxial tensile tests is demonstrated. It will be demonstrated later in this report that a similar model can also be used for a parameter study of plain concrete beams under bending.
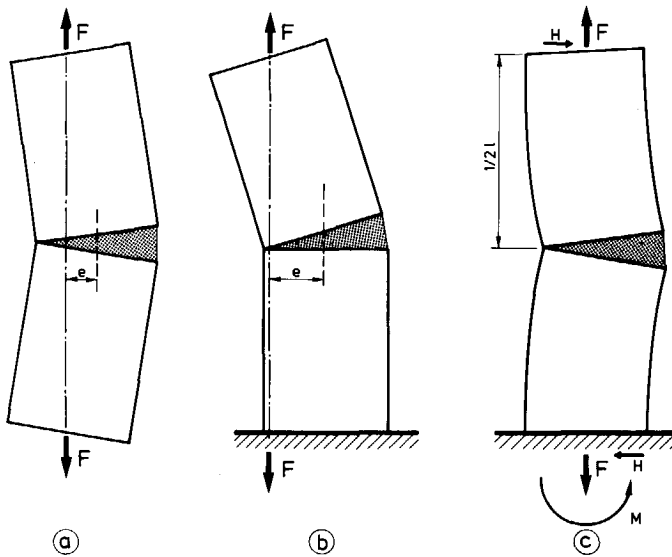
*Figure 5.19   Schematic plots showing contributions to the rotational stiffness of
the specimen's boundary for different types of support.*

5.6 Extended view

Previous sections have clarified how a structural behaviour can occur in deformation-
controlled uniaxial tensile tests on plain concrete. It appears that the observed
phenomena in experimental results can very well be explained with a process zone model
in combination with a FE analysis or with a simple mechanical model. If the fracture
mechanics parameters are taken directly from the σ-δ relations obtained in such a test,
then the descending branch is the most affected parameter. In the event of sudden jumps,
due to snap-back behaviour (see figure 5.9d), the area under the σ-δ curve (G_F) may also
be measured incorrectly, but this is probably of minor importance. According to the
simple model presented in Section 5.5, the peak load is not affected by this structural
behaviour. It has been shown that in a uniaxial tensile test on a softening material, a
bifurcation phenomenon is encountered. Eccentricities in load application as well as
those related to the material property mean that the bifurcation point will not be found
in experiments in the same way as it is encountered in the analyses. It should be noted,
however, that it is primarily the structural behaviour that causes the non-uniform crack
opening and not the eccentricity itself. Very small differences in the eccentricity will
hardly affect the results. Only for larger eccentricities will the obtained σ-δ relations and

61

especially the peak stress be significantly influenced. This parameter, however, is not investigated in this chapter.

Inclined crack path or second crack due to extreme non-uniformity
In the analyses presented so far, including those obtained with the FE code, the fracture zone was predetermined to occur in a certain cross-section, i.e. a plane fracture zone perpendicular to the tensile loading axis. In reality, however, the crack path may deviate from such a desired clear behaviour, especially when extreme non-uniformity occurs during test performance. In fact, the structure and consequently the direction of principle stresses near the crack tip changes continuously due to the non-uniform crack opening. Here, some observations in experiments, as far as crack path is concerned, will be discussed and on the basis of knowledge of the structural behaviour, possible (qualitative) explanations will be given.

In the uniaxial tensile experiments, a crack path as sketched in figure 5.20a was sometimes observed. Such cracks were mainly seen in tests on wide plates (250*220*50 mm^3 with two 20 mm deep notches), but sometimes they also occurred in narrow specimens (250*60*50 mm^3), especially when the non-uniform crack opening revealed only one direction. Another phenomenon is the creation of a second crack at the opposite side to the first crack. In this respect, the reader is referred to Heilmann et al.[69] (figure 5.20b), in whose experiments non-rotatable planes at a distance of 300 mm were created by means of three actuators (see also Hordijk[89c]). Van Mier and Nooru-Mohamed [90] reported a crack profile as sketched in figure 5.20c.
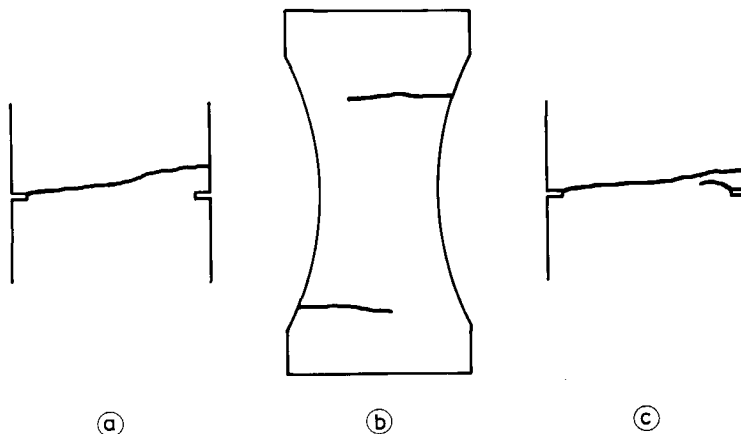
Figure 5.20   crack paths as observed in the Stevin Laboratory on wide plates (a), by Heilmann et al. [69] (b) and by Van Mier and Nooru-Mohamed [90] (c).

The crack profiles in figure 5.20 were obtained in tests in which two planes were kept parallel at a certain distance (non-rotatable loading platens or deformation-distribution control using three actuators). If for such a test, the non-uniform crack opening is pronounced (figure 5.21a), then the stress in the critical cross-section opposite the crack becomes negative (figure 5.21b). In the linear elastic parts of the specimen surrounding the fracture zone, the highest tensile stress occurs on the same specimen side as where compressive stresses are active in the fracture zone. In fact, during non-uniform crack opening, a stress situation exists in the specimen as schematically represented in figure 5.21c, which explains why a growing crack during extreme non-uniform crack opening deviates from a straight line. It should be obvious that the transition from compressive stresses in the fracture zone into tensile stresses outside this zone follows a gradual course. In the experiments by Heilmann et al.[69], who used necked instead of notched specimens, the tensile stress in the elastic parts probably reached the tensile strength before the fracture zone was forced to open uniformly again. Thereafter the two opposite cracks could further open non-uniformly without disturbance.

It is assumed that the phenomena discussed above mainly play an important role in cases of extreme non-uniform crack opening and a large cross-sectional dimension.
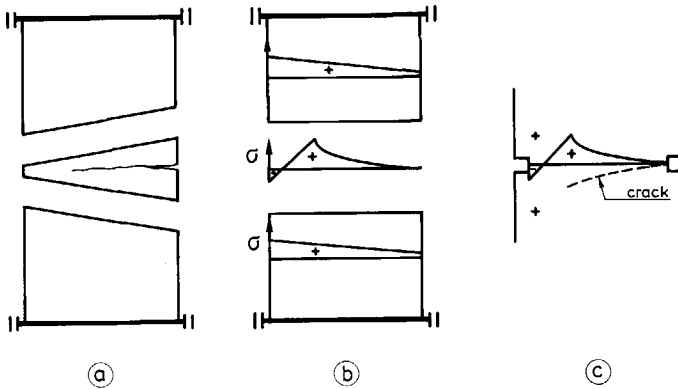
Figure 5.21   Explanation for inclined crack path; a) deformed fracture zone and linear elastic specimen parts, b) schematic representation of stress distributions and c) stress situation during non-uniform crack opening.

Significance for other experiments and analyses
The structural behaviour as discussed here for the uniaxial tensile test on concrete may also play a significant role in other circumstances. Firstly, it may be obvious that it can occur in uniaxial tensile tests on every softening material. In this respect, the results obtained on granite by Labuz et al.[85] should be mentioned. For rotatable loading devices

they observed similar results as discussed before. Secondly, this structural behaviour may also influence experiments with other types of uniaxial loading. For instance, it can be expected to be active in impact, fatigue and sustained tensile tests. It appears that the deformation distributions in the final fracture zone of a specimen under tensile fatigue loading are non-uniform (see Section 9.4). But a similar structural behaviour can also be encountered in deformation-controlled uniaxial compressive tests, as reported by Vonk et al[89]. Thirdly, even other types of test may display a behaviour that parallels the structural behaviour in the uniaxial tests, as demonstrated by Rots et al.[89a] in a FE analysis of a double notched shear beam test.

The discussions of the different features of fracture tests on softening materials clearly demonstrate that one must be very careful about making assumptions of symmetry or anti-symmetry (see Rots et al.[89a]). Though such an assumption may seem justified in many cases, it proves to be incorrect in most of them. This affects the interpretation of fracture tests as well as its modelling in calculations.

After all that has been said about the deformation-controlled uniaxial tensile test, the question may arise as to whether it is still a suitable test for determining the fracture mechanics properties and if so, how should such an experiment be performed? As far as the first question is concerned, it can be said that this is still the only test which directly yields all fracture mechanics parameters, even though it is not as direct as has been suggested before. In order to get results that are as accurate as possible, it is of course necessary to minimize the effects of a structural behaviour as effectively as possible. Later on in this report, it will be demonstrated that the stress-crack opening relation, as it is obtained in this investigation (eq. 6.1 in Section 6.3), approximates the real softening material property fairly well. The requirement that the stability criterion (eq. 5.1) must be fulfilled may seem to be a simple answer to the second question. Firstly, however, the unknown slope of the descending branch and secondly the resulting very short specimen length which causes the influence of loading platens to become significant, make the answer more complicated. Perhaps a further study or the use of brushes like in compression tests would provide the solution. However, it is questionable whether these contradictory requirements (high rotational stiffness and no influence of loading platens) can both be fulfilled at the same time. Furthermore it is doubtful whether the correctness of the results will be significantly improved. Some guidelines for deformation-controlled uniaxial tensile tests are:

– use a small critical cross-sectional area, i.e. dimensions of about 4 to 5 times the maximum aggregate size.
– for the specimen length take about two to three times the dimension of the cross-section.

– the rotational stiffness of the loading platens must be high compared to the specimen rotational stiffness.

It may be obvious that for proper tensile testing more decisions have to be made, like for instance those related to the application of notches, the curing conditions of the specimen, the measuring length to be applied and the connection between specimen and loading platen. That, however, is beyond the scope of this chapter. In Chapter 7 attention will be paid to the influence of notches and the applied curing condition on the obtained results. Furthermore, information about the performance of deformation-controlled tensile tests can be found in Hordijk[89c].

6 Tensile constitutive modelling

6.1 Introduction

In all calculations of structures, whether FE analyses or simply manual calculations, the constitutive relations for the material behaviour are the basic input parameters. Therefore experiments are being performed in order to determine these constitutive relations. In some cases, models are also available which predict these relations on the basis of the physical behaviour at a lower level. As far as the tensile behaviour of concrete is concerned, the constitutive relations for the uncracked material and for a crack (softening zone) are required for monotonic and cyclic loading. Experimentally determined relations will be presented in this chapter as well as constitutive models that have been derived for application in numerical codes. Yet, a sound physical model for the softening behaviour as a material property is not available. Nevertheless, the notion that cracking in matrix and aggregate, debonding and interlocking (sliding friction when aggregates are pulled out of the matrix) are basic phenomena in the fracture mechanism is well accepted among researchers. These phenomena in relation to the σ-δ relation for tensile loading will briefly be discussed in Section 6.2.

In this chapter, emphasis will be on the crack evolution rather than on the bulk behaviour, which is in proportion to the importance of cracks in the tensile fracture behaviour itself, where a single crack is the leading factor. The crack evolution is determined by the relation between crack opening and crack normal stress (σ-w relation). Despite the structural behaviour in a uniaxial tensile test (see Chapter 5), it is still the most direct test for obtaining a σ-w relation. Since the crack opening cannot be measured directly, it must be derived from the total deformation that is found for the applied measuring length. A procedure which has been used in the literature to derive a σ-w relation is shown in figure 6.1. In this approach, the crack opening (w) is assumed to be
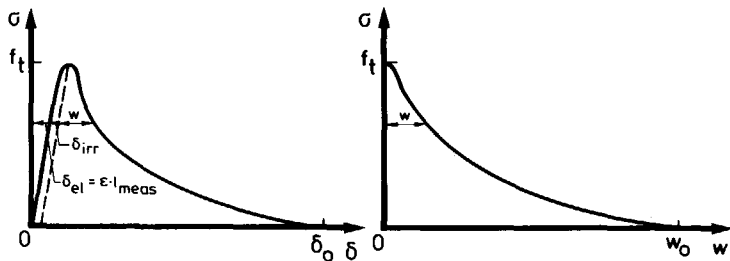

Figure 6.1   Procedure to derive a σ-w relation from a σ-δ relation, obtained from a deformation-controlled uniaxial tensile test.

equal to the total deformation (δ) minus the elastic deformation ($\delta_{el} = \sigma.l_{meas}/E_o$) and an irreversible deformation δ_{irr}, which accounts for non-elastic effects during unloading of the material adjacent to the crack faces. It is known, however, that the non-linear behaviour in the pre-peak region is due not only to micro-cracking in the specimen section within the measuring length (bulk behaviour), but also to pre-peak non-uniform stress distributions (Gustafsson[85], Hordijk and Reinhardt[90], Hordijk[89c]). Initial stresses due to differential shrinkage, stress concentrations due to notches or eccentric loading conditions are possible causes of these non-uniform stresses. Furthermore, the stress at peak load (f_t) decreases because of these phenomena (see also Sections 7.1 and 7.5). Nevertheless, if these effects are limited, then the error in the stress-crack opening relation is negligible.

Another approach, as compared to the 'direct' experimental determination of σ-w relations, is given by the indirect methods like the method of inverse modelling. In that approach, an experiment is simulated by means of a number of finite element calculations and the σ-w relation which gives the best fit is regarded as being the material property (see for example Wittmann et al.[87]). Such a procedure demands powerful computers but, even then, descending branches are provisionally still restricted to bilinear curves.

Since undisturbed stable tensile tests are difficult to perform, they are not suitable as a standard test. If it appears, however, that the shape of the σ-w relation is more or less similar for different concrete qualities, then it is sufficient to determine solely the tensile strength f_t and the fracture energy G_F (Petersson[81]). In order to check a possible unique relation for the shape of the σ-w curve, a comparison of stress-crack opening relations as reported in different investigations will be made in Section 6.3.

6.2 Fracture mechanism

Before presenting the constitutive relations for the crack evolution in the next section, the surmised fracture mechanism will be discussed here. This may be of help in discussing the experimental results of, for instance, the cyclic behaviour in cracks (Section 6.4) or the influence of different parameters on the tensile properties (Chapter 7).

At or just before peak load, existing micro-cracks start to grow and/or new micro-cracks originate due to debonding between the coarse aggregates and the matrix. Yet the width of the zone in which these microcracks occur is unknown. With increasing deformation, the micro-cracks coalesce, finally resulting in a single macro-crack. For an increasing deformation, the stress transferring capacity changes. At peak load (viz. f_t), it

is determined by the strength and stiffness of the aggregates, the mortar matrix and the bond capacity between these two constituents. When a continuous macro-crack exists, then it only consists of sliding friction (viz. aggregates are being pulled out of the matrix). For intermediate deformations it is assumed that both types of stress transfer occur. One can assume that the first one is decreasing with increasing deformation, while the contribution of the (aggregate) interlock first increases, whereafter for further increasing deformations this contribution also gradually decreases until finally δ_o is reached. Another possible contribution to stress transfer at intermediate deformations is the existence of intact grain bridges between overlapping cracks (Van Mier[91])

From the above it can be deduced that the tensile strength f_t and the fracture energy G_F are based partly on different material characteristics. The tensile strength depends on the undamaged material, while the fracture energy depends mainly on interlocking. However, interlock in turn depends on the strength and stiffness of the crack surfaces and of the concrete as such. It can be expected that the contribution of interlock to the fracture energy increases in the case of crack surfaces which are more tortuous. Figure 6.2 shows schematically the influence of the tortuosity of the crack path on the stress transferring capacity in the descending branch for larger deformations. In a lightweight concrete (LC), in which cracks run through the aggregates, the crack path is smooth as compared to a normal-weight concrete (NC). Therefore, for NC the descending branch lies above that for LC. Fibre-reinforced concrete (FRC) does not fit completely in this explanation since there is an extra contribution to the stress transferring capacity for larger deformations; the connection of the crack surfaces through the fibres. Nevertheless, FRC has been included because it demonstrates that, with an increasing
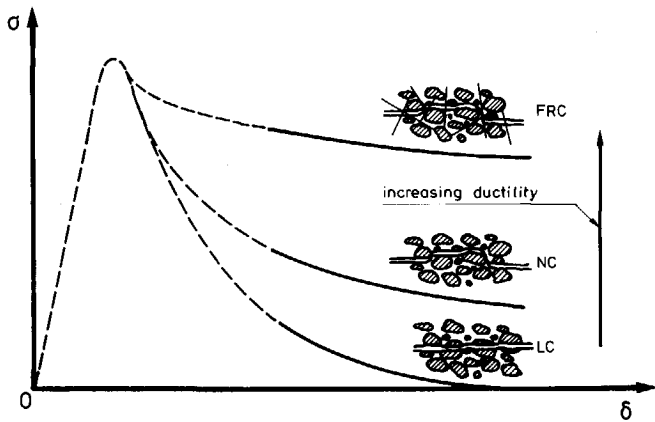

Figure 6.2   Influence of crack path tortuosity on the stress transferring capacity for larger crack openings (Hordijk et al. [89b]).

number of bridges between the crack surfaces, the descending branch rises. With the increasing level of the descending branch, the fracture energy and the characteristic length (for a definition see Section 7.1) increases, which means that the material becomes more ductile.

The explanation in this section only intends to separate the most important mechanisms in the softening branch. In reality, of course, the mechanism will be more complex and less sharp.

6.3 Crack evolution

The most important input parameter for nonlinear fracture mechanics calculations of concrete is undoubtedly the stress-crack opening relation. Its importance has been demonstrated by, among others, Petersson[81], Roelfstra and Wittmann[86] and Rots[86]. The fracture energy G_F is a derivative parameter of this relation; it represents the area under the σ-w relation. Nevertheless, over the past years many more research activities have been concentrated on the determination of G_F, rather than on the determination of σ-w relations. In this respect, the work of RILEM TC-50 "Fracture Mechanics of Concrete" (see Hillerborg[85a,85b]) can be mentioned. One reason for this is the fact that it is rather difficult to perform a deformation-controlled uniaxial tensile test in a stable manner. On the other hand, it is sufficient to determine solely f_t and G_F when the shape of the σ-w relation is known. It should be realized, however, that the shape of the softening relation dominates the fracture energy. For example, if only a linear softening relation is available in a FE code and if the cracks do not develop fully in the analysis, which means that the tail of the descending branch will not be reached, then it is obvious that the linear relation that fits the first part of the real σ-w relation (line A in figure 6.3) will yield better results than the relation that represents a realistic value for the fracture energy (line B in figure 6.3). For the prediction of the maximum load in three-point bending specimens, for instance, only the initial slope of an applied bilinear softening relation plays a role in most cases (Alvaredo and Torrent[87]). Gustafsson[85] found a similar result in calculations of DCB specimens.

Determination of a σ-w relation
The most direct way to obtain the σ-w relation for concrete is still the determination by means of a deformation-controlled uniaxial tensile test. A test series on a normal-weight concrete (in this report denoted as "preliminary") was used to determine a σ-w relation. Experimental details can be found in Cornelissen et al.[86a,86b] and in Appendix A. Data points of individual experiments, representing the relation between relative stress σ/f_t and crack opening w, are plotted in figure 6.4. The mean value for f_t was 3.2 MPa. Crack
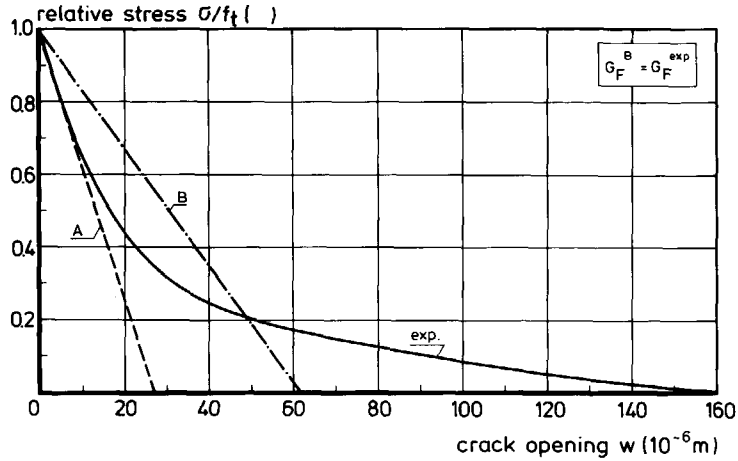
Figure 6.3   Two linear softening relations as compared with an experimentally determined relation (see figure 6.4).

openings were determined according to the procedure of figure 6.1. In this respect, it can be mentioned that the pre-peak nonlinearities were rather small (average δ_{irr} was 1.8 μm). The chosen expression for the stress-crack opening relation is:

$$\frac{\sigma}{f_t} = \{1 + (c_1 \frac{w}{w_c})^3\} \exp(-c_2 \frac{w}{w_c}) - \frac{w}{w_c}(1 + c_1^3) \exp(-c_2) \tag{6.1}$$

The best fit was obtained for $c_1 = 3$, $c_2 = 6.93$ and $w_c = 160$ μm. As far as the tail of the curve is concerned, the following remarks can be made. Firstly, only data points up to an arbitrarily chosen crack opening of 120 μm, where the transferable stress was already diminished to about 10% of f_t, were used in the numerical regression analysis. If more data points for larger crack openings were taken into account, this would give too much weight to that part of the curve in the regression analysis, which results in a less good fit for the smaller crack openings. The second remark is related to the maximum crack opening w_o. The function (eq. 6.1) was chosen in such a way that there is an intersection point w_c (critical crack opening) with the horizontal axis ($\sigma/f_t = 0$), which corresponds with the real material behaviour where the crack surfaces are completely separated at a certain crack opening. Although there is of course a correlation between w_c obtained from the regression analysis and the real maximum crack opening w_o, this does not mean that the value as found above ($w_c = 160$ μm) coincides with the real value for w_o. In equation 6.1, w_c is more or less used as a fitting parameter. The descending branch as can be observed in the experiments displays a long tail in which the stress gradually reaches a zero value. This makes it very difficult to give an experimental determination of the

70

maximum crack opening w_0 at which stress can no longer be transferred. In the literature, values for w_0 in the order of 400-500 μm were reported (see Hordijk et al.[89b]). In Section 7.1 it will be shown that this value can even be larger. The consequences of this long tail for the determination of the fracture energy will also be discussed in Section 7.1.
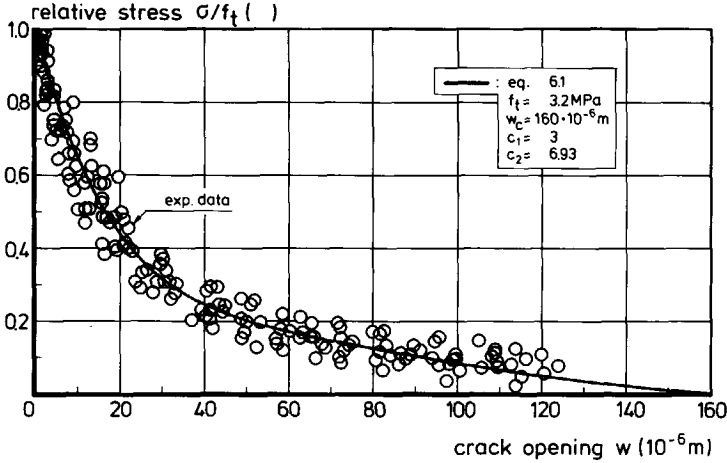
Figure 6.4   Regression analysis for the σ-w relation; data points and fitted relation (eq. 6.1).

With the tensile strength f_t, the critical crack opening w_c and the shape of the σ-w line, the fracture energy can be calculated. The integration $G_F = \int \sigma\, dw$ gives for equation 6.1:

$$G_F = f_t w_c[\frac{1}{c_2}\{1 + 6(\frac{c_1}{c_2})^3\} - \{\frac{1}{c_2} + c_1^3(\frac{1}{c_2} + \frac{3}{c_2^2} + \frac{6}{c_2^3} + \frac{6}{c_2^4}) + \frac{1}{2}(1 + c_1^3)\}\exp(-c_2)] \quad (6.2)$$

For the values of c_1, c_2 and w_c as given above and $f_t = 3.2$ MPa, G_F has a value of 99.7 J/m^2.

Comparison of σ-w relations from different uniaxial tensile tests
Petersson [81] compared stress-crack opening relations for different concrete mixes. It appeared that the shapes of the curves were about the same when they were plotted in a non-dimensional way with stress divided by the tensile strength and crack opening divided by the critical crack opening w_c. In the approximate bilinear σ-w relation that he proposed, w_c was taken as being equal to $3.6G_F/f_t$. For all the mixes the failure mechanism was the same, i.e. aggregates were pulled out of the cement paste. In order to verify whether the shape of the σ-w curve alters when the fracture mechanism is different (cracks running through the aggregates in case of lightweight or limestone concrete) and in order to

71

compare the σ-w relations obtained with different testing equipments, the results of a number of σ-δ curves or σ-w curves as they were reported in the literature are compared. The investigations that have been considered and some experimental information can be found in Table 6.1. From each investigation, only one curve was used. This is either a curve representing a single experiment or a curve that represents an average for a test series. Besides the usual types of tensile tests, the result of a recently developed test method in which tension is achieved by means of a compressive force is also included (Rokugo et al.[89]). The principle of this test method, which was originally proposed for rock-like materials, is outlined in figure 6.5.

Table 6.1   Information about deformation-controlled uniaxial tensile tests for which
*   σ-w relations are compared.*

No.	Reference	dimensions[1] (mm^3)	l_{meas} (mm)	f_c (MPa)	$f_{t,spl}$ (MPa)	w/c	d_{max} (mm)	age[2] (days)
1	Petersson [81]	50*30*20	40	-	-	0.50	8	28
2	Notter [82]	500*125*50	100	44	-	0.50	16	28
3	Gylltoft [83]	85*30*30	67	28	2.8	-	-	-
4	Reinhardt and Cornelissen[84b]	300*ø120	25	45	2.9	0.50	16	32
5	Eligehausen and Sawade[85]	600*ø100	100	35	3.0	0.76	16	150
6	Gopalaratnam and Shah[85] [3]	305*60*19	85	44	-	0.45	10	28
7	Körmeling [86]	100*ø74	100	44	3.5	0.50	8	-
8	Hordijk et al.[87] [4]	150*50*50	35	50	3.4	0.59	8	150
9	Guo and Zhang[87]	210*70*70	155	31	2.4	0.60	-	33
10	Scheidler [87]	450*300*150	450	-	-	0.70	16	28
11	Wolinski et al.[87]	150*50*50	35	47	3.1	0.50	8	32
12	Rokugo et al.[89] [5]	-	-	58	-	0.52	15	-

1) length*width*depth or length*diameter for the critical cross-sectional area
2) mean age in case of a range
3) crushed limestone for the bigger aggregates
4) lightweight concrete with sintered expanded clay 4-8 mm
5) Tube Tension Test (see figure 6.5)

To analyze the results from the literature, the curves were first digitized. Thereafter crack opening was determined according to the procedure shown in figure 6.1 and stress was divided by f_t. The resulting σ/f_t-w relations are plotted in figure 6.6. Values for f_t are given in Table 6.2. The shaded area in figure 6.6 corresponds to the scatter band of the results given in figure 6.4. As can be seen, most of the curves are positioned within this scatter band. The shape of curves 3, 6 and 8 which differ most strongly belong to particular

types of concrete mixes, i.e. rather low compressive strength (curve 3), limestone aggregates (curve 6) or lightweight concrete (curve 8). This suggests that with f_t and the shape function (eq. 6.1), a rather good approximation of the σ-w curve for an ordinary type of concrete can be given.

Figure 6.5   Principle of the Tube Tension Test (Rokugo et al.[89]).

To improve the description of the σ-w curve for a certain concrete mix, the fracture energy can be used as a third parameter (G_F-method). Therefore, G_F in combination with f_t will be used to normalize the crack opening w similar to the procedure proposed by Petersson[81]. Now, however, the critical crack opening w_c is chosen in accordance with the results of figure 6.4 (f_t= 3.2 MPa, w_c= 160 μm and G_F= 99.7 J/m^2). For the critical crack opening this gives the relation: $w_c = 5.14 G_F/f_t$. In the analyses of the results from the literature, the tensile strength is assumed to be equal to the peak stress in the
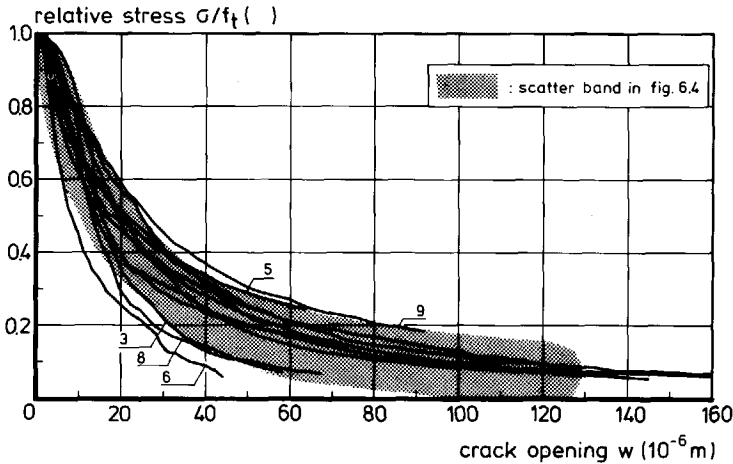

Figure 6.6 σ/f_t-w relations for the investigations listed in Table 6.1.

73

σ-δ curves. The determination of G_F, however, is more complicated. Since all the curves were stopped somewhere in the descending branch, where a certain stress could still be transferred, the fracture energy is determined according to the procedure described in Section 7.1 and sketched in the inset of figure 6.7. Values for f_t and the calculated values for G_F and w_c are given in Table 6.2 and the σ/f_t- w/w_c curves are presented in figure 6.7. As can be seen, all curves, including those representing deviating concrete mixes, are now positioned in a narrow band. Consequently, it can be concluded that it is sufficient to determine f_t and G_F. The stress-crack opening relation can then be obtained by eq. 6.1 in which $c_1 = 3$, $c_2 = 6.93$ and $w_c = 5.14 G_F/f_t$.

Table 6.2   *Values for f_t, G_F and w_c as obtained in the analysis of σ-δ relations from the literature (see also Table 6.1).*

No.	Reference	tensile strength f_t (MPa)	fracture energy G_F (J/m^2)	critical crack opening[1] w_c (10^{-6} m)
1	Petersson [81]	4.61	161	180
2	Notter [82]	2.29	87	194
3	Gylltoft [83]	2.78	68	126
4	Reinhardt and Cornelissen[84b]	2.80	95	174
5	Eligehausen and Sawade[85]	3.20	138	250
6	Gopalaratnam and Shah[85]	3.68	65	91
7	Körmeling [86]	3.15	124	203
8	Hordijk et al.[87]	3.31	80	125
9	Guo and Zhang[87]	2.82	138	250
10	Scheidler [87]	1.85	68	187
11	Wolinski [87]	2.79	109	202
12	Roguko et al[89]	3.39	112	170

1) $w_c = 5.14 G_F/f_t$

The results presented above are to some extent remarkable. Not only the concrete mixes varied between the different investigations, but also totally different loading equipments and specimen dimensions were applied. For instance, stiff loading equipment in which non-uniform crack opening (see Chapter 5) was limited (Nos. 1, 8 and 11) was used, but results were also included which showed extreme non-uniform crack opening (Nos. 2 and 10). This suggests that the influence of non-uniform crack opening on the shape of the σ-w relation is not very important (curves of individual test results with very

74

pronounced irregularities in the descending branch excluded). Obviously, opposing influences are averaged out in practical testing.
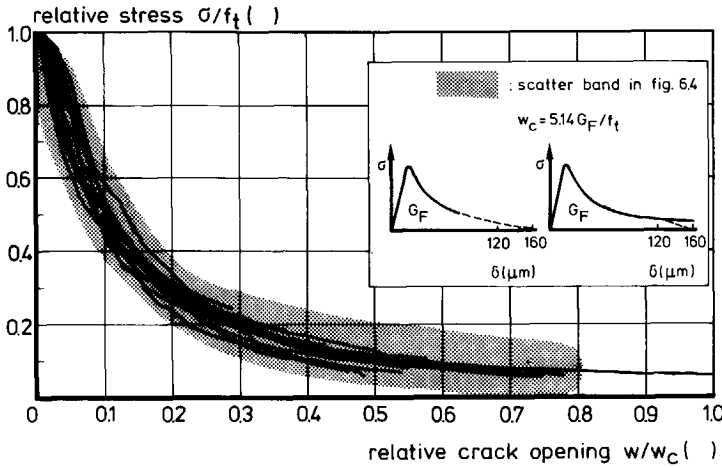

Figure 6.7   The relations of figure 6.6 with w normalized by w_c.

Indirect methods

Two other methods in which the σ–w relation of concrete is determined in an indirect way will be briefly discussed. The first method is based on data fitting (inverse modelling). In this method, experiments are simulated with a number of FE simulations and the σ-w relation giving the best fit is regarded as being the material property. At the Swiss Federal Institute of Technology in Lausanne, a computer program was developed for this purpose and applied for different types of tests (Roelfstra and Wittmann[86], Wittmann et al.[87,88]). Bilinear σ-w relations can be predicted with this program. It appeared, however, that several softening relations can simulate the real behaviour equally well, which reduces this method to only an approximating one. For a number of concrete mixes and loading rates, optimum bilinear relations were determined, while the stress at the break-point was fixed at 1/4 f_t (Wittmann et al.[88]). The normalized σ-w relations did not differ much from each other, which is in agreement with the results presented in figure 6.7. Furthermore, they appear to be a good approximation of the directly determined softening relation (eq. 6.1) as can be seen in figure 6.8. Both the initial slope and the slope of the second part of the descending branch coincide very well, while the parameter w_c was coincidentally the same.

Li[85] proposed an indirect method for the determination of the σ-w relation which is based on the J-integral. With measurements on two similar notched specimens that differ

only in notch length, a J-w relation is determined. Then the σ-w relation can be obtained by differentiation of J(w) with respect to w. For more information about the theoretical basis, the reader is referred to Li et al.[87]. In the author's opinion, the applicability of this technique for a normal type of concrete has not yet fully been proved. The fact that the stress for a certain crack opening has to be determined by differentiation of an experimentally determined energy-crack opening relation makes it sensitive to errors.
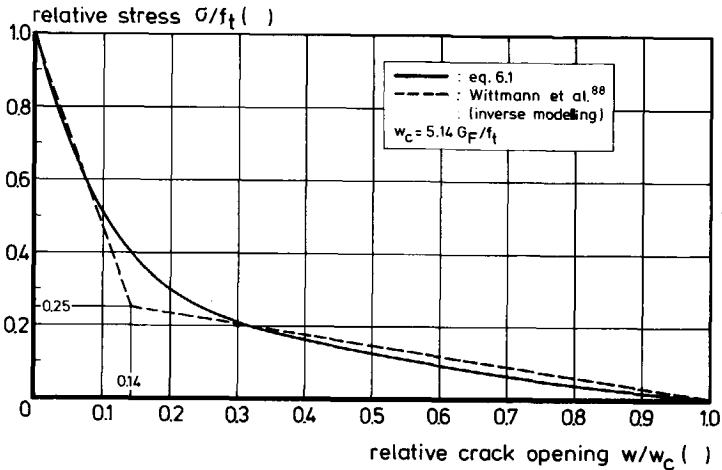
Figure 6.8   Bilinear softening relation by inverse modelling as compared with the relation obtained from uniaxial tensile tests.

Concluding remarks
In this section it has been demonstrated that for most types of concrete, the shape of the normalized stress-crack opening relation is almost the same. It appeared that this shape can very well be described with eq. 6.1, while the critical crack opening w_c is equal to $5.14 G_F/f_t$. This means that the σ-w relation for a certain type of concrete is known if the tensile strength and the fracture energy are known. Consequently, a proper σ-w relation now depends on the correct determination of the parameters f_t and G_F. Standard test methods are available, like the uniaxial tensile test or the tensile splitting test for f_t and the three-point bending test for G_F. However, results from these tests may be affected by several factors, a few of which will be discussed in Chapter 7.

For the sake of clarity, the values for f_t and G_F as they were taken from the reported curves (Table 6.2), probably do not all represent the real values for the investigated concrete. Nevertheless, it appears that the shapes of the descending branches did not differ very much when compared in the way described.

76

It can be assumed that eq. 6.1 is an adequate relation for concrete softening. This is supported by the results obtained by inverse modelling as well as by the good simulations that have been achieved with it in FE simulations (Rots[86]). With the verification tests (Chapter 8), the correctness of the σ-w relation for crack openings up to about 150 μm will also be demonstrated. There, however, it will become clear that the relation can be improved for larger crack openings. In this section, emphasis was on the constitutive relation for concrete softening. As far as modelling is concerned, two recently proposed models can be mentioned. These are a rheological model by Curbach[87] and a grain model by Duda[90]. Both models proved very suitable for describing the experimental results as presented in figure 6.4.

6.4 Crack cyclic behaviour

The number of investigations concerning deformation-controlled uniaxial tensile tests appeared to be limited. However, those of them which also applied post-peak cyclic loading are even more scarce. For the fatigue approach of plain concrete, as proposed in this report, the cyclic behaviour in the fracture zone is an essential parameter. A proper description of this material property, however, is not only required for analyses of structures under fatigue or cyclic loading. Also in case of a monotonic increasing load, the structure may partially unload due to the creation of new cracks which causes a redistribution of stresses. Yet, in most FE codes, there is either no option for unloading in the softening zone or only a simple secant unloading (linear through the origin) is available.

In the Stevin Laboratory, deformation-controlled uniaxial tensile tests with cyclic loading in the post-peak region have been performed for a number of years. These experiments concerned repeated tensile-tensile loading as well as alternating tensile-compressive loading. In the literature, only a few investigations with post-peak cyclic loading (Terrien[80], Gylltoft[83], Gopalaratnam and Shah[85], Willam et al.[85] and Guo and Zhang[87]) have been found by the author. Based on the experimental results obtained in the Stevin Laboratory, a number of different models for the constitutive relations of concrete under cyclic loading have been proposed (Reinhardt et al.[86], Yankelevsky and Reinhardt[87a,87b,89], Wolinski[89]). These models, together with the model by Gylltoft[83], will be briefly discussed in this section. From these models, the "Focal-point model" by Yankelevsky and Reinhardt[87b,89], which uses a multi-linear description for the cycles and a new model, which will be presented below and which is based on continuous functions for the loops, will be discussed in more detail and compared with experimental results.

Preliminary experimental results

A test series was performed in which the loading histories I to IV were applied (see Appendix A). A normal-weight as well as a lightweight concrete were investigated. Results have been reported before (Cornelissen et al.[86a,86b]). Those for the normal-weight concrete will be briefly summarized. The change of the cycles with increasing crack opening was determined by the parameters: stiffness degradation C/C_0, relative stress drop $\Delta\sigma/\sigma_{eu}$ (σ_{eu}: stress at the envelope curve at the start of unloading) and for type IV loading tests, the residual crack opening at a stress level equal to $-f_t$, w_r. The meaning of these parameters is illustrated in figure 6.9 for a typical result of a type II and a type IV loading experiment respectively. Results for the normal-weight concrete are presented in figure 6.10 with crack opening according the procedure of figure 6.1. The lines for the stiffness degradation are averages of three individual tests. It should be noted that due to the short cycle in the type II loading tests, the stiffness degradation was determined slightly differently as compared to those of type III and IV loading (see also the inset in figures 6.10a and 6.10b). This rules out a direct comparison of these specific results. The straight lines in figure 6.10c were obtained by linear regression to the data points. As can
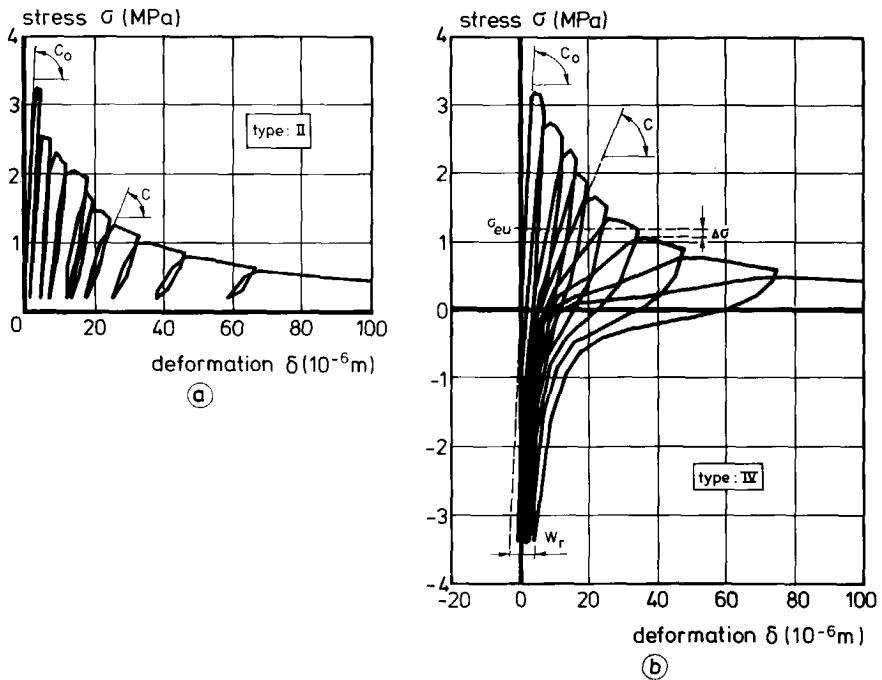
Figure 6.9   Experimental result for a type II (a) and IV (b) loading test and the explanation of parameters used for the description of post-peak cycles (Reinhardt et al. [86]).

be seen, the scatter implies that only tendencies can be discussed. Finally the line in figure 6.10d is a hand-smoothed curve for the data points.
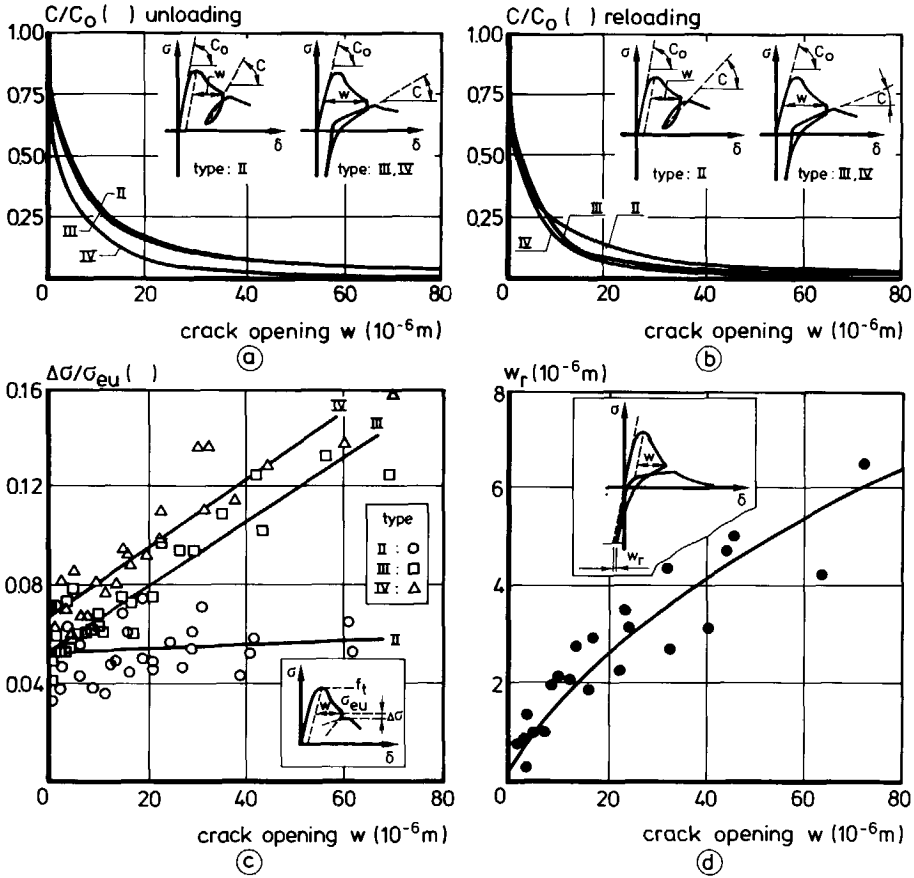
Figure 6.10   Parameters for crack cyclic behaviour (C/C₀ unloading (a), C/C₀ reloading (b), Δσ/σₑᵤ (c) and wᵣ (d)) as function of crack opening (Cornelissen et al.[86a,86b]).

The tests made it clear first of all that the envelope curve was not significantly affected by the cyclic loading. Furthermore, the following preliminary conclusions could be drawn from the results in figure 6.10:

– The unloading and reloading stiffness show a steep decrease with increasing crack opening. This is more pronounced for the reloading curves than for the unloading curves, as had already been seen from the shape of the cycles in figure 6.9 where the

79

slope of the linear part in the reloading curve is less steep than that in the unloading curve.

– The rather small differences between the unloading stiffness degradation lines for the different loading types, especially when the scatter is taken into account, seem to be in agreement with the assumption that the relation between stress and crack opening at the envelope curve is not affected by the preceding loading history.

– The relative stress drop-crack opening relation shows that a compressive lower stress level is more detrimental than a tensile lower stress level. A similar damaging effect of stress reversals (crack closure) was found in fatigue tests (see Section 2.3).

– At tensile unloading or compressive loading, the mismatch of the crack surfaces, represented by w_r, increases with increasing crack opening at unloading.

It should be noted that the parameter stiffness degradation, as it was determined C/C_0, depends on the applied measuring length which makes it a less good parameter for general application.

The results presented above were obtained with the equipment without the inner loading platen (see Section 4.1). This means that the results might be a little affected by friction in the guiding system of the tensile equipment, since this is active in opposite directions for the unloading and reloading parts of a cycle. This was one reason why a new test series was performed with post-peak cyclic loading. The possibility of recording much more data due to a more sophisticated data-acquisition equipment as well as the desire to include some more lower stress-levels for the loops were the other arguments justifying the performance of a new test series.

New test series and the influence of non-uniform crack opening
General experimental details of the new test series for determining the crack cyclic behaviour can be found in Appendix A. Specific results will be presented later in this section. In total, six different loading histories were applied. Besides the tests with monotonic increasing deformation, five different lower stress levels (σ_L is approximately 1 MPa, 0 MPa, -1 MPa, -3 MPa and -15 MPa) for post-peak cyclic loading were chosen. For each loading type, three experiments were performed. Sometimes, however, glue fracture occurred at a rather low average deformation. On average, for the tensile strength a value of 2.8 MPa was found with a coefficient of variation of 8.5%. The fracture energy, determined according to the procedure that will be discussed in Section 7.1 (data points up to $\delta = 120$ μm and an assumed δ_0 of 160 μm), was 95.3 J/m^2 with a coefficient of variation of 7.6%.

Naturally, the non-uniform crack opening in uniaxial tensile tests, as discussed in Chapter 5 for a monotonic increasing deformation, also occurs in the experiments with

80

post-peak cyclic loading. This means that for an unloading and reloading cycle at a small mean deformation, the crack closes and re-opens only on one side of the specimen, while the other side remains uncracked. This phenomenon will be illustrated by the result of a particular experiment. For modelling the crack cyclic behaviour, it is important to know how the experimental σ-w cycles are affected by this non-uniform opening and closing of the crack.

In the test that will be discussed in more detail, a lower stress-level of about -3 MPa was applied. In this particular test, the non-uniform crack opening occurred mainly between the front and rear side of the specimen (figure 6.11a), while furthermore, accidentally, a few cycles were performed at an average deformation at the envelope curve, at the start of the transition from non-uniform crack opening to what is again a more or less uniform crack opening (figure 6.11b). In figure 6.11c, two cycles are plotted for which the first cycle, denoted as loop C, had a deformation distribution which was highly non-uniform, as can be seen by the deformation distributions that belong to points 1 to 5 (figure 6.11d). The deformation at the front side of the specimen appeared to vary between 17.8 µm and -0.8 µm, while the deformation at the rear side did not exceed a value of 1.2 µm ($\approx$ 34 µstrain). For loop D, the deformation distributions were much more uniformly distributed. The non-uniformity that still existed was probably due to a small undesired eccentric loading. Loops A and B (figure 6.11b) start from a point of the envelope curve which is characterized by the fact that after this point the non-uniformity no longer increases, but alters with increasing average deformation to more uniform deformation distributions. These two loops give some indication about the influence of the non-uniform crack opening on the shape of the loading cycle. The unloading curve of loop B crosses the unloading curve of loop A, even though the complete unloading curves are usually positioned beside each other. Some more information about the influence of this phenomenon can be obtained from figure 6.13 in the next paragraph, where unloading curves of different loading types are compared. Based on these results, it can be concluded that there is some influence of the phenomenon of non-uniform crack opening on the shape of the σ-w cycles. Nevertheless, it is believed that the error made by using the obtained results for modelling the crack cyclic behaviour is negligible. However, in other tensile equipment displaying much more pronounced non-uniform crack openings, this should be checked again.

Is the relation between σ and w on the envelope curve unique?
From the preliminary investigations it was concluded that the envelope curves were not significantly affected by the preceding loading history. This phenomenon, denoted as the "envelope concept", will now be checked by the envelope curves and the unloading curves of the new experiments. If the relation between σ and w on the envelope curve is

independent of the preceding loading history, then it can be assumed that this also holds true for the fracture process (configuration of micro-cracks). In fact, the effect of a loading cycle, which concerns frictional forces between the crack surfaces or the creation of new micro-cracks, is probably overshadowed or neutralized by the creation of new, more important micro-cracks at the envelope curve. This means that the unloading curves (those that start from the envelope curve) must be equal for the different loading types applied.
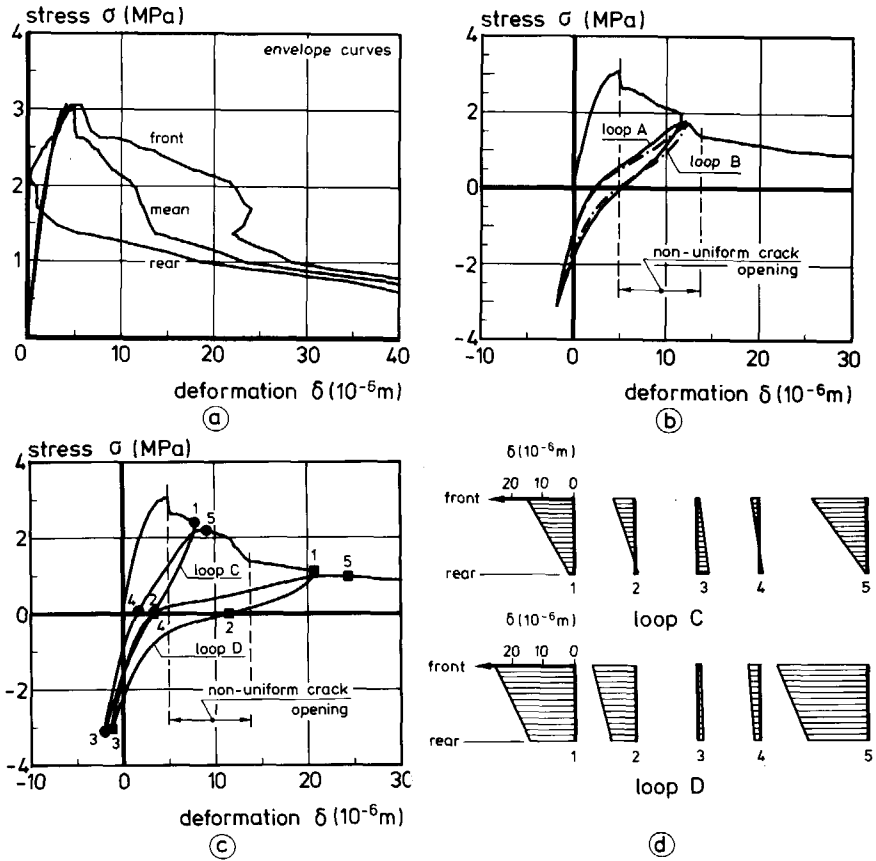
Figure 6.11   Specific test result focusing on non-uniform crack opening;
a) σ-w relations, b)two loops around an envelope crack opening with
maximum non-uniformity, c) σ-w loops for which the deformation
distributions of the marked points are plotted in d).

Before the results are presented, some general remarks will be made. If the envelope concept exists, then it is only valid for the σ-w relation. As soon as a deformation is applied over a certain measuring length, which always has to be done in experiments, then the

phenomenon will be blurred by the irreversible deformations in the concrete outside the crack (bulk behaviour). For a repeated tensile loading, this effect will probably not be important. For a lower stress level in compression, however, it can have a significant influence. Obviously, these effects can be minimized by applying a short measuring length. Similar points are raised for discussion in Section 7.6 where the influence of a compressive preloading will be dealt with and in Section 9.4 where deformations in static and fatigue tests are compared.

For this test series the σ-w relations were determined by subtracting the elastic deformations from the total deformations. This means that the irreversible deformation at peak load is considered to be only the result of non-uniform stress distributions (see also Sections 6.3, 7.1 and 7.5). As a result, the σ-w relations display an increase of stress with increasing crack opening for small values of w, which does not coincide with the expected physical behaviour. For the analyses of the test results, however, this will have no significant consequences. Furthermore, for comparison of unloading curves, the stress will not be normalized with the peak stress. Since the non-uniform stress distributions significantly influence the peak load (small or no crack opening) as compared to the load at larger crack openings, it is expected to have a significant influence. The average σ-w relations for the different types of test (envelope curves) are plotted in figure 6.12. The fact that the curve for monotonic increasing deformation is positioned above those for the other types of loading suggests that the relation between σ and w at the envelope curve is not unique. If, however, the scatter bands are taken into account and if the remark about bulk behaviour is considered, then the differences in the σ-w curves cannot be regarded as significant.
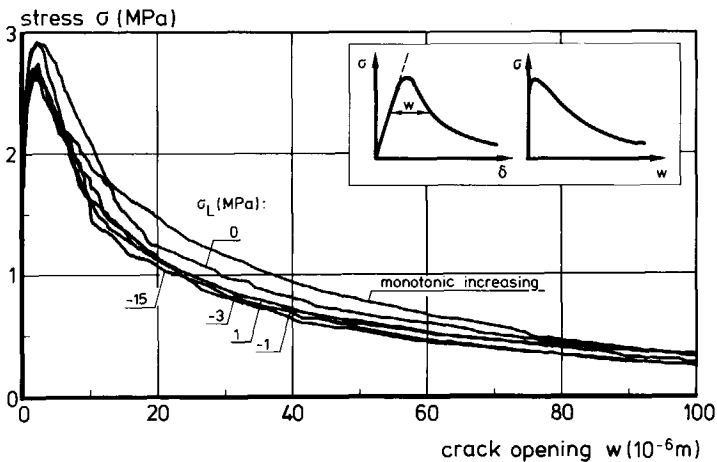

Figure 6.12   Average σ-w relations (envelope curves)

83

In order to compare the unloading curves of the different tests, the crack openings (w_σ with for σ: 1, 0, -0.5, -1, and -3 MPa respectively) as a function of the crack opening at the point of leaving the envelope curve w_{eu} (see figure 6.13a) were determined by means of linear interpolation between data points. In figure 6.13b, the points (w_σ, w_{eu}) for stress levels 1 MPa, 0 MPa and -0.5 MPa are plotted. As can be seen, the points for a certain stress level in the unloading curves and for tests with a different loading history, i.e. with different lower stress levels σ_L, are very well positioned on one line, which indicates that the unloading curves starting from a point on the envelope curve are unique and this in turn supports the envelope concept. Close inspection of the separate results shows that the points for a certain stress level can be represented as two linear relations
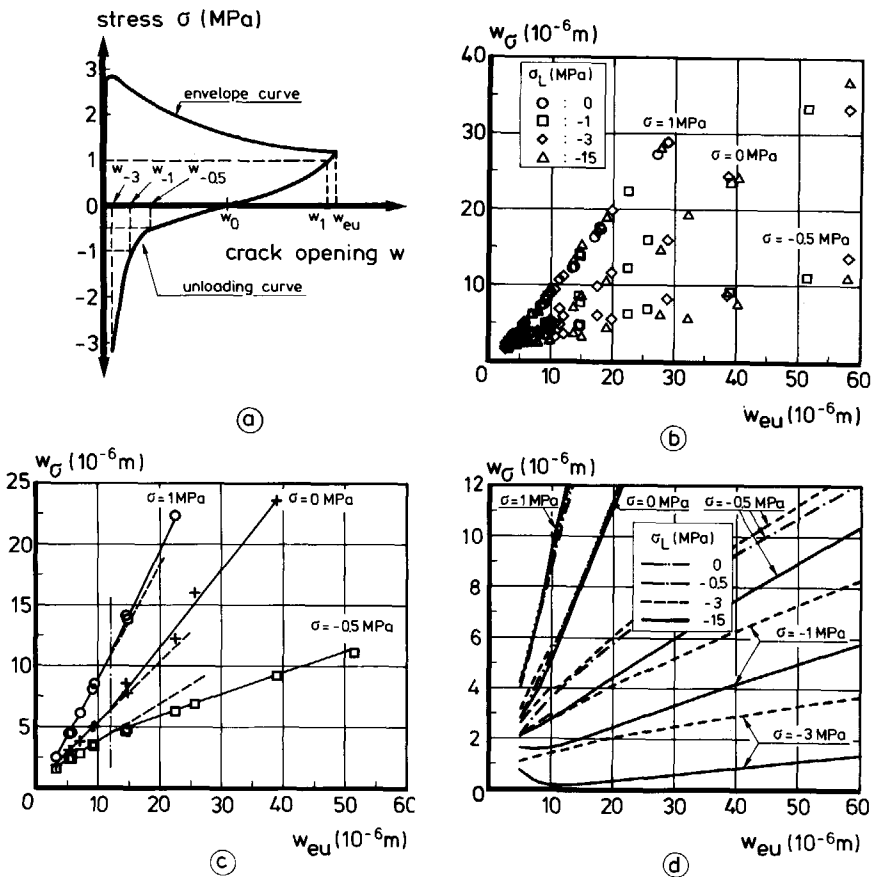

Figure 6.13   Comparison of the unloading curves for different types of test; a) explanation, b), c) and d) crack opening in the unloading curve at a certain stress level, w_σ as a function of the crack opening at the envelope curve.

84

with slightly different slopes. To illustrate this, the data points for the tests with $\sigma_L = -1$ MPa are plotted in figure 6.13c. The assumed linear relations are also given, and it can be seen that for all three stress levels (1, 0 and -0.5 MPa) the transition between the two linear curves appears at a crack opening at the envelope curve, w_{eu}, of about 12 µm. This result may probably be explained by the phenomenon of non-uniform crack opening. First of all, the crack opening at the kink between the two straight lines is approximately where the non-uniformity in the crack opening reaches its maximum. Furthermore, the increasing slope for $\sigma = 1$ MPa and the decreasing slope for $\sigma = -0.5$ MPa are in agreement with the changes in the shape of the loops as shown in figure 6.11b. An impression about the influence of the irreversible deformations within the measuring length can be obtained from figure 6.13d. In this plot the results of figure 6.13b are partly enlarged, while the results for stress levels -1 MPa and -3 MPa are added. As was expected, at a decreasing lower stress level of the post-peak cycles (increasing compressive stresses), the compressive irreversible deformation increases, resulting in apparently lower crack openings

Existing models for crack cyclic behaviour

The models for crack cyclic behaviour which the author has found in the literature are schematically represented in figure 6.14. All the models are given by means of a stress-crack opening relation. For those models that were originally proposed by means of a stress-strain relation (a) or a stress-deformation relation (c,d), elastic deformations were subtracted from the total deformations. Though the shape of the envelope curve is not being dealt with here, it was decided to plot those that were used in the original publications.

The model by Gylltoft[83] deviates from the other models as well as from experimental results due to the fact that it does not assume a unique envelope curve. It is based on an energy criterion. The area enclosed by the unloading-reloading cycle A_I is regarded as being the energy supplied to the fracture zone (micro-cracking) and is therefore equal to area A_{II}. This means that frictional effects, which probably play a major role, are not taken into account. The model by Reinhardt et al.[86] was the first model which was based on the experimental results obtained in the Stevin Laboratory (figures 6.10c and 6.10d). A distinction is made between tensile-tensile ($\sigma_L \geq 0$) and tensile-compressive ($\sigma_L < 0$) loading. Yet the model by Yankelevsky and Reinhardt[87a] is the only model that uses continuous functions instead of multilinear descriptions for the loops. It is, however, only applicable down to a lower stress level of about $-0.1f_t$. One drawback of this model is that the given analytical expressions are related to a certain gauge length (35 mm). A second model by the same authors (Yankelevsky and Reinhardt[87b,89]) uses a set of geometrical loci (so-called "focal points") to compute the piecewise linear branches of the unloading-
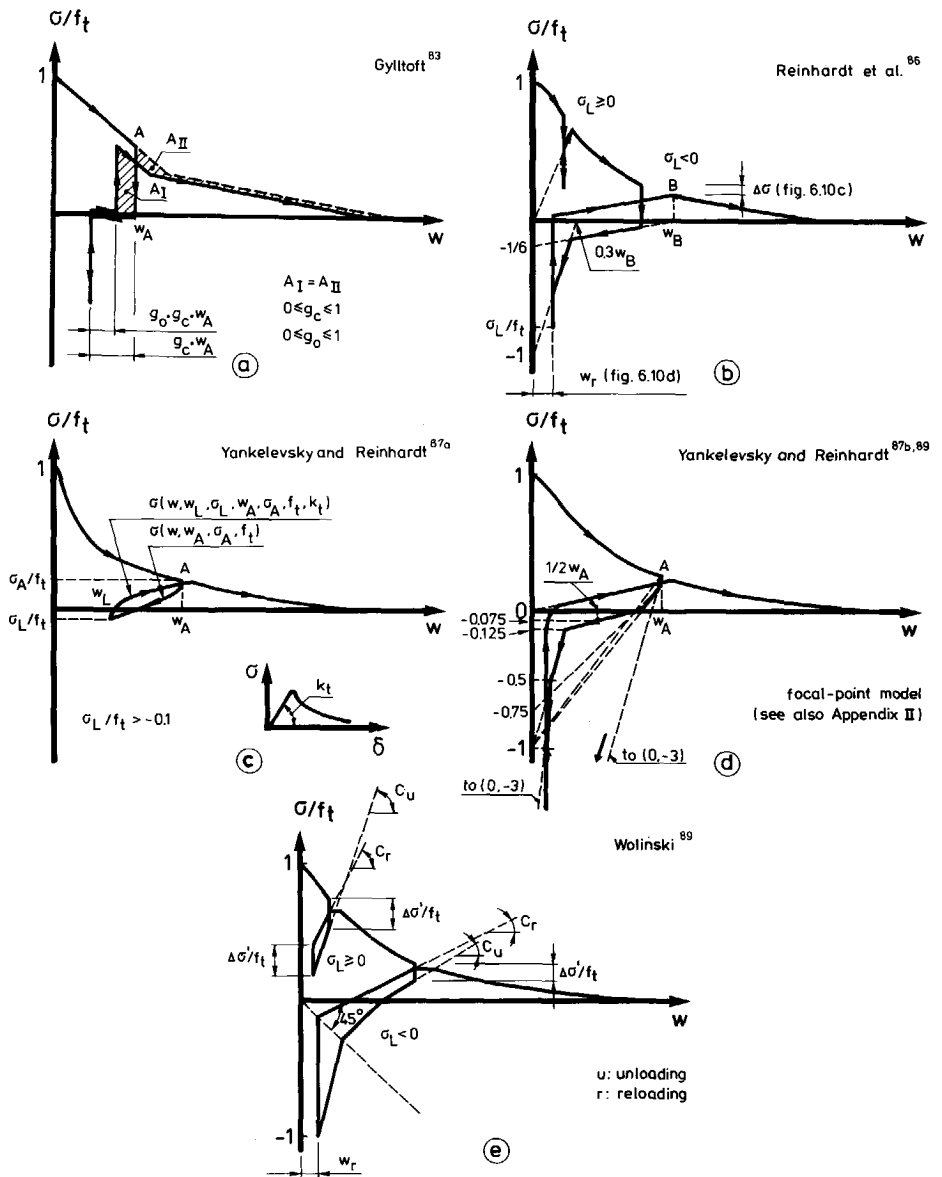
*Figure 6.14   Models for crack cyclic behaviour of plain concrete, as found in
the literature.*

reloading cycles. The experimental loops at different crack openings for tensile as well
as compressive lower stress levels can be described very well with this model. However,
the model was found to yield erroneous results for very small crack openings. Therefore

a small modification of the model is proposed in Appendix B. There, the formulae for the keypoints in the loops are given. Furthermore, a comparison with the results of the new test series and a new model, which will be proposed in the next paragraph, will be given later on in this section. The model by Wolinski[89] can be regarded as a variation on the model shown in figure 6.14b and requires similar experimental data as input like those given in figure 6.10. Finally, it can be mentioned that a rheological model for the cyclic behaviour was recently proposed by Duda and König[90].

A new model based on continuous functions
Of the models presented, the focal-point model (FPM) probably gives the best approach of the real cyclic behaviour. This model is suitable for implementation in FE codes. The formulae for the coordinates of the keypoints are given in Appendix B.1. For the sake of clarity, these formulae deviate from those in the original publication due to the transition from σ-δ relations into σ-w relations. However, the model itself is obviously not affected by this transition.

If the focal-point model represents the actual material behaviour quite well and if it can be used for numerical implementation, why ever develop a new model? The reason for this has to do with the simplicity of numerical modelling and the number of operations that have to be executed in a FE analysis. An analytical description for the unloading curve and the reloading curve would in this respect be preferable to the focal-point model which demands many more operations. So, it was felt worthwhile to search for such analytical expressions, in addition to which the complexity of the expressions themselves is not very important.

Besides the expression for the envelope curve, the new model basically consists of three expressions (figure 6.15). These are respectively: expressions for the unloading curve (I), the gap in the envelope curve (II) and the reloading curve (III). As yet, deformation reversals in the loop itself will not be taken into account. It has been chosen to use only characteristic points in the σ-w relation (f_t,w_c,w_{eu},σ_{eu},σ_L) as variables in the expressions. Before the expressions are presented, it should be made clear that the aim was to tackle the whole problem (unloading starting between crack openings 0 and w_c and lower stress levels σ_L, between f_t and f_c) by using only these three expressions and, of course, the expression for the envelope curve, while furthermore continuous functions were preferred. Therefore, the name "Continuous-function model" (CFM) will be used in the sequel of this report.
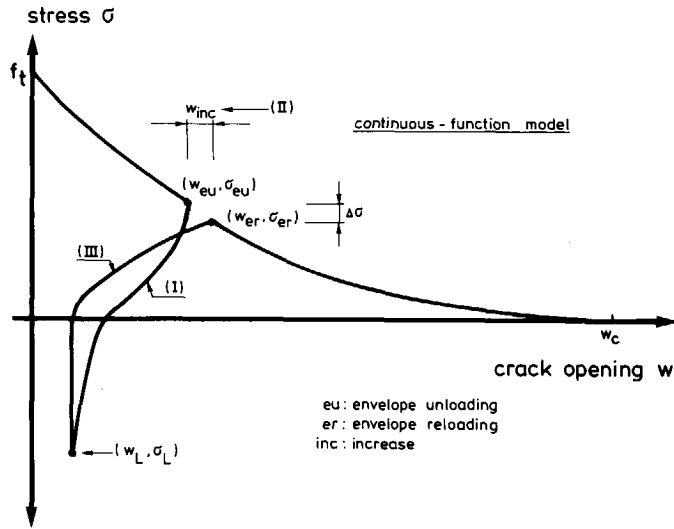
Figure 6.15   *Set-up for the description of crack cyclic behaviour with the continuous-function model.*

The expressions that were chosen are based on a close inspection of the experimental results. Starting from point (w_{eu}, σ_{eu}) at the envelope curve, the unloading curve is determined by:

$$\frac{\sigma}{f_t} = \frac{\sigma_{eu}}{f_t} + \{\frac{1}{3(w_{eu}/w_c) + 0.4}\}[0.014\{\ln(\frac{w}{w_{eu}})\}^5 - 0.57(1 - \frac{w}{w_{eu}})^{0.5}] \tag{6.3}$$

For the description of the gap in the envelope curve, either the stress-drop $\Delta\sigma$ $(\sigma_{eu} - \sigma_{er})$ or the increase in crack opening w_{inc} $(w_{er} - w_{eu})$ can be used. Since for a known w_{inc}, the corresponding $\Delta\sigma$ can be directly determined with the σ-w relation for the envelope curve (eq. 6.1), while for a known $\Delta\sigma$ an iterative procedure has to be applied in order to find w_{inc}, the description of w_{inc} was preferred. The expression for w_{inc} as a function of the coordinates at the point of leaving the envelope curve and of the lower stress level is:

$$\frac{w_{inc}}{w_c} = 0.1 \frac{w_{eu}}{w_c}\{\ln(1 + 3\frac{\sigma_{eu} - \sigma_L}{f_t})\} \tag{6.4}$$

The coordinates of the returning point on the envelope curve (w_{er}, σ_{er}) can now be found with

$$w_{er} = w_{eu} + w_{inc} \tag{6.5}$$

and eq. 6.1. Starting from the point at the lower stress level (w_L, σ_L) up to point (w_{er}, σ_{er})

88

at the envelope curve, the reloading curve is determined by

$$\frac{\sigma}{\sigma_L} = 1 + [\frac{1}{c_3}\{\frac{(w-w_L)}{(w_{er}-w_L)}\}^{0.2c_3} + \{1-(1-\frac{(w-w_L)}{(w_{er}-w_L)})^2\}^{c_4}](\frac{c_3}{c_3+1})(\frac{\sigma_{er}}{\sigma_L}-1) \qquad (6.6a)$$

with for the coefficients c_3 and c_4:

$$c_3 = 3(3\frac{f_t-\sigma_L}{f_t})^{(-1-0.5\frac{w_{eu}}{w_c})}\{1-(\frac{w_{eu}}{w_c})^{(\frac{0.71f_t}{f_t-\sigma_L})}\} \qquad (6.6b)$$

$$c_4 = [2(3\frac{f_t-\sigma_L}{f_t})^{-3} + 0.5]^{-1} \qquad (6.6c)$$

The procedure for reversals of crack opening within a loop will be given later on in this section, while a summary of the total model can be found in Appendix B.2.

Comparison between experimental results and numerical models
The focal-point model and the continuous-function model have been compared with the experimental loops as found in the new test series. The results for a number of cycles can found in figure 6.16. More comparisons can be found in Appendix B.3. For the prediction of the loops the following procedure was applied. For f_t and G_F in eqs. 6.3 to 6.6, the average value for the total test series was used. In order to find a point where the reloading curve meets the envelope curve again (w_{er},σ_{er}), an assumption had to be made for the relation of the envelope curve. Here, the relation (eq. 6.1) usually applied in this report has been used, with w_c equal to the value that was obtained with the average values for f_t and G_F ($5.14G_F/f_t = 175\,\mu m$) and for f_t a fictive value which is chosen in such a way that point (w_{eu},σ_{eu}) is part of the envelope curve. Finally, the predictions were done using w_{eu}, σ_{eu} and σ_L as input. Though both models appear to predict the cyclic behaviour very well, it looks as if the continuous-function model approaches the experimental results a little better than the focal-point model does.

Besides the comparison of the total loops, it was also decided to compare the values of w_{inc} and $\Delta\sigma$ as a function of crack opening, w_{eu}, and lower stress level, σ_L. For values of σ_L corresponding with those applied in the experiments and crack openings of up to $0.4w_c$, the w_{inc}-w_{eu}/w_c relations are plotted in figure 6.17a. Here again, the average values for f_t and G_F have been used, which yields a value of 175 μm for w_c. As can be seen, in the continuous-function model the increase in the crack opening after an unloading-re-loading cycle increases with decreasing lower stress level (σ_L), while in the focal-point model this value is independent of σ_L. The preliminary experiments had already revealed the detrimental effect of a lower value of σ_L. A comparison of the experimental values with the predicted relations (figures 6.17b to 6.17f) show that the CFM predicts the results better than the FPM. It should be mentioned, however, that in the experiments w_{inc} is
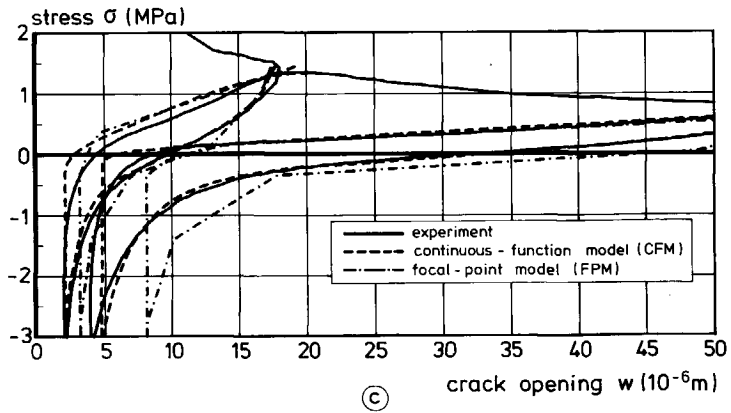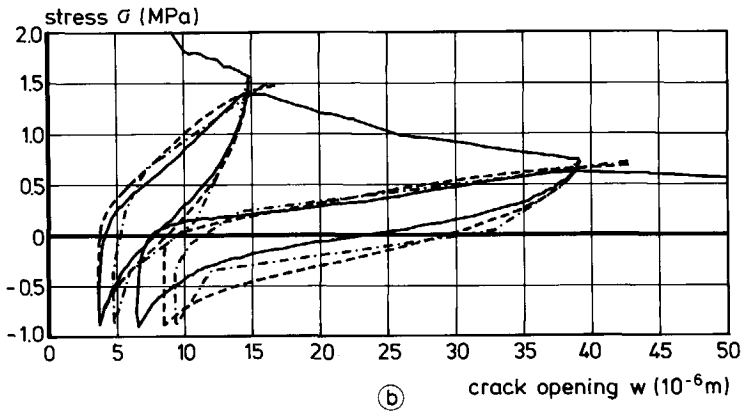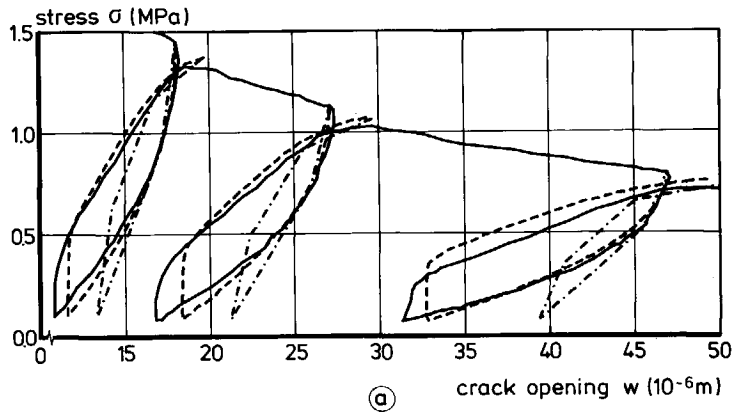
89

Figure 6.16   Experimental results for crack cyclic loops and the predictions
with CFM and FPM.

difficult to determine exactly due to the gradual transition of reloading curve into envelope curve (see, for instance, figure 6.16).
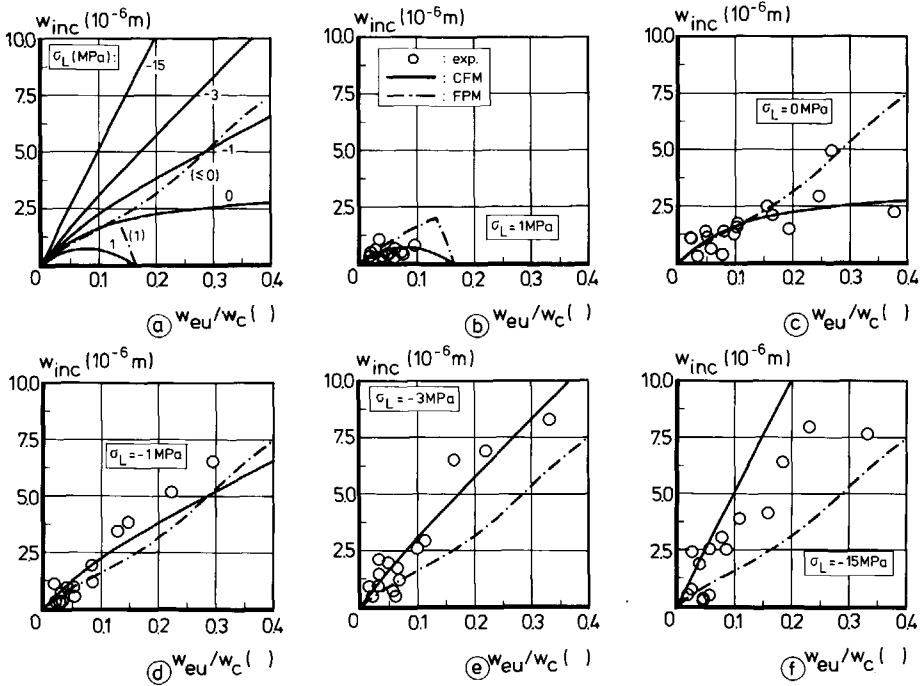

Figure 6.17   Model predictions and experimental results for the relation between w_{inc} and w_{eu}/w_c.

By applying eqs. 6.5 and 6.1 respectively, values for σ_{er} that correspond to the values of w_{inc} in figure 6.17 can be calculated. Thereafter, $\Delta\sigma$ ($=\sigma_{eu}-\sigma_{er}$) is also known. Similar to the plots in figure 6.17, the $\Delta\sigma/\sigma_{eu}$-w_{eu}/w_c relations are plotted in figure 6.18. The same tendencies as seen in figure 6.17 can be observed.

A closer inspection of the experimental results shows that there is a significant difference in w_{inc} and $\Delta\sigma/\sigma_{eu}$ values between a tensile or zero lower stress level on the one hand and a compressive lower stress level on the other. Between the values of $\sigma_L = -1$, -3 and -15 MPa, however, there is no longer much difference. As mentioned before, this phenomenon of an especially damaging effect of stress reversals was also observed in fatigue tests (Cornelissen[84]).

Predictions of cycles as reported in the literature can be found in figures 6.19 and B.11 to B.14 (App. B.3). Though the predictions with FPM as well as with CFM are not as good

as for the results of the new test series, they still can be regarded as fairly good. For the sake of clarity, the same procedure as used for the new test series was applied.
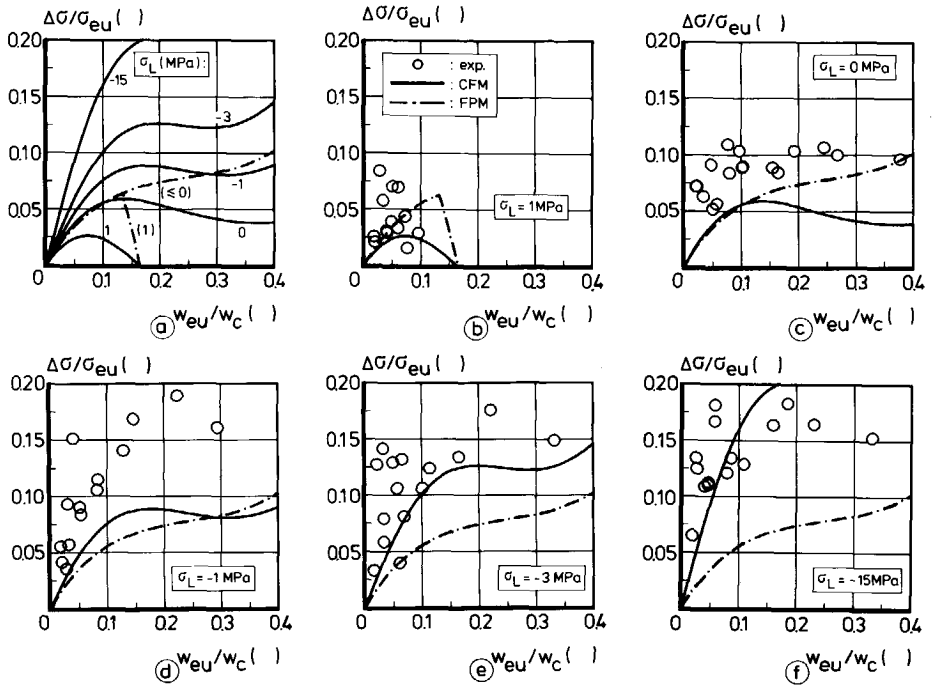

Figure 6.18   Model predictions and experimental results for the relation
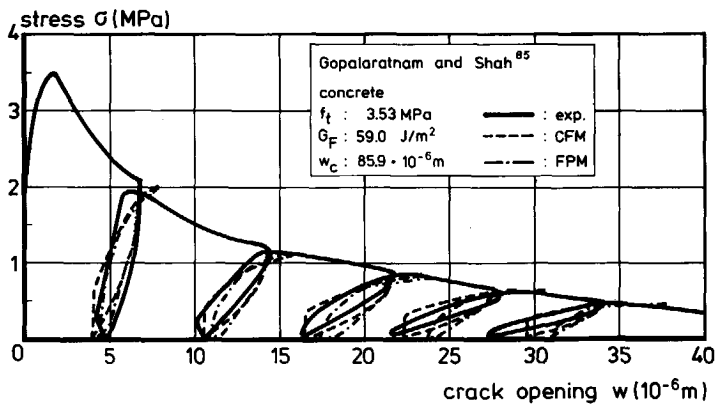between $\Delta\sigma/\sigma_{eu}$ and w_{eu}/w_c.

Figure 6.19   Predictions for the unloading-reloading curves reported by
Gopalaratnam and Shah [85].

Inner loops

So far, constitutive relations have been given for post-peak cyclic loading with loops that start from and return to the envelope curve with only one reversal in the crack opening direction at the lower stress level σ_L. Obviously, in reality, reversals from an opening crack into a closing crack, or vice versa, may occur at any place in the loading history. Therefore, for the sake of completeness, FE codes also require a description for these so-called "inner" loops.

Figure 6.20 plots two examples of experimentally determined inner loops with a constant value for the lower crack opening. From these and other results, it appears that for unloading starting at a point of a reloading curve, the σ-w relation gradually approaches the preceding unloading curve. Furthermore, the inner loops affect the shape of the reloading curves starting from the same crack opening. However, this effect is not very significant.
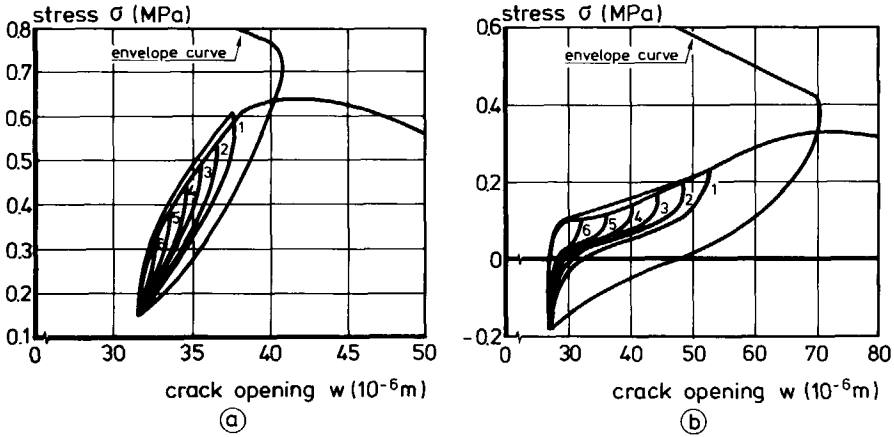
Figure 6.20   Details of an experimentally determined σ-w relation with so-called "inner loops ".

A procedure for the description of inner loops that can be used in FE codes is given in Appendix B.2. In the proposed procedure, there is no damaging effect of reversals within a loop. Although this does not completely agree with reality, it is not very important for the time being. The principle of the procedure is schematically presented in figure 6.21.

A flow chart which can be used for implementation in a FE program is also given Appendix B.2. As an example, a σ-w relation with different cyclic loading regimes, as obtained by the proposed procedure, is given in figure 6.22.

Figure 6.21   Schematic representation of the procedure used for unloading and reloading within a loop.

Figure 6.22   σ-w relation for an arbitrarily chosen loading path as predicted with the continuous-function model.

7 Tensile properties of concrete as influenced by different variables

7.1 Introduction

The tensile behaviour for an ordinary type of concrete ($f_{cc} \approx 50$ MPa) has been extensively discussed in the previous chapter. It should be obvious, however, that the application of fracture mechanics in engineering practice will also require information about the influence of different variables on the tensile properties of concrete. In this respect it should be known, for instance, how the fracture mechanics parameters vary with the material structure, or mix composition. Yet, the influence of mix parameters like water-cement ratio or maximum aggregate size on the fracture energy has not been extensively investigated. The same holds true for a possible relation between compressive strength and fracture energy. Such information can be of help when an analysis has to be performed in case where G_F was not determined experimentally, or for the optimization of a concrete composition when a certain ductility is required.

A complete knowledge of the tensile behaviour also calls for a knowledge of how other variables like environmental conditions and loading conditions influence the material property. One example of the former type of variable is the curing condition of the concrete, while the latter conditions may relate, for instance, to preloaded or biaxially loaded concrete.

In this investigation the influence of a number of variables on the tensile properties of concrete has been investigated. In this chapter the results will be summarized and compared with other results known from the literature. For a similar discussion the reader is referred to Hordijk et al[89b]. Before the results are presented in the separate sections, some attention will first be paid to the determination of the parameters f_t, G_F and E_o in these investigations and how these parameters may be affected. Emphasis will be placed on the method applied in the Stevin Laboratory: the deformation-controlled uniaxial tensile test.

Determination of the tensile strength of concrete
The tensile strength had already been considered to be a material property in the classical strength theory. Therefore, standard test methods have been available for a long time. Of these tests, the uniaxial tensile test and the splitting test (also called the Brazilian splitting test) are still being used, while the knowledge of fracture mechanics has meanwhile shown that the (bending) strength parameter as previously determined in bending tests does not directly represent the tensile strength of the concrete.

For both the uniaxial tensile test and the splitting test, arguments can be given for the correctness of the value of f_t obtained. Worth mentioning in this respect is the fact that the fracture plane is predetermined in a splitting test, while in a uniaxial tensile test on an unnotched specimen, fracture will take place at the weakest cross-section, and the fact that in the splitting test a biaxial tensile-compressive stress-state occurs. Here, the intention is to focus on the tensile strength as determined in a uniaxial tensile test.

In a uniaxial tensile test on an elastic-softening material like concrete, the recorded maximum tensile load divided by the cross-sectional area of the fracture zone will only represent the tensile strength if the deformation distribution and, consequently the stress distribution in the fracture zone are uniform up to the peak load. It may be obvious that in this respect deformation and stress are considered at a macro-level. Therefore, possible causes of non-uniformity, as sketched in figure 7.1, will be referred to as "macro-structural" effects. The effects in figures 7.1a and 7.1c may occur in every uniaxial tensile test, while the one in figure 7.1b refers only to notched or necked tensile specimens. Compared to the situation of uniform deformation distributions up to peak load, the effect of these macro-structural effects on the complete tensile load-deformation relation is (see also Gustafsson [85] and Hordijk[89c]):

— the maximum load will be lowered and the average stress at peak load does not represent the tensile stress properly.
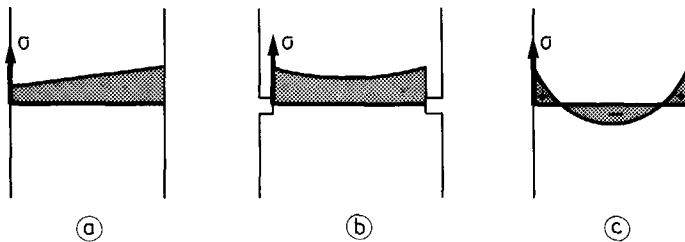— pre-peak nonlinearity will increase.

Figure 7.1   Non-uniform stress distribution in a uniaxial tensile test due to eccentric loading (a), notches (b) or differential shrinkage or temperature (c).

In Section 7.5 more attention will be paid to the phenomenon of initial stresses due to differential shrinkage. Though it was intended to minimize the discussed effects in the various investigations, it is certain that the results presented in the following sections will also have suffered from them to some extent. Nevertheless, since it is believed that the results are a good approximation of the real material property, the tensile strength f_t will be used for the average stress at peak load.

Determination of fracture energy

The fracture energy G_F is the energy required to create one unit area of crack surface. For the determination of G_F, a three-point bending test was recommended by RILEM Committee TC-50 (Hillerborg[85a]). Besides these bending tests, G_F is also determined in other types of test, such as various types of wedge splitting tests (see for instance Brühwiler[90]). These methods, as well as determination of G_F by means of a deformation-controlled uniaxial tensile test, are based on the principle that G_F is determined as the energy supplied to a concrete specimen, divided by the fractured area (mode I fracture). Apart from this, Bazant (see for instance Bazant and Prat[88]) proposed a method for the determination of G_F which is based on the size-effect law (Bazant[84]). For that method the maximum load of at least three, geometrically similar specimens with different dimensions has to be determined.

In various investigations a size dependency for G_F has been observed. Here it is not the intention to discuss the different methods for determination of G_F. Brameshuber[88] discussed several causes for the observed size dependency of G_F. Furthermore, Planas and Elices[89] discussed possible errors in the determination of G_F by means of the three-point bending test. In the author's opinion, there are indeed several phenomena that may affect the determination of G_F and some of these are not yet clearly understood. A number of these effects, most of which work out differently dependent on specimen size, will also come up for discussion later in this chapter. The fact that these phenomena are not yet fully understood is a possible cause of the observed differences in G_F values obtained in different types of test. For this reason, when relations between G_F and a certain parameter are being compared with results from the literature, only tendencies will be compared.

In the investigations that will be discussed, fracture energy is determined by means of deformation-controlled uniaxial tensile tests. Even though this type of test is the most direct way of determining G_F, it proved difficult to give an exact value for G_F. This is due to the fact that the descending branch approaches the horizontal axis (stress is zero) very gradually (see figure7.2a). In most of the experiments the test was stopped at a deformation of about 100 to 140 µm. For the normal type of concrete, the stress that could still be transferred at these deformations was about 0.2 to 0.3 MPa ($\approx 0.1f_t$). This means that to determine a value for G_F, an assumption had to be made for the energy that can be consumed at larger deformations. In the test series, it was intended to compare values for G_F obtained with different values for the investigated variable. For that reason and due to the fact that experiments were not always stopped at the same deformation, an arbitrary value for δ_o was chosen, while a linear relation was assumed for the relation between the last data point (or a point at a chosen maximum deformation) and δ_o (see
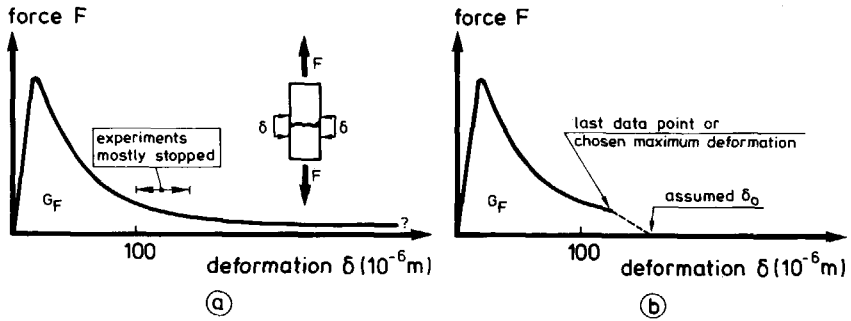
Figure 7.2   Experimental σ-δ relation gradually approaching zero load (a) and procedure applied for the determination of G_F.

figure 7.2b). Unfortunately, δ_o was not equal in the various test series (140 μm for LC; 160 or 200 μm for NC). The procedure chosen for extrapolation of the σ-δ relation obviously affects the absolute value of G_F. To illustrate this, figure 7.3 shows the result of an experiment which was not stopped before a deformation of about 600 μm. Figure 7.3b shows the energy represented by the area under the σ-δ curve up to a certain deformation (denoted as W) as a function of this deformation. It appears that for $\delta = 600$ μm the energy had still not reached its maximum, G_F. Or, δ_o had still not been reached. Since a horizontal σ-δ line not equal to σ=0, indicating that δ_o has been passed and due to an incorrect force measurement, also causes an increasing energy with increasing deformation, it should be checked whether the transferable stress still decreased at these large deformations. In the inset of figure 7.3a, it can be seen that this is indeed true for deformations of between 400 μm and 600 μm. In addition, due to the large values of δ, the value of G_F is very sensitive to an incorrect load measurement. For an error in zero load equal to a stress of 0.03 MPa ($\approx 1\%$ of f_t), the error in G_F (for $0 < \delta < 600$ μm) is 18 J/m^2 ($\approx 10\%$). Figure 7.3b shows that the consumed energy W up to $\delta=600$ μm may be about 40% more than the energy consumed up to $\delta = 150$ μm. In the case of a latter δ value of 100 μm, the difference may be as much as 63%. This means that the energy in the tail of the σ-δ relation and any assumption made for this part of the curve may strongly affect the absolute value of G_F.

Furthermore the following remarks can be made as regards the determination of δ_o in relation to G_F:

– In the literature, values for δ of about 400 μm have been reported by Wecharatana[86] and Guo and Zhang[87].
– From a physical point of view, the fact that small frictional forces are active up to deformations of about 0.5 mm (several times smaller than d_{max}) is not remarkable.

– It can be surmised that the energy in the tail of the descending branch, and the extrapolation that has to be made (see also Brameshuber[88]), is also a parameter which influences the determination of G_F in other types of test.
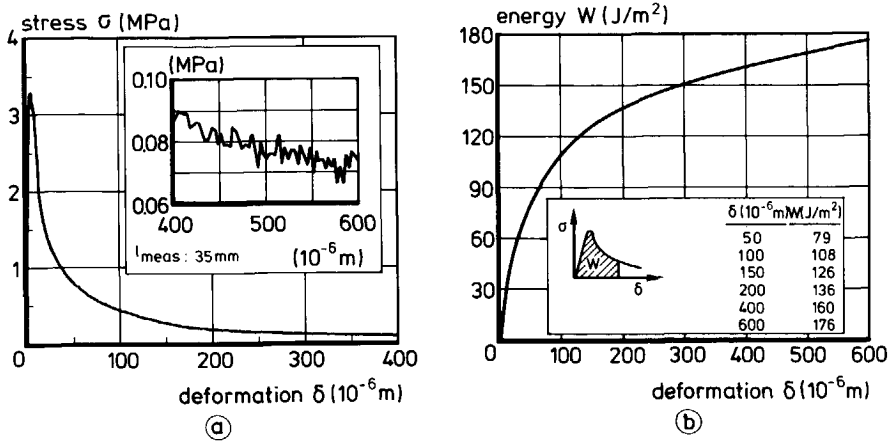

Figure 7.3   Stress-deformation relation (a) and the corresponding energy-deformation relation (b).

Finally it must be realized that, to determine the work W supplied by the external load F (W = $\int F d\delta$), δ should correspond to the point of load application. In the deformation-controlled uniaxial tensile tests, the average deformation over a certain measuring length (35 mm in this report) is mostly used for δ. When the imaginary planes in the specimen at a distance of the measuring length remain plane, then the work is still correctly measured. In all other cases, for instance as a result of important stress concentrations in combination with a very short measuring length or initial shrinkage stresses, an error in the experimentally determined value of G_F may obviously also occur due to this incorrect δ measurement.

Determination of Young's modulus
The tensile experiments with the applied specimen dimensions and notches are not very suitable for the determination of Young's modulus. Nevertheless, values for E_0 have been determined. First of all they are an indication of the real E_0 value and, secondly, they can be used for comparison between the different concretes within a test series. Comparison between the separate test series is not possible. The reason for this is that over the years the testing rig, specimen size and arrangement of the measuring devices have been modified (see also Appendix A).

Characteristic length

For characterizing the material by means of a single parameter, the characteristic length l_{ch} ($l_{ch} = E_o G_F/f_t^2$) is used (see Petersson[81]). The value is smaller for more "brittle" materials. It should be obvious that possible influences on the determination of the separate values of f_t, G_F and E_o will also affect the value for l_{ch}.

Scatter in results

As usually observed in tensile experiments, the test results display a fairly significant scatter. Nevertheless, if the results within a test series are compared, a number of tendencies can easily be deduced. However, if the results are compared for the same standard mix (NC) with $d_{max} = 8$ mm determined in separate test series, then rather substantial differences can be observed in the average values for some material parameters. These differences can be explained partly by changes in test performance (specimen length) or curing condition (age; drying time). In some cases, however, no clear explanation could be found.

7.2 Type of concrete

Besides the normal type of concrete (NC) with river gravel aggregates, a lightweight concrete (LC) was investigated. For this concrete, which can be characterized as being a structural lightweight concrete, a sintered clay was used for the bigger aggregates (4-8 mm). This concrete was also used to study the phenomenon of non-uniform crack opening (Section 5.3) and the influence of curing conditions (Section 7.5). Furthermore, the tensile properties of a very lightweight concrete (foamed concrete) were determined.

Structural lightweight concrete

Experimental details for the different investigations can be found in Appendix A (see also Cornelissen et al.[86a,86b], Hordijk et al.[87,90]). Comparison of the values obtained for f_t and G_F shows a significant scatter which can be explained by differences in drying time in the laboratory before testing (see also Section 7.5). Nevertheless, on average, the fracture energy G_F was lower (approximately 30 to 40%) for LC than for NC. For the procedure applied to determine G_F (see Section 7.1), a realistic value for the fracture energy of NC is 100 to 110 J/m^2. The difference in G_F is mainly caused by the fact that the transferable stresses at larger crack openings in the descending branch are significantly smaller for LC, which supports the theory about crack path tortuosity described in Section 6.1 (smooth crack path for LC due to cracks running through the aggregates). To illustrate this, average curves as obtained in the preliminary investigations (see Appendix A) are given in figure 7.4. For the sake of clarity, the first part of the curve for LC does not accurately represent the material behaviour. In fact, it is meanwhile known

100

that in these tests non-uniform crack opening and initial stresses must have played an important role, resulting in a less sharp peak (an apparently more ductile behaviour just beyond peak load) for LC than for NC. Results of tests in which these effects were minimized show a higher peak and a steeper stress drop beyond this peak. The characteristic length clearly shows that LC is more brittle than NC. The tensile strength is in fact approximately the same ($\approx$ 3 MPa), while Young's modulus and fracture energy are smaller for LC than for NC. In Table 7.1 values for l_{ch} are given for representative values of f_t, E_0 and G_F of the types of concrete investigated. Lower G_F values for LC than for NC have also been reported by Petersson[81] and Wu and Zhang[89].
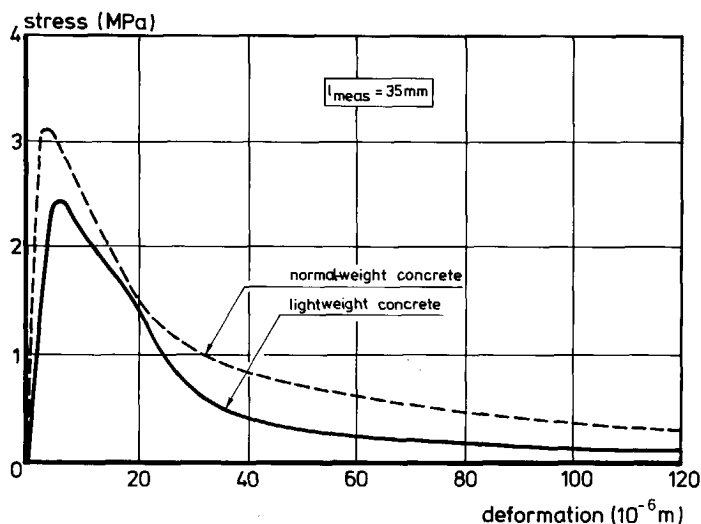

Figure 7.4   Average σ-δ relations for NC and LC (Cornelissen et al. [86b]).

Results for the post-peak cyclic behaviour presented in the same way as in figure 6.10 can be found in Cornelissen et al.[86a]. Similar trends as found for NC were observed. Some small differences, like higher values for the residual crack opening at a stress level equal to -f_t, were explained by the smoothness of the crack surfaces. In the case of NC the crack surfaces may fit rather well during unloading, whereas in the case of LC the smooth crack surface may result in small transverse displacements which prevent crack closure on unloading and consequently give rise to extra damage.

Foamed concrete
Foamed concrete is a very lightweight concrete (Actually it is no real concrete as the maximum aggregate size is 0.5 mm). It consists of a great many pores which are introduced

into the concrete by adding a foaming agent to the fresh mix. Salet[90] investigated the application of an isulation material (foamed concrete) in multi-layered structures. As part of that study, the tensile properties have been determined in the Stevin Laboratory (Hordijk and Salet[89e]). In general, the density of a foamed concrete may vary between 400 and 1200 kg/m^3. The type that was investigated had a theoretical density of 615 kg/m^3. It had a cube compressive strength of 2.9 MPa.

Table 7.1   Values for the characteristic length l_{ch} of the types of concrete investigated and representative values of f_t, E_o and G_F.

type of concrete investigated	f_{cc} (MPa)	f_t (MPa)	E_o (MPa)	G_F (J/m^2)	l_{ch} (mm)
normal-weight concrete	50	3.0	30000	105	350
lightweight concrete	50	3.0	18000	70	140
foamed concrete	2.9[1]	0.28	1500	25	478

[1] obtained on 100*100*500 mm^3 prisms

An average stress-deformation curve for a measuring length of 35 mm, obtained on specimens with a length of 100 mm and a critical cross-sectional area of 50*50 mm^2, is plotted in figure 7.5. For the tensile strength, Young's modulus and the fracture energy values of 0.28 MPa, 1500 MPa and 25 J/m^2 respectively were found. Close inspection of the specimens, however, showed that before testing, small cracks occurred at the tip of the saw cuts, which must have decreased the value of f_t and G_F. Therefore, the measured behaviour is no more than an approximation of the real material property. Nevertheless, for the determined parameters, a characteristic length l_{ch} of 478 mm (Table 7.1) can be calculated, which means that the foamed concrete behaves in a more ductile manner than the types of NC and LC investigated.

7.3 Maximum aggregate size

The crack path can be expected to become more tortuous with an increasing maximum aggregate size d_{max}, resulting in an increasing fracture energy. However, the influence of this variable on f_t and on l_{ch} is not quite clear. Based on the results obtained from about 700 beam tests, Hillerborg[85b] concluded that there is a tendency for G_F to increase with d_{max} increasing from 8 to 20 mm. However, this tendency was uncertain because of the large scatter in the results. In the Stevin Laboratory, five medium strength concretes with a constant water-cement ratio, workability, type of cement and type of aggregate were investigated (see Wolinski[86] and Wolinski et al.[87]). The main results will be summarized

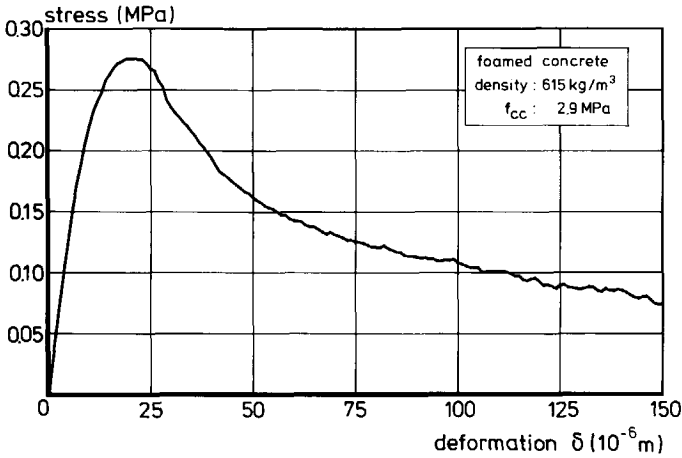here, while information about the applied mix compositions can be found in Appendix A.

Figure 7.5   Tensile stress-deformation relation for the foamed concrete investigated (Hordijk and Salet [89e]).

Starting point for mix design and applied specimen dimensions
The main factor that varied between the different concretes was the maximum aggregate size of the particles, d_{max} being 2, 4, 8, 16 and 32 mm. The water-cement ratio was kept constant at 0.5 in order to attain the same concrete strength. To obtain approximately similar workability, the cement content was varied. In consequence, the total mass of aggregate increased with increasing d_{max}. Mix compositions, properties of the fresh concrete and 28-day mechanical properties can be found in Appendix A. (Tables A.1 and A.3).

Initially, it was intended to use specimens $60*50*150$ mm^3 with a critical cross-sectional area of $50*50$ mm^2 for d_{max} is 2, 4, 8 and 16 mm and specimens $120*100*250$ mm^3 with a critical cross-sectional area of $100*100$ mm^2 for d_{max} is 16 and 32 mm. The aim was that the concrete with $d_{max} = 16$ mm which was to be tested for both specimen types should show how the results depend on the applied specimen dimensions. It appeared, however, that there was a significant difference in σ-δ curves obtained with the two specimen types (see figure 7.6). It is meanwhile known that the observed differences are probably mainly due to initial stresses caused by differential shrinkage (see Sections 7.1 and 7.5). Besides, for a larger critical cross-sectional area it is generally more difficult to see that each area of this cross-section reaches its the maximum tensile force at the same

103

instant. Nevertheless, based on the results as shown in figure 7.6, it was decided not to use the larger specimen type. Though it was realized that the cross-sectional area of the small specimen (50*50 mm^2) was too small for the mix with d$_{max}$=32 mm, all experiments were nevertheless performed on this specimen type. The effect of this on the results, especially for the mixes with larger aggregates, will be discussed later in this section.
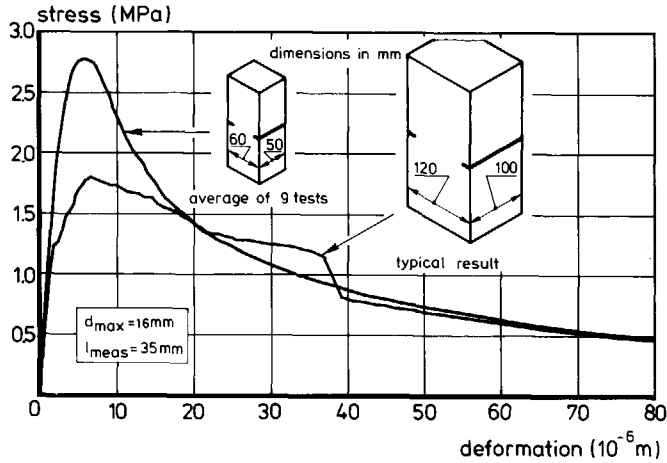

Figure 7.6   σ-δ relations for d$_{max}$= 16 mm obtained on a large and a small specimen.

Experimental results
Static (continuously increasing deformation) as well as post-peak cyclic experiments were performed. All types of test were included in the analysis of σ-δ relations. Average stress-deformation relations are plotted in figure 7.7. It can be seen that for the larger aggregates (d$_{max}$= 8, 16 and 32 mm) the curve is positioned well above that for the smaller aggregates (d$_{max}$= 2 and 4 mm). This outcome was also expected on the basis of crack path tortuosity. Differences between d$_{max}$= 2 and 4 mm on one hand and d$_{max}$= 8, 16 and 32 mm on the other appeared to be less significant. The same tendency can, of course, be seen when the fracture mechanics parameters are considered separately (Table 7.2 and figure 7.8). For the determination of G$_F$, an assumed δ$_0$ equal to 200 μm(!) was applied. As can be seen, the average values for E$_0$ and l$_{ch}$ did not differ significantly between the five mixes.

Comparison with results known from the literature
As far as the influence of mix parameters like d$_{max}$ is concerned, one should bear in mind that it is not possible to vary one parameter without changing the other mix parameters.
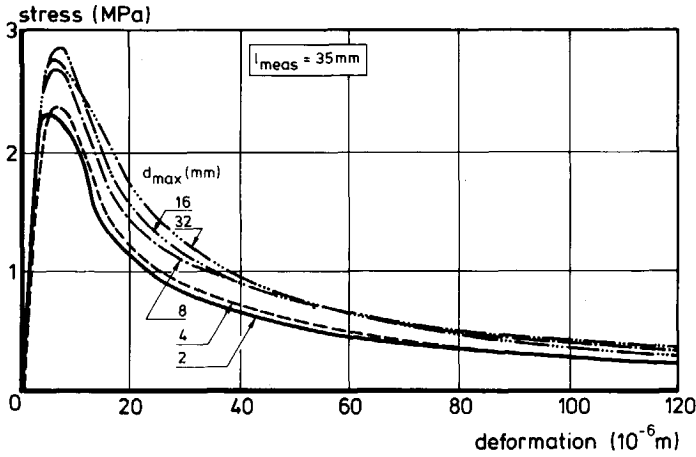
Figure 7.7   Average stress-deformation relations for the concrete mixes with different maximum aggregate size.

Furthermore, it is probably not only the maximum aggregate size but, even more so, the concentration of the coarse aggregates which influences the fracture behaviour. These factors mean that a simple comparison of experimental results by different investigators may lead to divergent results. Nevertheless, a comparison is given in figure 7.9 for the fracture energy. As can be seen, there is a general tendency for G_F to increase with d_{max}. An explanation for the deviating results of the experiments in the Stevin Laboratory, as far as the more or less constant value between $d_{max}= 8$ mm and $d_{max}= 32$ mm is concerned, will be given later.
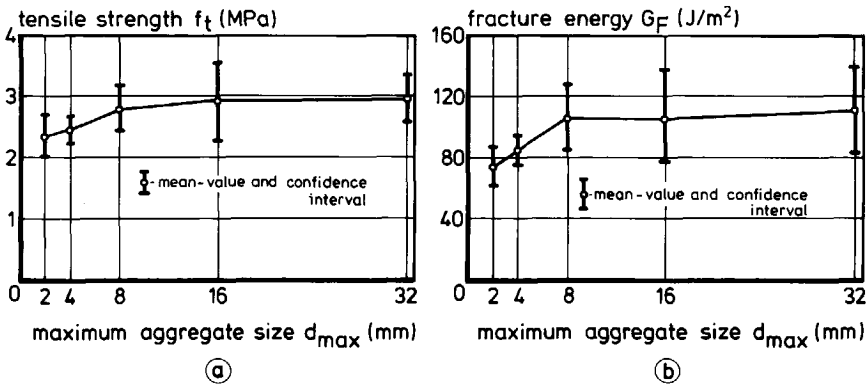

Figure 7.8   Variation of direct tensile strength (a) and fracture energy (b) with maximum aggregate size (Wolinski et al. [87])

105

Table 7.2   Fracture mechanics parameters; coefficient of variation in brackets (%) (Wolinski et al.[87]).

d_{max} (mm)	f_t (MPa)	G_F (J/m^2)	E_o (MPa)	l_{ch} (mm)
2	2.31 (8.9)	75.9 (11.2)	32670 (7.3)	465
4	2.39 (4.9)	84.9 (5.4)	33190 (12.6)	493
8	2.78 (8.8)	108.4 (12.2)	31560 (11.1)	443
16	2.89 (13.4)	108.6 (18.6)	33690 (13.3)	438
32	2.90 (8.2)	112.3 (16.7)	32660 (14.1)	436

In the first preliminary draft of the CEB-FIP Model Code 1990[88], a relation between compressive strength and fracture energy is given which contains a coefficient that depends on the maximum aggregate size. There it is proposed that, "in the absence of experimental data" G_F in (J/m^2) should be estimated by

$$G_F = \alpha\, f_{ck}^{0.7} \qquad (7.1)$$

in which f_{ck} (MPa) is the characteristic strength. For some comparisons with experimental data in this chapter, f_{ck} will arbitrarily be taken as equal to the cube compressive strength, f_{cc} in (MPa). The coefficient α is equal to 4, 6 and 12* for d_{max} values of 8, 16 and 32 mm respectively. In figure 7.9, G_F values calculated with eq. 7.1 for an assumed f_{cc} of 50 MPa are connected by the dashed lines. The tendency of G_F to increase with increasing d_{max} coincides well with experimental results.

Discussion
Based on the results as presented in figures 7.7 and 7.8 it had previously been concluded that the mixes investigated could be subdivided into a 'mortar' material comprising d_{max}= 2 and 4 mm and a 'concrete' material with d_{max}= 8, 16 and 32 mm (Wolinski et al.[87]). However, it is more likely that the fact that there were minor differences between the mixes with d_{max}= 8, 16 and 32 mm was caused by too small a cross-sectional area. The chance of a large aggregate being positioned between the saw cuts and thus affecting the fracture zone is rather small. For d_{max}= 16 mm, the aggregates with d_{max}> 8 mm occupy about 17% of the total volume, while it is 27% for d_{max}= 32 mm. So, firstly the

---

*   In the recently released first draft version of the CEB-FIP Model Code 1990[90], the coefficient α for d_{max}= 32 mm was changed from 12 to 10. The curves in figures 7.9 and 7.11 are based on the relation given in the first prelimanary draft version.

106

fracture behaviour between the saw cuts for the mixes with larger aggregates will probably not differ much from the mix with d_{max} is 8 mm. Secondly, since it can be assumed that in a number of specimens larger aggregates will still have affected this fracture behaviour, a larger scatter can be expected for the mixes with larger aggregates, which indeed corresponds with the test results (see figure 7.8).
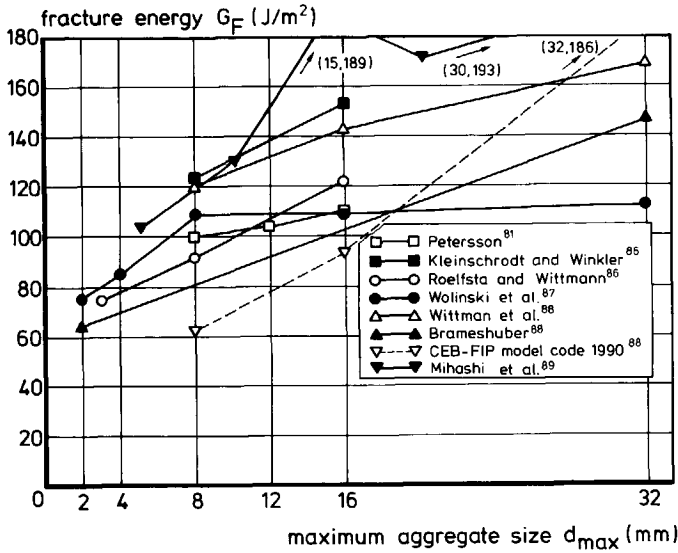

Figure 7.9   Fracture energy as a function of d_{max} for a number of investigations.

7.4 Concrete quality; water-cement ratio

So far, the types of normal-weight concrete and structural lightweight concrete investigated all had a medium compressive strength in the range from 40 to 50 MPa. In order to investigate a possible relation between the concrete quality, as represented by the cube compressive strength, and the fracture energy, two mixes (d_{max}= 8 mm) with a deviating concrete quality were also investigated. The average cube compressive strength of the concretes was 36 and 77 MPa respectively, while for the latter type of concrete, silica fume was added to the mix. In the analysis of the test results, the tests for the mix with d_{max}= 8 mm ($f_{cc} \approx$ 47 MPa) which were part of the test series concerning d_{max} will also be taken into account.

Test results

Details about mix composition and 28-day mechanical properties can be found in Appendix A. For the sake of clarity, only the three static tests are taken into account for the medium strength concrete, while furthermore the analysis of the results deviates slightly (for instance as regards the δ_0 value) from the procedure applied in the previous section, which yields some slightly different results. Average stress-deformation curves are plotted in figure 7.10 and mean values for the fracture mechanics parameters can be found in Table 7.3.
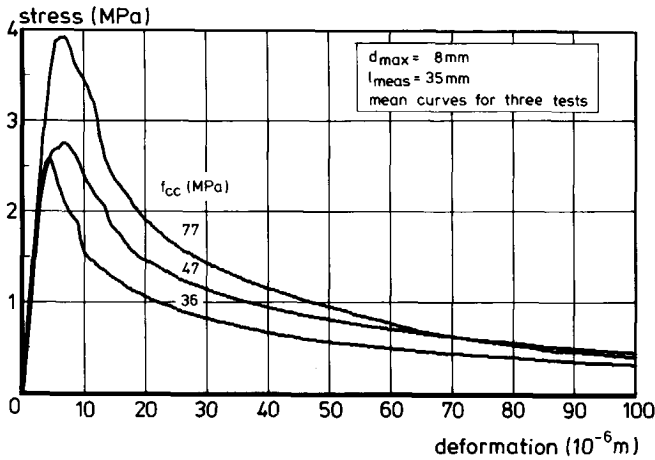

Figure 7.10   Average σ-δ relations for three different concrete qualities.

Comparison with results known from the literature

Again, the results will be compared with a number of results known from the literature (see figure 7.11). For the sake of clarity, G_F has been measured and evaluated in different ways by different researchers, which explains some of the differences. As can be seen, all

Table 7.3   Fracture mechanics parameters

strength	f_{cc} (MPa)	f_t (MPa)	G_F (J/m^2)	E_0 (MPa)	l_{ch} (mm)
low	36	2.60 (6.4)[1]	86.3 (9.9)	32670 (4.7)	465
medium	47	2.80 (6.0)	118.7 (8.2)	33190 (11.1)	493
high	77	4.05 (2.3)	138.3 (20.7)	31560[2] (0.4)	443

1) coefficient of variation in brackets

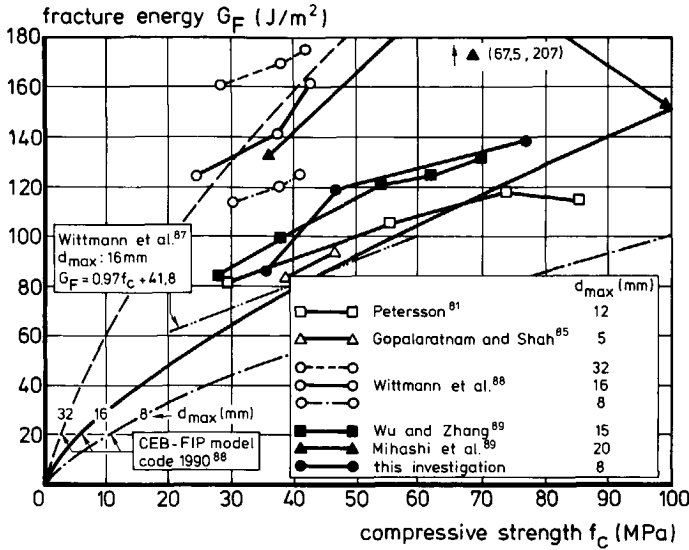2) for only two tests; all other values are the average of three tests

Figure 7.11   Fracture energy as a function of compressive strength for a number of investigations.

presented investigations, including the relation presented in the preliminary draft of the CEB-FIP Model-Code 1990[88] (eq. 7.1), show more or less the same tendency for G_F; increasing with compressive strength f_c. If it is realized that the difference in strength is mainly caused by a difference in water-cement ratio, then the results of figure 7.11 can also show a relation between G_F and water-cement ratio (see figure 7.12). As can be seen, the decrease in G_F with increasing water-cement ratio shows good resemblance between the different investigations.

7.5 Curing conditions; water content

Based on the results of preceding test series in which there were considerable differences in age at testing and consequently a difference in drying time of the specimens in the laboratory, it was surmised that the curing condition has a significant influence the results obtained. In order to assess this for both types of concrete (normal-weight concrete and lightweight concrete) a new test series was performed (Hordijk and Reinhardt[90]). Besides the procedure previously applied, two extreme conditions were applied with respect to moisture content (wet and oven-dry). Furthermore, in an additional test series, the influence of drying time (under laboratory conditions) was investigated for NC.
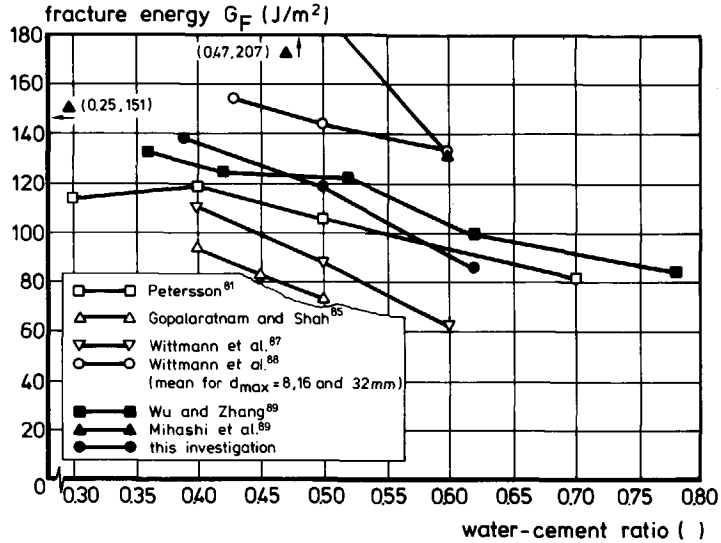
Figure 7.12   Fracture energy as a function of water-cement ratio for the results
of figure 7.11.

Effects of curing condition

The water content of concrete may vary due to the curing condition of the specimens. Generally, the strength of concrete is lower for wet (saturated) concrete than for dry concrete. Mills[60] suggested that this strength reduction is due to dilation of the cement gel by absorbed water, causing a reduction in the cohesion forces of the solid particles.

Besides the action of water as discussed above, which can be regarded as a material property, curing conditions can also influence test results in a way that can be regarded as a form of macro-structural behaviour (see Section 7.1). If specimens are allowed to dry for some time before testing, a strong reduction in strength can be observed (Johnston and Sidwell[69], Bonzel[70], Fouré[85]). For longer drying periods, this strength reduction vanishes and may change into a strength increase. Figure 7.13 gives an example of the tensile strength of concrete with a compressive strength of 52.3 MPa (Bonzel[70]). This strength reduction can be explained by differential shrinkage in the drying specimens, causing eigenstresses. It may be expected that this phenomenon depends on specimen dimensions. Contrary to uniaxial tensile and flexural strength, the splitting strength appears to be less affected by drying (Bonzel[70], Raphael[84]) due to the biaxial compressive region under load application, which coincides with the region of tensile eigenstresses.
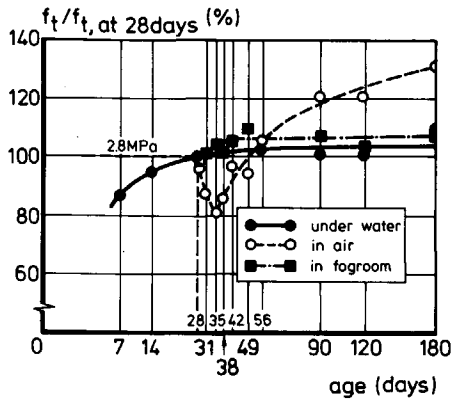
110

Figure 7.13   Relative uniaxial tensile strength for different curing conditions (Bonzel [70]).

Applied methods of curing

According to the procedure normally applied, specimens were sawn out of slabs (300*300*50 mm³) which were demoulded two days after casting and subsequently cured under water for two weeks. Then all specimens were sawn. After that, those to be tested under wet conditions were stored under water for another two to three weeks. The rest were stored in the laboratory (20°C, 60% relative humidity). After one week in the laboratory, those to be tested under fully dried conditions were placed in an oven at 110°C. On average, tests were performed at an age of 35 days. Below, specimens cured according to the three different methods will be denoted by WET, LAB and OVEN-DRY respectively. In the additional test series (denoted as DRYING TIME), the specimens were cured according to those for the LAB specimens, while the drying time in the laboratory was varied, resulting in an age at testing of 16, 17, 18, 21, 25, 28 and 56 days respectively.

Since it was not possible to glue a specimen with wet end-faces in the testing machine, the WET specimens were taken out of the water one day before testing and were wrapped in foil except for the end-faces. Then the end-faces were blow-dried and coated. To attach the steel supports of the measuring devices, small openings were made in the foil, so that the foil could be kept in place during testing.

The specimens were weighed at three different points in time, in order to determine the water loss during drying. Results are presented in figure 7.14. 28-day mechanical properties can be found in Appendix A.

Fracture mechanics parameters

For each variable, three experiments were performed. Mean values for the stress at peak load (f_t), the fracture energy (G_F), the initial Young's modulus (E_o) and the characteristic length (l_{ch}) are listed in Table 7.4.
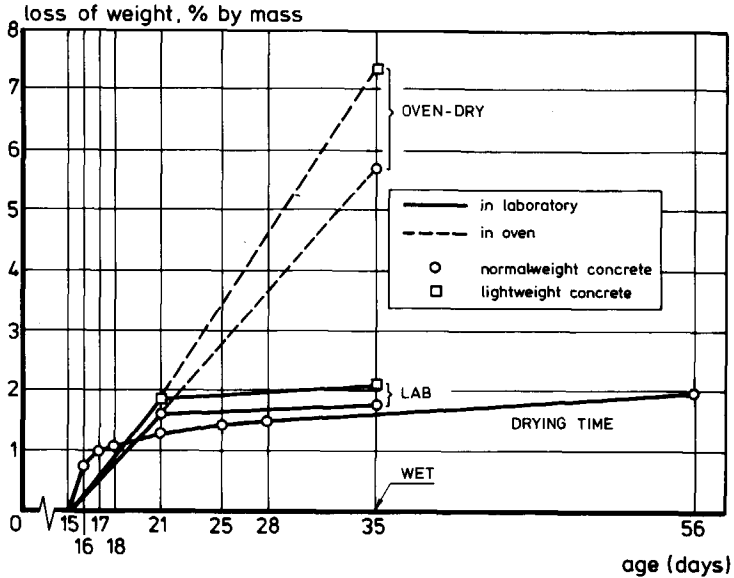

Figure 7.14   Loss of weight for the specimens cured under different conditions.

Lightweight concrete

Averaged stress-deformation curves for the lightweight concrete are presented in figure 7.15 and the enlarged pre-peak curves are plotted in the inset. It appears that Young's modulus (see Table 7.4) for OVEN-DRY is much lower than for LAB and WET, which are both in the same order of magnitude. A possible explanation is that drying in the oven has caused small cracks in the hardened cement paste (HCP) and at the interface of grains (α_T is smaller for lightweight grains). It can be expected that these cracks have also reduced the strength of the concrete to a value which happens to be equal to that for WET specimens. This means that the strength of dry LC would probably be higher than of wet LC if the specimens had been dried very carefully, thus causing fewer or no cracks. The considerably lower peak value for LAB can be explained by eigenstresses due to differential shrinkage. The initial eigenstresses not only lower the peak value but also cause a more pronounced pre-peak nonlinearity. Obviously, the peak value in this case no longer represents the actual material property "tensile strength". Nevertheless, as already stated before, the tensile strength f_t will be used for the peak value in this chapter, even though it is influenced by structural effects.

As far as fracture energy is concerned, the expectation is that initial stresses will also lower this value. This may be obvious for the case in which the tensile eigenstresses have already reached the tensile strength. But even for lower tensile eigenstresses a reduction in G_F can be expected. The eigenstresses are in fact accompanied by energy which is stored in the specimen and which is partly released after fracturing of the specimen. This amount of energy, which is as yet unknown, should in fact be added to the externally supplied energy in order to obtain a proper value for G_F. A problem in studying this phenomenon experimentally is that the creation of eigenstresses due to drying is always accompanied by a loss of water, which leads to material changes. Simulation by means of numerical models circumvents this problem and therefore provides a good support for experimental investigations.
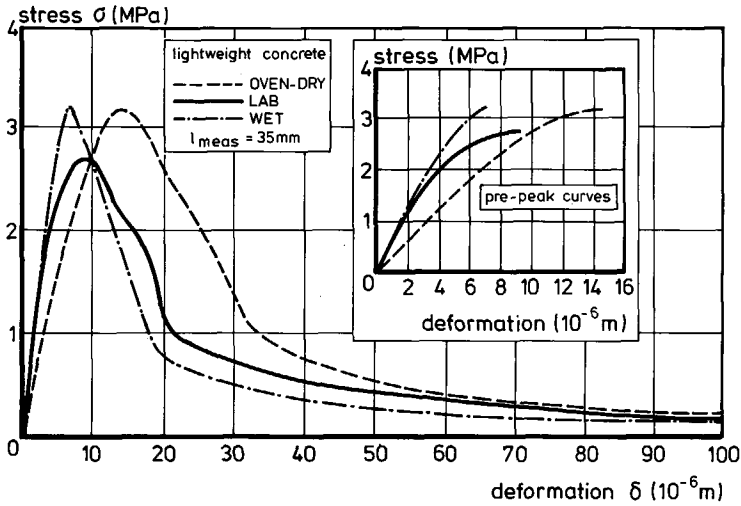

Figure 7.15   Average stress-deformation curves for the lightweight concrete investigated.

Apart from the effects discussed above, it can be seen that G_F increases with drying. A water loss of 5% by mass (from LAB to OVEN-DRY) causes an increase of G_F by 23.5 J/m^2, from WET to LAB (about 2% by mass) causes a G_F gain of about 15 J/m^2. As this relates to a physical explanation for higher G_F values for drier concrete, it may be assumed that the action of water has a similar influence on G_F as it has on f_t. Furthermore, for larger crack openings, the water will reduce sliding friction, which reduces G_F as well. More attention will be paid to this phenomenon in the discussion on NC .

Table 7.4   Fracture mechanics parameters.

	f_t (MPa)		G_F (J/m²)		E_o[1] (MPa)		l_{ch} (mm)
LC OVEN-DRY	3.20	(6.7)[2]	100.6	(11.7)	9970	(7.9)	98
LAB	2.75	(6.1)	77.1	(13.4)	18660	(2.9)	190
WET	3.21	(4.1)	62.3	(5.1)	20270	(11.4)	123
NC OVEN-DRY	2.60	(6.6)	96.5	(17.8)	17220	(9.8)	246
LAB	2.97	(10.8)	110.9	(19.7)	28810	(13.7)	362
WET	2.04	(7.7)	66.0	(14.6)	29170	(18.1)	463
NC DRYING-TIME							
16 days	2.47	(7.6)	74.5	(15.0)	26240	(24.4)	320
17 days	2.35	(1.1)	85.4	(4.8)	23280	(19.1)	360
18 days	2.47	(4.6)	89.8	(8.3)	25740	(12.0)	379
21 days	2.68	(6.8)	111.0[3]	(2.5)	24950	(20.7)	386
25 days	2.75	(12.1)	92.4	(12.0)	21510	(29.4)	263
28 days	2.96	(9.1)	92.5[3]	(2.6)	23340 [3]	(28.5)	246
56 days	3.52	(11.8)	95.6[3]	(1.6)	26150	(20.9)	202

1) measuring length is 110 mm

2) coefficient of variation

3) result of 2 tests only

With respect to l_{ch} it can be stated that the effect of cracks on E_o and of eigenstresses on f_t and G_F is combined in its influence on this parameter.

Normal-weight concrete

Averaged stress-deformation curves for the normal-weight concrete are presented in figure 7.16 with the enlarged pre-peak curves plotted in the inset. As for LC, the small value of E_o for OVEN-DRY (see Table 7.4) can be explained by the existence of small cracks due to the forced method of drying. These cracks are probably also the reason for the strength reduction, as compared with LAB specimens. The linear ascending branch for LAB, almost up to the peak load, indicates that eigenstresses were not dominantly present in these tests. This means that the differential drying process for NC is spread over a shorter period than for LC, which is confirmed by the literature (Bonzel[70], Fouré[85]). The water absorbed in the lightweight aggregates, acting as a buffer, may be held responsible for this fact. The low tensile strength for WET may be partly explained by the dilation of the hydrated cement paste. Splitting tests on cubes tested shortly after removal from water curing displayed a higher tensile strength (this will be shown in

114

figure 7.17), which makes it doubtful whether this is the only reason for the low f_t value. Possibly, the procedure of wrapping the specimens in foil was not sufficient to prevent the NC specimens from drying out, resulting in eigenstresses. This explanation is supported by the pre-peak nonlinearity for WET (see inset of figure 7.16).
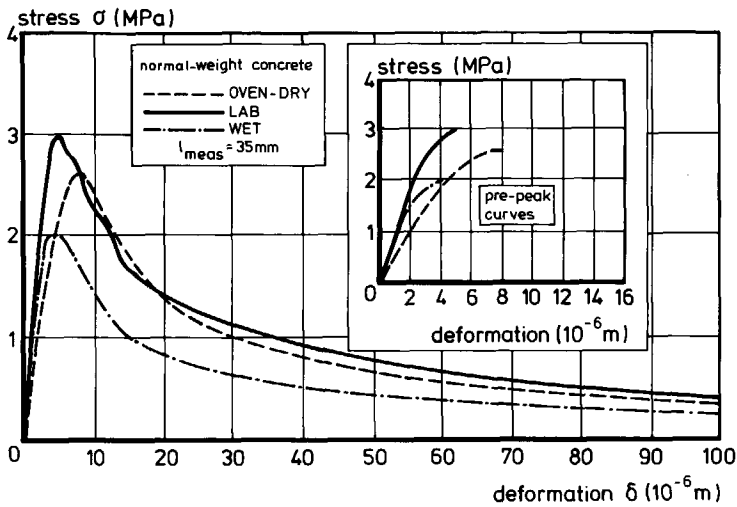

Figure 7.16   Average stress-deformation curves for the normal-weight concrete investigated.

As for LC, the fracture energy has the lowest value in the case of curing under water. One reason for this is the dilation of HCP, which is analogous to the influence of water on f_t. For larger deformations (crack openings), however, another phenomenon may be responsible for a lower G_F value. For these crack openings, the main contribution to the stress-transferring capacity is expected to be the interlocking effect, due to the tortuosity of the crack path (see also Section 6.1). The sliding friction can be expected to be lower in the case where water is available between the two crack surfaces. Furthermore, shrinkage of the cement paste may embed the aggregates more strongly in the matrix, resulting in higher sliding friction for dry specimens. Indeed, figures 7.16 and 7.17 show the descending branch to be the lowest for WET specimens. The fact that the crack path passes through the aggregates in the case of LC and around the aggregates in the case of NC (more tortuous crack path for NC) implies that this phenomenon is more important for NC.

The fracture energy for OVEN-DRY is lower than for LAB, which seems to contradict a possible relation between water content (loss of weight) and G_F. It should be noted, however, that the G_F values for NC are accompanied by high values for the coefficient

of variation. Furthermore, the damaging effect due to oven drying may reduce G_F as well. As far l_{ch} is concerned, it can be calculated that l_{ch} changes with moisture content. Obviously, the concrete becomes more brittle with lower moisture content.

Drying time for normal-weight concrete

As regards the results for DRYING TIME, it should be noted that high values of the coefficient of variation were obtained for some parameters (Table 7.4). Nevertheless, attempts will be made to derive some tendencies from these results. Figure 7.17 shows the relation between f_t, G_F and l_{ch} and the age (drying time). The results for E_o and δ_{peak} have not been plotted because of the large coefficient of variation.

As figure 7.17a shows, the lowest peak value (f_t) for the applied type of specimen is obtained two days after taking the specimens out of the water. Apparently, G_F increases with drying (figure 7.17b). This is in agreement with the observation for oven-dry specimens. The 21-day value is considerably higher and does not fit in this line. The characteristic length (figure 7.17c) first shows an increase, which is due to the lower f_t value for these ages (structural effect). Subsequently this value decreases with increasing age and decreasing moisture content (material property). This is in agreement with the results for NC, as presented above.

Discussion

To the author's knowledge, deformation-controlled uniaxial tensile tests for different curing conditions (water content) have only been performed by Guo and Zhang[87]. However, the influence on the complete σ-δ diagram was not reported and as far as f_t, δ_{peak} and E are concerned, no clear tendencies can be obtained from the reported results. Brameshuber [88], investigated the influence of drying time and curing condition on the fracture energy by means of three-point bending tests. Besides water curing, specimens were also wrapped in foil. Specimens were tested at an age of about 28 days. In addition to the reference specimens which were not allowed to dry, a drying time of 6, 24 and 72 hours was adopted. Results are presented in figure 7.18. The fact that G_F increases after 24 and 72 hours drying, as compared with no drying, corresponds with the results presented in this section, although the increase as reported by Brameshuber[88] is much stronger. The decrease in G_F after only 6 hours drying time may be explained by the fact that in this case the decrease due to the release of energy (eigenstresses) is stronger than the increase due to drying.

The results presented in this section clearly show that the curing condition, including the drying time of the specimens, and hence the moisture content of the concrete, has a significant influence on the fracture mechanics parameters. This influence obviously
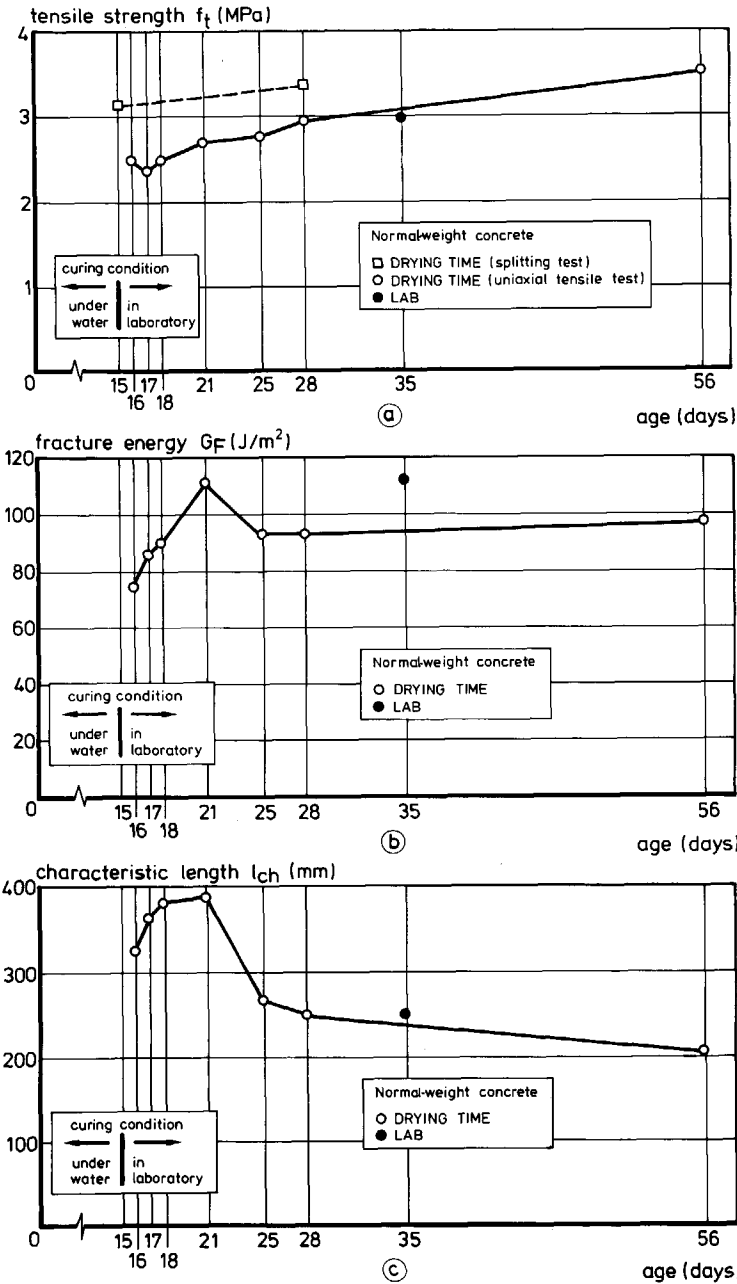
116

Figure 7.17 f_t, G_F and l_{ch} as a function of drying time in the laboratory.
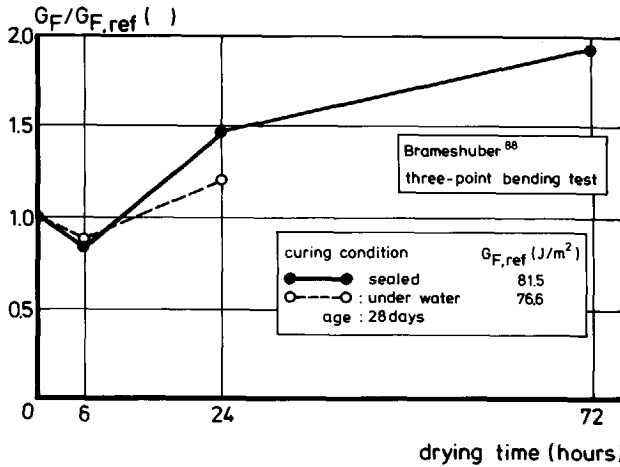
Figure 7.18 G_F as influenced by drying time (Brameshuber [88]).

cannot be neglected when comparing fracture mechanics parameters, and especially when comparing G_F obtained on different specimen types and sizes. Finally, the author believes that the typical shape of the crack front (see figure 7.19) as reported for precracked notched three-point bending beams (Bascoul et al.[89], Swartz and Refai[89]) may also be due to differential drying of the specimens.
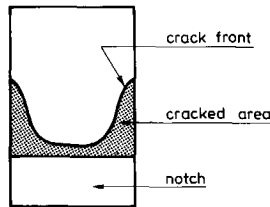

Figure 7.19   Typical shape of the crack front as found in bending tests (Bascoul et al. [89] and Swartz and Refai [89]).

7.6 Compressive preloading

As a rule, material properties are determined on "virgin" specimens. In reality, however, concrete structures are subjected to different types of loading over a long period of time. Especially during the building stage, the type of loading may differ strongly from that

118

during the service life. Consequently, the influence of the loading history should be taken into account in the calculations.

In Section 2.3 the influence of a compressive cyclic preloading on the compressive strength of concrete was discussed. A small increase in strength after cyclic preloading was reported in the literature. As far as the tensile properties of concrete are concerned, most information about the effects of preloading as yet only concerns the influence on Young's modulus and on tensile strength. To the author's knowledge, post-peak behaviour in uniaxial tensile tests after (compressive) preloading has to date only been obtained by Brühwiler[87]. However, this concerned only a few experiments, so that no strong conclusions could be drawn. In this investigation, the influence of a compressive preloading on the tensile properties of concrete was investigated (see also Hordijk and Reinhardt [89d]). The specimens were preloaded in compression up to a preset compressive stress-level (σ_{cp}), after which these specimens were fractured in tension in a deformation-controlled manner.

Tensile behaviour as influenced by preloading
Cook and Chindaprasirt[81] performed tensile tests after sustained tensile preloading (30 days) and cyclic tensile preloading (1000 cycles). They concluded that the sustained tensile load decreased the strength, while for the cyclic tensile load no significant effect upon the strength could be observed. The elastic modulus appeared to be slightly reduced for both types of preloading. Sri Ravindrarajah[82] observed a reduction in flexural strength after sustained flexure. The influence of compressive preloading on the tensile properties has been studied by Tinic and Brühwiler[85], Brühwiler[87] and Brühwiler and Wittmann[90]. A normal type of concrete and a type used for dams was investigated, while the loading rate was also varied. From tensile tests it appeared that f_t decreased with compressive preloading in the case of normal concrete, while for dam concrete no influence was observed. For both types of concrete, E_0 decreased after compressive preloading. In an extensive research programme, the influence of static (tensile and compressive) and fatigue (tensile-tensile and tensile-compressive) preloading on the pre-peak tensile properties was investigated in the Stevin Laboratory (Cornelissen and Reinhardt[86c]). For tensile preloading no effect on the reloading strength and stiffness was observed. Probably no significant damage was caused by such a type of preloading. A compressive preloading in the direction of the tensile reloading did not appear to influence strength either, but stiffness was strongly reduced. This phenomenon was explained by the fact that a compressive loading creates longitudinal micro-cracks which affect the cooperation between the stiff aggregates and the weaker matrix. The same mechanism is probably also responsible for the strong stiffness reduction as was observed for alternating tensile-compressive preloading. The results of preloading discussed so far were all obtained on

specimens for which the direction of compressive preloading was the same as the direction of tensile loading. Tests in which specimens were preloaded in compression, after which tensile loading was applied in a perpendicular direction, were performed by Delibes Liniers[87]. These showed that tensile strength decreased strongly compared to non-preloaded specimens. This result can be understood when it is realized that in this case micro-cracks due to the compressive preloading are orientated in a direction parallel to the final tensile fracture plane (see also figure 9.14).

For fracture energy, Brühwiler and Wittmann[90] observed that for dam concrete a reduction occurred with increasing compressive preload level. G_F was determined by means of the wedge splitting test and the direction of the initially applied compressive load was again perpendicular to the fracture plane.

Results for compressive preloading
The applied compressive preloading stress levels (σ_{cp}) were chosen as 0% (non-preloaded), 10%, 30%, 50% and 75% of the cube compressive strength (f_{cc}), with stress being taken as the average stress in the critical cross-section. Four experiments were performed for each type of preloading.

After compressive preloading and unloading, a compressive deformation can be observed at zero load. This deformation, henceforth denoted as irreversible deformation, δ_{irr}, is taken as the origin for the stress-deformation relations in figure 7.20. In this figure, each line represents the mean of four tests and deformation is the average value of the four 35 mm LVDTs, while stress is the applied force divided by the critical cross-sectional area. The most distinct fact to emerge from this figure is that the preloaded specimens have a flatter peak, after which the shape of the descending branch looks to be more or less the same. The average curves for the different preload levels do not differ significantly from each other.

Values for the fracture mechanics parameters, some characteristic deformations and dissipated energy during compressive preloading, as a function of the compressive preloading stress level, are plotted in figure 7.21. The dashed lines in the plots connect the average values for the different preloading levels. It appears that the compressive preloading did not influence f_t (figure 7.21a). For G_F a small increase can be observed in the case of preloaded specimens compared to non-preloaded specimens. This increase had already been seen in figure 7.20. The preloading stress level did not have much influence on G_F, especially if the scatter band is taken into account. It should be mentioned that the G_F value for the normally loaded specimens ($\sigma_{cp} = 0$ MPa) is rather low as compared to values obtained in other test series. Unfortunately, no explanation

could be found for this result. Nevertheless, since all specimens in this test series were treated in the same way and originate from the same mixes, the observed differences in G_F and especially in the shape near peak load are assumed to be realistic.
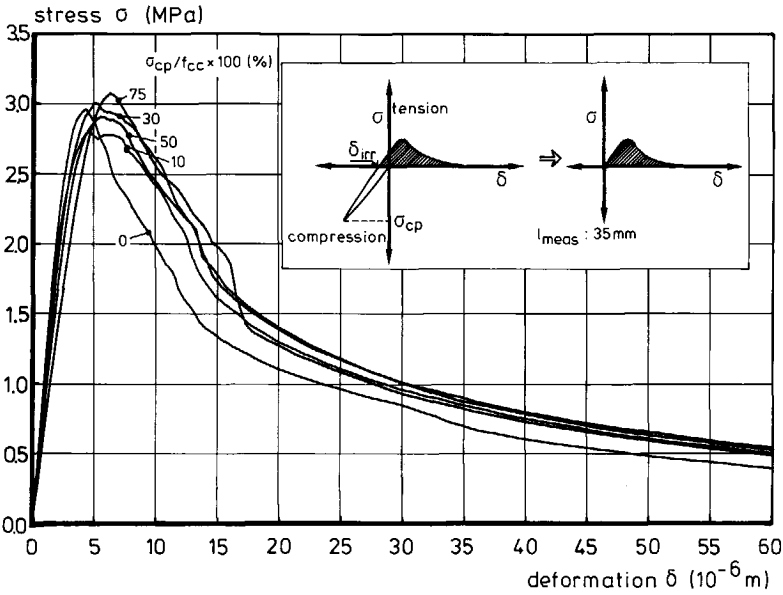

Figure 7.20   Tensile σ-δ relations obtained after compressive preloading.

In accordance with the results found in the literature, Young's modulus appears to reduce in line with the initially applied compressive stress level (figure 7.21c). For the tangent modulus in compression, an average value of 36200 MPa was determined. The meaning of the characteristic deformations in figure 7.21d can be seen in the inset. The dissipated energy, W_d (figure 7.21e), was determined as the area under the σ-δ relation (see inset). It can be seen that damage due to compressive loading, as characterized by δ_{irr} and W_d, increases more than proportionally with the initially applied maximum compressive stress level.

Discussion
For the fracture energy, a tendency to increase a little with compressive preloading was observed, while the compressive stress level did not appear to influence the amount of increase. This result seems to contradict the results of Brühwiler and Wittmann[90], who observed a decrease with initially applied compressive loading. In this respect, however, it should be noted that they used a dam concrete which contained large aggregates and
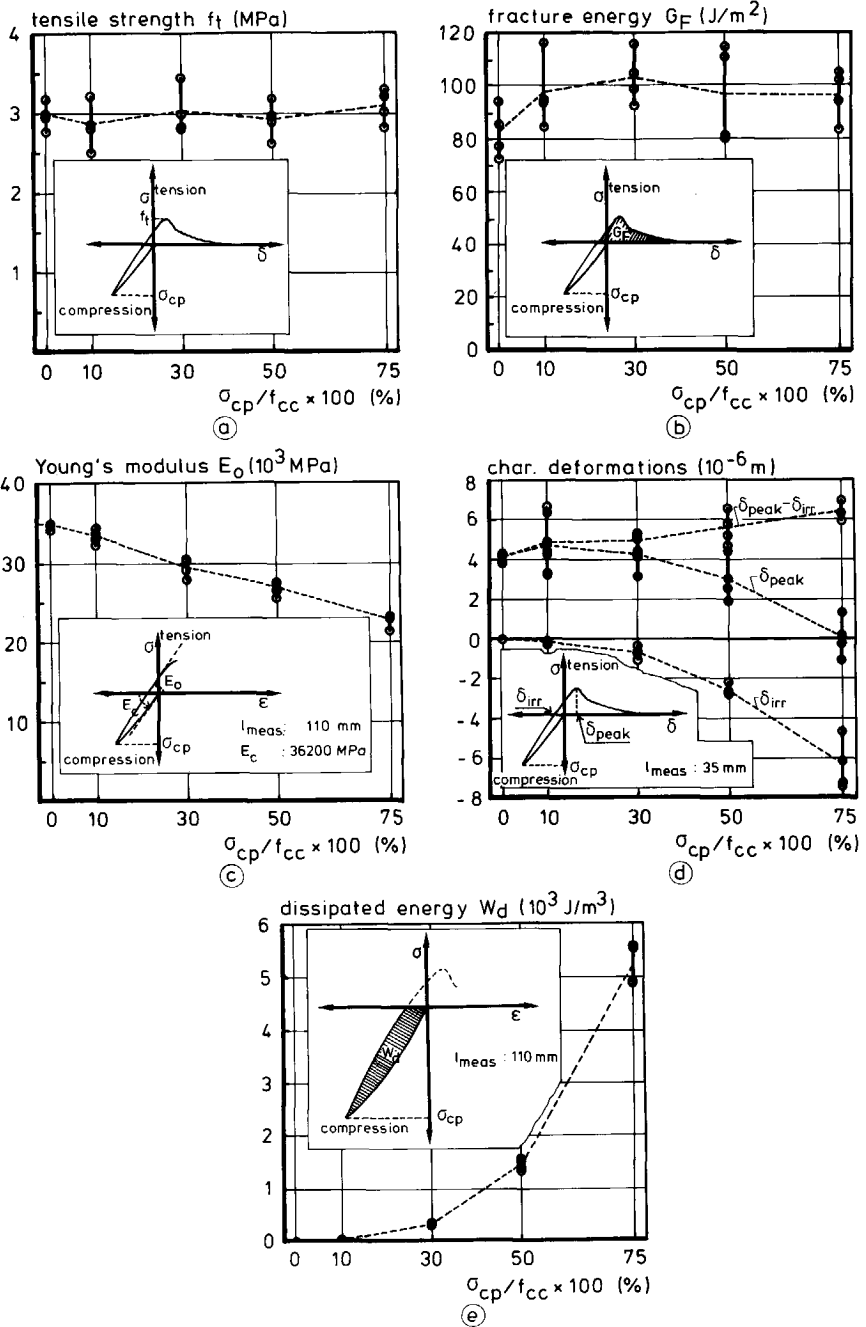
121

Figure 7.21   Different parameters as influenced by compressive preloading;
f_t (a), G_F (b), E_0 (c), characteristic deformations (d) and
compressive dissipated energy (e).

122

in which the fracture surface was characterized mainly by aggregate failures, while in these experiments mainly bond failure between aggregates and matrix could be observed.

The main differences between preloaded and "virgin" specimens (see figure 7.20) is that the preloaded specimens display a kind of horizontal plateau at or just after peak load, while in case of 'virgin' specimens, the stress drops almost directly after reaching peak load. The question arises as to whether it is possible that this increase of deformation at the higher stress levels may be due to the release of irreversible compressive deformations which exist at the beginning of tensile reloading. If this occurs, it is not likely to be the only contribution to the observed phenomenon since the descending branches are shifted over about 3.5 μm (see figure 7.20), while δ_{irr} was only -0.1, -0.7 and -2.6 μm for the 10%, 30% and 50% preloading respectively (see figure 7.21d). Nevertheless, the energy consumed by such a phenomenon pertains to the bulk material and should therefore not be taken into account in the calculation of G_F. Another explanation for the observed phenomena concerns the fracture process zone. In fact the material structure has been changed due to the longitudinal micro-cracks that have been created. This changed material structure may also have changed the way of tensile fracturing. It is possible that the process zone contains more micro-cracks (increasing width of the process zone), but the final fracture surface on the micro-scale may also have been altered. A more tortuous crack path results in more sliding friction when aggregates are being pulled out of the matrix. Unfortunately, techniques are not available to verify these explanations. Finally, there is also the possibility that the obtained result is due to the applied notches. In that respect, the reader is also referred to Section 9.4.

Since this is only the result of one investigation, more research in this direction is required in order to verify whether the observed phenomenon is generally valid. It should be clear that an effect of a compressive preloading on the fracture energy also has its consequences for some other fracture tests that are used to determine G_F. In the bending tests, for instance, half of the fracture zone is preloaded in compression, before fracturing in tension.

8 Verification tests and numerical analyses

8.1 General

So far, the material behaviour of plain concrete under tensile loading has been discussed in previous chapters and described by a constitutive model. Subsequently, as is usual in research, the model needs to be verified. A possible way of doing this is to investigate a structure experimentally and to see whether its behaviour can be predicted with the model. An even better approach is to investigate several structures, since the model is only proven to be a proper description of the real material behaviour if it can predict the behaviour of all structures in which the behaviour described in the model is active. In doing this, however, one should see that the structure under investigation predominantly fails under the mechanism that is modelled. Otherwise, there is a possibility that the simulation is blurred by other, improperly modelled mechanisms. In this chapter, experimental results of different types of test in which mode I fracture is the leading mechanism will be discussed and the validity of the "continuous- function model" will be verified by several simulation techniques.

Besides deformation-controlled uniaxial tensile tests, which were used to determine the material properties, f_t, E_o and G_F, four-point bending tests and tensile tests on single notched plates were performed. A schematic representation of the test program, including type of loading and measured data, can be seen in figure 8.1. Details about the different tests are given in Section 4.4. Since three different values for the notch depth of the bending specimens have been applied, five different structures have actually been investigated. The results of the deformation-controlled uniaxial tensile tests will be discussed in this section, while those of the bending experiments will be presented in Section 8.2. Results of numerical analyses for the beams can be found in Sections 8.2, 8.3 and 8.4. This concerns analyses with a FE code, analyses with a multi-layer model and analyses with a technique in which some of the experimental results are used as input respectively. In Section 8.5 the results of the tensile tests on the single notched plates will be discussed, which is followed by concluding remarks in Section 8.6.

Material parameters
Deformation-controlled uniaxial tensile tests as well as standard tests on cubes were used to determine the material parameters experimentally. These specimens were taken from the same batch as all other specimens and tested at approximately the same age. The normal-weight type of concrete, denoted as NC, was used and the usual curing procedure was applied, i.e. concrete slabs were cured under water for two weeks, after which specimens were sawn out of these slabs and stored in the laboratory until testing. The age

124

of the specimens at testing varied between 65 and 86 days. Standard cube compressive and splitting tests were performed at 28 days and 78 days. The cubes tested at 78 days were cured in a similar way as the specimens. The results of the cube tests and of the deformation-controlled uniaxial tensile tests (servo-controlled by the deformation of a 15 mm base) are listed in Table 8.1. The following remarks can be made about these results. First of all, it appears that the values for the different material parameters are relatively high as compared with other results found for the same mix (see Chapter 7). This result must be due to the greater age of the specimens at testing. This is confirmed by the strength increase from 28 days to 78 days that was observed for the cubes. Secondly, it should be noted that a significant scatter was found for the tensile strength and the fracture energy.
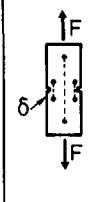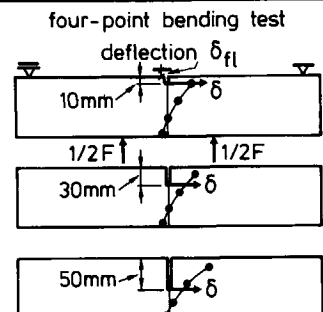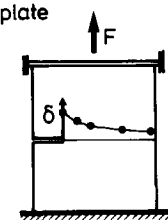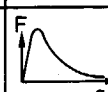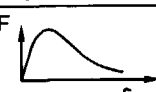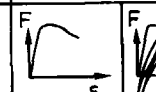

type of test	def.-contr. uniaxial tensile test	four-point bending test		tensile test on single notched plate
100mm		deflection δ_{fl} 10mm		
		30mm		
		50mm		
measured data	F and δ $\rightarrow f_t, E_0, G_F$	- Load F - deflection δ_{fl} - deformation distribution over the fracture zone		- Load F - deformation distri- bution over the fracture zone
type of loading				
number of experiments	4	3 × 1	3 × 1	2	1

Figure 8.1   Experimental program for the "verification tests".

8.2 Four-point bending tests; Results of experiments and FE analyses.

The continuous-function model was implemented in the finite element code DIANA. This code was used to simulate the four-point bending tests. In this report, emphasis will be on the results of the numerical analyses rather than on the applied numerical techniques. Details about the analyses can be found in Janssen[90].

Table 8.1 Material parameters obtained from 150 mm^3 cube tests and deformation-controlled uniaxial tensile tests.

		28 days		at testing (65-86 days)	
from cube tests:					
compressive strength	(MPa)	48.1	(0.8)[1]	59.5	(2.6)
splitting strength	(MPa)	2.96	(8.2)	3.30	(6.9)
from tensile tests:					
tensile strength	(MPa)			3.45	(15.2)
fracture energy[2]	(J/m^2)			115	(18.7)
Young's modulus (l_{meas}= 110 mm)	(MPa)			37500	(3.4)
Young's modulus (l_{meas}= 75 mm)[3]	(MPa)			43470	(8.6)

1) coefficient of variation in brackets

2) data points up to 120 μm and linear to an assumed δ_0 of 160 μm

3) Due to the notches, Young's modulus for l_{meas}= 75 mm is greater than for l_{meas}= 110 mm (see App. A.1). No explanation, however, was found for the observed large difference that can partly be explained by disturbances near the notches (see Section 9.4). In analyses, a value of 40000 MPa will be used.

FE idealization*

Symmetry was used for the applied FE idealization as can be seen in figure 8.2, where the FE idealization for the specimen with a 50 mm deep notch is shown. For the concrete, eight-node and six-node quadratic elements were used, while six-node interface elements were applied to model the crack (discrete crack approach). For the interface elements, the vertical displacements of each two nodes positioned beside each other were assigned to be equal. In the horizontal direction, the interface elements use a finite initial stiffness. In order to represent the uncracked beam properly, a large value will be chosen for this initial stiffness. The continuous-function model becomes active as soon as the tensile strength is reached. To enable comparison with the experiments, the vertical displacement of point A (see figure 8.2) was used for the deflection of the beam, while the horizontal displacements of points 1 to 4 were used to compare crack openings (see also figure 4.7).

126

Simulations

For the FE analyses, the input parameters were kept the same for the three different beams. First of all, the input parameters chosen were closely related to the experimentally determined values (see Section 8.1), i.e. tensile strength is 3.3 MPa, Young's modulus is 40000 MPa and fracture energy is 120 J/m^2. Though, in general, the curves were in rather good agreement with those experimentally determined, the maximum load was slightly overestimated for all three beams. The overestimation was 17, 7 and 5 % for the beams with a 10, 30 and 50 mm deep notch respectively. Then the input parameters were slightly adjusted in order to obtain an even better prediction. For these analyses, the parameters were chosen as: tensile strength $f_t = 3.0$ MPa, Young's modulus $E_0 = 38000$ MPa and fracture energy $G_F = 125$ J/m^2. All results of FE analyses, as presented in this chapter, were obtained with these input parameters.
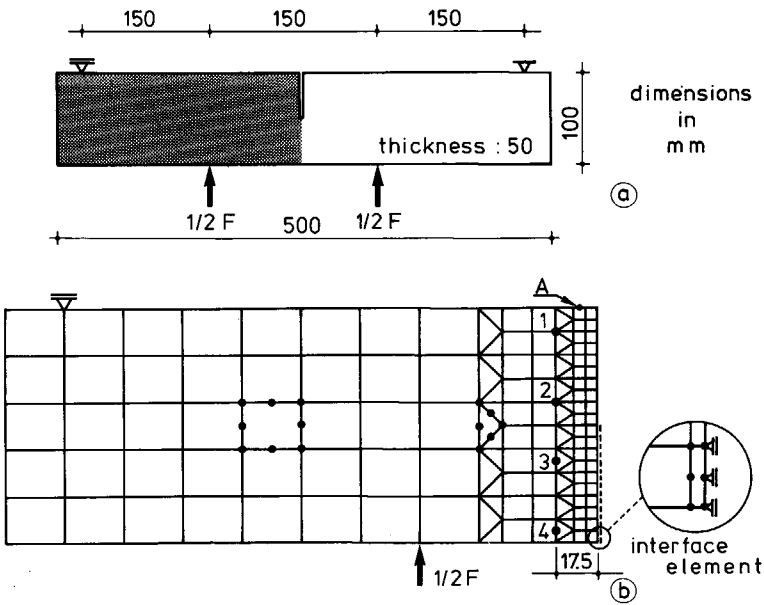

Figure 8.2   FE idealization for the beam with a 50 mm notch depth.

In Appendix C, results for the four-point bending tests are presented, i.e. load-deflection curves and deformation distributions over the fracture zone. Load-deflection curves for the experiments with static loading and those obtained from the FE analyses are plotted in figure 8.3. In these analyses, the initial stiffness of the interface elements was 10^{12} MPa/mm.

127

For the 30 mm and 50 mm deep beams, the predictions up to a deflection of about 0.25 mm appear to be very good, though for the beam with the 10 mm notch, this prediction is less good. The envelope curve in the cyclic test for the 10 mm deep beam, however, shows also a good agreement with the numerical result (see figure C.1a in Appendix C). For deflections above 0.25 mm the load predictions by the FE analyses are too low as compared with the experiments. In the author's opinion this phenomenon is due to the stress transfer at larger crack openings which is found in experiments (see Section 7.1) and which is not modelled in the CFM. In the next section, this phenomenon will be elucidated with some analyses based on a simple numerical model.
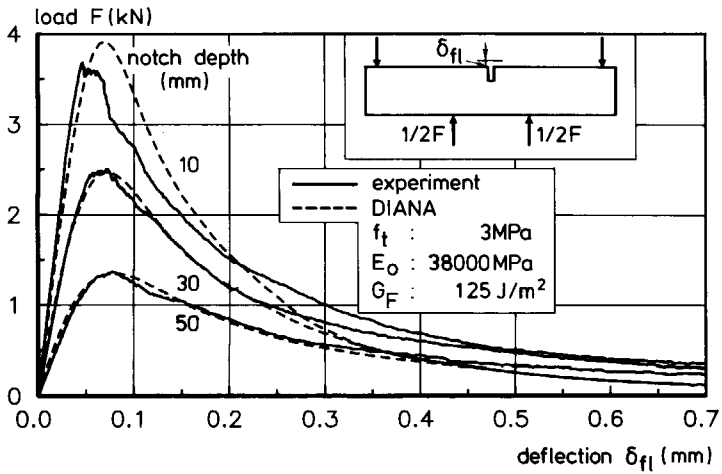

Figure 8.3   Load-deflection curves for the bending specimens under monotonic increasing deflections.

In figure 8.4, deformation distributions (l_{meas} = 35 mm) over the fracture zone are compared for three points in the loading history of the beam with the 50 mm deep notch. More comparisons can be found in Appendix C. Here, again, the experimental and numerical results appear to coincide very well.

Nonlinear deformation distributions are found for the loading points in the pre-peak region and for peak load, while for deflections of about 150 10^{-6} m and 290 10^{-6} m (see Appendix C.1) a more or less linear distribution over the beam height is found. In figure 8.4c, the corresponding calculated stress distributions are plotted. From this figure, it can be seen how the softening zone grows through the specimen. It appears that at a deflection of 0.15 mm, the softening zone has already spread over a depth of 40 mm, resulting in a small compressive zone with large compressive stresses.
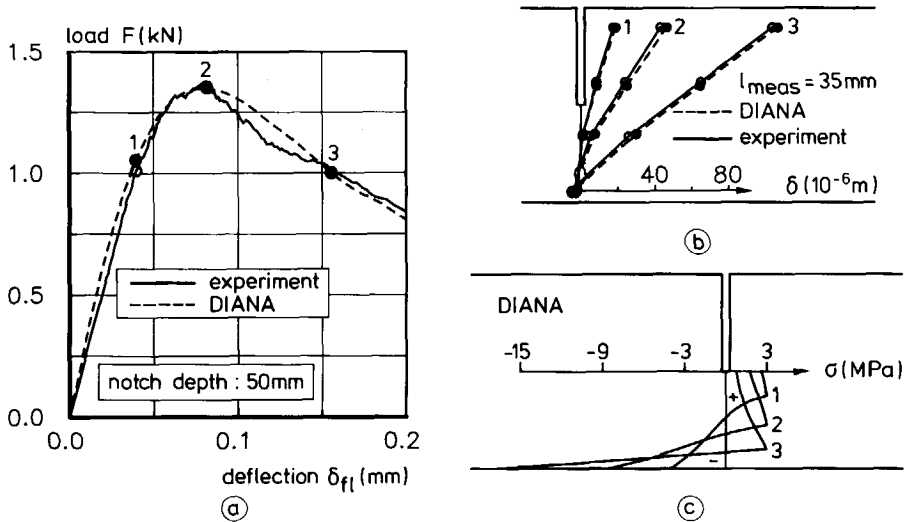
128

Figure 8.4   Results for the beam with the 50 mm notch depth; a) F-δ_{fl} relations, b) deformation distributions and c) stress distributions.

Load-deflection relations for the cyclic test on the beam with a 10 mm deep notch depth are plotted in figure 8.5. The predictions show a very good agreement with the experimental results (see also Appendix C). As far as the analyses with post-peak cyclic loading are concerned, the following remarks should be made. In the FE analyses it sometimes appeared difficult to reach the convergence criterion in an unloading-reloading cycle. In order to improve this, the type of interface element was changed while, the initial stiffness was reduced to 10^4 MPa/mm for the beams with a notch depth of 10 mm and 30 mm. These alterations caused the peak loads to reduce by about 3 to 4%. Moreover, an erroneous result was sometimes found in the first part of the reloading curve (see for instance the fourth loop in figure 8.5). Such erroneous results could be circumvented by choosing appropriate loading steps.

Fracture energy from the bending tests

The bending tests can also be used to determine a value for the fracture energy of the concrete. Because of its simplicity, the three-point bending test has even been recommended for the determination of this value (Hillerborg[85a]). Here, it is intended to calculate a G_F value from the bending tests and to compare it with the value obtained from the uniaxial tensile tests. The fact that the chosen calculation procedure significantly affects the absolute value (see Section 7.1) makes such a comparison difficult. Furthermore, in order to calculate the energy supplied to the specimen, the vertical displacement

129

at the point of load application should be known. This displacement, however, was not measured. Nevertheless, it is possible, on the basis of some assumptions, to calculate G_F values that should correspond to the value obtained from the tensile tests (see Table 8.1). The first assumption concerns the vertical displacement at the loading point. Therefore, a linear relation for this displacement over half the specimen length is assumed (see inset b in figure 8.6). This results in a vertical displacement at the loading point equal to $(150/217.5)*\delta_{fl}$. Consequently, the fracture energy is equal to the area under the $F-\delta_{fl}$ curve divided by the net cross-sectional area and multiplied by $(150/217.5)$.
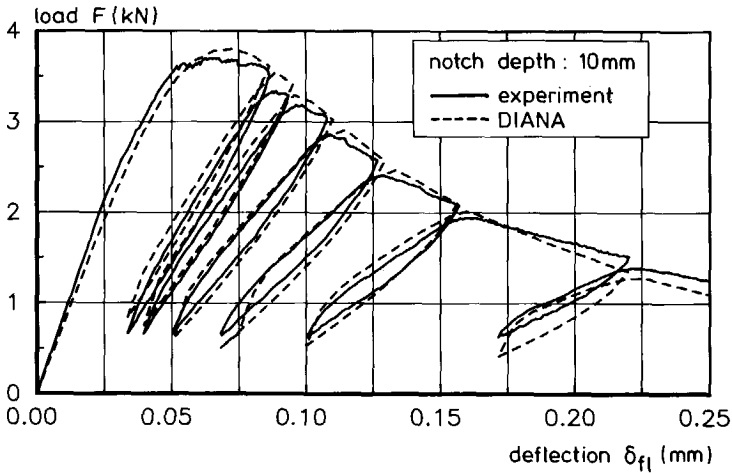

Figure 8.5   F-δ_{fl} relations for the beam with the 10 mm notch depth under post-peak cyclic loading.

The second assumption concerns the last part of the $F-\delta_{fl}$ curve. In the uniaxial tensile tests, the data point at a deformation of $120 \ 10^{-6}$m was taken as the last data point, which was followed by a linear relation until an assumed δ_o of $160 \ 10^{-6}$ m (equal to 4/3 times the deformation of the last data point). For the bending tests, the last data point was chosen in such a way, that the average deformation over the net cross-sectional area is equal to $120 \ 10^{-6}$m (see inset a in figure 8.6). Then a linear relation is assumed up to a deflection equal to 4/3 times the deflection of the last data point. Average values for G_F, calculated according to this procedure, are 104, 115 and 115 J/m^2 for the beams with 10, 30 and 50 mm notch depth respectively. The agreement with the value determined in the tensile tests, 115 J/m^2, is remarkable.
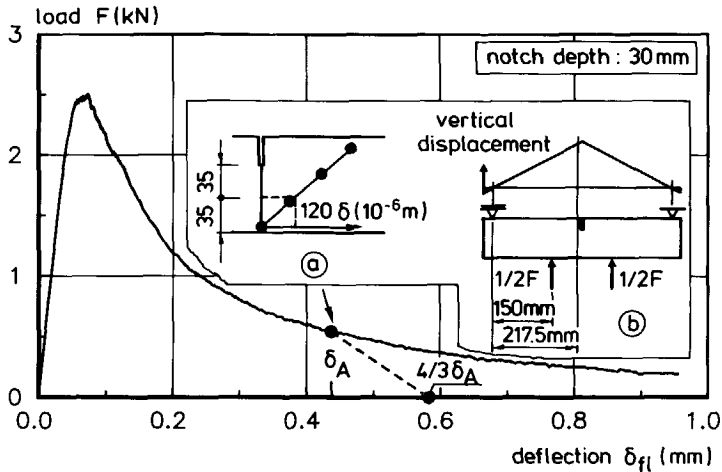
130

Figure 8.6   Procedure applied to calculate G_F from the bending experiments.

8.3 Simulation by a multi-layer model

In the bending tests, fracture only occurs in a narrow zone, while the rest of the specimen behaves linear elastically. The same held true for the deformation-controlled uniaxial tensile tests, where it appeared possible to approximate this behaviour with a simple model (see Section 5.5). Similarly, the bending tests will be simulated with a simple model (multi-layer model). However, this model is slightly different from the model in Section 5.5. For the sake of clarity, it is only intended to show that, with some assumptions, the behaviour of plain concrete in bending tests can rather easily be studied. For more accurate simulations, an FE analysis has to be performed. The model can be used to perform a parameter study. Here, it will be used to show the influence of the tail of the stress-crack opening relation on the last part of the F-δ_{fl} curve. In Chapter 9, the same model will be used to predict the behaviour of a beam under fatigue loading.

The principle of the model, which is shown schematically in figure 8.7, is the same as used for the tensile test model (Section 5.5). A fictive part of the beam, encompassing the fracture zone, is replaced by springs, representing the behaviour of small layers. For simplicity, "fracture zone" will also be used in this section to describe this part of the beam. The load-deformation (or stress-deformation) characteristic of the springs is determined by the combination of the stress-crack opening relation (CFM) and the elastic deformation over the arbitrarily chosen length of the fracture zone l_f (see figure 8.7a). In fact, the smeared crack approach is used. The remaining parts of the beam are assumed to behave
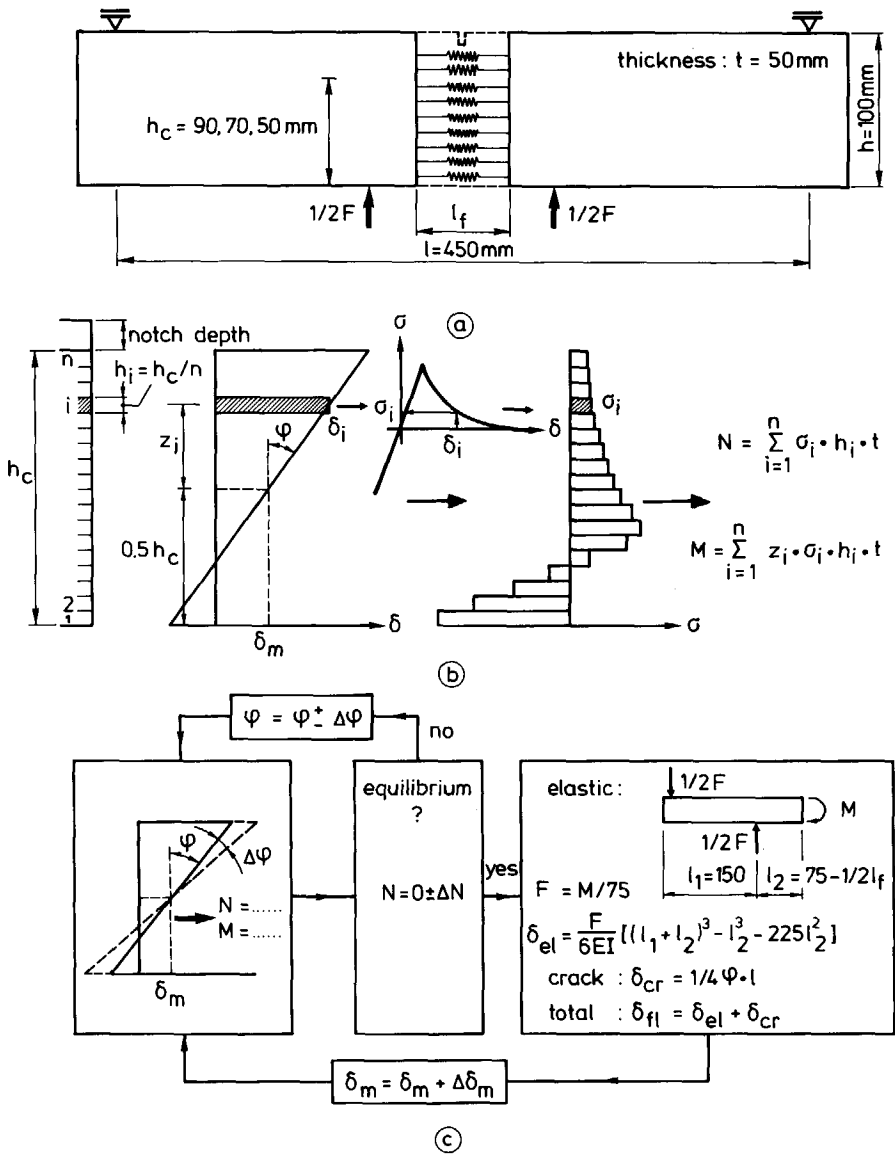
131

Figure 8.7   Principles of the multi-layer model.

elastically. The main characteristic of the model is that for a deformation distribution of the fracture zone, the corresponding resulting force N and moment M are calculated (figure 8.7b). Therefore, the net cross-sectional area is subdivided over its height into n

elements or layers. For each element, the deformation is determined by an average deformation δ_m and a rotation φ of the fracture zone. Then, with the aid of an iterative procedure, the corresponding stress can be determined, after which summing up over all elements yields the internal force N and moment M. Equilibrium is found when N is equal to zero. Unlike in Section 5.5, an incremental procedure is applied (see figure 8.7c). For an average deformation δ_m, the rotation φ is adjusted until N is equal to zero, within a certain range ($\pm \Delta$ N). Then, with the corresponding internal moment M, the external load F and the deflection δ_{fl} are calculated. In the subsequent step, the average deformation is increased by $\Delta \delta_m$, while in the first iteration of this step, the rotation as found for equilibrium in the previous step is used. In the analyses whose results will be presented, the element height was chosen as equal to 1 mm, resulting in 90, 70 and 50 elements for the three different types of beam.

Just as for the tensile tests, the length of the fracture zone l_f must be chosen arbitrarily and this affects the solution. The influence of this length on the F-δ_{fl} relation for the beam with a 10 mm notch depth is shown in figure 8.8. It can be seen that the value of l_f primarily affects the peak load, while the initial slope and the curve beyond 0.1 mm is only slightly affected. For the simulation of the three different beams, a constant value of l_f which is 50 mm, was chosen. A comparison with the DIANA FE analyses is shown in figure 8.9. Despite the simplicity of the layer model, there appears to be a good resemblance. The limitation of the layer model, especially for peak load, also becomes clear from figure 8.10, where the ratio between a calculated bending strength and the tensile strength are plotted for the three different beams. For a constant value of l_f, no size effect will be
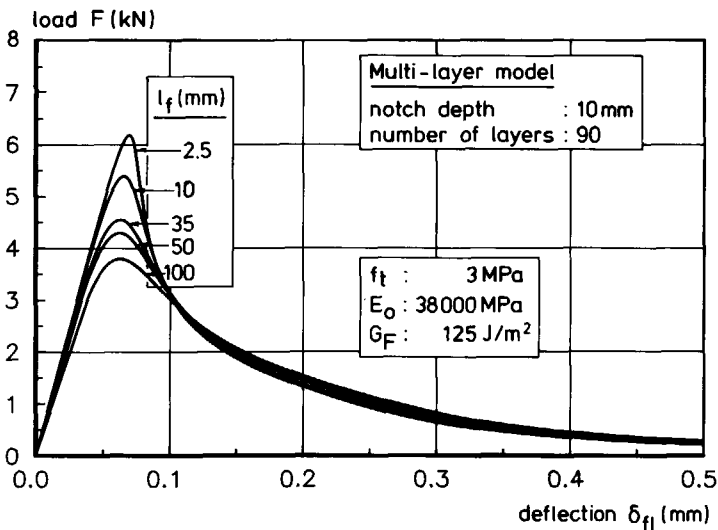

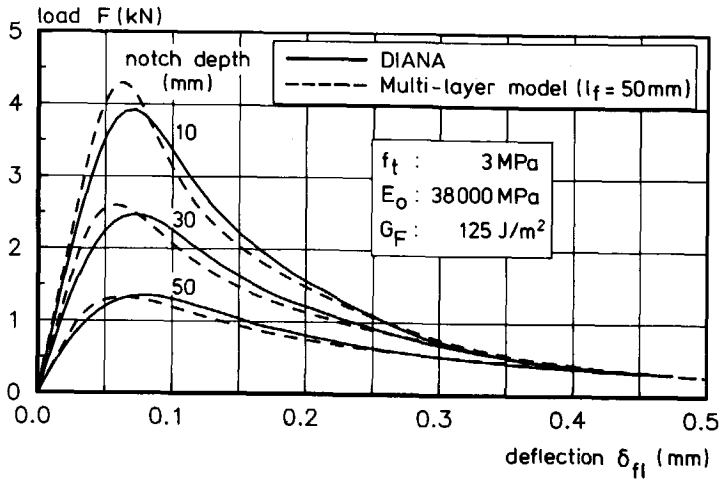Figure 8.8 The influence of l_f on the F-δ_{fl} relation.

133

Figure 8.9   *F-δ_fl relations predicted with DIANA and the multi-layer model with l_f = 50 mm.*

found with the multi-layer model. Nevertheless, it can very well be used to study the influence of the tail of the σ-w relation (see also figure 7.3) on the F-δ_fl relation. Therefore, the calculations of figure 8.9 were repeated, while the σ-w relation was extended with a linear relation from w = 160 μm until a w_o at w = 1 mm (see inset in figure 8.11). The effect of this extension is that the load-bearing capacity at larger deflections increases (figure 8.11). As a result, the predicted curves approach the experimental curves (see also figure 8.3). This means that the existence of a long tail, as observed in tensile tests, is confirmed by the experimental results of the bending tests.
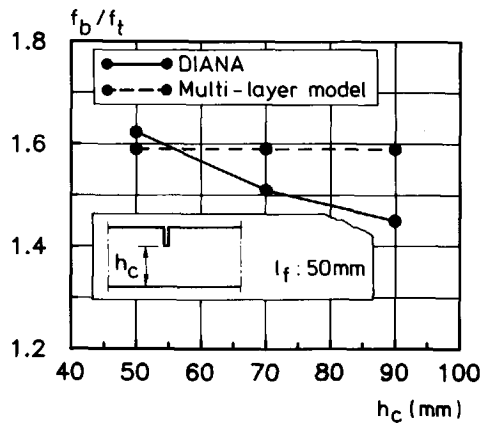

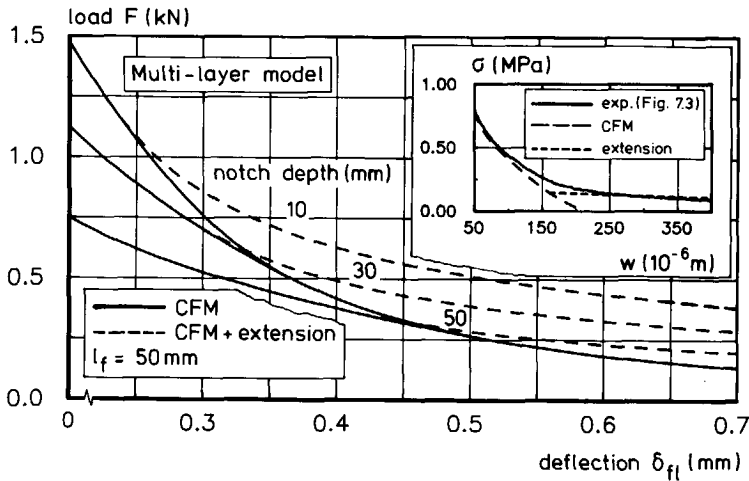Figure 8.10   *Relative bending strength as a function of h_c.*

134

Figure 8.11   The influence of a long tail of the σ-w relation on the F-δ_fl curves.

8.4 Hybrid method

In previous sections the validity of the material model was verified by simulating the experiments using models in which only the material behaviour was used as input. There is, however, also a possibility of verifying the material model by using a method which also uses some of the experimental results as input and which will therefore be called the "hybrid method". The part of the experimental results used as input is formed by the deformation distributions over the fracture zone. With these deformation distributions and the material model, the corresponding externally applied loads can be predicted. The procedure is sketched in figure 8.12. For each point in the loading history, the measured deformation distribution (l_{meas}= 35 mm) is converted to a stress distribution which yields a normal force N and a moment M. Now, two checks are available. First of all, it can be verified how much N deviates from zero, while secondly, the moment M yields a calculated force F_{calc} (F_{calc}=M/75) that can be compared with the measured force F_{meas}. As can be seen, there is a great similarity with the multi-layer model. This procedure was applied earlier for tensile tests on plates (Cornelissen et al.[86b]).

Results for the beam with a 30 mm notch depth are plotted in figure 8.13. The parameters for the material model were chosen so that they are closely related to the values obtained from the uniaxial tensile tests; i.e. tensile strength is 3.3 MPa, Young's modulus is 40000 MPa and fracture energy is 115 J/m^2. In figure 8.13a, the normal force due to positive stresses (N^+) and that due to negative stresses (N^-) are plotted versus the deflection. It appears that the resultant force N is almost equal to zero up to a deflection
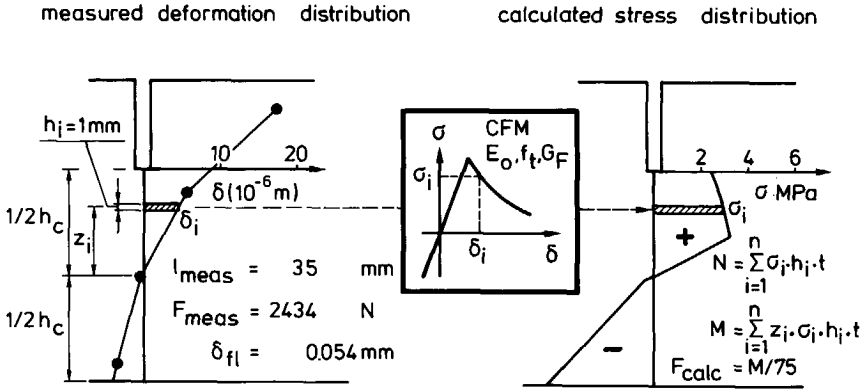
135

Figure 8.12   Procedure to calculate the stress distribution, the normal force N, the moment M and the external load F respectively, based on the measured deformation distribution and the material model ("hybrid method").

of about 0.15 mm, after which the decrease of N^+ is stronger than the increase of N^-, resulting in a negative resultant normal force N. In the simulation, the CFM is used without the extension as discussed in the previous section. Adjusting the CFM with this extension will increase N^+ for larger deflections and consequently reduce N. However, this will also yield a larger moment M and thus a larger calculated external load. In figure 8.13b it can be seen that without the extension, the predicted load is already above the measured one. Therefore, it is believed that at larger deflections (beyond 0.15 mm),
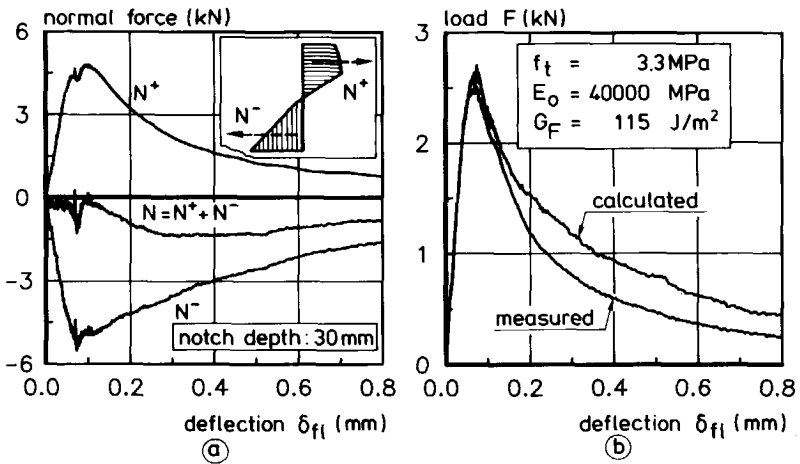

Figure 8.13   Results of the hybrid method for the beam with a 30 mm notch depth.

136

the negative normal force and the overestimated load, are the result of erroneous compressive stresses. It should be pointed out that due to the fact that $N \neq 0$ the calculated moment depends on the point that is chosen as moment axis. The fact that N^- is probably incorrect may very well be the reason, since the compressive zone is very small, while large compressive stresses occur (see also Section 8.2). Nevertheless, the prediction of the external load up to a deflection of about 0.15 mm is very good. Similar results were found for the two other types of beams (see Appendix C.2).

In the analysis presented above, a linear relation for compression was used. The analyses can be improved if a nonlinear relation is adopted for the compressive behaviour. Since we are here interested in the tensile behaviour of the concrete, rather than in its compressive behaviour, some analyses were performed in which only the deformation distribution in the tensile region of the fracture zone is used. Therefore, the tensile stresses are calculated over the depth of the beam with positive deformations, resulting in the positive normal force N^+. Then, for the area where the deformations are negative, a linear stress distribution is assumed corresponding to a force N^- equal to $-N^+$ (see inset in figure 8.14). The predicted load-deflection relations for the CFM with, and without, the extension are plotted in figure 8.14 (for the other beams see Appendix C.2). It can be concluded that the calculated loads approximate the measured loads very well. For the beams with the 10 mm and the 50 mm notch (Appendix C.2) the peak load is overestimated a little. Furthermore, the existence of a long tail in the σ-w relation is again confirmed.
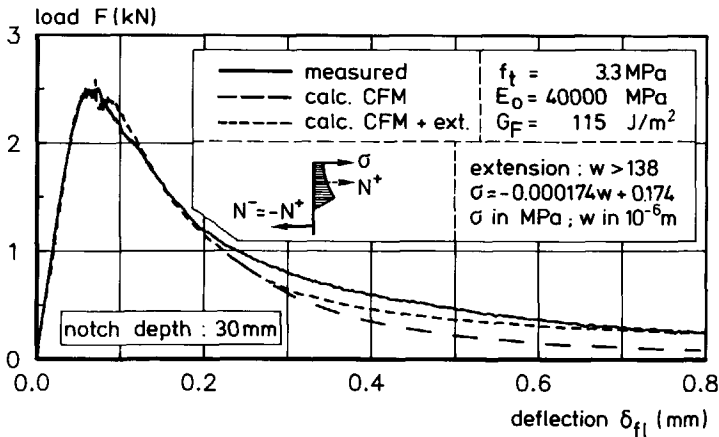

Figure 8.14   Results of the hybrid method for the assumption of a linear stress distribution in the compressive zone corresponding to a zero normal force.

Finally, the hybrid method was applied to a test with post-peak cyclic loading. The result of that analysis is plotted in figure 8.15. In order to separate the unloading and reloading parts of the different loops, time is used for the horizontal axis in this figure. It can be seen that in the loops, too, the calculated load corresponds very well with the measured load, while the resultant force N also approaches a zero value. This means that these analyses show that the CFM provides an adequate description of the material behaviour.
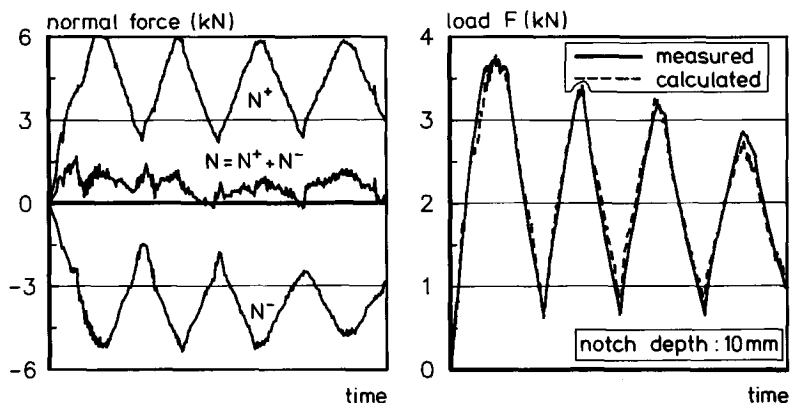

Figure 8.15   Load predictions by the hybrid method for a beam under post-peak cyclic loading.

8.5 Tensile tests on single edge notched plates.

Similar to the procedure used for the bending tests, the tensile tests on single notched plates were also simulated by a number of analyses. Since these tests were not simulated with the FE code, only predictions by the multi-layer model and the hybrid method will be discussed.

Experimental results
The load-deformation relations of the three experiments (envelope curve in case of cyclic loading) did not differ very much. Therefore, in the discussion of the results, only one experiment will be considered. The load-deformation relation for this experiment is plotted in figure 8.16. It should be realized that, compared to the deformation-controlled uniaxial tensile tests on small specimens, the σ-δ curve depends strongly on the configuration of the measuring devices that are used to determine δ. Here, the deformation is taken as the average value of the LVDT readings 1, 3, 4 and 5 on the front and rear sides of the specimen (see inset in figure 8.16). In this test, the average signal of the two LVDTs

at position 3 was used as control parameter. As can be seen in figure 8.16, the test was able to proceed until δ is about 40 μm. Then, the test suddenly stopped. Restarting of the experiment showed a curve, as can be seen in the lower right corner of the figure.
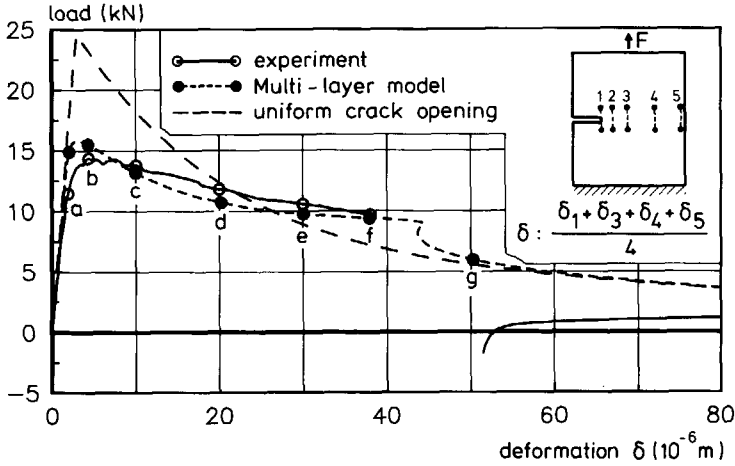

Figure 8.16   Load-deformation relations for the tensile test on a single notched plate; Experimental result and model prediction.

The following explanations can be given for the observed behaviour. First, it appeared that the curve after peak load was rather flat, which can be clearly seen when the curve is compared with the relation that represents a uniform crack opening (similar to the input material model). Due to the eccentric loading, the different areas in the fracture zone reach their peak loads one after the other which causes the peak to be less sharp (see also Section 7.1). In this respect, the similarity with the curves in figure 7.6, in which the results of a small and large tensile specimen are plotted, is striking. At a deformation of about 40 μm there is probably a snap-back in the load-deformation curve of the control parameter. This snap-back could not be followed by the equipment. The characteristic of a snap-back is that equilibrium can only be found after a sudden drop in load (figure 8.17), which is mostly also accompanied by a substantial change in the deformation distribution of the fracture zone. Directly after point A in the loading path is passed, the deformation increases much more than the prescribed deformation. As a result, the servo-control system directly reduces the load strongly in order to attain the desired deformation. Due to the sudden loading and unloading, however, this load reduction may be very much higher than that needed to find a new equilibrium. The unloading may very well go into compression. In these tests, this is what happened, with the result that the limitation of the maximum compressive load that had been built into the equipment

139

stopped the experiment. After restarting the test, the reloading curve of an unloading-reloading loop is in fact followed. In 1969, Heilmann et al.[69] were the first to observe this particular behaviour, a sudden drop followed first by a reloading curve, in eccentric loaded tensile tests (see also Hordijk[89c]). And they already gave the above described explanation for it. In results reported by Budnik[85] and Van Mier and Schlangen[89], a similar behaviour can be observed.
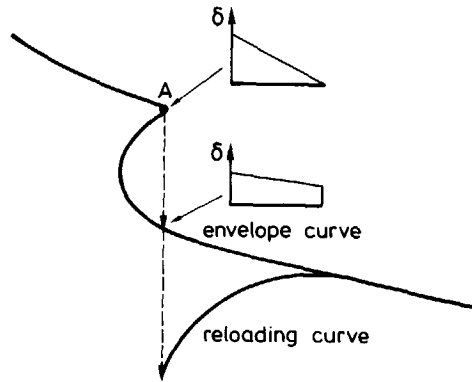

Figure 8.17   Behaviour that may be observed in an experiment after a snap-back.

Predictions by the multi-layer model

Due to the large cross-sectional area of the fracture zone, this test is less suitable for simulation with the multi-layer model. Nevertheless, such a simulation is still valuable for the investigation of certain phenomena. The result for an analysis with a 35 mm length of the fracture zone is plotted in figure 8.16. The requirements for equilibrium, the applied rotational stiffness of the boundary of the specimen and the solution procedure applied was the same as in the analysis in Section 5.5. The material parameters were chosen as: tensile strength is 3.3 MPa, Young's modulus is 40000 MPa and fracture energy is 115 J/m^2. The σ-δ relation predicted by the model is plotted in figure 8.16. It can be seen that the model predicts the behaviour very well up to a deformation of about 40 μm. Subsequently, a snap-back is indeed found in the analysis, as had already been surmised on the basis of the experimental result. For the sake of clarity, it should be noted that especially around peak load, the shape of the curve depends strongly on the arbitrarily chosen length of the fracture zone.

The deformation distributions for the points marked in figure 8.16 are plotted in figure 8.18. It can be seen that the measured deformation distributions for the 35 mm

measuring length are, at small deformations, highly non-uniform. Nevertheless, the deformation distributions predicted by the multi-layer model provide a fairly good representation of an average crack opening. For larger deformations, the differences gradually disappear.
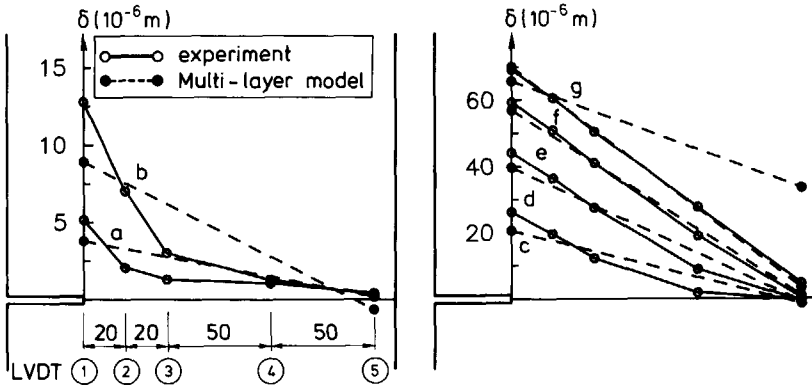

Figure 8.18   Measured and predicted deformation distributions for points in the loading history marked in figure 8.16.

Position of LVDTs used for test control
In the different tests on single notched plates, the location of the LVDTs used for the servo-control was varied. Nevertheless, in none of the three tests did it appear possible to pass the snap-back properly. Now, the results of the multi-layer model analysis will be used to show the influence of the position of the LVDTs used for the control parameter on the test performance. In figure 8.19, the load-deformation relations for the five positions of the LVDTs, as predicted by the multi-layer model, are plotted. In this figure, it can be seen that for location 4, no snap-back is predicted. This means that this location could best have been chosen for the control parameter. So, for this type of test, not only the measuring length but also the location of the measuring devices used as control parameter should be chosen properly. It must, however, be realized that in reality the behaviour can differ from the behaviour predicted by the multi-layer model due to the nonlinearity of the deformation distributions and due to non-uniform crack openings in the direction perpendicular to the plate.

Hybrid method
The results of analyses with the hybrid method are plotted in figure 8.20. The predictions of the external load based on the deformation distribution over the fracture zone and the

material model correspond very well with the load measured in the experiment. This holds true for the experiment with monotonic increasing deformation (figure 8.20a) as well as for the experiment with post-peak cyclic loading (figure 8.20b). Again, the material parameters as obtained from the uniaxial tensile tests were used and the cross-section was subdivided into parts of 1 mm size.
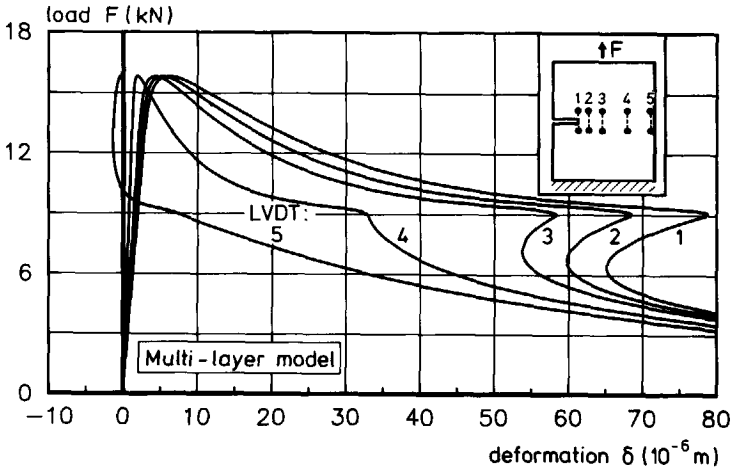

Figure 8.19   Load-deformation relation for the different LVDT positions, as predicted by the multi-layer model.
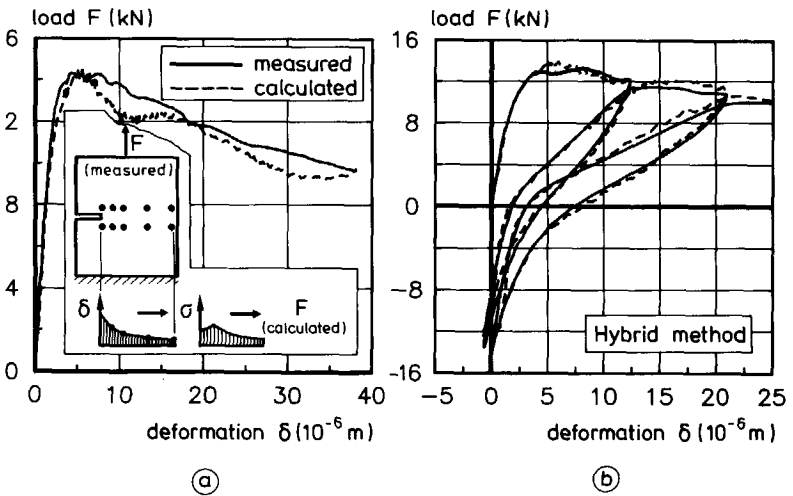

Figure 8.20   Load predictions by the hybrid method; a) static loading and b) cyclic loading.

Eccentricity

In the experiments four load cells were used to measure the total load (see Section 4.2). This means that the separate readings of these load cells give information about the load eccentricity. It appeared that the readings of the two load cells that are positioned in a line perpendicular to the specimen were equal. Using the two other load cells, positioned on the left and right sides of the specimen and with a centre to centre distance equal to 225 mm, it was possible to determine the load eccentricity. In figure 8.21, the measured eccentricity is compared with the eccentricity predicted by the multi-layer model and that obtained with the hybrid method. Qualitatively, the agreement between these results is good. Quantitatively, the measured eccentricity is slightly larger than the two predicted ones. In this respect, however, it can be remarked that the predicted eccentricity belongs to the fracture zone, while the eccentricity was measured in the load cells under the loading lower platen. This means that undesired horizontal forces, possibly caused by the guiding system, are also included in the measured eccentricity.
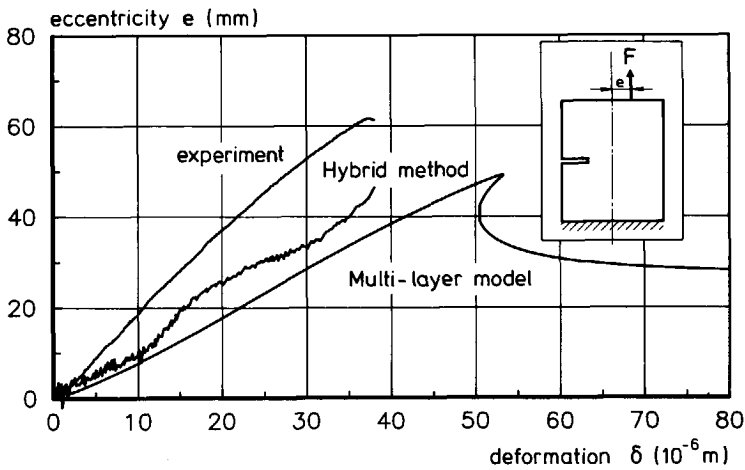
Figure 8.21   Measured and predicted eccentricity in the experiment on the single notched plate.

8.6 Concluding remarks

In this chapter, the correctness of the material model was verified by simulations of a number of four-point bending tests and of uniaxial tensile tests on single notched plates. In general, it can be concluded that the experimentally determined results could be predicted very well with the material model and the various simulation techniques. In the FE analyses, the best fit was found with input parameters that deviated slightly from those

determined in deformation-controlled uniaxial tensile tests on narrow specimens. In this respect it should be realized that there is always a scatter in the experimental results and that only a limited number of experiments were performed. Furthermore, the process of making a notch as well as the drying procedure used for the specimen (see also Section 7.5) may have caused initial cracking in front of the notch or elsewhere in the fracture zone. These effects, resulting in a less stiff and a less strong (lower peak load) behaviour, are not taken into account in the FE analyses. On the other hand, the predictions of stiffness and peak load by the hybrid method corresponded very well with the experimental results for the input obtained from the tensile tests.

A model similar to the simple model presented in Section 5.5 - referred to here as the multi-layer model - enabled a very good study to be made of the behaviour of the experiments investigated. Despite the large cross-sectional area in the tensile tests on the single notched plates several phenomena that occur could be demonstrated very well with the model, even for this type of test.

The results of the bending tests confirm that the tail of the stress-crack opening relation is much longer than defined in the CFM (see also Section 7.1). Therefore, for those analyses in which large crack openings are expected to occur, it is recommended that the σ-w relation should be extended by adding a linear curve as presented in Section 8.3 (see also inset in figure 8.11).

144

9   Fatigue analyses and experiments

9.1 Introduction

In this chapter the results of numerical fatigue analyses will be presented. First, in Section 9.1 the results of a few analyses with the FE code DIANA* will be discussed. These analyses were found to be quite time-consuming. However, analyses with the multi-layer model can be performed in a much shorter time period thanks to the simple way of modelling. Therefore, the multi-layer model is a very suitable tool for studying fatigue phenomena. An investigation will be into the extent to which fatigue results can be explained by the local approach applying the continuous-function model (Section 9.3). For the sake of clarity, only low cycle, high amplitude fatigue analyses were performed. For most analyses, the number of cycles to failure is so small that it would in fact be better to use the term repeated loading rather than fatigue. Nevertheless, the term fatigue will in general be used in the remainder of this chapter.

A limited number of tensile fatigue experiments were performed in order to study the relation between deformations in a quasi-static tensile test and in a tensile fatigue test. Results from these experiments are presented and discussed in Section 9.4.

9.2 Fatigue analyses with DIANA

The DIANA finite element code has been used to investigate the fatigue behaviour of a notched beam (Janssen[90]). Here, only some principal results will be presented. For the analyses, the beam with the 50 mm notch depth was taken. The same FE idealization as used in Chapter 8 (see figure 8.2) was applied, while the material parameters were also the same ($\upsilon = 0.2$, $f_t = 3.0$ MPa, $E_0 = 38000$ MPa and $G_F = 125$ J/m^2).

Load-deflection relations
The load-deflection relation for a continuously increasing deformation is plotted in figure 9.1 by the dashed line. For the force at peak load F_{max}, a value of 1292 N was found. For the purpose of the fatigue analysis, the load was applied by load steps (load-controlled). First, load steps up to a maximum of 95% of the peak load were performed. Subsequently, the beam was unloaded until zero load again, followed by a reloading up

---

to the same upper value of 0.95 F_{max}. For the unloading as well as for the reloading path, nine load steps of equal size were performed. This procedure was repeated until it was no longer possible to find a new equilibrium. It should be remarked that in the first part of the reloading curves it was in most cases not possible to reach the preset convergence criterion. However, this did not affect the rest of the results. The result of this analysis, as far as the load-deflection relation is concerned, can be seen in figure 9.1. It was found that 35 unloading-reloading loops could be performed, while in the subsequent reloading part it was not possible to find a solution at the upper load level. It can be assumed that for smaller loading steps the descending branch as found in the quasi-static analysis would have been reached at a load level smaller than F_{upp}. The conclusion from this is that the descending branch of a quasi-static analysis was an envelope curve and also formed the failure criterion for the fatigue loading.
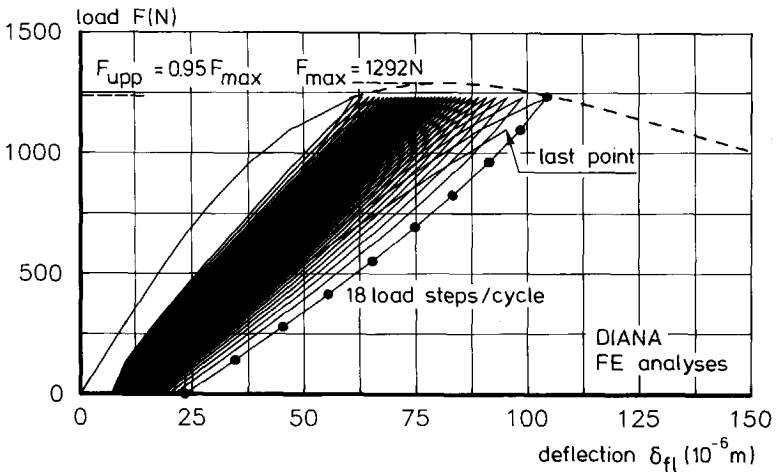
Figure 9.1   Load-deflection relations predicted by FE analyses.

Stress distributions

For a number of loops the stress distributions at the upper ($F= F_{upp}$) and lower ($F= 0$) load levels are plotted in figure 9.2. First of all, it can be seen that the length of the softening zone increases with the number of load cycles. Furthermore, the stress distributions at zero load show that major residual stresses are active after a preloading up to 95% of the maximum load. It appears that the tensile residual stresses in the centre part of the cross-section increase with the number of cycles performed.

146

Figure 9.2   Stress distributions at the upper and lower load level for a number of load cycles .

Cyclic creep curves

It is now interesting to see whether the deformation at the upper load level versus the number of load cycles shows the same specific shape (cyclic creep curve; see figure 2.8) as is known from fatigue experiments. In figure 9.3a, it can be seen that such a curve is indeed found. In two other analyses upper load levels of $0.999F_{max}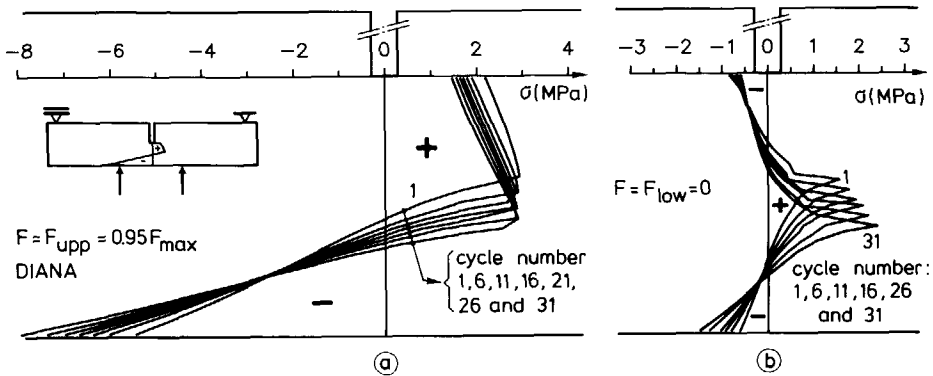$ and $0.906F_{max}$ respectively were applied. For the former one, only three loops could be performed, while the latter one was stopped after 25 loops when the increase of deformation per load cycle appeared to be very small. Though only a very limited number of analyses were performed, it is clear that the number of load cycles increases with a decreasing upper load level. A number of cycles were also performed for two analyses with the same upper load level ($F_{upp} = 0.954F_{max}$), but with different lower load levels. The results presented in figure 9.3b indicate that a decreasing lower load level is probably accompanied by a decreasing number of cycles to failure.

9.3   Fatigue analyses with the multi-layer model

The analyses made with the DIANA FE code and described in the previous section had already shown some promising results as far as the fatigue approach in this report is concerned. Though the analyses are quite time-consuming, the FE code can now be used to make further investigations of the fatigue behaviour of concrete. However, since the only intention is to study phenomena, the use of the multi-layer model for such a study is much more suitable, because the analyses are much less time-consuming. Therefore, a number of analyses were performed with that model. The results of these will be presented in this section. In figure 8.8 it was shown that the parameter l_f (length of the

147

fracture zone) in the multi-layer model specifically affects the load-deflection relation around peak load. Since the upper load level in fatigue experiments is generally represented by a percentage of the peak load in static tests, it should be obvious that a quantitative comparison with experimental results is in fact not possible. Despite this limitation the multi-layer model can very well be used, as will shortly be shown. First, some details are given about the analyses. Then the results of one particular analysis are discussed in detail. After that, the results of a number of analyses with different upper and lower load levels are presented.
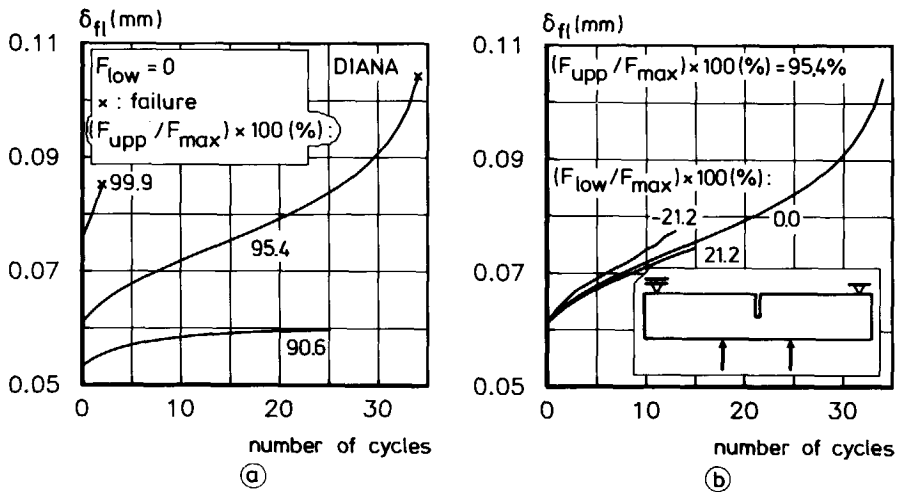

Figure 9.3 *Deflection at the upper load level versus number of cycles for constant lower load level (a) and constant upper load level (b) respectively.*

For all the analyses in this section, the chosen specimen type and material properties were the same as for the finite element analyses, i.e. four-point bending specimen with a 50 mm notch depth, E_o= 38000 MPa, f_t = 3 MPa and G_F = 125 J/m^2. The value for the length of the fracture zone l_f was chosen as equal to 35 mm, which was kept the same for all the analyses. Finally, it should be remarked that the procedure for inner loops was omitted in the analyses. This means, for instance, that if the deformation direction reverses within a loop from loading into unloading, the unloading curve of the previous load cycle is immediately followed. This simplification probably does not affect the results significantly, as will be discussed later on in this section.

For the principle of the multi-layer model, the reader is referred to figure 8.7. In the analyses, a number of iterative procedures are used. First of all, the stress for a certain layer pertaining to the deformation of that layer has to be determined by iteration.

148

Therefore, the crack opening is varied until the corresponding deformation differs by less than a certain tolerance value from the deformation of the layer. For this tolerance a value of 0.0001 μm is taken. The second iteration concerns equilibrium. For an average crack opening, which in fact is the control parameter in the analyses, the rotation φ is varied until the resulting normal force approaches zero. As stop criterion for this iteration, a value of 0.001 N is chosen. Since a deformation-controlled loading procedure is applied, the upper and lower load level must also be found by iteration, and in this case a tolerance of 0.1 N is used. Despite the relatively small values for the tolerances, it was possible to perform most of the analyses without interruption. Sometimes, however, it was not possible to keep within the tolerances. This sometimes occurred after reversal of the loading direction. In order to be able to continue the analyses in those cases, the maximum number of iterations was set as equal to 25 which - in the author's opinion - does not affect the results significantly. Finally, the analyses were performed with 100 layers. In other words: the critical cross-section (height = 50 mm) is subdivided into layers with a height h_i of 0.5 mm each.

Results of a specific experiment
For the structure under investigation a value of 1403.6 N was found for the peak load, F_{max}. For the fatigue analysis that is to be discussed, an upper load level of 0.94 F_{max} and a lower load level equal to zero were chosen. It appeared that 146 loops could be performed before the descending branch of the static test was reached. Three loops (1, 100 and 146 respectively) are plotted in figure 9.4. Due to the fact that in this analysis the average crack opening is used as control parameter, the number of load steps per loop varies during loading. The deformation-controlled manner of loading is also the reason
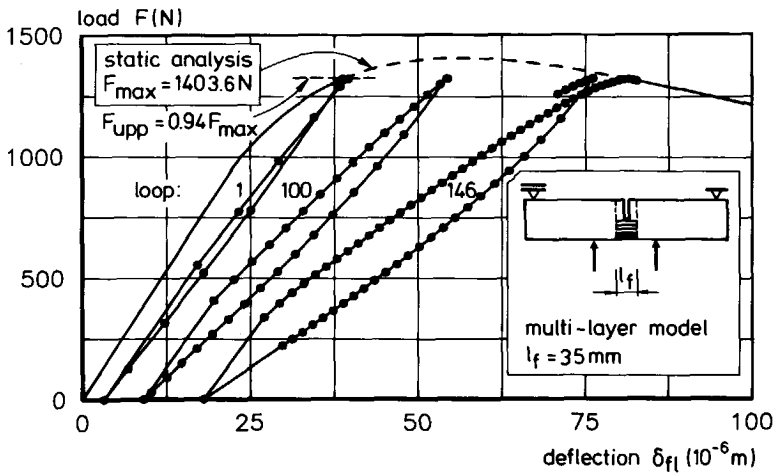

Figure 9.4   Load-deflection relations obtained with the multi-layer model.

why, in contrast to the finite element analyses which were load-controlled, the last loop continues directly with the descending branch of the static test.

In figure 9.5 it is shown how the stress distribution changes within an unloading-reloading cycle. Generally, the stress distribution varies gradually during unloading and reloading. In the first step, after reversal of the loading direction, the stress distribution in the softening zone changes slightly more abruptly. This result, which is shown most clearly for loading step 10, can be explained by the steep first part of the reloading curve in the CFM. Furthermore, it can be seen that, after unloading to a zero load level, significant stresses are still present in the specimen. Finally, when the upper stress level is reached again at loading point 17, the length of the softening zone and the deflection are slightly increased as compared with loading point 1. The increase per loop, however, is so small that it cannot be seen from this figure. For that purpose, the stress distributions at the upper load level for a number of loops are plotted in figure 9.6a. In figure 9.6b the stress distributions at the lower load levels are plotted. The similarity to the results obtained in the FE analysis (see figure 9.2) is evident.
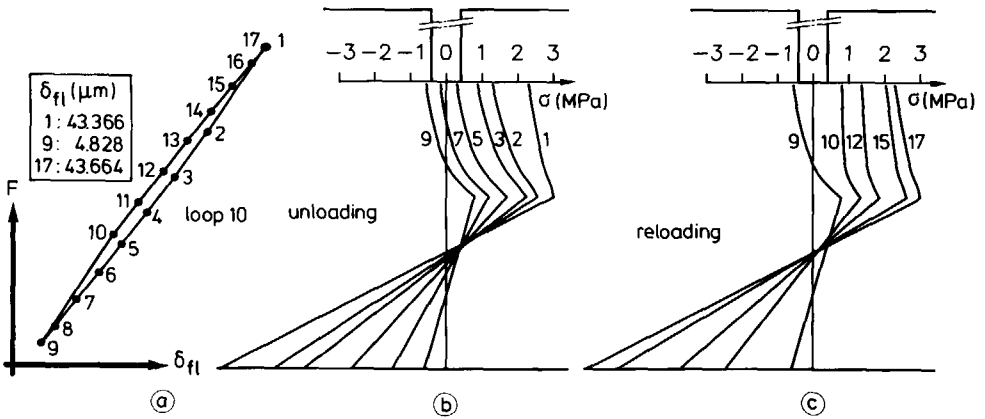
Figure 9.5   Stress distributions for a number of loading points within a loop (multi-layer model).

The development of four different parameters in relation to the number of cycles is plotted in figure 9.7. Similar to what was observed in the finite element analysis, the deflection versus the number of cycles displays a typical cyclic creep curve (figure 9.7a). The growth of the softening zone with the number of cycles can be seen in figure 9.7b. If this parameter is regarded as a crack length, then the resemblance with crack growth

150

curves for metals (see figure 2.12a) is clear. In fatigue compression tests, Holmen[79] observed that the secant modulus of elasticity decreases with the number of cycles (figure 2.9). A similar relation as noted in the compression tests is found for the development of the secant stiffness k_{sec} with the number of cycles (figure 9.7c). Finally, the area enclosed by a loop is sometimes also used as a parameter to show the development in fatigue tests. The development of the energy W with the number of cycles is plotted in figure 9.7d, with the energy being defined according to the schematic representation given in the inset of that figure. All four curves in figure 9.7 display three different stages, the second one of which is a linear relation like in cyclic creep curves.
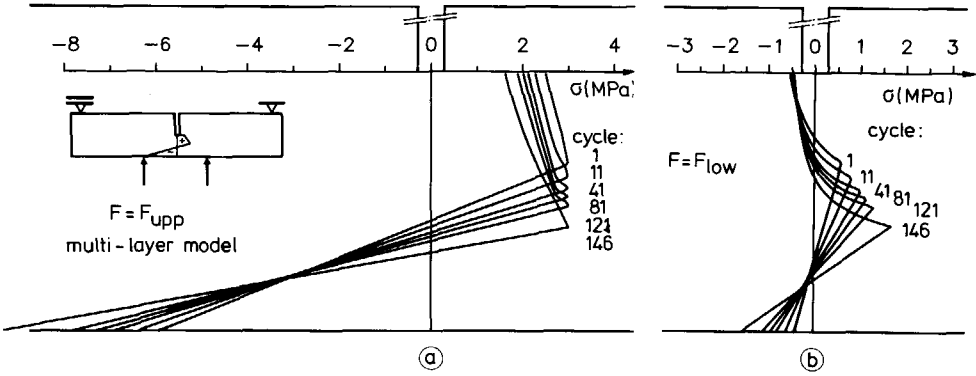

Figure 9.6   Stress distributions at the upper and lower load level for a number of loading cycles (multi-layer model).

Fatigue analyses with different load levels
A number of analyses were performed with different upper and lower load levels. For the upper load level, the values applied were equal to 99, 98, 97, 96, 95 and 94 per cent of the maximum load in a static test respectively, while for the lower load level -50, 0 and 50 per cent of F_{max} were used. The results of these analyses, plotted in S-N curves, can be seen in figure 9.8. Before disussing this result, a remark first has to be made about inner loops. For most of the analyses inner loops were not active. This means that in those analyses the crack opening increased in every loop for every layer in the softening zone. For the smaller upper load levels, especially for $F_{upp} = 0.94F_{max}$, inner loops were encountered. The occurrence of inner loops and the fact that damage in inner loops is not taken into account in the continuous-function model is probably the reason why analyses with smaller upper load levels could not be performed. In fact, after a number of cycles in such analyses, all the layers in the softening zone are in inner loops, which means that the deflection no longer increases with the number of cycles.
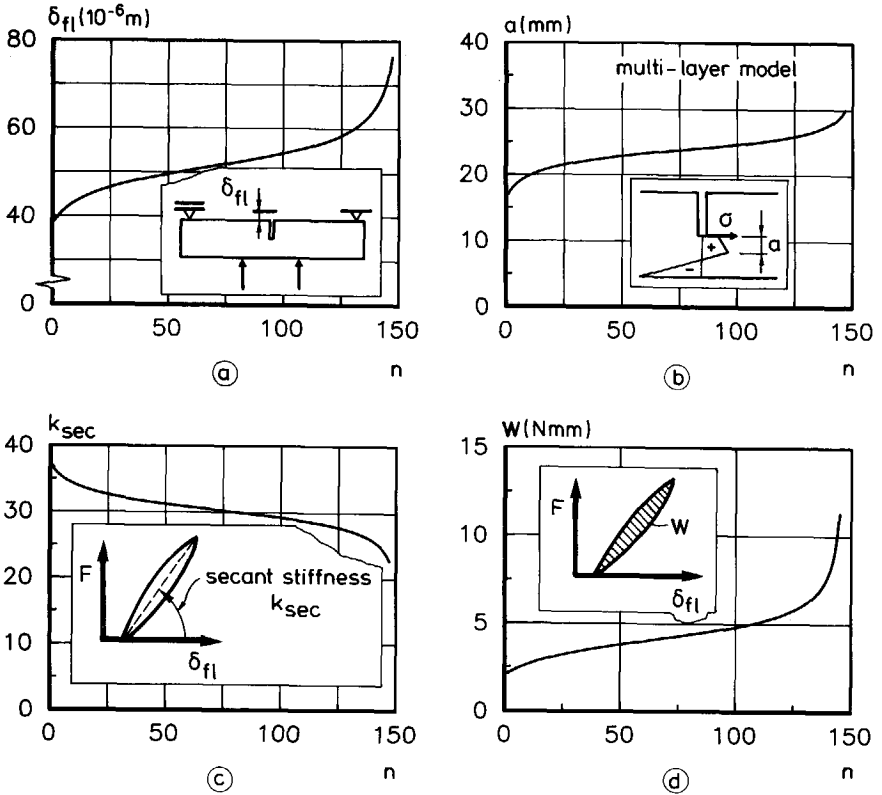
Figure 9.7   The variation of four different parameters: deflection (a), length of fracture zone (b), secant stiffness (c) and a parameter to represent the energy within a loop (d); in relation to the number of cycles.

As already mentioned above, the results of the analyses with the multi-layer model cannot be directly used for a quantitative comparison with experimental results. Nevertheless, see the inset in figure 9.8 for an illustration of the relation between the obtained results and experimental results. The straight line represents a regression equation of the S-N curve for flexural tension in the case of a zero lower load level (Cornelissen[84]). Experimental results are not available for load levels as applied in the analyses. Nor, as a matter of fact, is this possible, since in experiments the maximum load is not known exactly due to scatter in the results. Notwithstanding this, the results of the analyses will now be looked upon as fatigue results. The first noteworthy aspect is that the number of cycles plotted on a semi-logarithmic scale is almost linear, as is usually observed in fatigue tests. As far as the influence of the lower load level on the number of cycles to failure is concerned, a number of remarks can also be made. If the results for the lower load levels equal to 0 and $-0.5F_{max}$ are compared, then a decrease in the lower load level indeed

152

results in a smaller number of cycles to failure, as could be expected from the principle of the model. None the less, the two curves in figure 9.8 are almost parallel to each other, while in fatigue experiments the transition from a positive or zero lower load (or stress) level to a negative one is accompanied by a change in the slope of the S-N curve (see figure 2.6b). This result can be directly explained on the basis of the continuous-function model and the experimental results of post-peak cyclic tensile tests (Section 6.4 and figures 6.17 and 6.18). For the increase of crack opening as function of the lower stress
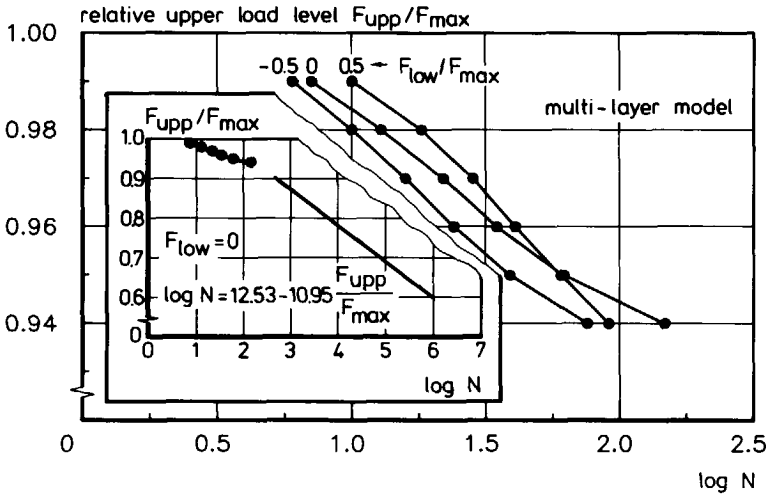

Figure 9.8   Results from the multi-layer model plotted as S-N curves.

level in the loop the experimental results show a discontinuity at a zero lower stress level. This discontinuity (a suddenly stronger increase in crack opening for negative lower stress levels) is not taken into account in the CFM. It can be expected that, once this part of the CFM has been improved so that it gives an even closer description of the experimental results, the results of fatigue analyses will also provide a better approximation of the experimental fatigue results. As regards the S-N curve for the lower load level equal to $0.5F_{max}$, a rather peculiar result is encountered. For the upper load levels equal to $0.95F_{max}$ and $0.94F_{max}$, N is smaller for the lower load level equal to $0.5F_{max}$ than for the zero lower load level. For a constitutive model that is based on a decrease in damaging effect with an increasing lower stress level, this result does not seem to be possible. However, the increase in crack opening (or increase in stress drop) depends not only on the lower stress level, but also on the crack opening of the point where the envelope curve is left. A close inspection of the CFM (see for instance figures 6.17a and 6.18a) shows that it may be possible that, despite a higher value for σ_L and a smaller w_{eu}, the increase

153

in stress drop may be greater (see figure 9.9). So far, the author believes that this is the reason for the observed result. Nevertheless, further investigations should clarify this peculiar result.
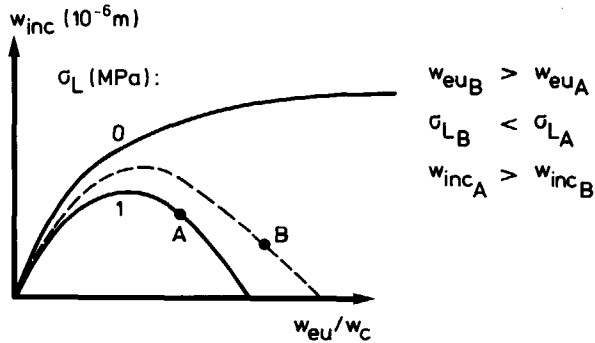

Figure 9.9   Schematic representation of a detail of figure 6.17a.

In figure 9.10a, the development of the deflection with the number of cycles is plotted for the analyses with a zero lower load level. The dots in the figure represent the deflection at the descending branch in the static test. For a decreasing value of F_{upp}, the maximum value of δ_{fl} increases. The number of cycles to failure, however, is predominantly determined by the slope of the secondary branch. In figure 9.10b, the influence of the lower load level is shown. For $F_{low}/F_{max}=-0.50$, the slope of the secondary branch is steeper than for the zero lower load level. The result for $F_{low}/F_{max}=0.50$ is related to the peculiar result of figure 9.8. Here, it can be seen that for the first 10 or so cycles, the increase in deflection is smaller than for the lower load level equal to zero, while for the following cycles this increase is greater.

Sequence effect
Finally, the multi-layer model is used to study the sequence effect. For this purpose an analysis was first made in which 74 cycles ($\approx 0.5N$) were performed at an upper load level equal to $0.94\ F_{max}$ (see figure 9.11). Subsequently, 30 cycles could be performed at an upper load level equal to $0.95\ F_{max}$, which is also equal to $0.5N$. This indicates that there is no sequence effect. For the reversed order of load application, a little increase in number of cycles could be observed. Though the difference is too small to allow strong conclusions, the observed difference may be partly explained by the fact that for the latter analyses, the descending branch is reached at a larger deflection (see dots in figure 9.11). In this respect the following further remarks can be made. The difference in the deflection at the descending branch is very small due to the very small difference in upper load level.
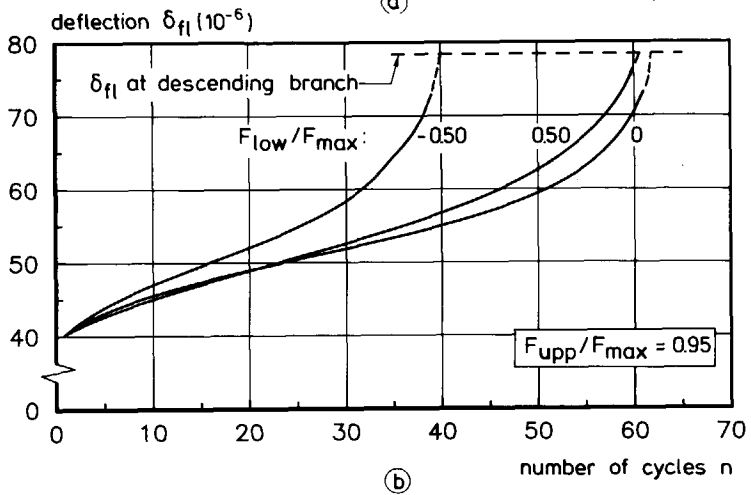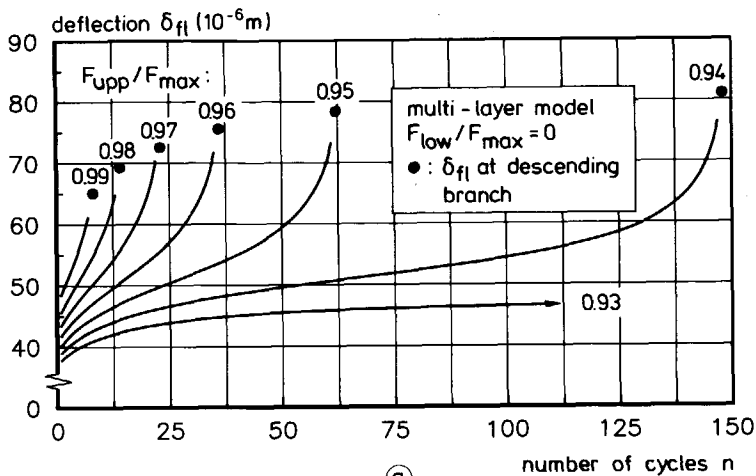
*Figure 9.10   Deflection versus number of cycles for a constant lower load level
(a) and a constant upper load level (b) respectively.*

For load levels as normally applied in fatigue experiments, this difference may be significantly larger. Therefore the author believes that this phenomenon, at least, contributes to the existence of a sequence effect. Secondly, it should be remarked that the above explanation means that a longer fatigue life will be encountered when first a number of load cycles are applied at a given upper load level, followed by cycles at a lower upper load level, compared with the reversed order of load application. This is contrary to what was observed for compressive tests (see Section 2.3). More research is required in order to explain this phenomenon.

155

Figure 9.11   Deflection versus number of cycles for two two-stage loadings.

Concluding remarks

From the analyses with the multi-layer model the following conclusions can be drawn. In general, the results of the fatigue analyses show qualitatively rather good similarity with results of fatigue experiments. For two aspects, both concerning the increase in crack opening w_{inc}, or stress drop $\Delta\sigma$, it was demonstrated how the CFM can be improved. With the CFM, only the fatigue behaviour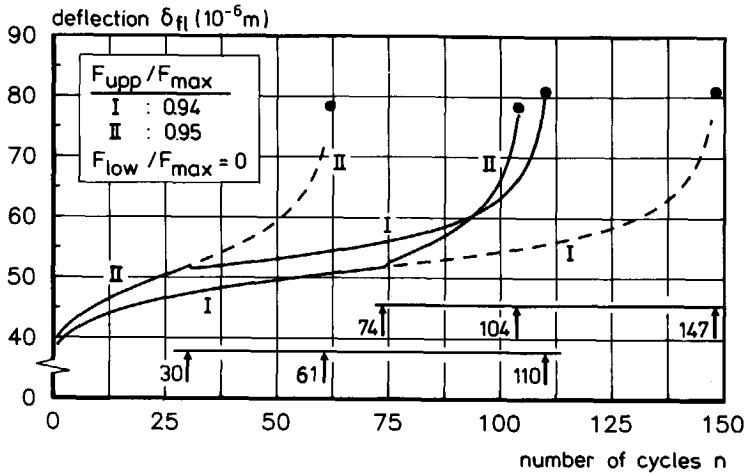 for very high upper load levels could be investigated so far. For a further study of fatigue along the lines of the approach used in this report, it will be necessary also to incorporate damage effects in inner loops. Therefore, damaging effects in inner loops for different parts in the loading history and different upper and lower stress levels must be studied accurately. In the author's opinion, this will not be easy due to the very small differences in deformations between subsequent loading cycles and limitations in measuring devices. Nevertheless, the author believes that this provides the best method for further study of the mechanism of fatigue. Another possibility is, of course, to assume a certain relation for the damaging effect in inner loops and to fit the results of fatigue analyses with fatigue experiments. Once the procedure for inner loops has been modified, analyses similar to those whose results are presented in this section can be performed for more ($<0.94F_{max}$) lower load levels.

9.4 Fatigue experiments

In order to investigate more thoroughly the development of deformations in a uniaxial tensile fatigue test, a limited number of these experiments were performed. With these experiments, it was mainly intended to compare deformations in a static test with those

156

in a fatigue test and to get an answer to the question of whether the descending branch in a static test is also the failure envelope in a fatigue test. Besides, the non-uniformity in crack opening in a fatigue test will also be demonstrated and some attention will be paid to the topics of sequence effect and remnant strength after cyclic preloading.

Details of the specially designed data-acquisition system are given in Section 4.5. The normal type of concrete was used. The properties of the fresh concrete and 28-day strength values can be obtained from Table A.3 in Appendix A. The age of the specimens varied between 84 and 127 days. Initially, it was intended to use unnotched specimens. The reason for that was that the process of localization in a fatigue test was also to be investigated. Notches in the specimens cause such a local increase in stress that one may not draw conclusions on the phenomenon of localization when notched specimens are used. Tests on unnotched specimens, however, are very difficult to perform. In most of the experiments, fracture occurred near a glue platen. Nevertheless, one fatigue experiment and one static experiment were successful. Furthermore, a number of fatigue experiments were performed on notched specimens. The applied upper and lower stress levels and the number of cycles to failure, N, can be obtained from Table 9.1. Additionally, four specimens were loaded under a continuous increasing deformation (denoted as static tests). The results of these tests will be used as reference for the fatigue tests.

Table 9.1 Upper and lower stress levels in the fatigue tests and number of cycles to failure.

experiment No.	notched/unnotched	σ_{upp} (MPa)	σ_{low} (MPa)	N
1	unnotched	2.51	-2.75	12812
2	notched	3.18	-5.30	86
3	notched	3.00	0.67	13026
4	notched	3.00	0.05	1951
5	notched	2.75	-5.20	2378
6	notched	2.69	-5.14	10784
7	notched	2.50	-4.82	50720

Localization; results of a particular experiment
For static tensile experiments it is now well-known that localization occurs. Fracture takes place in a small zone, the process zone, while the rest of the specimen behaves elastically. Now it is interesting to see how the same specimen behaves when it is loaded dynamically. Or in other words, we are interested in the question: "To what extent does fracture occur

in the total specimen?" In order to obtain some answer to this question, the results of the experiment on the unnotched specimen (No. 1) will now be shown.

In the experiment on the unnotched specimen, fracture fortunately occurred within the base of the 35 mm LVDTs. The number of cycles to failure was 12812. In figure 9.12a, the stress-deformation relation for a number of loops is plotted, while deformation is the average of the four 35 mm LVDTs. In the same figure the stress-deformation relation for the static test on the unnotched specimen is plotted. As can be seen the deformation at the upper stress level for the last loop that was recorded, more or less coincided with the descending branch of the static test. However, two remarks need to be made. First of all, it is not known whether the last recorded loop is also the last loop that was performed. There is a possibility that three more loops were performed. Since the increase in deformation is the greatest in the last loops, this may have a significant effect on the measured deformation at failure. In actual fact, the real value for the deformation at failure is equal to or larger than the last one recorded. The second remark concerns the result of the static test. Here, only the result of one experiment is shown. It should be borne in mind, however, that due to scatter, the position of the descending branch may vary significantly, especially in this part of the stress-deformation relation where non-uni-form crack opening occurs. This will become also clear from the results obtained on the notched specimens.
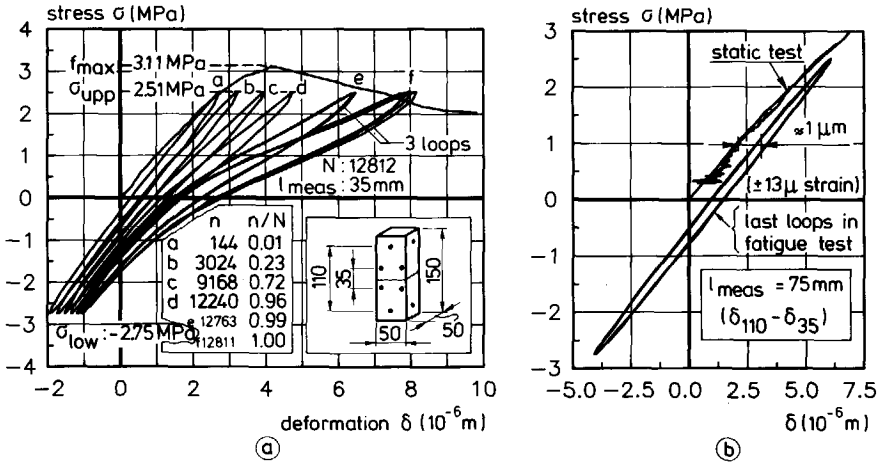

Figure 9.12   Stress-deformation relation from a static and a fatigue tensile experiment on an unnotched specimen.

In order to quantify the damage that occurred outside the final fracture zone, the deformations obtained with the 35 mm LVDTs were subtracted from the deformations

obtained with the 110 mm LVDTs. This results in a deformation pertaining to a measuring length of 75 mm (two parts of 37.5 mm each), which does not encompass the final fracture zone. It appeared that the shape of the stress-deformation curve of a loop varied only a little in the beginning of the test, while it remained more or less the same during the subsequent cycles to failure. The shape of the last cycles is shown in figure 9.12b. The irreversible deformation is about 1 µm, which is equal to about 13 µstrain. This result shows that also in a tensile fatigue test, fracture mainly occurs in a small zone. This can also be seen when the deformations at the upper stress level in a cycle are plotted versus the cycle ratio n/N (see figure 9.13). This figure also clearly shows that the largest part of increase in deformations in the fracture zone occurs during the last cycles before failure.
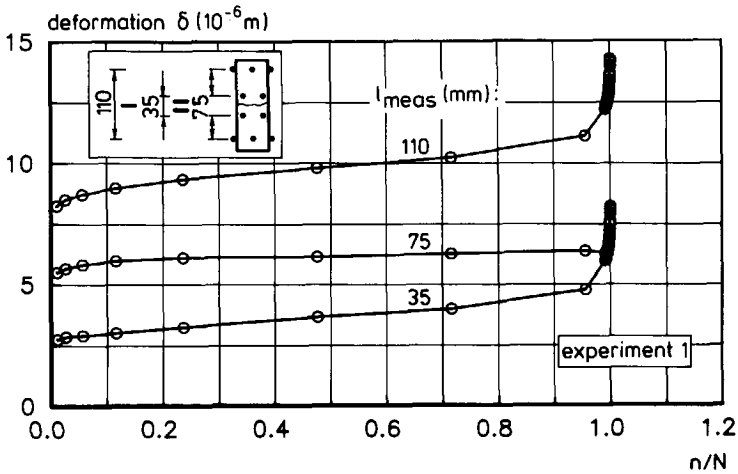
Figure 9.13   Deformations at the upper stress levels versus the cycle ratio.

The observed irreversible deformation outside the final fracture zone may be the result of distributed tensile cracking (figure 9.14a). In the author's opinion, however, it might also be possible that the loading in compression (σ_{low}= -2.75 MPa) contributed to this increase in deformation. The compressive loading in fact causes small micro-cracks in the vertical direction (figure 9.14b), reducing the stiffness of the concrete (see also Section 7.6). This phenomenon may also play an important role in the case where the deformation at the descending branch of a static test is compared with the deformation at failure in a fatigue test.

The result of the experiment on the unnotched specimen has also been used to calculate the development of the secant stiffness and the energy within a cycle respectively, with the cycle ratio. In figure 9.15, it can be seen that the obtained relations show

good similarity with those found in the fatigue analyses (figures 9.7c and 9.7d) and, as far as the secant modulus is concerned, with results from compressive fatigue tests (figure 2.9).
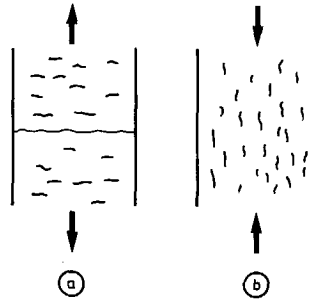
Figure 9.14   Possible micro-cracking due to tensile fatigue (a) and compressive (b) loading.

Non-uniform crack opening

In Chapter 5 the non-uniform crack opening in tensile experiments was investigated. There, the phenomenon was explained by a structural behaviour and it was surmised that it plays a role in many more tests on a softening material like concrete. One of these tests in which it can also be expected to occur is the tensile fatigue test. Therefore, the non-uniformity in crack opening in the fatigue experiments was also investigated. First, in figure 9.16, the deformation of the four 35 mm LVDTs is plotted separately for the experiment on the unnotched specimen. This figure already clearly confirms the existence of the phenomenon in tensile fatigue tests. While the deformation of LVDT 3 (for the

Figure 9.15   Secant stiffness (a) and energy within a cycle (b) versus cycle ratio.

160

position on the specimen, see the schematic representation in the inset) increases with the cycle ratio, that of LVDT 1 decreases. The figure in the inset shows how the fracture zone opens with an increasing number of cycles. Similar to figure 5.7, the non-uniform crack opening can be shown by the combination of the in-plane rotation (φ_{ip})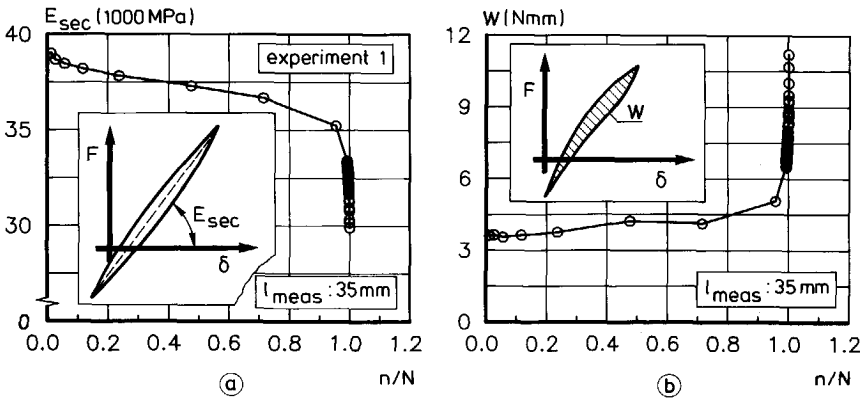 and the out-of-plane rotation (φ_{op}). This relation is plotted in figure 9.17. Also the combinations of φ_{ip} and φ_{op} pertaining to the last recorded upper stress levels in the tests with notched specimens are plotted in this figure. The similarity with results from static tests (figure 5.7) is rather good. The fact that the dots are much less well situated on one line than in the static experiments is again related to the fact that it is not clear whether the last recorded cycle is also actually the last cycle. In the static test, the crack opening will always reach its maximum non-uniformity, while for the described reason, this is not necessarily true in the fatigue tests. Nevertheless, if the result of test 5 is omitted, a more or less linear relation between the maximum values of φ_{ip} and φ_{op} can again be seen.
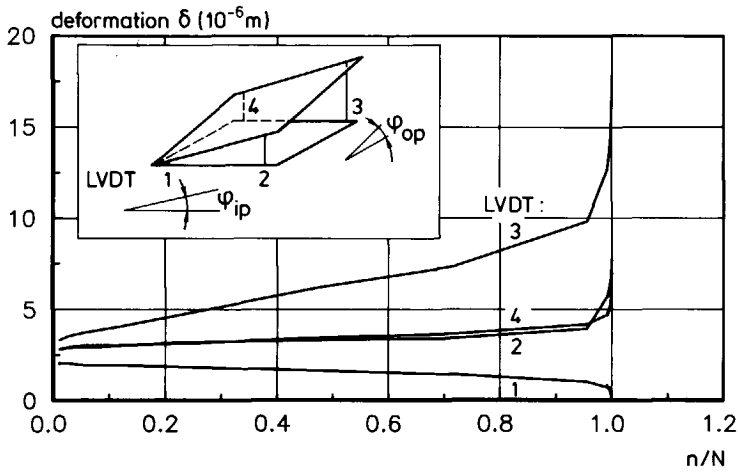
Figure 9.16   Development of the deformation of the four 35 mm LVDTs with the number of cycles.

Deformations in a static test versus deformations in a fatigue test
For the experiment on the unnotched specimen, it was found that the descending branch of the static test coincided more or less with the failure point in the fatigue test. Now the same comparison of deformations will be made for the notched specimens, while the relation between characteristic points in the cyclic creep curve and the stress-deformation relation will also be investigated. First, however, the results of the static tests which serve as a reference will be presented.

The stress-deformation relations for the four static experiments are plotted by the thin lines in figure 9.18. As can be seen, a rather significant scatter can be observed in the descending branches. However, this scatter is no larger than that found in previous experiments (compare figure 6.4). The thick solid line represents the average of the four separate tests and will be used for comparisons with fatigue results in the remainder of this section. The thick dashed line relates to the test on the unnotched specimen. No significant difference from the average curve for the notched specimens can be seen.
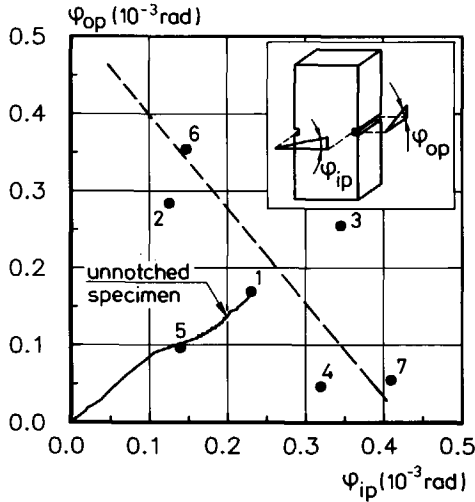
Figure 9.17   Combinations of maximum in-plane and out-of-plane rotations in the tensile fatigue tests.

Previously in this report, fairly substantial differences in values for Young's modulus were reported. One explanation for this result was that Young's modulus was not always determined in the same way (see also Section 7.1 and Appendix A). Furthermore, it was realized that the rather small specimens with the notches are not suitable for the determination of Young's modulus. Nevertheless, in Section 8.1, a fairly considerable difference ($\approx$ 16 %) was found between Young's modulus calculated with the 110 mm LVDTs and that belonging to a 75 mm base. Since an experimental result from an unnotched specimen is now available, it can be investigated to what extent the notches may have contributed to the observed difference. Therefore, in Table 9.2, the values for E_0 are compared. As can be seen, the value for the 75 mm base is significantly larger ($\approx$ 8%) than for the 110 mm base in the case of notched specimens. Though the observed difference is still not as much as found in the experiments in Section 8.1, it is demonstrated that the notches are for a large part responsible for the differences in Young's modulus

162

for the 110 mm and the 75 mm base. This probably also has to do with the position of the 35 mm LVDTs on the specimen; near the notches. The fact that the values for the 110 mm base of the notched and unnotched specimen are equal is accidental. Of course, for exactly the same concrete, a difference in these values will also be found.
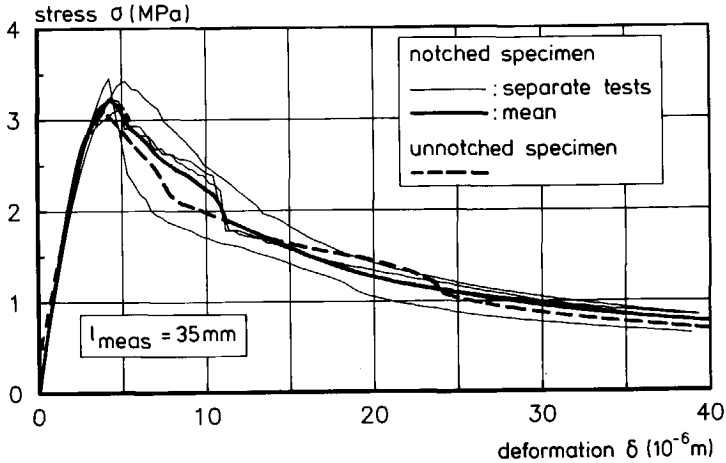
Figure 9.18   Stress-deformation relations obtained in the static tests.

Now the relation between deformations in a fatigue experiment and in a static test will be shown. In the upper part of figure 9.19, the average σ-δ relation for the static experiments is plotted, while in the lower part of the same figure, the cyclic creep curve for fatigue test 7 is plotted in such a way that the axes for the deformation correspond. Characteristic points in the cyclic creep curve denoted as B, C and D are projected in the σ-δ diagram. Similarly, the points B, C and D for all the fatigue experiments are plotted in figure 9.20. No distinct relation can be obtained from the results. Nevertheless, the following remarks can be made. Except for the result of the unnotched specimen, the deformation at failure in the fatigue experiments is larger than the deformation for σ_{upp}

Table 9.2   Young's moduli (in MPa) from notched specimens as compared with those from the unnotched specimen.

measuring length (mm)	notched specimens (mean of four experiments)	unnotched specimen
110	35300	35320
75 (=110-35)	38060	35980

163

at the descending branch in the static experiments, even if the scatter in the static experiments is taken into account. This result may also suggest that in this case the notches play an important role. Further research should clarify to what extent the notches are responsible for the observed results.
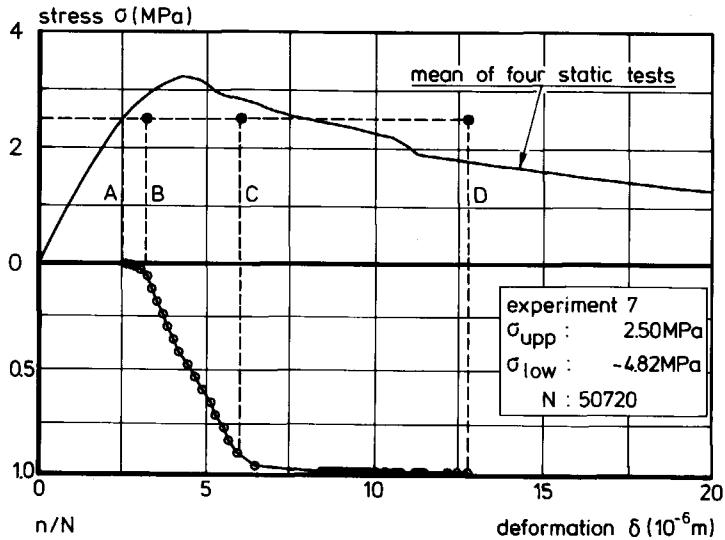
Figure 9.19   Average stress-deformation relation of the static tests and the cycle ratio versus deformation of fatigue test 7.

Furthermore, the remark made previously about deformations in the bulk of the specimen due to compressive loading should be kept in mind when interpreting these results. The points C indicating the ending of the secondary branch in the cyclic creep curve do not give a decisive answer to the question of whether this point coincides with the deformation at peak load in static tests, as was assumed by Balázs[86] for the stress-slip behaviour of a bar pulled out of the concrete. In the author's opinion, however, there are several reasons why such a relation is not possible in these experiments. The main reason is that the deformation at peak load depends on the measuring length; elastic deformation (see figure 2.5), while the deformation at point B is partly due to elastic deformation and partly due to the opening of the crack or process zone, which is independent of the measuring length. Therefore, if there is a criterion based on a deformation marking the end of the secondary branch in the cyclic creep curve, it will be related to a crack opening.

Relation between cyclic strain rate and number of cycles to failure
Previous investigations have demonstrated a strong linear relation between the strain rate in the secondary branch $\dot{\varepsilon}_{sec}$ and the logarithm of the number of cycles to failure (see figure 2.10). In the experiments described here such a linear relation was also found, as can be seen in figure 9.21. Based on the fact that localization also occurs in the fatigue experiments, as demonstrated in this section, it can be assumed that there is a unique relation between the increase of crack opening per cycle and the number of cycles to failure, rather than between the strain rate and the number of cycles to failure.
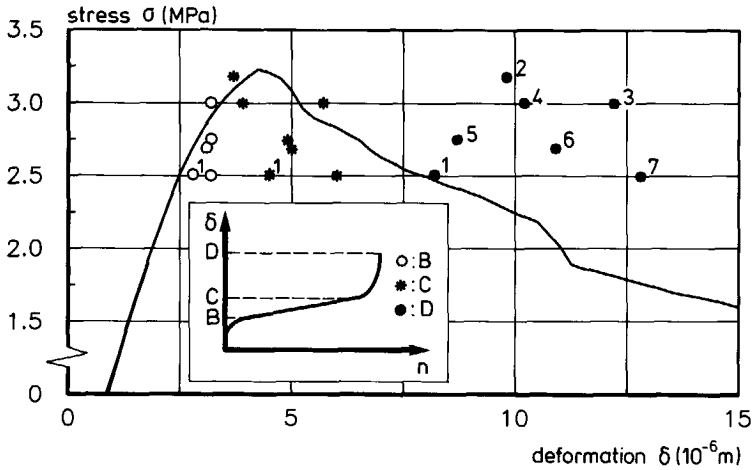
Figure 9.20   Characteristic points in the cyclic creep curves of fatigue tests, compared with the average σ-δ relation of the static test.

Sequence effect and remnant strength
Via two other experiments, which are not included in Table 9.1, it was intended to investigate the phenomenon of sequence effect. For that purpose a two-stage fatigue loading was performed. In the first stage of experiment A (see figure 9.22), the stress levels were chosen as equal to those of experiment 3. In this respect it should be mentioned that it was not possible to install the actual average stress levels exactly. Therefore, the stress levels deviated a little, as can be seen in the inset of figure 9.22. In the first stage, 5000 cycles were performed, after which the test was stopped and restarted with an upper stress level equal to 2.68 MPa and a lower stress level equal to 0.00 MPa. Unfortunately, fracture occurred near one of the glue platens after about another 20000 cycles had been performed. In experiment B, the reversed order of load application was applied. The relation between strain and the number of cycles can be seen in figure 9.22. Despite the fact that the upper stress level in the first 5000 cycles was lower than in

experiment A, the increase in deformation is greater. So far it is not clear whether this result is due to σ_{low}, which is lower than for experiment A, or due to scatter in the results. It may be clear that this single test result, with a relatively low number of cycles and involving stress levels which do not differ too much between the two stages of loading, cannot be used to draw strong conclusions. Nevertheless, the development of deformation with the number of cycles gives the impression that, for the applied stress ranges, a high σ_{upp} followed by a lower σ_{upp} leads to a longer fatigue life than the reversed order of load application, which is contradictory to what was observed in compressive fatigue tests (Section 2.3). In the author's opinion, more research is required in order to gain a better insight into the sequence effect in fatigue behaviour. The fatigue model presented in this report is a good tool for such a study, in which the influence of the lower stress level should also be taken into account.
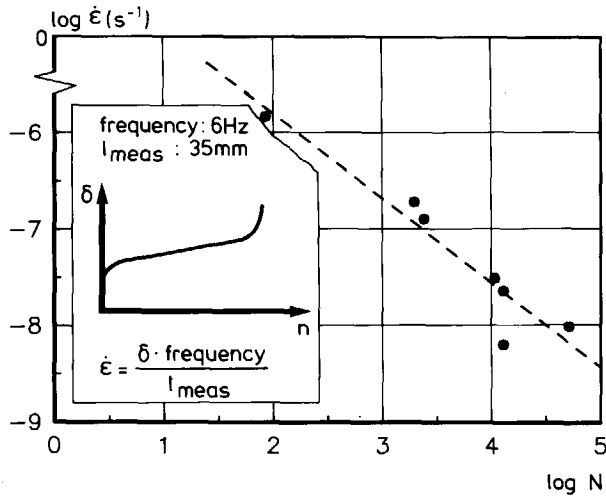
Figure 9.21   Relation between cyclic strain rate and number of cycles to failure.

Experiment B in figure 9.22 was unloaded after 25000 load cycles. Subsequently, the same specimen was loaded statically. The total result of this test in a stress-deformation diagram is plotted in figure 9.23. Compared to the average curve for the non-preloaded specimens (dashed line), a small increase in maximum stress can be observed. However, this increase still lies within the scatter band of the separate results. A comparison of the two pre-peak parts of the curves further shows that the nonlinearity just before peak load is much less for the specimen that was cyclically preloaded. The observed phenomena are in agreement with what was also found in compressive fatigue experiments (see

166

Section 2.3). Though no clear evidence is available yet, the author has the following explanation for these phenomena. In Section 7.1, the influence of non-uniform stress distributions on the σ-δ relation in a uniaxial tensile test was discussed. These non-uniform stress distributions, for which several causes may exist (see, for instance figure 7.1), result in a lower maximum load and an increased pre-peak nonlinearity. These are exactly the two phenomena that can be observed in the non-preloaded specimen as compared with the preloaded specimen. Or, put in another way, non-uniform stresses, like eigenstresses due to differential shrinkage in a virgin specimen cause the different areas in the fracture zone to reach their peak load one after another. Due to the cyclic preloading, some micro-cracking may have occurred in the most stressed regions, resulting in stress redistribution. These micro-cracks may have very locally decreased the strength of the concrete slightly. That, however, is outweighed by the increase in maximum load that is attained by the more uniform stress distribution that was reached after stress redistribution. In this respect, one need not only think of initial stresses at the macro-level, as discussed in Section 7.1, but also of such stresses at the micro-level.
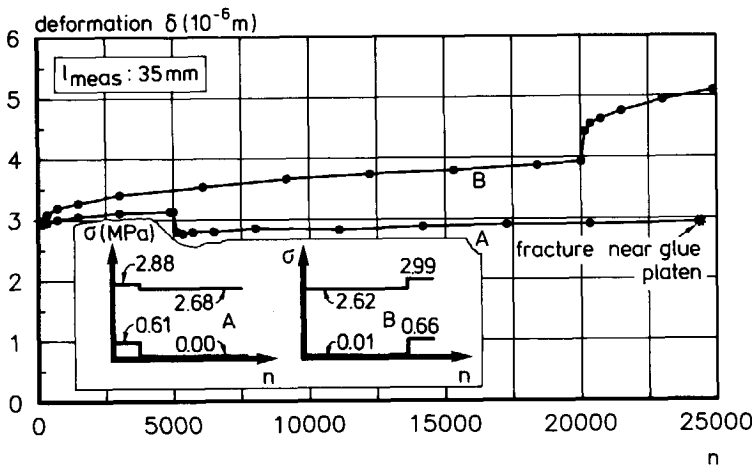
Figure 9.22 Deformation versus number of cycles for two two-stage loading experiments.

The fact that the descending branch of the preloaded specimen is positioned more to the right than that of the nonpreloaded specimens is in agreement with the results of the fatigue tests. As last notable point in the σ-δ curve of the preloaded specimen in figure 9.23 concerns the small nonlinearity in the first part of the solid curve. This is in agreement with the reloading curves in the post-peak cyclic region (compare figure 6.16).
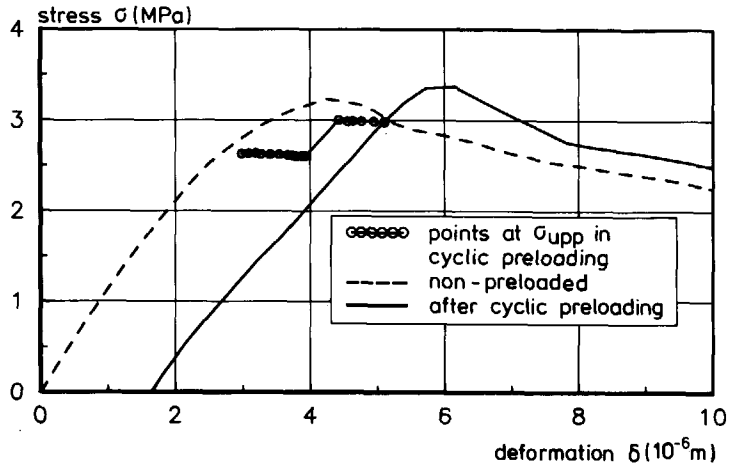
*Figure 9.23   Stress-deformation history for the cyclic preloaded specimen
compared to the average σ-δ relation of non-preloaded specimens*

Concluding remarks

Summarizing the results of the fatigue experiments in this section, the following main conclusions can be drawn:

– The specially developed data-acquisition system is suitable for studying the tensile fatigue behaviour more thoroughly.
– Tensile fatigue failure is a local phenomenon like tensile failure in a static experiment.
– The non-uniform crack opening that is the result of a structural behaviour has also been demonstrated for tensile fatigue experiments.
– As regards a failure criterion based on deformations, sequence effect and remnant strength, more research is required before conclusions can be drawn about the mechanisms which occur.

168

10 Retrospective view and concluding remarks

The importance of fracture mechanics for concrete building practice is more and more recognized nowadays. As a result, many investigations deal with this topic at the moment. In this report, a fracture mechanics approach is applied to study the fatigue behaviour of plain concrete. Furthermore in this report, much attention is paid to the tensile behaviour of concrete, which was to some extent part of the fatigue approach. Finally, the fact that experimental results can be blurred by several effects is raised for discussion in several sections of this report. Now, these three main lines of this report will be further elaborated in the reversed order. Then some remarks will be made about the applied experimental techniques and numerical analyses and finally some main conclusions will be drawn.

Experimental results blurred by several phenomena
Generally, analyses are performed to study the behaviour of structures. Input for these analyses are the material properties of the components of the structure. In order to obtain these material properties, experiments are performed mostly on relatively small specimens. Then, with some assumptions, the material properties are deduced from these experiments. The same approach is applied in this report as far as the tensile behaviour of concrete is concerned. In the author's opinion, this method is suitable for obtaining material properties that approximate the real material properties. Nevertheless, this procedure cannot be applied unrestrictedly. One should always realize that the specimen in the experiment in turn behaves as a structure. For the tensile experiments, several effects that can affect the experimental results have been investigated in this report. These effects include: the non-uniform crack opening in uniaxial experiments on a softening material (Chapter 5), the influence of initial stresses, like those due to differential shrinkage, on the σ-δ relation (Sections 7.1 and 7.5) and the effect of the notches (Section 9.4). If the influence of these phenomena on the obtained results is not taken into account, then it may be possible that a deduced material property differs strongly from the actual one. In the author's opinion, not enough attention is paid to these phenomena in many investigations. Nevertheless, despite all this, it is still possible to approximate the real material property fairly well.

Softening behaviour of concrete
Together with the increasing interest in fracture mechanics of concrete, as stated in the beginning of this chapter, there is an increase in the number of investigations aimed at determining the softening behaviour of concrete. In this report the softening behaviour (stress-crack opening relation) is determined by means of deformation-controlled uniaxial tensile tests. In the proposed relation (eq. 6.1), the tensile strength and the fracture energy are the input material variables. By comparing a number of experimental results

from the literature (Section 6.3), it was observed that the shape of the softening curve (stress normalized by f_t and crack opening normalized by $w_c = 5.14G_F/f_t$) does not differ significantly between the different investigations, even if other types of concrete, like lightweight concrete, are included and is very well described by the proposed relation. In this respect, however, it should be noted that special attention must be paid to the correct procedure of calculating G_F. The numerical analyses in Chapter 8 support the conclusion that the proposed softening relation describes the material behaviour properly. One restriction has to be made as far as the tail of the stress-crack opening relation is concerned (Sections 7.1 and 8.3). However, this is not important for most analyses of concrete structures.

While fracture mechanics are being applied more and more, especially by means of FE analyses, there is a lack of information as regards the influence of different variables on the fracture mechanics parameters. In this report, attention is paid to fracture mechanics parameters in relation to the variables: type of concrete, maximum aggregate size, concrete quality, water-cement ratio, curing condition (water content) and compressive preloading.

As compared to the softening behaviour of concrete for monotonic increasing deformation, its behaviour during unloading and reloading has so far received rather limited attention. The continuous-function model that has been proposed in this report appeared to describe the experimental results rather well. A flow chart of the model is presented, which makes it fairly simple to implement as a mathematical subroutine in numerical programs. With only the two material parameters, tensile strength and fracture energy, the complete unloading-reloading behaviour of the tensile as well as the tensile-compressive region is determined. Further research should clarify whether the model without adaptations can also be applied to other types of concrete. A promising thing in this respect is the fact that experimental results of some other investigations could also be predicted rather well.

Model for the fatigue behaviour of concrete
The numerical analyses of the four-point bending beams under repeated loading showed promising results, as far as the fatigue approach based on the uniaxial post-peak cyclic behaviour is concerned. Qualitatively, the fatigue results, like cyclic creep curves and S-N curves showed good similarity with those usually found in fatigue experiments. So far, only low cycle high amplitude fatigue could be investigated. In order to enable high cycle low amplitude fatigue to be studied as well, it is necessary also to include damaging effects in inner loops. Furthermore, it can be expected that for a quantitative comparison with experimental results, time effects should also be taken into account.

170

The approach to fatigue of plain concrete as a local phenomenon was supported by experimental results of a fatigue test on an unnotched specimen, where fracture also occurred mainly locally.

The fatigue model is presented on a macro-level and becomes active as soon as a softening zone exists in the structure. Generally, cracks or softening zones occur in concrete structures, so that the process of stress redistribution will take place in most structures when the loading varies in time. In the author's opinion, a similar model can be applied on a meso-level, where stress concentrations and micro-cracks or softening zones occur in the vicinity of aggregates.

Experimental techniques and numerical analyses
Special requirements had to be fulfilled in order to detect the loops in fatigue experiments properly. By applying some special techniques, it appeared possible to obtain this information. Deformations in the order of magnitude of 0.05 μm were measured, while the test ran with a frequency of 6 Hz, which can be regarded as rather advanced for experiments on concrete.

For a proper analysis of structures, it is necessary to apply sophisticated numerical programs like FE codes. In this report, the FE code DIANA was successfully applied on several occasions. If it is only intended to study phenomena, then it might sometimes be very suitable to apply a cruder, but very simple model. An example of such a model is the simple numerical model in Section 5.5 and the multi-layer model in Chapters 8 and 9. After the numerical results of the model have first been checked against those of FE analyses, and after the influence of model parameters (length of fracture zone in the multi-layer model) on the results has been investigated, the model can very well be used to perform a parameter study.

Main conclusions
Based on the investigations of the tensile and fatigue behaviour of plain concrete that have been reported, the following main conclusions can be drawn:

– Deformation-controlled uniaxial tensile tests on softening materials are accompanied by a structural behaviour, which is related to a bifurcation problem and causes non-symmetry, despite symmetry in specimen shape and load application.
– The continuous-function model provides a proper description of the complete tensile and tensile-compressive behaviour of concrete.
– The local approach to fatigue of plain concrete showed very promising results and offers good prospects for further research in this direction.

171

Notation

The following symbols are used in this report:

A	=	cross-sectional area, energy	LC	=	lightweight concrete
a	=	crack length, length of process zone	LVDT	=	linear variable differential transducer
b	=	width	M	=	moment
C	=	stiffness	N	=	number of cycles to failure, normal force
c	=	coefficient			
CFM	=	continuous-function model	n	=	number of cycles, number of elements
d	=	diameter,depth			
DCB	=	double cantilever beam	NC	=	normal-weight concrete
E	=	Young's modulus	S	=	relative stress level
e	=	eccentricity	s	=	slip
exp	=	experiments	t	=	thickness
F	=	force, load	W	=	energy
f	=	strength	w	=	crack opening, width
FE	=	finite element	z	=	distance
FPM	=	focal-point model	α	=	coefficient, coefficient of expansion
FRC	=	fibre reinforced concrete			
G	=	energy	β	=	coefficient
H	=	horizontal force	σ	=	stress
h	=	height	δ	=	deformation, displacement
I	=	moment of inertia	ε	=	strain
K	=	stress intensity factor	ε̇	=	strain rate
k	=	stiffness	τ	=	shear stress
l, l	=	length	φ	=	rotation
LAB	=	laboratory	ω	=	frequency

Subscripts

b	=	bending	cr	=	crack
c	=	compressive, critical	d	=	dissipated
calc	=	calculated	el	=	elastic
cc	=	cube compressive	er	=	envelope reloading
ch	=	characteristic	eu	=	envelope unloading
ck	=	cube characteristic	ext	=	external
cp	=	compressive preloading	inc	=	increase

172

int	=	internal	o	=	initial, stress free
ip	=	in-plane	op	=	out-of-plane
irr	=	irreversible	peak	=	peak
F	=	fracture	r	=	rotational, residual
f	=	fracture zone	ref	=	reference
fl	=	flexural	s	=	secant
L	=	lower	sec	=	secondary
low	=	lower	t	=	tensile, translational
m	=	mean	T	=	temperature
max	=	maximum	upp	=	upper
meas	=	measuring			
min	=	minimum	σ	=	stress

Superscripts

exp	=	experiment
+	=	positive
-	=	negative

REFERENCES

Alvaredo, A.M. and Torrent, R.J. (1987) The effect of the shape of the strain-softening diagram on the bearing capacity of concrete beams. *RILEM Materials and Structures*, 20(120), pp 448-454.

Balázs, G.L. (1986) Bond behaviour under repeated loads. *Studi e Ricerche*, 8, pp. 395-430.

Barenblatt, G.I. (1962) The mathematical theory of equilibrium cracks in brittle fracture. *Advances in Applied Mechanics* ,7, pp. 55-129.

Bascoul, A., Kharchi, F. and Maso, J.C. (1989) Concerning the measurement of the fracture energy of a micro-concrete according to the crack growth in a three points bending test on notched beams. In *Fracture of Concrete and Rock* (Eds. S.P. Shah and S.E. Swartz), Springer-Verlag, pp. 396-408 .

Bazant, Z.P. and Oh, B.H. (1983) Crack band theory for fracture of concrete. *RILEM Materials and Structures*, 16(93), pp. 155-177.

Bazant, Z.P. (1984) Size effect in blunt fracture: concrete, rock, metal. *ASCE J. Engineering Mech.*, 110(4), pp 518-535.

Bazant, Z.P. and Prat, P.C. (1988) Effect of temperature and humidity on fracture energy of concrete. *ACI Materials Journal*, 4, pp. 262-271.

Blakey, F.A. and Beresford, F.D. (1955) A note on the strain distribution in concrete beams. *Civil Eng. and Public Works Review* (London) V.5o.

Bonzel, J. (1970) Einfluss der Nachbehandlung und des Feuchtigkeitszustandes auf die Zugfestigkeit des Betons. *Betontechnische Berichte 1970* (Ed. K. Walz), pp. 99-132.

Brameshuber, W. (1988) Bruchmechanische Eigenschaften von jungem Beton. *Doctoral Thesis*, University of Karlsruhe, Report 5, 233 pp.

Brühwiler, E. (1987) Experiments on the influence of compressive preloading on the behaviour of dam concrete in tension at high strain rates. *Test report*, LMC, Swiss Federal Institute of Technology, Lausanne (in German).

Brühwiler, E. (1988) Fracture mechanics of dam concrete subjected to quasi-static and seismic loading conditions. *Doctoral Thesis* No. 739, (LMC) Swiss Federal Institute of Technology, Lausanne, 169 pp. (in German).

Brühwiler, E. and Wittmann, F.H. (1990) Failure of dam concrete subjected to seismic loading conditions. *Engineering Fracture Mechanics*, 35(1/2/3), pp. 565-571.

174

Budnik, J. (1985) Bruch- und Verformungsverhalten harzmodifizierter und faserver-stärkter Betone bei einachsiger Zugbeanspruchung. *Doctoral Thesis*, Ruhr University, Bochum, 180 pp.

CEB (1988) Fatigue of concrete structures; State of the art report. *CEB Bulletin* No. 188.

CEB-FIP Model Code 1990 (1988) First Predraft; Chapters 1-5. *CEB Bulletin* No. 190a.

CEB-FIP Model Code 1990 (1990) First Draft; Chapters 1-5. *CEB Bulletin* No. 195.

Cook, D.J. and Chandaprasirt, P. (1981) Influence of loading history upon the tensile properties of concrete. *Mag. of Concrete Res.*, 33(116), pp. 154-160.

Cornelissen, H.A.W. (1984) Fatigue failure of concrete in tension. *Heron*, 29(4), 68 pp.

Cornelissen, H.A.W. and Siemes, A.J.M. (1985) Plain concrete under sustained tensile or tensile and compressive fatigue loadings. In *Proc. BOSS Conf.*, Elsevier, pp. 487-498.

Cornelissen, H.A.W., Hordijk, D.A. and Reinhardt, H.W. (1986a) Experimental deter-mination of crack softening characteristics of normalweight and lightweight concrete, *HERON*, 31(2), pp. 45-56.

Cornelissen, H.A.W., Hordijk, D.A. and Reinhardt, H.W. (1986b) Experiments and theory for the application of fracture mechanics to normal and lightweight concrete. In *Fracture Toughness and Fracture Energy* (Ed. F.H. Wittmann), Elsevier, pp. 565-575.

Cornelissen, H.A.W. and Reinhardt, H.W. (1986c) Effect of static and fatigue preloading on the residual strength and stiffness of plain concrete. In *Fracture Control of Engineering Structures* (Eds. H.C. van der Elst and A. Bakker), Vol. III, pp. 2087-2103.

Cornelissen, H.A.W. (1986d) State of the art report on fatigue of plain concrete. *Stevin report* 5-86-3, Delft University of Technology, 62 pp. and Chapter 3 "Fatigue perfor-mance of concrete", *CEB Bulletin* No. 188.

Cornelissen, H.A.W. (1988) Fatigue performance of concrete. *CEB Bullutin* No. 185, pp. 147-155.

CUR (1983) Fatigue of concrete, part 1: Compressive stresses. *CUR-VB report 112* in co-operation with MaTS-IRO, 80 pp. (in Dutch).

CUR (1984) Fatigue of concrete, part 2: Tensile and tensile-compressive stresses. *CUR-VB report 116* in co-operation with MaTS-IRO, 83 pp. (in Dutch).

CUR (1988) Fatigue of concrete, part 3: Tensile and tensile-compressive stresses (2). *CUR report 137* in co-operation with MaTS-IRO, 90 pp. (in Dutch).

CUR (1989) Fatigue of concrete, part 4: Random compressive stresses. *CUR report 150*, in co-operation with MaTS-IRO (in Dutch).

Curbach, M. (1987) Festigkeitssteigerung von Beton bei hohen Belastungsgeschwindigkeiten. *Doctoral Thesis*, University of Karlsruhe, Report 1, 154 pp.

De Borst, R. (1986) Non-linear analysis of frictional materials. *Doctoral Thesis*, Delft University of Technology, Delft, 140 pp.

Delibes Liniers, A. (1987) Microcracking of concrete under compression and its influence on tensile strength. *RILEM Materials and Structures*, 20(116), pp 111-116.

Duda, H. and König, G. (1990) Rheological model for the stress-crack-width relation of concrete under monotonic and cyclic tension. Preprints *Fracture Behaviour and Design of Materials and Structures* (Ed. D. Firrao), Vol. II, pp. 585-594.

Duda, H. (1991) Grain-model for the determination of the stress-crack-width-relation. In Analysis of Concrete Structures by Fracture Mechanics (Eds. L. Elfgren and S.P. Shah), pp. 88-96.

Dugdale, D.S. (1960) Yielding of steel sheets containing slits. *Journal of Mechanics and Physics of Solids*, 8, pp. 100-104.

Eligehausen, R. and Sawade, G. (1985) Verhalten von Beton auf Zug. *Betonwerk und Fertigteil-Technik*, 5, pp. 315-322.

Evans, R.H. and Marathe, M.S. (1968) Microcracking and stress-strain curves for concrete in tension. *RILEM Materials and Structures*, 1(1), pp 61-64.

Fouré, B. (1985) Note sur la chute de résistance à la traction du béton léger consécutive à l'arrêt de la cure humide. *Ann. de l'Inst. Techn. du Batiment et des Travaux Publics*, 432, pp. 1-15.

Gonnerman, H.F. and Shuman, E.C. (1928) Compression, flexure and tension tests of plain concrete. In *Proc. Amer. Soc. for Testing Materials*, 28(2), pp. 527-552.

Gopalaratnam, V.S. and Shah, S.P. (1985) Softening response of plain concrete in direct tension. *ACI-Journal*, 82(3), pp. 310-323.

Guo, Z. and Zhang, X., (1987) Investigation of complete stress-deformation curves for concrete in tension. *A CI-Journal*, 82(3), pp 310-324.

Gustafsson, P.J. (1985) Fracture mechanics studies of non-yielding materials like concrete. *Report TVBM-1007*, Lund Inst. of Technology, Sweden.

Gylltoft, K. (1983) Fracture mechanics models for fatigue in concrete structures. *Doctoral Thesis*, Luleå University of Technology, 210 pp.

Hassanzadeh, M., Hillerborg, A. and Zhou, F.P. (1987) Tests of material properties in mixed mode I and II. In *Fracture of Concrete and Rock* (Eds. S.P. Shah and S.E. Swartz), Preprint SEM-RILEM Int. Conf., Bethel, pp. 353-358.

Heilmann, H.G., Hilsdorf, H. and Finsterwalder, K. (1969) Festigkeit und Verformung von Beton unter Zugspannungen. *DAfStb* , Heft 203, 94 pp.

Hillerborg, A., Modeer, M. and Petersson, P.E. (1976) Analysis of crack formation and crack growth in concrete by means of fracture mechanics and finite elements. *Cement and Concrete Res.*, 6, pp. 773-782.

Hillerborg, A. (1985a) The theoretical basis of a method to determine the fracture energy G_f of concrete. *RILEM Materials and Structures*, 18(106), pp 291-296.

Hillerborg, A. (1985b) Results of three comparative test series for determining the fracture energy G_f of concrete. *RILEM Materials and Structures*, 18(107), pp 407-413.

Hillerborg, A. (1989) Stability problems in fracture mechanics testing. In *Fracture of Concrete and Rock; Recent Developments* (Eds. S.P. Shah et al.), Elsevier Applied Science, pp. 369-378.

Holmen, J.O. (1979) Fatigue of concrete by constant and variable amplitude loading. *Doctoral Thesis*, NTH Trondheim, 218 pp.

Hordijk, D.A., Reinhardt, H.W. and Cornelissen, H.A.W. (1987) Fracture mechanics parameters of concrete from uniaxial tensile tests as influenced by specimen length. In *Fracture of Concrete and Rock* (Eds. S.P. Shah and S.E. Swartz), Preprint SEM-RILEM Int. Conf., Bethel, pp. 138-149.

Hordijk, D.A. and Reinhardt, H.W. (1989a) Macro-structural effects in a uniaxial tensile test on concrete. In *Brittle Matrix Composites - 2* (Eds. A.M. Brandt and I.H. Marshall), Elsevier Applied Science, pp. 486-495.

Hordijk, D.A., Van Mier, J.G.M. and Reinhardt, H.W. (1989b) Material properties, Chapter 4 in *Fracture Mechanics of Concrete Structures; From theory to applications*. (Ed. L. Elfgren), Chapman and Hall, pp. 67-127.

Hordijk, D.A. (1989c) Deformation-controlled uniaxial tensile tests on concrete, A survey of the literature up to 1981. *Report 25.5-89-15/VFA (SR-84),* Stevin Laboratory, Delft University of Technology, 118 pp.

Hordijk, D.A. and Reinhardt, H.W. (1989d) Influence of load history on mode I fracture of concrete. In *Fracture Toughness and Fracture Energy; Test Methods for Concrete and Rock* (Eds. H. Mihashi et al.), Balkema, pp. 35- 46.

Hordijk, D.A. and Salet, T. (1989e) Experimental investigation into the tensile properties of a foamed concrete. *Report 25.5-89-03/VFA,* Stevin Laboratory, Delft University of Technology, 31 pp.

Hordijk, D.A. and Reinhardt, H.W. (1990) Fracture of concrete in uniaxial tensile experiments as influenced by curing conditions. *Engineering Fracture Mechanics* 35(4/5), pp. 819-826.

Hughes, B.P. and Chapman, G.P. (1965), Direct tensile test for concrete using modern adhesives. *RILEM Bulletin*, 26, pp. 77-80.

Janssen J.G. (1990) Mode-I fracture of plain concrete under monotonic and cyclic loading. *Graduate Thesis,* Delft University of Technology, IBBC-TNO report BI-90-110.

Johnston, C.D. and Sidwell, E.H. (1969) Influence of drying on strength of concrete specimens. *ACI Journal,* 66, pp. 748-755.

Kleinschrodt, H.D. and Winkler, H. (1986) The influence of the maximum aggregate size and the size of specimen on fracture mechanics parameters. In *Fracture Toughness and Fracture Energy* (Ed. F.H. Wittmann), Elsevier, pp. 391-402.

Körmeling, H.A. (1986) Strain rate and temperature behaviour of steel fibre concrete in tension. *Doctoral Thesis,* Delft University of Technology.

Labuz, J.F., Shah, S.P. and Dowding, C.H. (1985) Experimental analysis of crack propagation in granite. *Int. J. Rock Mech. Min. Sci. & Geomech. Abstr.,* 22(2), pp. 85-98.

Li, V.C. (1985) Fracture resistance parameters for cementitious materials and their experimental determinations. In *Application of Fracture Mechanics to Cementitious Composites*, (Ed. S.P. Shah), Martinus Nijhoff Publishers, pp. 431-449.

Li, V.C., Chan, C.M. and Leung, C. (1987) Experimental determination of the tension-softening relations for cementitious composites. *Cement and Concrete Res.,* 17(3), pp. 441-452.

Mihashi, H., Nomura, N. and Izumi, M. (1989) Influence of matrix strength and gravel grain size on fracture properties of concrete. In *Fracture of Concrete and Rock - Recent Developments* (Eds. S.P. Shah et al.), Elsevier Applied Science, pp. 503-512.

Mills, R.H. (1960) Strength-maturity relationships for concrete which is allowed to dry. In *Studies in concreting in hot countries* (Eds. R. Shalon and D. Ravina), pp. 1-28.

Miner, M.A. (1945) Cumulative damage in fatigue. *J. of Applied Mechanics, Trans. ASME*, 12(1), pp. A159-A164.

Notter, R. (1982) Schallemissionsanalyse für Beton im dehnungsgesteuerten Zugversuch. *Doctoral Thesis*, Zürich.

Palmgren, A. (1924) Die Lebensdauer von Kugellagern. *Zeitschrift Verein Deutscher Ingenieur*, 68(14), pp. 339-341.

Paris, P.C. and Erdogan, F. (1963) A critical analysis of crack propagation laws. *J. of Basic Engineering, Trans. ASME*, Series D 85, pp. 528-534.

Petersson, P.E. (1981) Crack growth and development of fracture zones in plain concrete and similar materials. *Report TVBM-1006*, Lund Inst. of Technology, Sweden, 174 pp.

Planas, J. and Elices, M. (1989) Conceptual and experimental problems in the determination of the fracture energy of concrete. In *Fracture Toughness and Fracture Energy; Test Methods for Concrete and Rock* (Eds. H. Mihashi et al.), Balkema, pp. 165-181.

Raphael, J.M. (1984) Tensile strength of concrete. *ACI Journal*, 81(2), pp. 158-165.

Reinhardt, H.W. (1984a) Fracture mechanics of an elastic softening material like concrete. *HERON*, 29(2), 42pp.

Reinhardt, H.W. and Cornelissen, H.A.W. (1984b) Post-peak cyclic behaviour of concrete in uniaxial and alternating tensile and compressive loading. *Cement and Concrete Res.*, 14, pp. 263-270.

Reinhardt, H.W., Cornelissen. H.A.W. and Hordijk, D.A. (1986) Tensile tests and failure analysis of concrete. *ASCE J. Structural Eng.*, 112(11), pp 2462-2477.

RILEM (1984) Long term random dynamic loading of concrete structures. Report by RILEM committee 36-RDL, *RILEM Materials and Structures*, 17(97), pp 1-28.

Roelfstra, P.E. and Wittmann, F.H. (1986) Numerical method to link strain softening with failure of concrete. In *Fracture Toughness and Fracture Energy* (Ed. F.H. Wittmann), Elsevier, pp. 163-175.

179

Rokugo, K., Iwasa, M., Suzuki, T. and Koyanagi, W. (1989) Testing methods to determine tensile strain softening curve and fracture energy of concrete. In *Fracture Toughness and Fracture Energy; Test Methods for Concrete and Rock* (Eds. H. Mihashi et al.), Balkema, pp. 153-163.

Rots, J.G. (1986) Strain-softening analysis of concrete fracture specimens. In *Fracture Toughness and Fracture Energy* (Ed. F.H. Wittmann), Elsevier, pp. 137-148.

Rots, J.G., Hordijk, D.A. and De Borst, R. (1987) Numerical simulation of concrete fracture in 'direct' tension. In *Numerical methods in Fracture Mechanics* (Eds. A.R. Luxmoore et al.), Pineridge Press, Swansea, pp. 457-471

Rots, J.G. (1988) Computational modeling of concrete fracture. *Doctoral Thesis*, Delft University of Technology, Delft, 132 pp..

Rots, J.G., Kusters, G.M.A. and Blaauwendraad, J. (1989a) Strain-softening simulations of mixed-mode concrete fracture. In *Fracture of Concrete and Rock* (Eds. S.P. Shah and S.E. Swartz), Springer-Verlag, pp. 175-188.

Rots, J.G. and De Borst, R. (1989b) Analysis of concrete fracture in 'direct' tension. *Int. J. of Solids and Structures*, 25(12), pp. 1381-1394.

Rüsch, H. and Hilsdorf, H. (1963) Verformungseigenschaften von Beton unter zentrischen Zugspannungen. *Bericht Nr. 44*, Materialprüfungsamt für das Bauwesen der Technischen Hochschule München.

Salet, T.A.M. (1990) Structural analysis of sandwich beams composed of reinforced concrete faces and a foamed concrete core. *Doctoral Thesis*, Eindhoven University of Technology, 161 pp.

Scheidler, D. (1987) Experimentelle und analytische Untersuchungen zur wirklichkeitsnahen Bestimmung der Bruchschnittgrössen unbewehrter Betonbauteile unter Zugbeanspruchung. *DAfStb*, Heft 379, 94 pp.

Siemes, A.J.M. (1988) Fatigue evaluation of concrete structures; Preliminary studies, procedure and examples. *HERON 33(3)*, 75 pp.

Sri Ravindrarajah, R. (1982) Additional data on the phenomenon of the effect of presustained loading. *Int. J. of Cement Composites and Lightweight Concrete*, 4(4), pp. 251-252.

Swartz, S.E. and Refai, T, (1989) Cracked surface revealed by dye and its utility in determining fracture parameters. In *Fracture Toughness and Fracture Energy; Test Methods for Concrete and Rock* (Eds. H. Mihashi et al.), Balkema, pp. 509-520.

180

Terrien, M. (1980) Emission acoustique et "comportement mécanique post-critique" d'un béton sollicité en traction. *Bulletin de Liaison Lab. Ponts et Chaussees*, 105(1), pp. 65-72.

Tinic, C. and Brühwiler, E. (1985) Effect of compressive loads on the tensile strength of concrete at high strain rates. *Int. J. of Cement Composites and Lightweight Concrete*, 7(2), pp. 103-108.

Van Mier, J.G.M. (1986) Fracture of concrete under complex stress. *HERON*, 31(3), 90 pp.

Van Mier, J.G.M. and Schlangen E. (1989) On the stability of softening systems. In *Fracture of Concrete and Rock; Recent Developments* (Eds. S.P. Shah et al.), Elsevier Applied Science, pp. 387-396.

Van Mier J.G.M. and Nooru-Mohamed, M.B. (1990) Geometrical and structural aspects of concrete fracture. *Engineering Fracture Mechanics* 35(4/5), pp. 617-628.

Van Mier J.G.M. (1991) Mode I fracture of concrete: discontinuous crack growth and crack interface grain bridging. *Cement and Cohcrete Res.*, 21(1), pp. 1-15.

Vonk, R., Rutten, H., Van Mier, J.G.M. and Fijneman, H. (1989) Influence of boundary conditions on softening of concrete loaded in compression. In *Fracture of Concrete and Rock; Recent Developments* (Eds. S.P. Shah et al.), Elsevier Applied Science, pp. 711-720.

Wecharatana, M. (1986) Specimen size effects on non-linear fracture parameters in concrete. In *Fracture Toughness and Fracture Energy* (Ed. F.H. Wittmann), Elsevier, pp. 437-440.

Willam, K., Hurlbut, B. and Sture, S. (1985) Experimental and constitutive aspects of concrete failure. In *Finite Element Analysis of Reinforced Concrete Structures* (Eds. C. Meyer and H. Okamura), pp. 226-254

Wittmann, F.H., Roelfstra, P.E., Mihashi, H., Huang, Y-Y., Zhang, X-H. and Nomura, N. (1987) Influence of age of loading, water-cement ratio and rate of loading on fracture energy of concrete. *RILEM Materials and Structures*, 20(116), pp. 103-110.

Wittmann, F.H., Rokugo, K., Brühwiler, E., Mihashi, H. and Simonin, P. (1988) Fracture energy and strain softening of concrete as determined by means of compact tension specimens. *RILEM Materials and Structures*, 21(121), pp. 21-32.

Wolinski, S. (1986) Influence of aggregate size and loading type on the tensile softening behaviour of concrete. *Stevin Report* 5-86-16, Delft University of Technology, 60 pp.

Wolinski, S., Hordijk, D.A., Reinhardt, H.W. and Cornelissen, H.A.W. (1987) Influence of aggregate size on fracture mechanics parameters of concrete. *Int. J. Cement Composites and Lightweight Concrete*, 9 (2), pp. 95-103.

Wolinski, S. (1989) Influence of aggregate size on the post-peak tensile behaviour of concrete in cyclic tests. In *Brittle Matrix Composites - 2* (Eds. A.M. Brandt and I.H. Marshall), Elsevier Applied Science, pp. 496-505.

Wu, K. and Zhang, B. (1989) Fracture energy of lightweight concrete. In *Fracture Toughness and Fracture Energy; Test Methods for Concrete and Rock* (Eds. H. Mihashi et al.), Balkema, pp. 117-124.

Yankelevsky, D.Z. and Reinhardt, H.W. (1987a) Response of plain concrete to cyclic tension. *ACI Materials Journal*, 84(5), pp. 365-373.

Yankelevsky, D.Z. and Reinhardt, H.W. (1987b) Focal points model for uniaxial cyclic behaviour of concrete. In *Computational Mechanics of Concrete Structures; Advances and Applications*, IABSE Colloquium, Delft, pp.99-106.

Yankelevsky, D.Z. and Reinhardt, H.W. (1989) Uniaxial behaviour of concrete in cyclic tension. *ASCE J. of Structural Eng.*, 115(1), pp. 166-182.

Zhou, F.P. (1988) Some aspects of tensile fracture behaviour and structural response of cementitious materials. *Report TVBM-1008*, Lund University of Technology, 76 pp.

Appendix A   Experimental data

In this appendix mix proportions, 28-day mechanical properties and other experimental data of the different test series are listed. First, general information will be given, followed by a compilation of relevant information and data for the different test series in Table A.3. This mainly concerns the deformation-controlled uniaxial tensile tests.

Mix proportions
Two types of concrete, denoted as normal-weight concrete (NC) and lightweight concrete (LC), were applied in several test series. The maximum aggregate size for NC was 8 mm. Furthermore, five different mix compositions with a varying maximum aggregate size, two mixes with a deviating concrete quality and a foamed concrete have been investigated. Mix proportions for the different mixes can be obtained from Table A.1.

The lightweight aggregate for LC was a sintered expanded clay, manufactured by Compagnie des Ciments Belges (Belgium) and designated as Isol S 4-8, with a bulk density of 1260 kg/m^3.

Properties of the fresh concrete and 28-day strength values
In order to determine the properties of the fresh concrete, air content, compaction index and density were determined for each batch. The 28-day mechanical properties, cube compressive strength and cube splitting strength were obtained on 150 mm cubes which were stored in water until testing at the age of 28 days.

Specimen dimensions
In the preliminary tests, a specimen length of 250 mm was applied which was later reduced to 150 mm (see Section 4.1). The generally applied total cross-sectional area was 60*50 mm^2, while the middle cross-section was reduced by two 5 mm deep saw cuts to 50*50 mm^2. Deviating specimen dimensions were applied in a number of test series. The different specimen dimensions can be obtained from Table A.2. In two tensile experiments, unnotched specimens were used (Section 9.4). For the specimen dimensions of the bending specimens and single notched plates, see Chapter 4.

Age at testing
After curing under water for two weeks, the specimens were stored in the laboratory until testing (see Section 4.2). This period of storage in the laboratory varied significantly between the different test series, resulting in different ages at testing.

Table A.1   Mix proportions (kg/m^3) of the tested types of concrete.

type of concrete	NC	LC	maximum aggregate size (mm)					quality		foamed
			2	4	8	16	32	low	high	
Portland cement	375	400	397	388	366	356	351	200	350	-
Hoogoven cement A	-	-	-	-	-	-	-	-	-	340
water	188	129	199	194	183	178	176	124	135	135
sand										
0.1 - 0.25 mm	127	172	153	157	124	128	130	216	172	-
0.25 - 0.5 mm	234	142	255	175	228	165	130	160	153	70
0.5 - 1 mm	272	142	358	279	266	202	186	228	218	-
1 - 2 mm	272	142	937	349	266	256	205	321	307	-
2 - 4 mm	363	-	-	785	354	256	223	455	435	-
gravel										
4 - 8 mm	540	-	-	-	527	365	261	641	615	-
8 - 16 mm	-	-	-	-	-	457	316	-	-	-
16 - 32 mm	-	-	-	-	-	-	409	-	-	-
ISOL 4-8[1]	-	732	-	-	-	-	-	-	-	-
silica fume	-	-	-	-	-	-	-	-	357	-
superplasticiser	-	6	-	-	-	-	-	3	7	-
foam (synthetic)	-	-	-	-	-	-	-	-	-	70
										(= 730l)
density[2]	2371	1865	2299	2327	2314	2363	2387	2348	2427	615
water-cement ratio	0.50	0.59	0.50	0.50	0.50	0.50	0.50	0.62[3]	0.39[4]	0.40[5]

1) 17% by weight, absorbed water included

2) theoretical value

3) (water+superplasticiser)-cement ratio : 0.64

4) (water+superplasticiser)-(cement+silica fume) ratio : 0.37

5) effective water-cement ratio : 0.60 (foam mainly consists of water)

Loading histories

For the deformation-controlled uniaxial tensile tests, monotonic increasing deformations as well as post-peak cyclic loading regimes were applied. Figure A.1 shows four types of loading history which were applied several times and will be denoted as loading history I,II,III and IV. Similar loading histories, but with different lower stress levels (1, 0, -1, -3 and -15 MPa respectively), were applied in a test series which was used to define a crack cyclic model (Section 6.4). Then there were the tests in which the influence of a compressive preloading was investigated (Section 7.6).
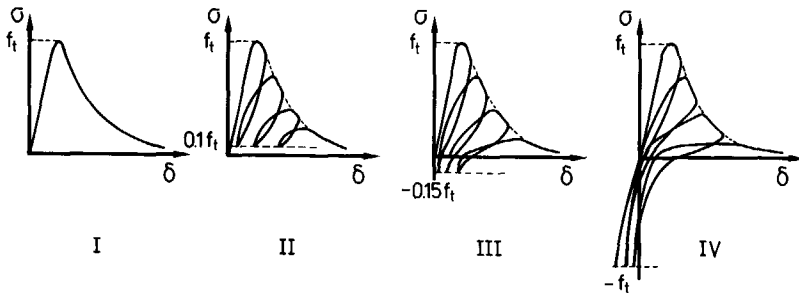
Figure A.1   Loading histories I to IV as applied in the uniaxial tensile tests.

Loading equipment and deformation measurements
The first test series ("preliminary") concerning deformation-controlled uniaxial tensile tests was applied with the loading equipment according to figure 4.2b. For all the other series the equipment sketched in figure 4.2c was used.

Throughout the test series, different arrangements for the deformation measurements were applied, while extensometers as well as LVDTs were also used (see Section 4.2). The arrangements used for the deformation-controlled uniaxial tensile tests are presented in figure A.2.

Tabel A.2   Specimen dimensions.

specimen type		A	B	C	D	E	F	G[2]
length	(mm)	250	125	50	250	150	100	150
width	(mm)	60	60	60	50	60	60	50
depth	(mm)	50	50	50	40	50	50	50
A_c[1]	(mm^2)	50*50	50*50	50*50	40*40	50*50	50*50	50*50

1) critical cross-sectional area

2) unnotched specimen

Determination of E_0 and G_F
For the determination of Young's modulus E_0 and fracture energy G_F not always the same procedure was used for the different test series (see also Section 7.1). As a result, comparison of these results between the test series cannot be done unrestrictedly. Within test series, however, the procedure was not varied. The procedure applied for the determination of G_F is sketched in figure 7.2. As far as the determination of E_0 is concerned, it can be said that deformations for the 110 mm base as well as deformations

185

for a 75 mm base (deformation for l_{meas}= 110 mm minus that for l_{meas}= 35 mm) were used. Generally, the slope of the linear part of the ascending branch up to 60% of the peak load was determined by means of linear regression.
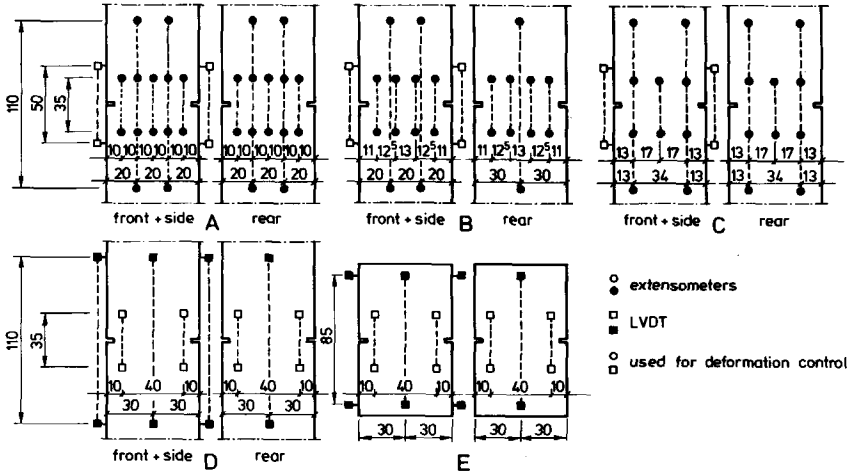

Figure A.2   Applied arrangements of measuring devices.

Experimental data
In Table A.3, relevant information for the test series is presented.

Table A.3   Information concerning the various test series.

test series	Section	type of concrete	density of fresh concrete kg/m³	air content (%)	compaction index	cube compressive strength (MPa)	cube splitting strength (MPa)	specimen dimensions (Table A.2)	age (days)	loading history (fig. A.1)	loading arrangement measuring devices (fig. A.2)
"preliminary"	6.3/6.4	NC	-	-	-	47.1 (6.0)	3.20 (9.4)	A	45-55	I,II,III,IV	A
	7.2	LC	-	-	-	48.6 (6.0)	3.66 (8.3)	A	45-55	I,II,III,IV	A
specimen length	5.3	LC	1829	2.6	1.27	50.4 (3.8)	3.44 (9.2)	A,B,C,D	146-157	I,IV	B
crack cyclic modelling	6.4	NC	2335	2.3	1.09	48.3 (3.1)	3.30 (9.6)	E	42-49	variable	D
foamed concrete	7.2	foamed	-	-	-	$2.9^{1)}$ -	-	F	45	I	E
maximum aggregate	7.3	2 mm	2279	3.0	1.11	41.8 (2.5)	3.00 (3.1)	E	28-31	I,II,IV	B
size (d_{max} =)		4 mm	2341	2.2	1.04	46.8 (3.0)	2.59 (7.4)	E	28-31	I,II,IV	B
		8 mm	2314	3.2	1.04	47.2 (3.8)	3.14 (4.5)	E	28-31	I,II,IV	B
		16 mm	2375	1.6	1.11	51.7 (2.7)	3.15 (1.7)	E	29-32	I,II,IV	B
		32 mm	2422	0.9	1.04	46.7 (4.2)	3.36 (3.7)	E	35-43	I,II,IV	C
concrete quality	7.4	low	2304	1.5	1.33	35.5 (0.7)	2.76(19.3)	E	31	I	B
		high	2423	1.9	1.14	77.3 (1.0)	4.49 (1.7)	E	31-32	I	B
curing conditions	7.5	NC	2348	2.3	1.05	44.5 (2.7)	3.00 (5.0)	E	33-37	I,II,IV	B
		LC	1799	3.4	1.24	50.9 (5.5)	3.47 (9.1)	E	28-41	I,II,IV	B
		NC	2349	1.7	1.09	48.5 (4.8)	3.35 (1.9)	E	variable	I	B
compressive preloading	7.6	NC	2337	2.2	1.09	48.2 (3.8)	3.19 (6.1)	E	42-46	I	D
verification tests	8.1	NC	2328	2.5	1.08	48.1 (0.8)	2.96 (8.2)	E	77-78	I	D
fatigue tests	9.4	NC	2336	2.3	1.07	46.8 (2.3)	3.22 (9.5)	E,G	84-127	I,fatigue	D

1) obtained on 100*100*500 mm³ prisms

187

Appendix B   Two crack cyclic behaviour models

B.1 Focal-point model (FPM) by Yankelevsky and Reinhardt[87b,89]

For the model rules of the focal-point model, which was proposed for σ-δ relations, the reader is referred to the original publication. In this appendix, the formulations for the keypoints in the loops will be given for the case of σ-w relations. The geometrical procedure for a particular loop can be obtained from the dashed lines in figure B.1.
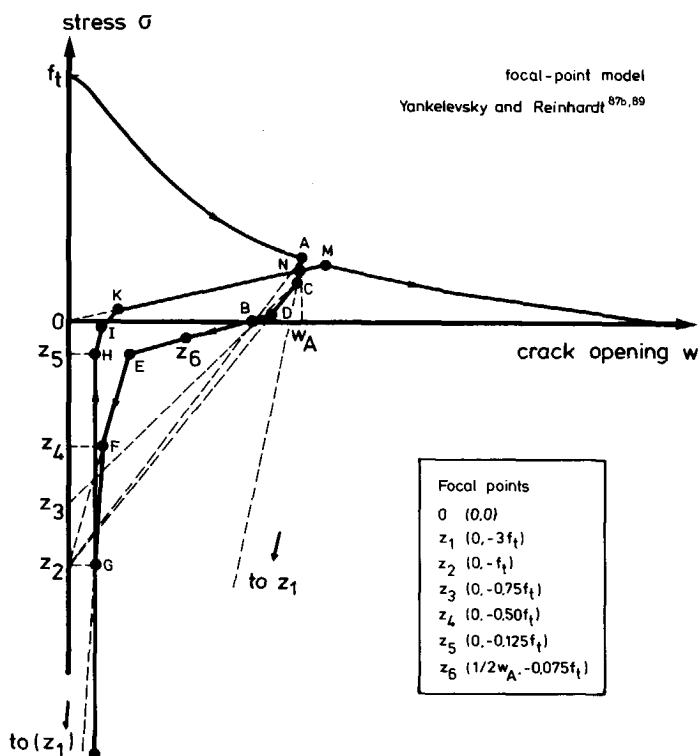

Figure B.1   Geometrical loci and procedure of the focal-point model by Yankelevsky and Reinhardt [87b,89]

Modification of the model
In applying the model, some erroneous results for very small crack openings were obtained. In order to illustrate this for a larger (figure B.2a) as well as for a smaller crack

opening (figure B.2b), the first part of the unloading curve will be constructed according to the original model rules. The model rules are:

1. The straight line determined by starting point A (δ_A, σ_A) and focal point Z_2 intersects the δ-axis at point B, which is the residual deformation if the stress drops to zero.

2. The line Z_3-B intersects line A-Z_1 at point C

3. In order to find the keypoints D and E, the line Z'_6-B is required. Intersection of this line with line C-Z_2 yields point D, while point E is a point on this line with a σ-coordinate equal to that one of Z_5.
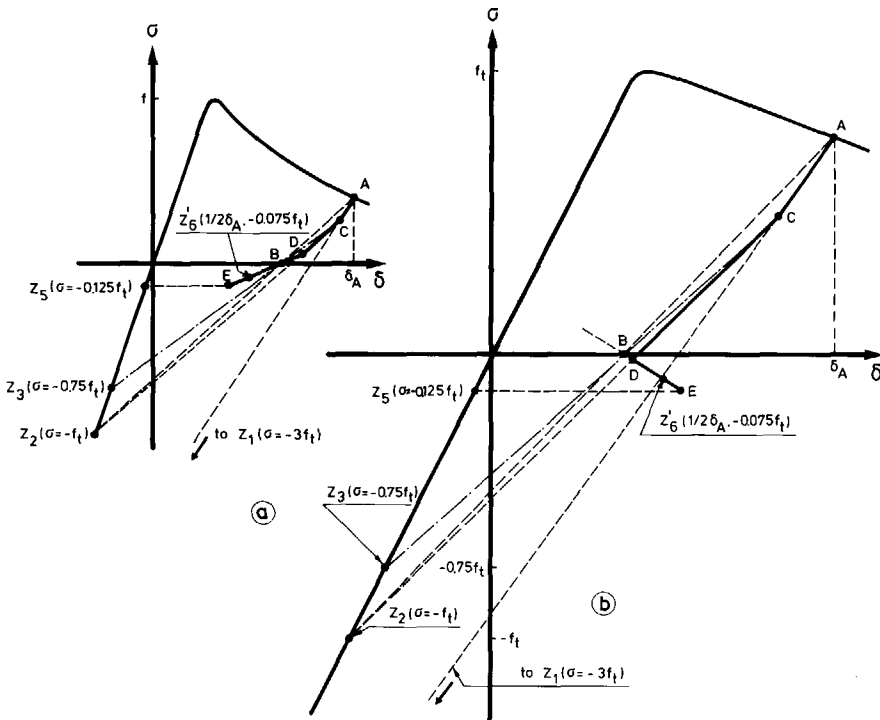
Figure B.2   The first part of a loading cycle constructed according to the focal-point model, for a large (a) and a small (b) crack opening (deformation).

The first part of the unloading curve is now determined by A-C-D-B-E. For starting point A in figure B.2a, this yields a curve that coincides well with experimental results. It can be seen in figure B.2b that problems may be encountered for small crack openings. This is due to the fact that for small crack openings point Z'_6 can be positioned below line Z_3-B. To circumvent this problem, a precondition is added to the model rules. This

189

concerns the determination of points D and E. According to this precondition, line Z'_6-B is replaced by line Z_3-B and point D is equal to point B in the case where point Z'_6 is positioned below line Z_3-B. Finally, it should be noted that the maximum crack opening for which the situation sketched in figure B.2b occurs, increases with increasing applied length for the deformation measurement. Furthermore, the δ-coordinate of focal point Z'_6 in the original model $(0.5\delta_A)$ causes the model to be dependent on the applied measuring length, although this will not be significant due to the small value of the σ-coordinate of focal point Z'_6 $(-0.075f_t)$.

Formulae for keypoint coordinates
With the focal points (figure B.1) and the model rules, the formulae for the keypoint coordinates can be derived. The modifications as compared to the original model rules are outlined. For the *unloading curve* the coordinates are:

B:
$$w_B = \frac{w_A\, f_t}{\sigma_A + f_t} \qquad\qquad \sigma_B = 0 \qquad\qquad (B.1)$$

C:
$$w_C = \frac{2.25 f_t}{(\dfrac{\sigma_A + 3f_t}{w_A} - \dfrac{0.75 f_t}{w_B})} \qquad \sigma_C = 0.75 f_t(\frac{w_C}{w_B} - 1) \qquad (B.2)$$

D: $\dfrac{w_A}{w_B} < 1.8$
$$w_D = \frac{(\dfrac{0.075 f_t w_B}{0.5 w_A - w_B}) + f_t}{(\dfrac{0.075 f_t}{0.5 w_A - w_B}) + (\dfrac{\sigma_C + f_t}{w_C})} \qquad \sigma_D = (\sigma_C + f_t)(\frac{w_D}{w_C}) - f_t \quad (B.3a)$$

$\dfrac{w_A}{w_B} \geq 1.8$
$$w_D = w_B \qquad\qquad\qquad \sigma_D = \sigma_B \qquad\qquad (B.3b)$$

E: $\dfrac{w_A}{w_B} < 1.8$
$$w_E = \frac{5}{6} w_A - \frac{2}{3} w_B \qquad\qquad \sigma_E = -0.125 f_t \qquad\qquad (B.4a)$$

$\dfrac{w_A}{w_B} \geq 1.8$
$$w_E = \frac{5}{6} w_B \qquad\qquad\qquad \sigma_E = -0.125 f_t \qquad\qquad (B.4b)$$

F:
$$W_F = \frac{0.5 f_t\, w_E}{\sigma_E + f_t} \qquad\qquad \sigma_F = -0.5 f_t \qquad\qquad (B.5)$$

G:
$$w_G = \frac{2 f_t\, w_G}{\sigma_F + 3 f_t} \qquad\qquad \sigma_G = -f_t \qquad\qquad (B.6)$$

190

Assume that unloading proceeds until a point L (w_L, σ_L). Then, the keypoint coordinates of the *reloading curve* are:

H: $\sigma_L < -0.125f_t$ $\quad w_H = w_L$ $\qquad\qquad \sigma_H = -0.125f_t$ $\quad (\rightarrow N)$ (B.7a)

$\quad\ \ \sigma_L \geq -0.125f_t$ $\quad w_H = w_L$ $\qquad\qquad \sigma_H = \sigma_L$ $\qquad\quad (\rightarrow N)$ (B.7b)

N: $\boxed{\sigma_L < 0.85\sigma_A}$ $\quad w_N = \dfrac{w_A(3f_t + 0.85\sigma_A)}{3f_t + \sigma_A}$ $\quad \sigma_N = 0.85\sigma_A$ $\qquad (\rightarrow I)$ (B.8a)

$\quad\ \ \sigma_L \geq 0.85\sigma_A$ $\quad w_N = w_L$ $\qquad\qquad\qquad \sigma_N = \sigma_L$ $\qquad\quad$ [LM] (B.8b)

I: $\qquad\qquad\qquad w_I = w_A - w_C + w_H$ $\qquad \sigma_I = \sigma_A - \sigma_C + \sigma_H$ $\quad (\rightarrow J)$ (B.9)

J: $\sigma_L < \sigma_C$ $\quad \bullet \quad w_J = w_C - w_D + w_I$ $\qquad \sigma_J = \sigma_C - \sigma_D + \sigma_I$ $\quad (\rightarrow K)$ (B.10)

$\quad\ \ \sigma_L \geq \sigma_C$ $\qquad\qquad\qquad\qquad\qquad\qquad\qquad\qquad\qquad (\rightarrow K)$

K: $\dfrac{\sigma_N}{w_N} \leq \dfrac{\sigma_I}{w_I}$ $\quad w_K = \dfrac{\left(\dfrac{\sigma_H - \sigma_I}{w_H - w_I}\right)w_H - \sigma_H}{\left(\dfrac{\sigma_H - \sigma_I}{w_H - w_I}\right) - \left(\dfrac{\sigma_N}{w_N}\right)}$ $\quad \sigma_K = \dfrac{\sigma_N}{w_N}w_K$ $\quad$ [LHKM] (B.11a)

$\dfrac{\sigma_I}{w_I} < \dfrac{\sigma_N}{w_N} \leq \dfrac{\sigma_J}{w_J}$ $\quad w_K = \dfrac{\left(\dfrac{\sigma_I - \sigma_J}{w_I - w_J}\right)w_I - \sigma_I}{\left(\dfrac{\sigma_I - \sigma_J}{w_I - w_J}\right) - \left(\dfrac{\sigma_N}{w_N}\right)}$ $\quad \sigma_K = \dfrac{\sigma_N}{w_N}w_K$ $\quad$ [LHIKM] (B.11b)

$\dfrac{\sigma_J}{w_J} < \dfrac{\sigma_N}{w_N}$ $\quad w_K = \dfrac{\sigma_J + \left(\dfrac{0.075f_t w_J}{0.5w_A - w_B}\right)}{\dfrac{\sigma_N}{w_N} + \left(\dfrac{0.075f_t}{0.5w_A - w_B}\right)}$ $\quad \sigma_K = \dfrac{\sigma_N}{w_N}w_K$ $\quad$ [LHIJKM] (B.11c)

The keypoints that are part of the reloading curve are indicated by the letters between the brackets [ ]. M is the point where the loop meets the envelope curve again and can be found as the intersection point of line O-N with the envelope curve. In some cases, different keypoints, for instance L and H, may coincide.

B.2 Continuous-function model (CFM)

Here the complete model for the constitutive relations of concrete under tensile loading, as proposed in this report (continuous-function model), will be summarized. This means that besides the model for a complete loop (starting from and ending at the envelope curve), the description for the envelope curve itself as well as for load reversals in a loop will also be given (see figure B.3).
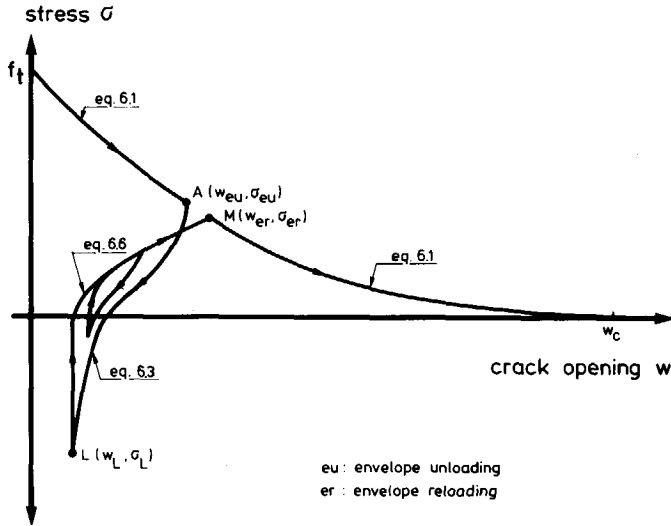

Figure B.3   Schematic representation of the continuous-function model.

Envelope curve

$$\frac{\sigma}{f_t} = \{1 + (c_1\frac{w}{w_c})^3\}\exp(-c_2\frac{w}{w_c}) - (1 + c_1^3)\exp(-c_2) \tag{6.1}$$

$c_1 = 3$, $c_2 = 6.93$ and $w_c = 5.14G_F/f_t$

Unloading from the envelope curve
Starting from point (w_{eu}, σ_{eu}):

$$\frac{\sigma}{f_t} = \frac{\sigma_{eu}}{f_t} + \{\frac{1}{3(w_{eu}/w_c) + 0.4}\}[0.014\{\ln(\frac{w}{w_{eu}})\}^5 - 0.57(1-\frac{w}{w_{eu}})^{0.5}] \tag{6.3}$$

192

Gap in the envelope curve

$$\frac{w_{inc}}{w_c} = 0.1 \left(\frac{w_{eu}}{w_c}\right)\{\ln(1 + 3\frac{\sigma_{eu}-\sigma_L}{f_t})\}$$

(6.4)

$$w_{er} = w_{eu} + w_{inc}$$

(6.5)

σ_{er} can be found with w_{er} and equation 6.1

Reloading curve

Starting from point (w_L, σ_L) up to point (w_{er}, σ_{er}) at the envelope curve

$$\frac{\sigma}{\sigma_L} = 1 + [\frac{1}{c_3}\{\frac{(w-w_L)}{(w_{er}-w_L)}\}^{0.2c_3} + \{1-(1-\frac{(w-w_L)}{(w_{er}-w_L)})^2\}^{c_4}](\frac{c_3}{c_3+1})(\frac{\sigma_{er}}{\sigma_L}-1)$$

(6.6a)

$$c_3 = 3(3\frac{f_t-\sigma_L}{f_t})^{(-1-0.5\frac{w_{eu}}{w_c})}\{1-(\frac{w_{eu}}{w_c})^{(\frac{0.71f_t}{f_t-\sigma_L})}\}$$

(6.6b)

$$c_4 = [2(3\frac{f_t-\sigma_L}{f_t})^{-3} + 0.5]^{-1}$$

(6.6c)

Reversals in crack opening direction in a loop

For the description of the inner loops, a counter i will be used, which is taken as equal to zero for the envelope curve and increases by 1 each time there is a reversal in crack opening direction before the crack opening at the previous reversal has been reached (see figure B.4). The principle that is used for inner loops is that they return to the same point they started from. This means that a damaging effect due to cycling within a loop is not taken into account. As far as notation is concerned, A_i is used for a point where the direction changes from an opening crack into a closing crack and L_i is used for the opposite reversal in crack opening direction. Furthermore, there are the variables $\Delta\sigma_{A_i}$ and $\Delta\sigma_{L_i}$, while $\sigma_{u_i}(w)$ and $\sigma_{r_i}(w)$ denote the stresses as a function of crack opening for unloading and reloading curves respectively. The *unloading curves* are now determined by:

$$\Delta\sigma_{A_i} = \sigma_{A_i} - \sigma_{u_1}(w_{A_i}) - \sum_{n=3}^{i}(\frac{w_{A_i} - w_{L_{n-2}}}{w_{A_{n-1}} - w_{L_{n-2}}})^2 \Delta\sigma_{A_{n-1}}$$

(B.12)

$$\sigma_{u_i}(w) = \sigma_{u_1}(w) + \sum_{n=2}^{i}(\frac{w - w_{L_{n-1}}}{w_{A_n} - w_{L_{n-1}}})^2 \Delta\sigma_{A_n}$$

(B.13)

and the *reloading curves* can be found with

$$\Delta \sigma_{L_i} = \sigma_{r_1}(w_{L_i}) - \sigma_{L_i} - \sum_{n=3}^{i} \left(\frac{w_{L_i} - w_{A_{n-1}}}{w_{L_{n-1}} - w_{A_{n-1}}}\right)^8 \Delta \sigma_{L_{n-1}} \tag{B.14}$$

$$\sigma_{r_i}(w) = \sigma_{r_1}(w) - \sum_{n=2}^{i} \left(\frac{w - w_{A_n}}{w_{L_n} - w_{A_n}}\right)^8 \Delta \sigma_{L_n} \tag{B.15}$$

After completion of an inner loop, the counter i decreases by 1, which can be expressed by:

$$
\begin{aligned}
&\text{if} \quad w \geq w_{A_i} \quad \text{then} \quad i = i - 1 \\
&\text{if} \quad w \leq w_{L_{i-1}} \quad \text{then} \quad i = i - 1
\end{aligned}
\tag{B.16}
$$
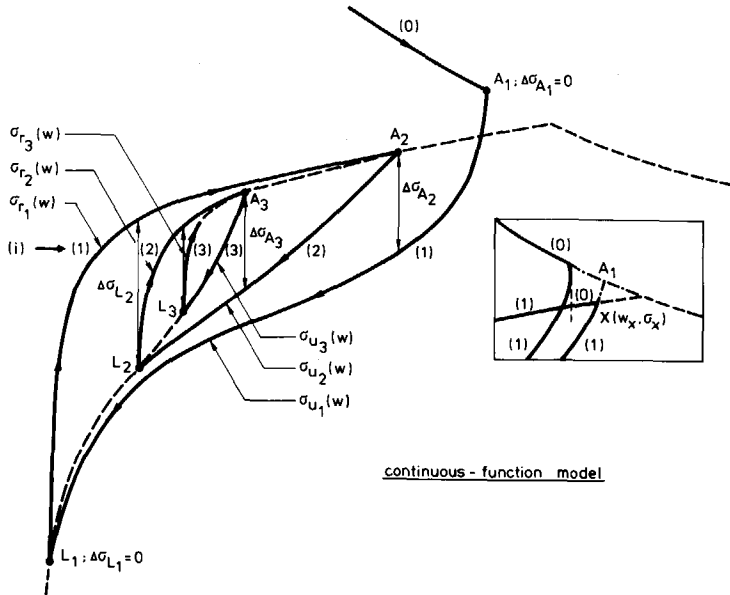
Figure B.4   Procedure for inner loops in the CFM.

In the formulations presented above, only crack opening reversals at crack openings corresponding to the gap in the envelope curve have not yet been described. For the case where unloading starts at point X, it is proposed to determine point A_1 as sketched in the inset of figure B.4. This point is the intersection point of the envelope curve (eq. 6.1) and

194

an unloading curve (eq. 6.3), while $X(w_X, \sigma_X)$ is part of this latter curve. This intersection point can be obtained by an iterative procedure.

Now, a complete description for post-peak tensile loading is given. Figure B.5 shows the flow chart of the applied procedure, which can be used for a mathematical subroutine in numerical simulation programs.

B.3 Model predictions of experimental results

For each type of test in the test series with post-peak cyclic loading, as discussed in Section 6.4, three arbitrarily chosen loops were compared with the model predictions of the focal-point model (FPM) and the continuous-function model (CFM). Since it was intended to compare only the individual loops, the crack opening (w_{eu}) and stress (σ_{eu}) at the starting point as well as the lower stress level σ_L have been used as input in the models. For f_t and G_F, the average values for the total test series (2.8 MPa and 95.3 J/m^2 respectively) were taken. For determining the point where the reloading curve meets the envelope curve again, eq. 6.1 was used, with w_c being equal to the value that was obtained with the average values for f_t and G_F ($5.14 G_F/f_t = 175\,\mu m$) and for f_t a fictive value which is chosen in such a way that point (w_{eu}, σ_{eu}) is part of the envelope curve. The results of the model predictions can be found in figures B.6 to B.10.

Figures B.11 to B.14 show the comparison between the experimental σ-w relations reported in the literature and the predictions for the post-peak cycles. For the determination of the σ-w relations, elastic deformations were subtracted from the originally presented curves (see also Section 6.4).
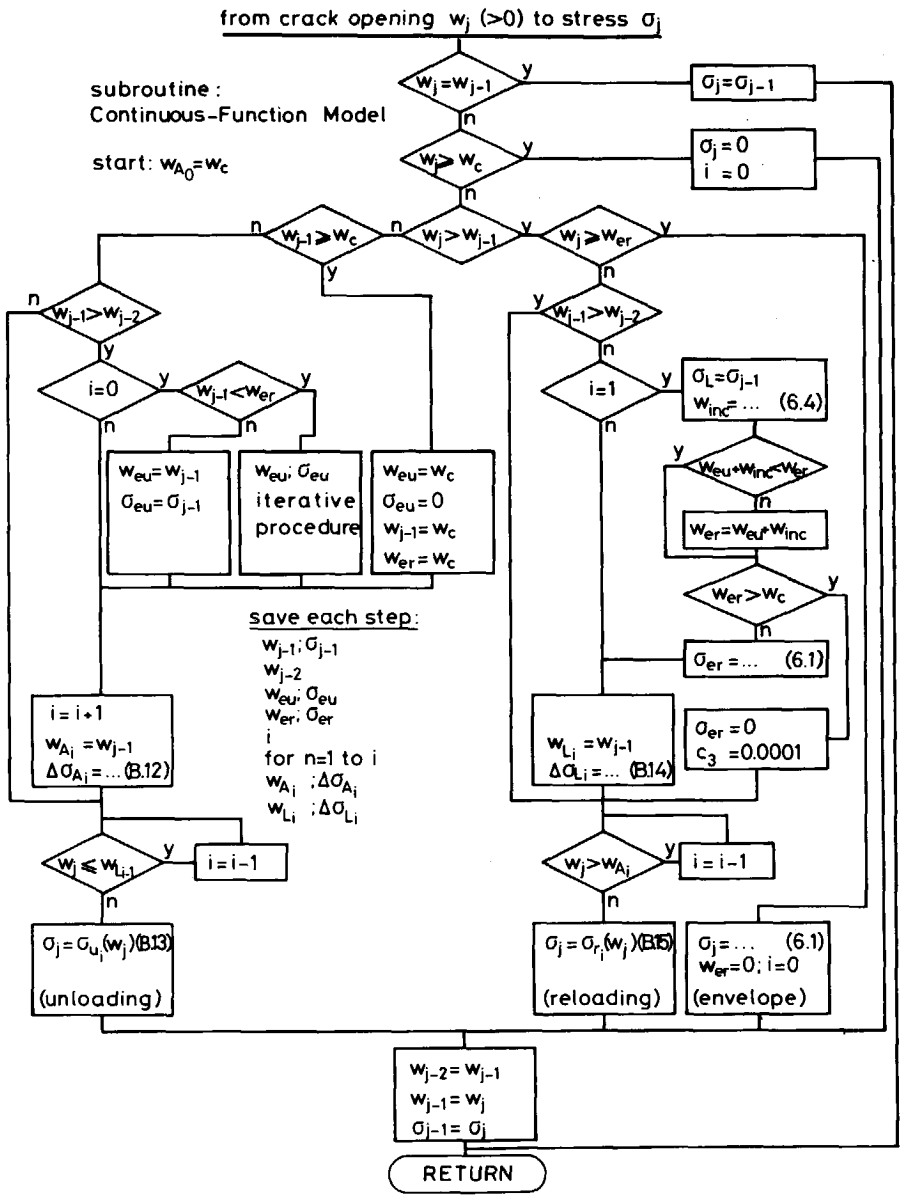
from crack opening w_j (>0) to stress σ_j

subroutine :
Continuous-Function Model

start: $w_{A_0} = w_c$

$w_j = w_{j-1}$ — y → $\sigma_j = \sigma_{j-1}$
n

$w_j > w_c$ — y → $\sigma_j = 0$; $i = 0$
n

$w_{j-1} > w_c$ —n— $w_j > w_{j-1}$ —y— $w_j \geq w_{er}$ —y
y (down) ... n

$w_{j-1} > w_{j-2}$
y / n

$i = 0$ —y— $w_{j-1} < w_{er}$ —y
n / n

$w_{eu} = w_{j-1}$
$\sigma_{eu} = \sigma_{j-1}$

$w_{eu}; \sigma_{eu}$
iterative
procedure

$w_{eu} = w_c$
$\sigma_{eu} = 0$
$w_{j-1} = w_c$
$w_{er} = w_c$

save each step:
$w_{j-1}; \sigma_{j-1}$
w_{j-2}
$w_{eu}; \sigma_{eu}$
$w_{er}; \sigma_{er}$
i
for n=1 to i
w_{A_i} ; $\Delta\sigma_{A_i}$
w_{L_i} ; $\Delta\sigma_{L_i}$

$i = i + 1$
$w_{A_i} = w_{j-1}$
$\Delta\sigma_{A_i} = ...$ (B.12)

$w_j \leq w_{L_{i-1}}$ —y→ $i = i - 1$
n

$\sigma_j = \sigma_{u_i}(w_j)$ (B.13)
(unloading)

$w_{j-1} > w_{j-2}$
y / n

$i = 1$ —y→ $\sigma_L = \sigma_{j-1}$; $w_{inc} = ...$ (6.4)
n

$w_{eu} + w_{inc} < w_{er}$
y ... n

$w_{er} = w_{eu} + w_{inc}$

$w_{er} > w_c$ —y
n

$\sigma_{er} = ...$ (6.1)

$\sigma_{er} = 0$
$c_3 = 0.0001$

$w_{L_i} = w_{j-1}$
$\Delta\sigma_{L_i} = ...$ (B.14)

$w_j > w_{A_i}$ —y→ $i = i - 1$
n

$\sigma_j = \sigma_r(w_j)$ (B.15)
(reloading)

$\sigma_j = ...$ (6.1)
$w_{er} = 0$; $i = 0$
(envelope)

$w_{j-2} = w_{j-1}$
$w_{j-1} = w_j$
$\sigma_{j-1} = \sigma_j$

RETURN

Figure B.5   Flow chart for the continuous-function model; mode I crack cyclic behaviour.

196
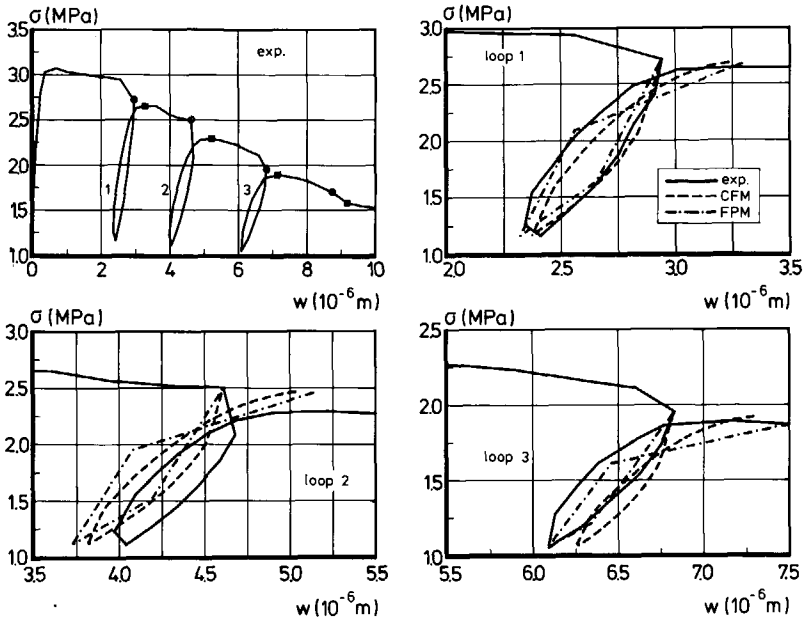
Figure B.6   Experimental loops and model predictions for a test with $\sigma_L \approx 1$ MPa.
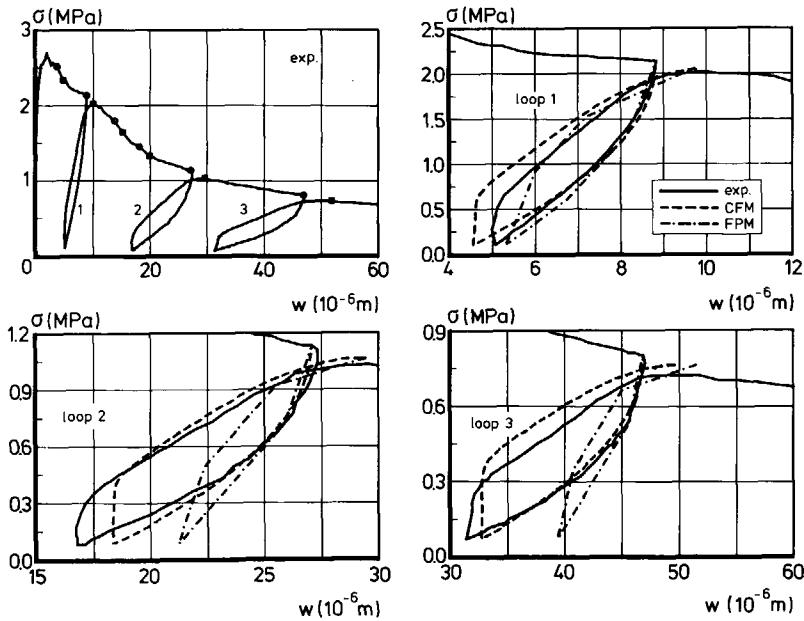
Figure B.7   Experimental loops and model predictions for a test with $\sigma_L \approx 0$ MPa.
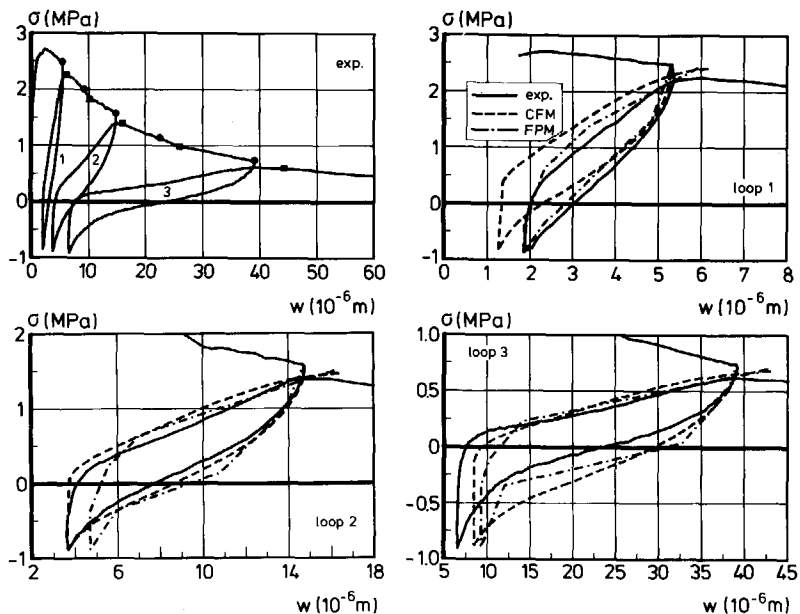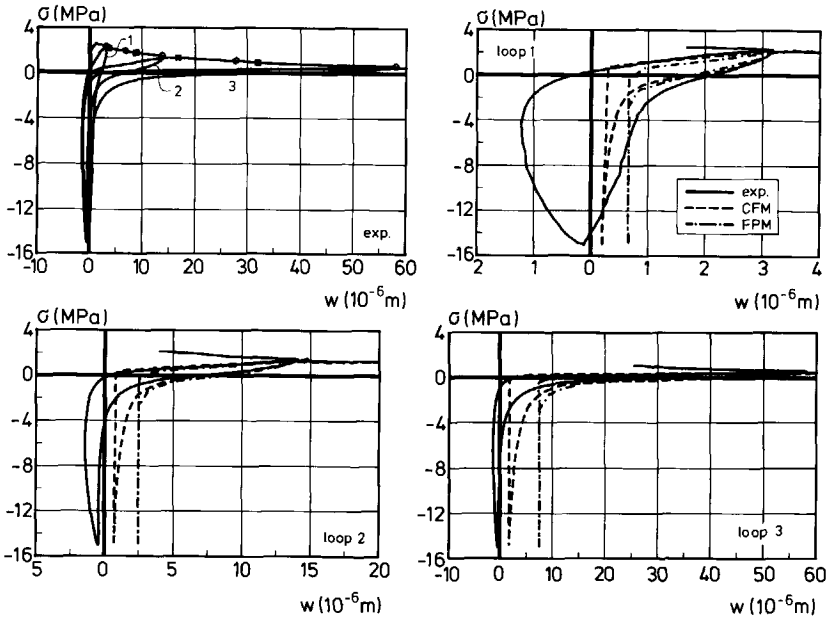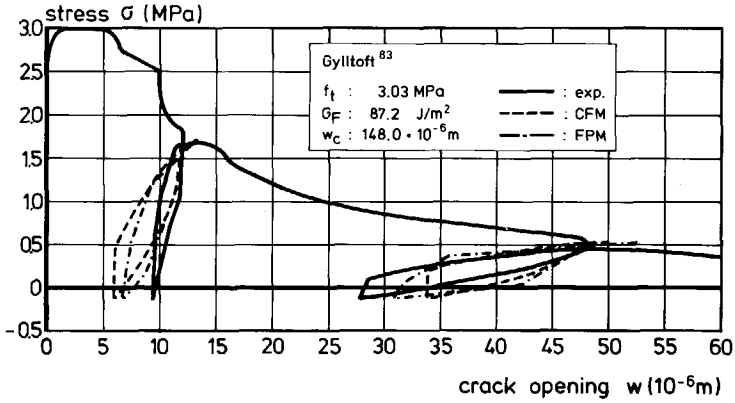
Figure B.8   *Experimental loops and model predictions for a test with* $\sigma_L \approx -1$ *MPa.*
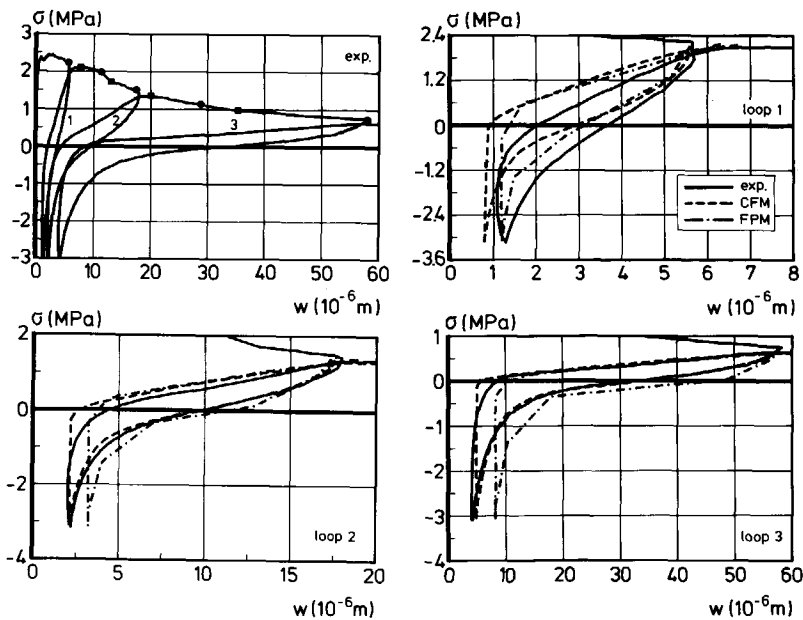
Figure B.9   *Experimental loops and model predictions for a test with* $\sigma_L \approx -3$ *MPa.*

198

Figure B.10 Experimental loops and model predictions for a test with $\sigma_L \approx -15$ MPa.

Figure B.11   Predictions for the loops reported by Gylltoft [83].
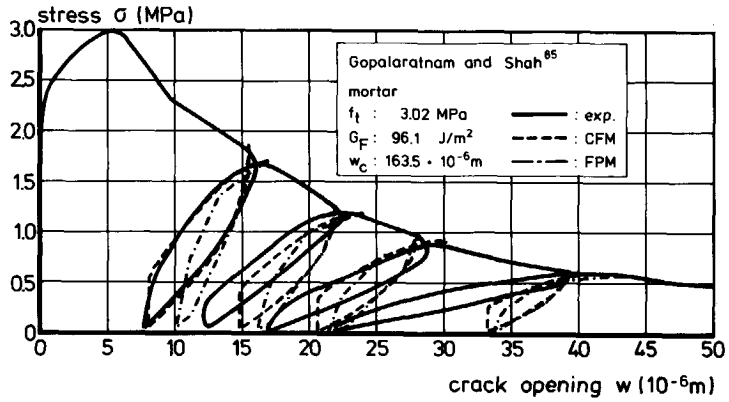
Figure B.12   Predictions for the loops reported by Gopalaratnam and Shah [85].
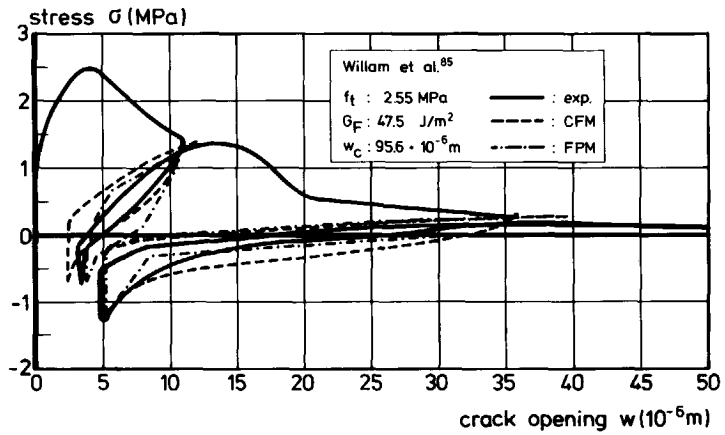
Figure B.13   Predictions for the loops reported by Willam et al. [85].
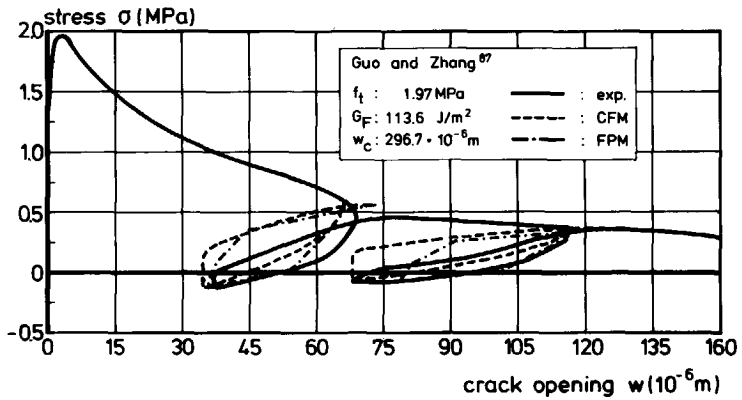
Figure B.14   Predictions for the loops reported by Guo and Zhang [87].

Appendix C Experimental and numerical results for the verification tests

C.1 Four-point bending tests; Results from experiments and FE analyses

The separate readings of LVDTs on the front and rear sides of the specimen did not show significant differences. Therefore, the readings of corresponding LVDTs have been averaged. Results for the bending tests are presented in figures C.1 to C.3. In the upper part of the figures (a), the load-deflection curves for static loading and for the envelope curve in the case of cyclic loading are plotted. The input parameters for the FE analyses were chosen as: tensile strength $f_t = 3.0$ MPa, Young's modulus $E_o = 38000$ MPa and fracture energy $G_F = 125$ J/m^2 (see also Section 8.2). The initial stiffness of the interface elements was 10^{12} MPa/mm. In the middle part of the figures (b and c), the deformation distributions ($l_{meas} = 35$ mm) over the fracture zones are compared for four points in the loading history of the static tests. The points denoted as 1, 3 and 4 relate to a deflection of about $40 \cdot 10^{-6}$ m, $150 \cdot 10^{-6}$ m and $290 \cdot 10^{-6}$ m respectively, while point 2 corresponds to the deflection at peak load in the FE analysis. Finally, in the lower part of the figures (d) the experimental and predicted load-deflection curves for the post-peak cyclic tests are plotted. For the loops, it was chosen to take the deflection at the start of the loop and the deflection at the lower load level, equal to the corresponding deflections in the experiments. In the analyses of the cyclic tests, the initial stiffness of interface elements was chosen as equal to 10^4 MPa/mm. The influence of the initial stiffness on the F-δ_{fl} curves is discussed in Section 8.2, where attention is also paid to the typical shape of the fourth loop in figure C.1d.

C.2 Prediction of F-δ_{fl} relations with the hybrid method

In Section 8.4 the hybrid method is described. Here, the predicted load-deflection curves are presented together with the experimentally determined relations. For the results in figure C.4, the deformation distribution over the fracture zone was converted into a stress distribution. The lower curves in the diagrams represent the resulting normal force, while the other two curves are F-δ_{fl} relations. In the analysis, the continuous-function model was applied.
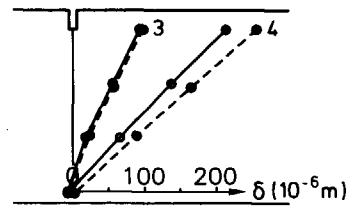
For the predicted F-δ_{fl} curves in figure C.5, only the calculated stress distribution over the tensile region of the fracture zone was used, while for the compressive zone a linear relation resulting in a zero normal force was assumed.
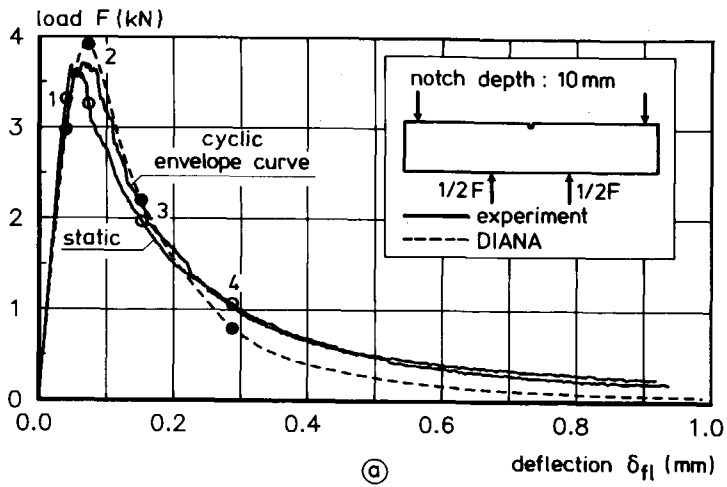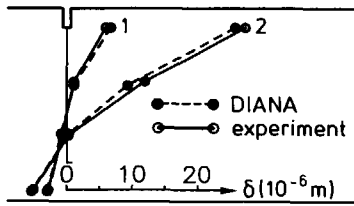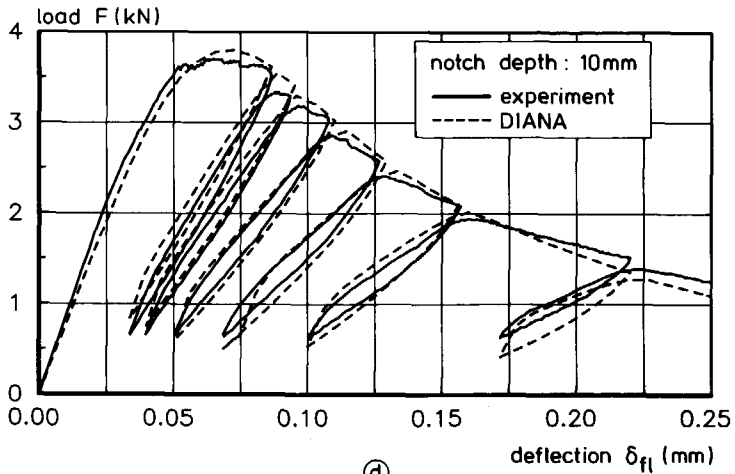
Figure C.1   Results for the beams with a 10 mm deep notch.

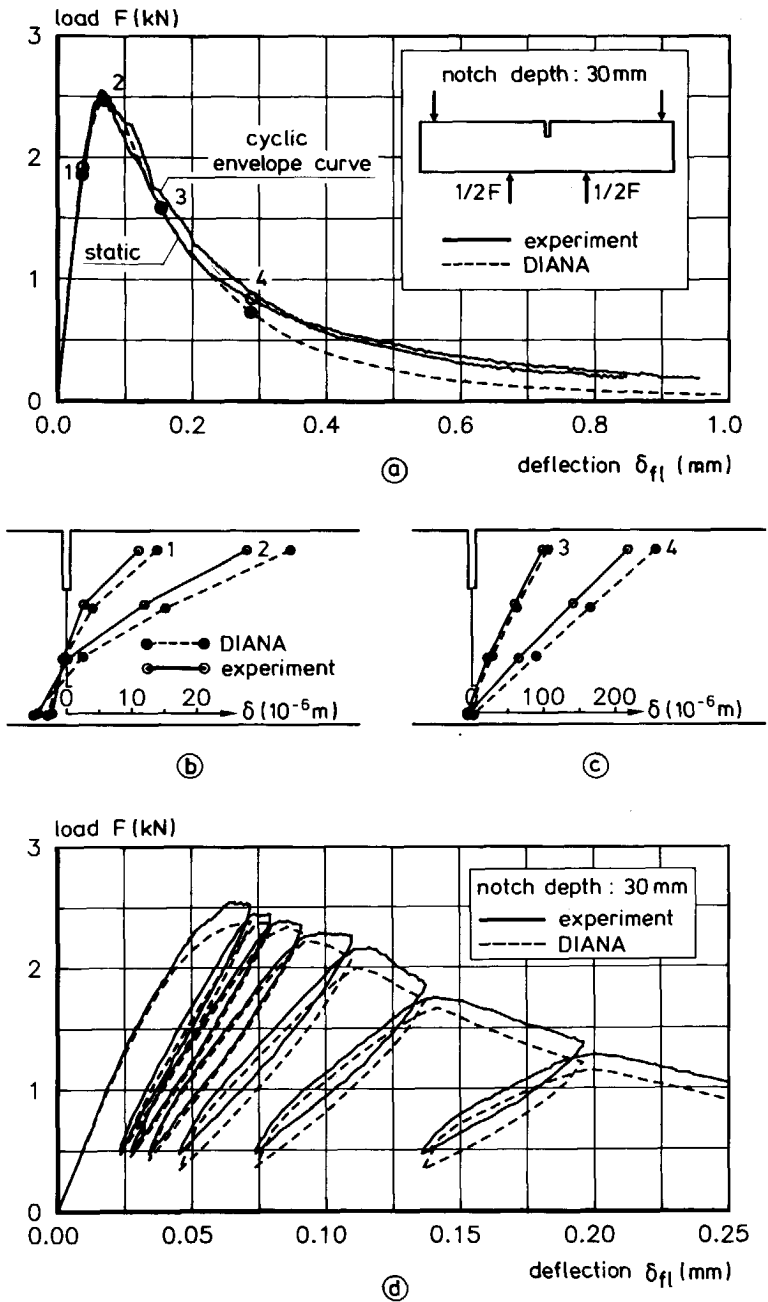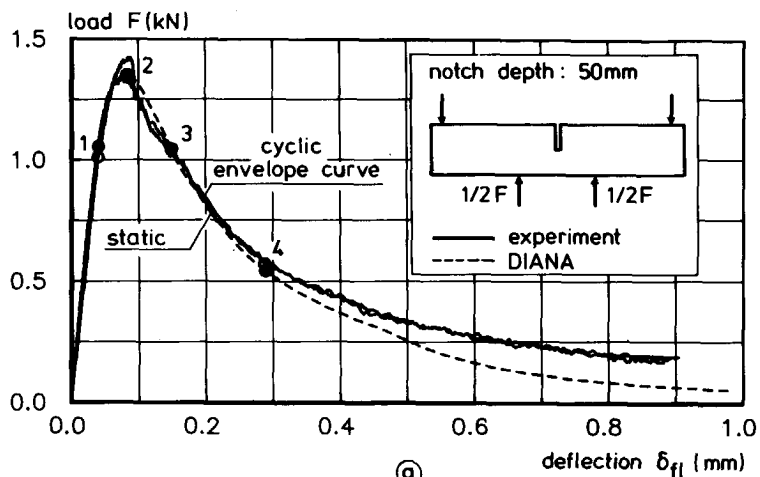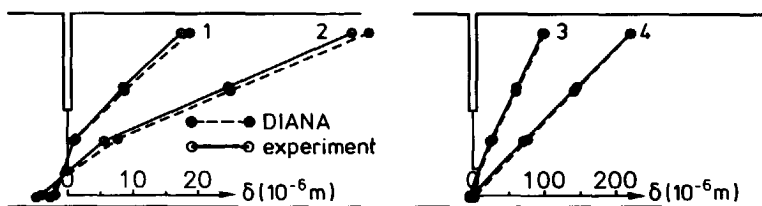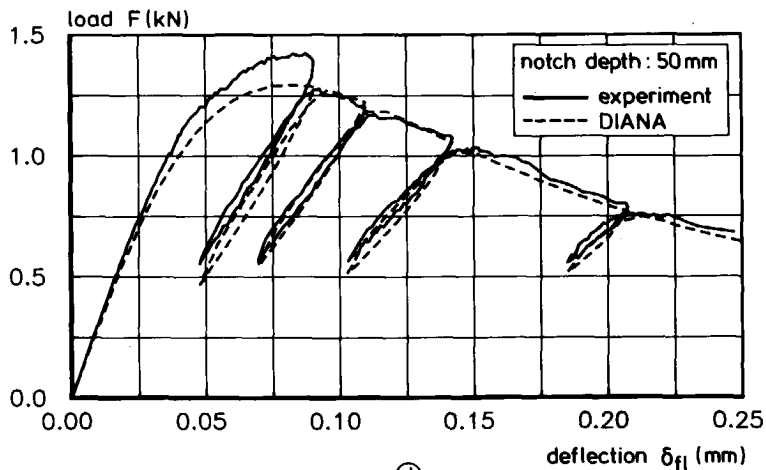Figure C.2   Results for the beams with a 30 mm deep notch.

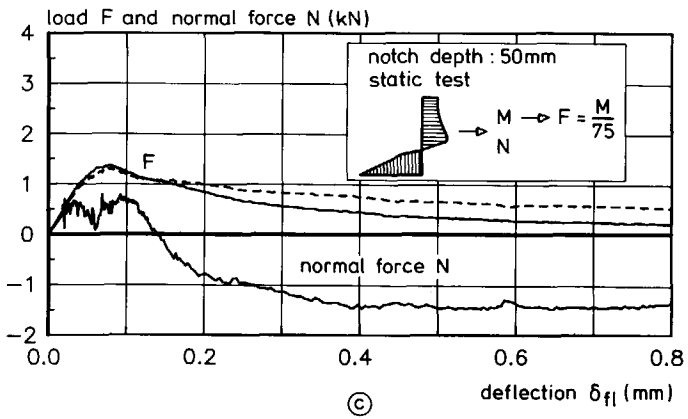*Figure C.3   Results for the beams with a 50 mm deep notch.*
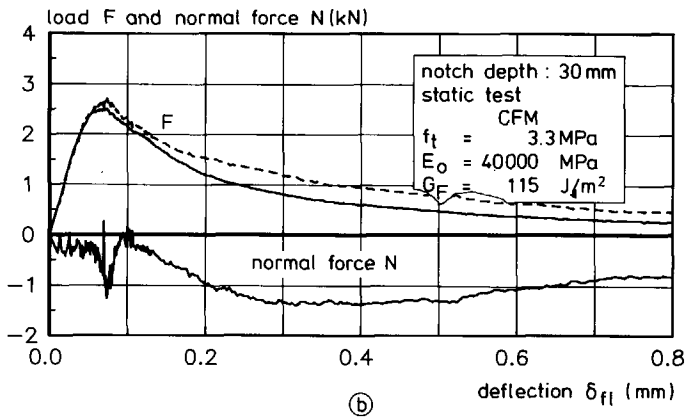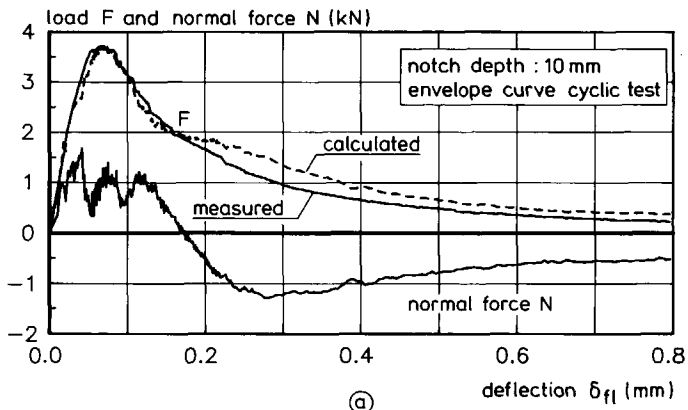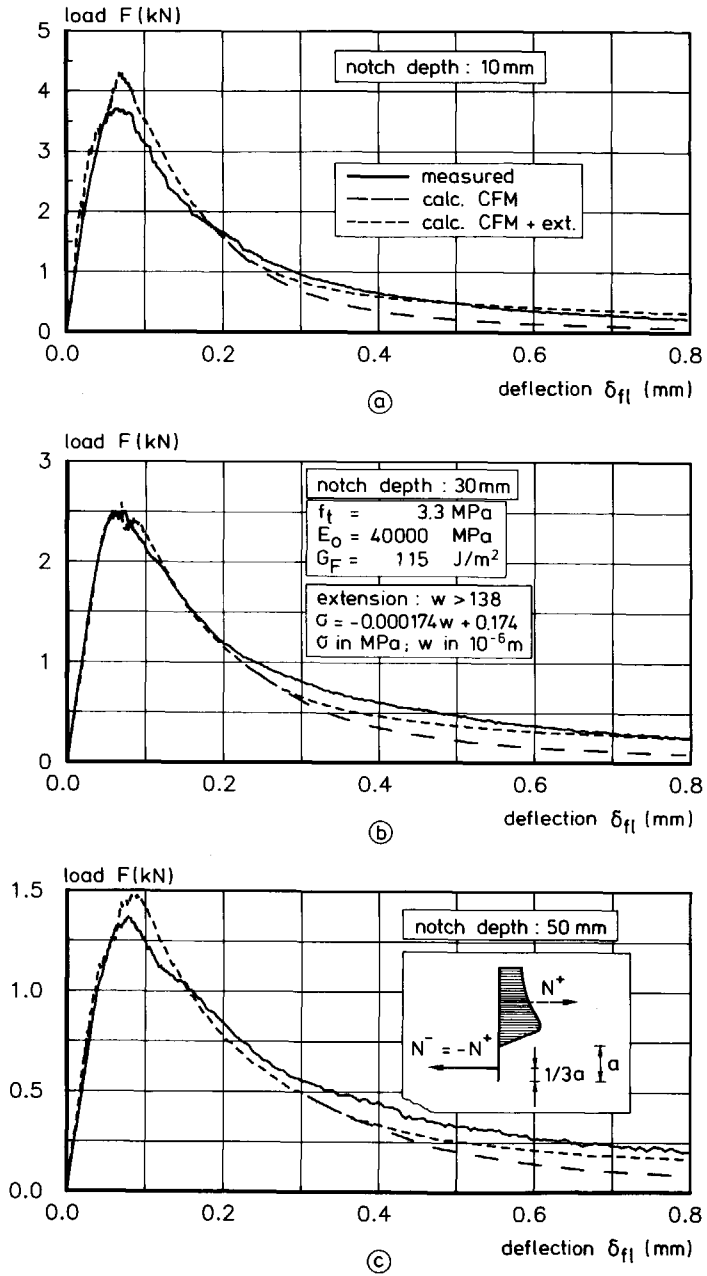
Figure C.4   Results for the hybrid method.

Figure C.5   Results for the hybrid method with the assumption of a zero normal force (equilibrium).

Summary

Various types of structures are subjected to fatigue loading. Especially since the oil crisis in the 'seventies, when concrete offshore platforms came on the scene, the interest in the properties of concrete under fatigue or cyclic loading has increased strongly. So far, fatigue of concrete has mainly been studied in a phenomenological way, while the knowledge about the cause and mechanism of concrete fatigue is still very limited. In this research, a model based on a local approach is proposed for the fatigue behaviour of concrete. Starting point in the model is the stress state in the so-called softening zone and the stress redistribution after an unloading-reloading cycle. Input in the model is the stress-crack opening relation, especially for unloading-reloading loops. Based on experimental results of deformation-controlled uniaxial tensile tests, a complete model (continuous-function model) is proposed for the tensile behaviour of concrete (Chapter 6). That constitutive model was also found to give a proper description of experimental results of other research known from the literature. Furthermore, the validity of the model is verified by numerical simulation of four-point bending tests and tensile tests on single notched plates (Chapter 8). For these numerical analyses, the FE code DIANA, a simple numerical "multi-layer model" and a hybrid method were applied. The FE code and the multi-layer model were also used to perform the fatigue analyses (Chapter 9). The results of the fatigue analyses, in terms of crack growth, cyclic creep curves and S-N curves, showed good similarity with those usually found in fatigue experiments (Chapter 2).

In the uniaxial tensile tests some specific features were observed. These features were explained by a structural behaviour that occurs in such a test. That structural behaviour has been extensively studied by experiments and by numerical analyses (Chapter 5). Furthermore, attention is paid to other phenomena that may affect the results obtained in deformation-controlled uniaxial tensile tests, like the effect of a pre-peak non-uniform stress distribution due, for instance, to eigenstresses caused by differential shrinkage (Chapter 7). Fracture mechanics parameters as influenced by different variables were determined. These parameters have been determined for different types of concrete, a varying maximum aggregate size, three concrete qualities, different curing conditions and for concrete that was preloaded in compression (Chapter 7).

In order to study the behaviour of concrete in fatigue tests more thoroughly and to investigate its relation with static tests, a new data-acquisition system was developed. That system made it possible to accurately measure a number of deformations on a rather large number of points in a loading cycle. Among other results, these unique experiments showed that damage and fracture in uniaxial tensile fatigue experiments also occurs very locally, just as in static tensile tests (Chapter 9).

Samenvatting

titel: **Lokale benadering van vermoeiing van beton**

Verschillende constructies worden onderworpen aan vermoeiingsbelasting. Vooral na de oliecrisis in de zeventiger jaren, toen betonnen offshore platforms hun intrede deden, is de belangstelling voor de eigenschappen van beton onder vermoeiingsbelasting of wisselende belasting sterk toegenomen. Tot op heden is de vermoeiing van beton hoofdzakelijk op een fenomenologische manier bestudeerd, terwijl de kennis omtrent de oorzaak en het mechanisme van vermoeiing van beton nog zeer beperkt is. In dit onderzoek is een model gepresenteerd voor de vermoeiing van beton, dat gebaseerd is op een lokale benadering. Uitgangspunt van het model is de spanningstoestand in de zogenoemde "softening zone" en de spanningsherverdeling na een lastwisseling. Invoer in het model is de spanningsscheuropeningsrelatie, met name voor ontlasten en herbelasten. Gebaseerd op experimentele resultaten van vervormingsgestuurde éénassige trekproeven is een compleet model ("continuous-function model") gepresenteerd voor het trekgedrag van beton (hoofdstuk 6). Het constitutieve model bleek ook de experimentele resultaten van andere, uit de literatuur bekende onderzoeken, op een adequate manier te beschrijven. Verder is de geldigheid van het model geverifieerd door middel van numerieke simulatie van vierpuntsbuigproeven en trekproeven op platen met aan één zijde een kerf (hoofdstuk 8). Voor de numerieke berekeningen is het eindige elementenpakket DIANA, een eenvoudig numeriek model "multi-layer model" en een hybride methode gebruikt. Het eindige elementenpakket en het "multi-layer" model zijn ook gebruikt om vermoeiingsberekeningen uit te voeren (hoofdstuk 9). Het resultaat van deze vermoeiingsberekeningen, voor wat betreft scheurgroei, cyclische kruipcurven en S-N curven, liet goede overeenkomsten zien met resultaten die gewoonlijk in vermoeiingsproeven worden gevonden (hoofdstuk 2).

In de éénassige trekproeven zijn enkele bijzondere kenmerken waargenomen. Deze kenmerken zijn verklaard met het specifieke constructiegedrag dat optreedt in een dergelijke proef. Het constructiegedrag is uitvoerig bestudeerd door middel van experimenteel en numeriek onderzoek (hoofdstuk 5). Verder is aandacht besteed aan andere fenomenen die de resultaten van vervormingsgestuurde éénassige trekproeven mogelijk kunnen beinvloeden. Een voorbeeld hiervan is een niet-uniforme spanningsverdeling in het gebied voordat de maximale belasting is bereikt, die het gevolg kan zijn van bijvoorbeeld eigenspanningen veroorzaakt door ongelijkmatige krimp (hoofdstuk 7). Breukmechanica-parameters zijn vastgelegd en de manier waarop die worden beinvloed door een aantal variabelen is onderzocht. Deze breukmechanica-parameters zijn bepaald

voor verschillende typen beton, een variërende maximale korrelafmeting, drie sterk-
teklassen, verschillende verhardingsomstandigheden en beton dat was voorbe-
last met een drukspanning (hoofdstuk 7).

Om het gedrag van beton in vermoeiingsproeven diepgaander te kunnen bestuderen
en om de relatie met statische proeven te kunnen onderzoeken is een nieuw gegevens-
verwerkingssysteem ontwikkeld. Dat systeem maakte het mogelijk om een aantal
vervormingen op een tamelijk groot aantal punten in een lus nauwkeurig te kunnen
meten. Naast andere resultaten lieten deze unieke experimenten zien dat beschadiging
en breuk in éénassige vermoeiingstrekproeven, evenals in statische trekproeven, zeer
lokaal optreden (hoofdstuk 9).

Curriculum vitae

Naam	Dirk Arend Hordijk
3 oktober 1957	Geboren te Westmaas
1977	Atheneum diploma R.S.G. Oud-Beijerland
1982-1983	wiskundeleraar R.S.G. Oud-Beijerland
1985	Diploma TU Delft, Faculteit der Civiele Techniek afstudeerrichting Betonconstructies
1985-1990	Wetenschappelijk medewerker in het Stevinlaboratorium van de Technische Universiteit Delft, voor een onderzoek van de Stichting voor de Technische Wetenschappen.
1990-heden	Werkzaam bij TNO-Bouw, afdeling Constructies

29 augustus 1986	Gehuwd met Simone Paula Tolenaars
17 november 1987	Geboren Karen Simone
14 november 1989	Geboren José Arenda